AEDC-TR-71-25

$C.1$

EXPERIMENTAL STUDY OF SIMULATED HIGH ALTITUDE ROCKET EXHAUST PLUMES

Wendell Norman, Max Kinslow, and J. W. L. Lewis

ARO, Inc.

July 1971

VON KÁRMÁN GAS DYNAMICS FACILITY
ARNOLD ENGINEERING DEVELOPMENi CENTER
AIR FORCE SYSTEMS COMMAND
ARNOLD AIR FORCE STATION, TENNESSEE

NOTICES

EXPERIMENTAL STUDY OF
SIMULATED HIGH ALTITUDE
ROCKET EXHAUST PLUMES

Wendell Norman, Max Kinslow, and J. W. L. Lewis
ARO, Inc.

FOREWORD

The work reported herein was done at the request of the Air Force Rocket Propulsion Laboratory (AFRPL), Air Force Systems Command (AFSC), under Program Element 62302F. The program manager was Dr. Larry Quinn, and technical guidance was provided by Dr. J. D. Stewart of the Aerospace Corporation.

The results of tests presented were obtained by ARO, Inc. (a subsidiary of Sverdrup & Parcel and Associates, Inc.), contract operator of the Arnold Engineering Development Center (AEDC), AFSC, Arnold Air Force Station, Tennessee, under Contract F40600-71-C-0002. The tests were conducted from February 18 to May 1, 1970, under ARO Project No. VT0050, and the manuscript was submitted for publication on September 10, 1970.

The contributions of several others are gratefully acknowledged: W. D. Williams did much of the work on the electron beam; R. D. Mitchell and R. F. Armstrong performed the actual testing in Tunnel M. and the former also participated in other phases of this work; Jerry Hahn was Project Engineer for the Tunnel D entry.

This technical report has been reviewed and is approved.

Emmett A. Niblack, Jr.
Lt Colonel, USAF
AF Representative, VKF
Directorate of Test

Joseph R. Henry
Colonel, USAF
Director of Test

ABSTRACT

The gas dynamic structure of high altitude rocket plumes has been studied in a low density tunnel to obtain basic data on plume size and shape and to determine the extent of the mixing region between the free-stream and rocket gases. The rocket was simulated by specially designed ejectors using helium and CO_2 as the gases, with conditions chosen to simulate a 100,000-lb-thrust rocket at an altitude of 80 km. Data taken included impact pressure surveys, density measurements of the free-stream and plume gas, temperature measurements, and color photographs. The last three of these were taken using electron beam techniques. The result of the study is a set of basic data. Analysis and interpretation of the data will be performed under a separate study.

CONTENTS

ILLUSTRATIONS

TABLES

APPENDIXES

NOMENCLATURE

		First Appearance or Definition
A	Einstein's spontaneous emission coefficient	Eq. (II-1)

A^*	Throat area of nozzle	Eq. (3)
A_e	Exit area of nozzle	Fig. 3
B_o	Rotational constant for the $v''' = 0$ state of $N_2 X' \Sigma$	Eq. (II-5)
C, C_0, C_1, C_2	Constants	Appendix II
C_F	Thrust coefficient of rocket	Eq. (5)
C_{F_m}	Maximum thrust coefficient of a rocket (exhausting into a vacuum)	Eq. (6)
c	Speed of light	Eq. (II-1)
d^*	Diameter of nozzle throat	Table I
d_e	Diameter of nozzle exit = $2y_e$	Table I
F	Vacuum thrust of rocket	Eq. (4)
F_m	Maximum vacuum thrust of rocket $(A_e/A^* \rightarrow \infty)$	Eq. (6)
$[G]_0$	Muntz G-factor	Eq. (II-6)
h	Planck's constant	Eq. (II-1)
h_o	Stagnation enthalpy of tunnel gas	Table II
I	Radiation intensity	Eq. (II-1)
I_{oo}^o	Value of I_{oo} with no collisonal decay losses	Eq. (II-14)
$I_{v'',K'-1}^{v'K'}$	Radiation intensity of vibration-rotation emission	Eq. (II-5)
$I_{v''}^{v'}$; $I_{v'v''}$	Radiation intensity of vibrational band v'v"	Eq. (II-7)
j	Current density of electron beam	Eq. (II-1)
K_1	Constant	Eq. (1)
K', K'', K'''	Rotational quantum numbers	Eq. (II-4)
$\widetilde{Kn}$	Knudsen number based upon orifice diameter, T_r, and p_w wall conditions	Appendix I
k	Boltzmann's constant	Eq. (II-4)
k	Quenching constant for helium intensities	Eq. (II-3)
k_o, k_1	Quenching constants for v = 0 and 1 for vibrational band intensities	Eq. (II-14)

L	Inviscid scaling parameter for plume geometry	Eq. (17)
M_e	Exit Mach number of rocket	Eq. (9)
M_∞	Free-stream Mach number	Eq. (12)
$\dot{m}$	Mass flow rate through rocket nozzle	Eq. (3)
N	Number density	Eq. (II-1)
p	Pressure	
$p(vv')$	Vibrational band strength for emission	Eq. (II-7)
$\tilde{p}(vv')$	Vibrational band strength for excitation	Eq. (II-7)
$\bar{p}$	Orifice effect parameter	Eq. (I-3)
p_c	Chamber pressure of rocket	Eq. (5)
p. f.	Partition function	Eq. (II-5)
p_i	Pressure inside orifice	Eq. (I-3)
$p_{i_{fm}}$	Free molecular limit of p_i	Eq. (I-3)
p_o	Reservoir pressure	Table II, Eq. (15)
p_o'	Measured impact (pitot probe) pressure	Table II
p_w	Wall pressure in the absence of an orifice	Eq. (I-1)
p_1	Pressure of rocket exhaust gas in plume	Eq. (10)
p_∞	Free-stream static pressure	Eq. (10)
$q(ij)$	Franck-Condon factor	Eq. (II-10)
q_∞	Free-stream dynamic pressure	Eq. (15)
$\dot{q}$	Heat-transfer rate	Eq. (I-7)
$\dot{q}_{fm}$	Free molecular value of $\dot{q}$	Eq. (I-9)
$\dot{q}_{FR}$	Continuum (Fay-Riddell) value of $\dot{q}$	Eq. (I-10)
R	Gas constant	Eq. (I-7)
.R	Density dependent factor for quenching corrections on vibrational intensity ratios	Eq. (II-20)

R_e	Electron transition moment	Eq. (II-9)
Re_O	Unit Reynolds number at a stagnation point $\rho_\infty V_\infty / \mu_O$	Table II
Re_2	Unit Reynolds number behind a standing normal shock $\rho_\infty U_\infty / \mu_2$	Table II
Re_{2,r_p}	Probe Reynolds number $\rho_\infty U_\infty r_p / \mu_2$	Eq. (I-1)
Re_∞	Unit Reynolds number based on free-stream condition $\rho_\infty U_\infty / \mu_\infty$	Table I
r	Radius from orgin to a point in the plume flow field	Eq. (1), Fig. 2
r^*	Throat radius of rocket nozzle	Eq. (12)
$\bar{r}_{ij}$	r-centroid	Eq. (II-12)
r_p	Radius of impact probe	Eq. (I-1)
T_R	Rotational temperature	Eq. (II-5)
T_r	Reference temperature	Eq. (I-6)
T_v	Vibrational temperature	Eq. (II-7)
T_w	Wall temperature	Eq. (I-2)
T_O	Reservoir temperature	Table II
T_{op}	Reservoir temperature of plume gas	Fig. 12a
T_∞	Tunnel free-stream static temperature	Table II
U_1	Velocity of rocket exhaust gas in plume	Eq. (10)
U_∞	Free-stream velocity	Eq. (10)
U_{lim}	Limiting velocity of rocket exhaust gas	Eq. (4)
U^*	Velocity of gas at rocket throat	Eq. (3)
U_r, U_θ	Components of velocity in plume	Eq. (1) Fig. 2
v	Vibrational quantum number	Appendix II
W	Normalized distance for plume	Eq. (12)
x	Axial distance from exit plane of rocket nozzle	Fig. 4
y	Perpendicular distance from axis to point in plume flow field	Fig. 2

y_e	Value of y for rocket exhaust	Eq. (14), Fig. 4
y_{max}	Maximum size of plume	Table I
z	Parameter for orifice effect	Eq. (I-4)
α	Thermal accommodation coefficient	Eq. (I-5)
β	Inclination angle of contact surface	Eq. (10), Fig. 4
γ	Ratio of specific heats	Eq. (8)
δ^*	Boundary-layer displacement thickness	Section 3.3
θ	Angle from axis to point in the flow field	Eq. (1), Fig. 2
θ_{lim}	Value of θ at edge of plume gas	Section 2.2
θ_m	Turning angle of rocket flow at corner	Fig. 4
θ_N	Nozzle angle	Fig. 2
κ	Dimensionless heat-transfer rate parameter	Eqs. (1-5), (I-7)
λ	Parameter for nozzle	Eqs. (1), (7)
λ	Wavelength	Eq. (II-1)
λ_∞	Mean free path at free-stream conditions	Tables I and II
$\lambda_{v''K''}^{v'K''}$	Wavelength of the vibration-rotation emission line	Eq. (II-5)
μ_0	Coefficient of viscosity at stagnation point	Eq. (I-10)
μ_2	Coefficient of viscosity behind standing normal shock	Table II
μ_∞	Coefficient of viscosity at free-stream conditions	Table II
ν	Prandtl-Meyer angle	Eq. (15)
ρ^*	Density of rocket exhaust at nozzle throat	Eq. (3)
ρ_1	Density of rocket exhaust gas in plume	Eq. (1)

ρ_2	Density behind a standing normal shock	Eq. (I-1)
ρ_∞	Free-stream density	Eq. (10)
τ_r	Radiation life time	Eq. (II-1)

SECTION I
INTRODUCTION

Thus far, attempts to account for the observed radiation of rocket plumes at altitude have been primarily concerned with the radiative characteristics of the exhaust gas itself, and the role of fluid mechanical interactions has not been widely studied experimentally. As yet, a satisfactory accounting for all of the observed features has not been obtained.

It is possible at high altitudes that additional radiation can be generated by the interaction of the plume gas with the free-stream gas by one of several processes. The work reported herein was undertaken to provide the information necessary to arrive at a gas dynamic description of the flow field at high altitudes. This information can then be used with knowledge of the reaction rates and radiative characteristics for the appropriate components of the gases to calculate the radiative intensity in the interaction or mixing zone between the two gases.

At lower altitudes the exhaust plume, which is the same order of magnitude in size as the rocket, behaves as an inviscid solid body as far as the external flow is concerned. In this regime the external flow of the atmospheric gas and the internal flow of rocket exhaust gas may be considered independently with the boundary condition that at the interface between the two regions there is equality of pressure in the two gas streams. The method of characteristics has been used to solve the basic inviscid flow equations for both the external and the internal flow fields. One of the most general of these method-of-characteristics programs was developed by Lockheed and is reported in Ref. 1.

At higher altitudes the ambient flow becomes more rarefied and the plume becomes larger until it far exceeds the rocket itself in size. At this altitude the rocket plume, the shape and characteristics of which are determined by the rocket motor and properties of the exhaust gas as well as rocket speed and atmospheric properties, is the major factor in the determination of the flow field about the rocket and the disturbance in the atmosphere. "Observables" such as radiation caused by the passage of the rocket through the atmosphere are largely determined by the properties of the rocket exhaust plume.

At lower altitudes the radiation is primarily due to the hot exhaust gases. At higher altitudes, as the flow becomes more rarefied, the atmospheric gases can penetrate the exhaust plume and thereby cause chemical reactions to take place between the high energy gases with subsequent emission of significant additional radiation. The need for information on the basic plume structure and the aerodynamics of this mixing region was the reason for the present experimental study.

Previous theoretical studies have been made (Refs. 2 through 7) of rocket exhaust plumes at high altitudes. These were primarily concerned with the prediction of the plume size and shape. Some of these (e.g., Refs. 2 and 3) were semiempirical in that simplified solutions for the plume boundary were obtained by fitting equations for the density variations to solutions obtained by the method of characteristics. Some experimental data had been obtained from plumes exhausting from a rocket into a vacuum or into a static pressure region. There was almost a complete absence of experimental results on the interaction of a plume and a high speed rarefied gas stream. The limited data that had been obtained comprised photographic and spectrographic results from actual rocket flights through the atmosphere.

The present work was carried out to determine the density variation of the exhaust and the ambient gases across the plume, as well as the size and shape of the free-stream and plume interaction region. The effect of parameters such as free-stream Mach number and density, exhaust gas properties, and rocket nozzle geometry on plume characteristics was investigated.

SECTION II
BASIC THEORY AND SELECTION OF TEST CONDITIONS

2.1 GENERAL FEATURES OF A PLUME

The general features of a rocket plume at high altitude are shown in Fig. 1. The plume is formed by the expansion of the rocket exhaust gases into the rarefied atmosphere. The oncoming free-stream gas causes the plume gas to be swept downstream. At lower altitudes than that for which Fig. 1 has been drawn, the free-stream pressure is higher, and the plume size consequently smaller.
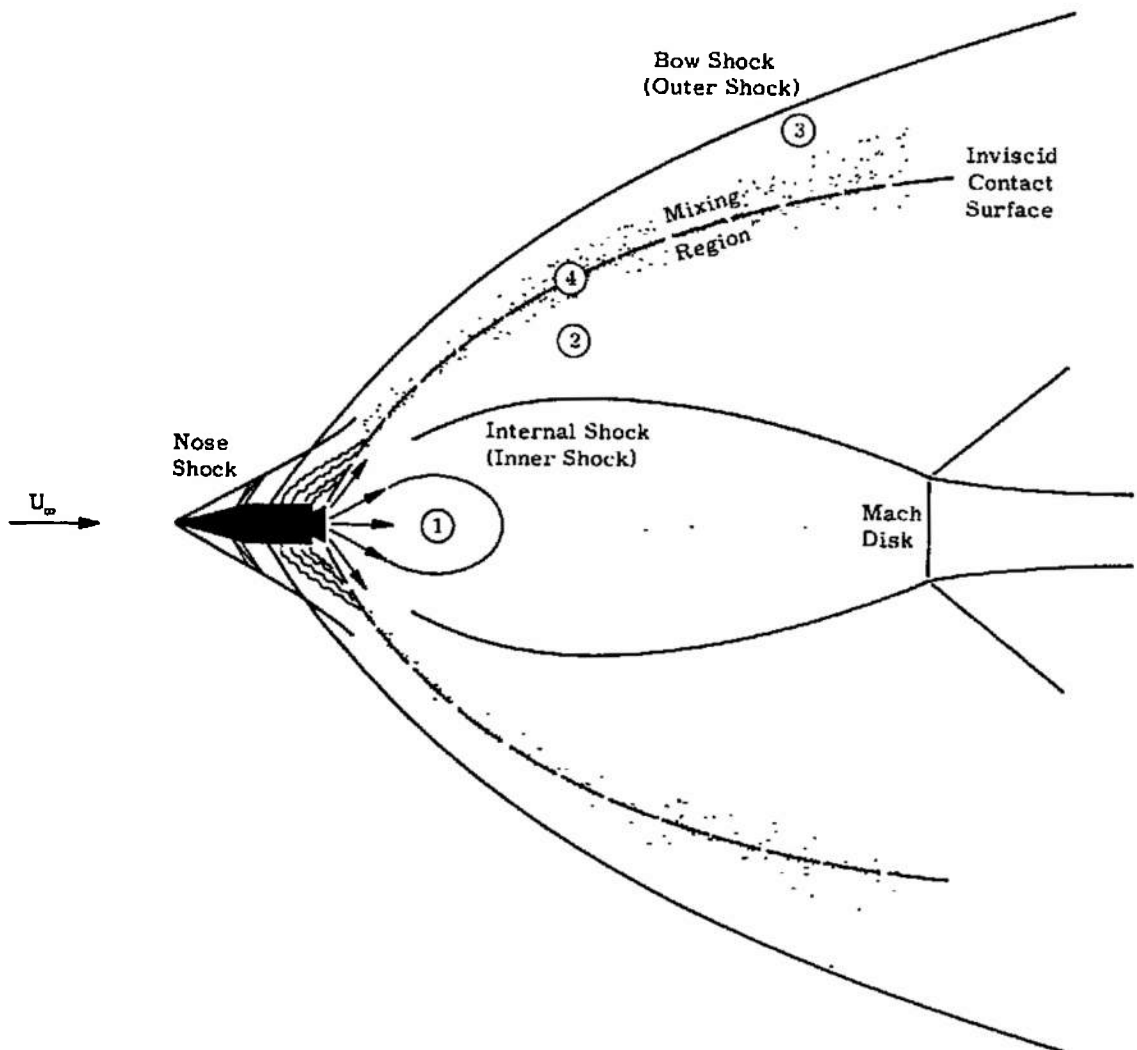
Fig. 1 General Features of a High Altitude Rocket Plume

The plume often induces flow separation on the vehicle forward of the exit plane of the nozzle. A shock is formed in front of the separated region, which interacts with the shock from the nose of the vehicle. The prominent bow shock is initiated by this interaction, but the bow shock is influenced primarily by the plume itself, which presents the appearance of a blunt body to the free stream. For the altitude range of interest in the present study, the plume is considerably larger than the vehicle so that the details of the interactions of the vehicle generated shocks are only of minor importance.

An additional shock is formed within the plume, because of the coalescing of pressure waves from the curved inviscid contact surface. This annular shock tends to close on itself farther downstream, leading to a normal shock, called the Mach disk, at some point in the flow.

Between the bow shock and the internal shock is a region within which the plume gas and the free-stream gas are in contact. It is often assumed, for simplicity, that the two gases are separated by an infinitesimally thin layer called the inviscid contact surface. Actually, diffusion between the two gases must take place so that there is a mixing region of finite thickness throughout which the two gases are present in varying amounts.

There are at least four regions of the flow field that can contribute to the total plume radiation (Fig. 1):

1. The region of hot exhaust gas near the exit plane and farther downstream.

2. The region of exhaust gas that has passed through the internal shock or Mach disk with a consequent increase in the static temperature.

3. The atmospheric gas heated by the strong bow shock.

4. The mixing region between the two gases in which chemical reactions between the components of the two gases can take place.

The purpose of the experimental study reported herein was to establish the fluid mechanics aspects of the last three of these regions. This was done by determining impact pressure distributions throughout the plume to establish the relative thicknesses of the regions, and by determining with an electron beam the distributions of temperature and density of the gases, with the emphasis on the mixing region. It was not possible to use an actual rocket in these studies, so direct measurements of radiation were not made. Instead, the gases were chosen for convenience in making the necessary measurements. Thus, nitrogen was used for the free-stream gas, and helium for the exhaust gas, because the electron beam techniques for determining densities and temperature are reasonably well established for these gases. Carbon dioxide was also used for the exhaust gas for some runs, in order to check the correctness of the scaling parameters used, but for this gas determination of the density and temperature by the electron beam technique is not presently practical.

2.2 SIMPLIFIED DESCRIPTIONS OF THE FLOW FIELD

The flow field of a rocket exhausting into a vacuum or a constant pressure region has received considerable study. The case of a rocket

exhausting into a moving free stream has received less study. Within the assumption of inviscid continuum fluid mechanics, exact solutions may be obtained for specific cases by use of one of the many axisymmetric characteristics computer codes available. There is a place, however, for simpler analytical solutions. Such a solution has been given in Ref. 2. The results given there are used here to determine an approximate relation for the location of the inviscid boundary between the plume gas and the free-stream gas. The purpose in presenting these results is not to obtain a result which necessarily gives the proper location, but to show what the basic similarity variables are.

Consider first the case of a rocket exhausting into a vacuum or a constant pressure region, as shown in Fig. 2. The flow field within the nozzle is normally assumed to be a simple source flow, or a uniform parallel flow, although the flow field within an actual nozzle may be considerably more complicated. At the corners of the nozzle, the flow will undergo a Prandtl-Meyer expansion through an angle sufficient to match the external pressure. The bounding streamline will then curve inward, because of the two-dimensional nature of the flow. The curvature of this line leads to a coalescing of pressure waves and the generation of the internal shock.
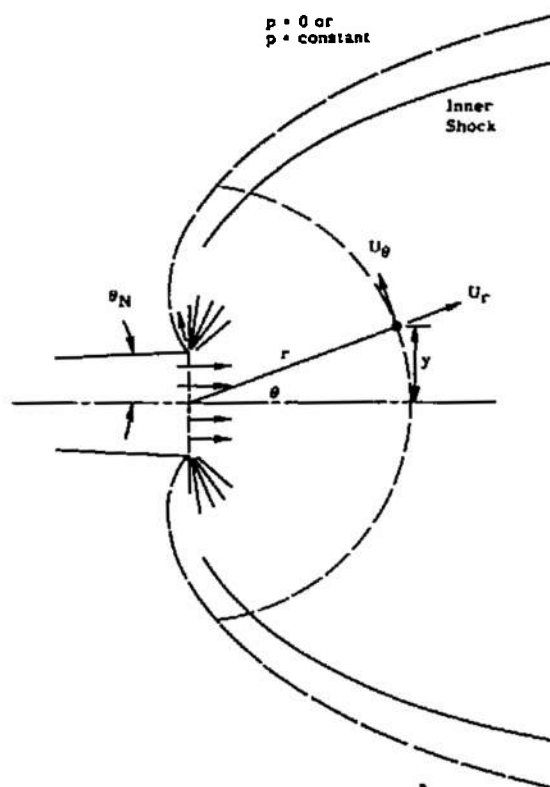
Fig. 2 Flow Field for Expansion into a Region of Uniform Pressure

The simplified result for the portion of the plume gas within the internal shock is based upon the observation that as the *limiting velocity* is reached, U_θ approaches zero. It then follows from the continuity equation that

$$\rho_1 U_r r^2 = \text{function of } \theta$$

It must be emphasized that this result is valid only for U_r near to U_{lim}. The form of the function was selected on the basis of analytical simplicity, and by fitting a number of exact numerical solutions. The form chosen in Ref. 2 and used here is

$$\rho_1 U_r r^2 = K_1 f(\theta)$$
$$= K_1 e^{-\lambda^2} (1 - \cos \theta)^2 \qquad (1)$$

with K_1 and λ constants. Reference 3 uses the function $(\dfrac{\cos\theta - \cos \theta_{lim}}{1 - \cos \theta_{lim}})$, but Eq. (1) is said to provide a better fit. The constants K_1 and λ are evaluated by requiring that the integrated forms of the continuity and momentum equations hold. The mass flow rate through the surface of constant radius r is

$$\dot{m} = 2\pi \int_0^{\theta_{lim}} \rho_1 U_r r^2 \sin \theta \, d\theta$$

Using the distribution of Eq. (1) gives

$$\dot{m} = (\pi^{3/2} K_1/\lambda) \, \text{erf} \, (\lambda(1 - \cos \theta_{lim}))$$

Practical values of λ are fairly high (>5) thus the value of the error function is very close to unity. Therefore

$$\dot{m} \approx \pi^{3/2} K_1/\lambda \qquad (2)$$

This must be equal to the mass flow rate of plume gas through the nozzle throat

$$\dot{m} = \rho^* U^* A^* \qquad (3)$$

Setting the error function equal to unity is necessary for reasons other than simplifying the resulting equations. The flow field interior to the internal shock is independent of the boundary, so that θ_{lim} should not appear in the final result. An alternate view is that the distribution of mass flow rate is very concentrated near the centerline, and the mass

flow rate in the outer portions of the plume is small. Note from Eq. (2) that for a given mass flow rate, λ must be a specific constant. Use of a variable λ as done in Ref. 2 is not justified.

The momentum equation is integrated along the exit plane and along a surface in the flow field of constant r. If F is the vacuum thrust of the rocket, then,

$$F = 2\pi \int_0^{\theta_{lim}} (\rho_1 U_r r^2) U_r \cos\theta \sin\theta \, d\theta$$

Letting $\theta_{lim} \to \infty$ and setting U_r to U_{lim} gives

$$F = \pi^{3/2} K_1 U_{lim} (1 - 1/\sqrt{\pi}\lambda)$$
$$= \dot{m} U_{lim} (1 - 1/\sqrt{\pi}\lambda) \tag{4}$$

The thrust coefficient, C_F, is defined by

$$F = C_F A^* p_c \tag{5}$$

and the maximum thrust coefficient, C_{F_m}, by

$$F_m = C_{F_m} A^* p_c$$
$$= \dot{m} U_{lim} \tag{6}$$

From these

$$\lambda = 1/\sqrt{\pi}\left(1 - \frac{C_F}{C_{F_{max}}}\right) \tag{7}$$

For an ideal gas

$$C_{F_m} = \gamma\sqrt{\frac{2}{\gamma-1}}\left(\frac{2}{\gamma+1}\right)^{\frac{\gamma+1}{2(\gamma-1)}} \tag{8}$$

and

$$\frac{C_F}{C_{F_m}} = \sqrt{\frac{\gamma-1}{2}} \frac{M_e(1 + 1/\gamma M_e^2)}{\left(1 + \frac{\gamma-1}{2}M_e^2\right)^{1/2}} \tag{9}$$

Figure 3 gives a plot of λ versus the nozzle area ratio for given values of γ.

-7
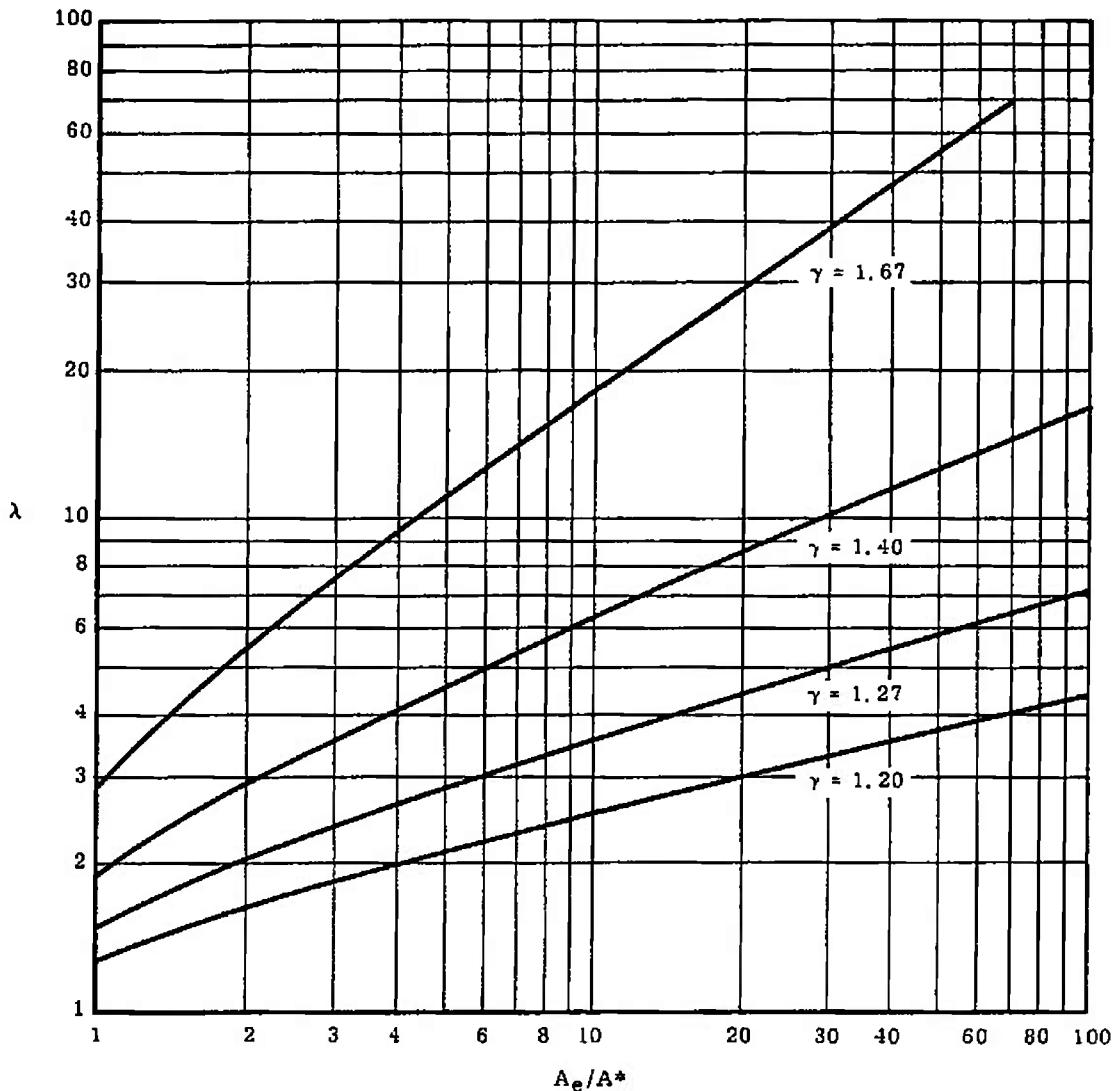
Fig. 3 Plume Spreading Parameter, λ

Now the problem of the location of the inviscid contact surface is considered. Figure 4 presents a simplified sketch. Basically, the slope of the contact surface at a location r, θ is assumed to be that for which the pressure on each side of the contact surface is the same. Thus, the pressure at a, which is determined by turning the free stream through the angle β, is equal to the pressure at 2, which is determined by turning the plume gas through the angle $\theta - \beta$. To formulate the equations, several assumptions are made. First, the contact surface is infinitesimally thin, and the regions between the bow shock and the internal plume shock are very thin. Second, the influence

8
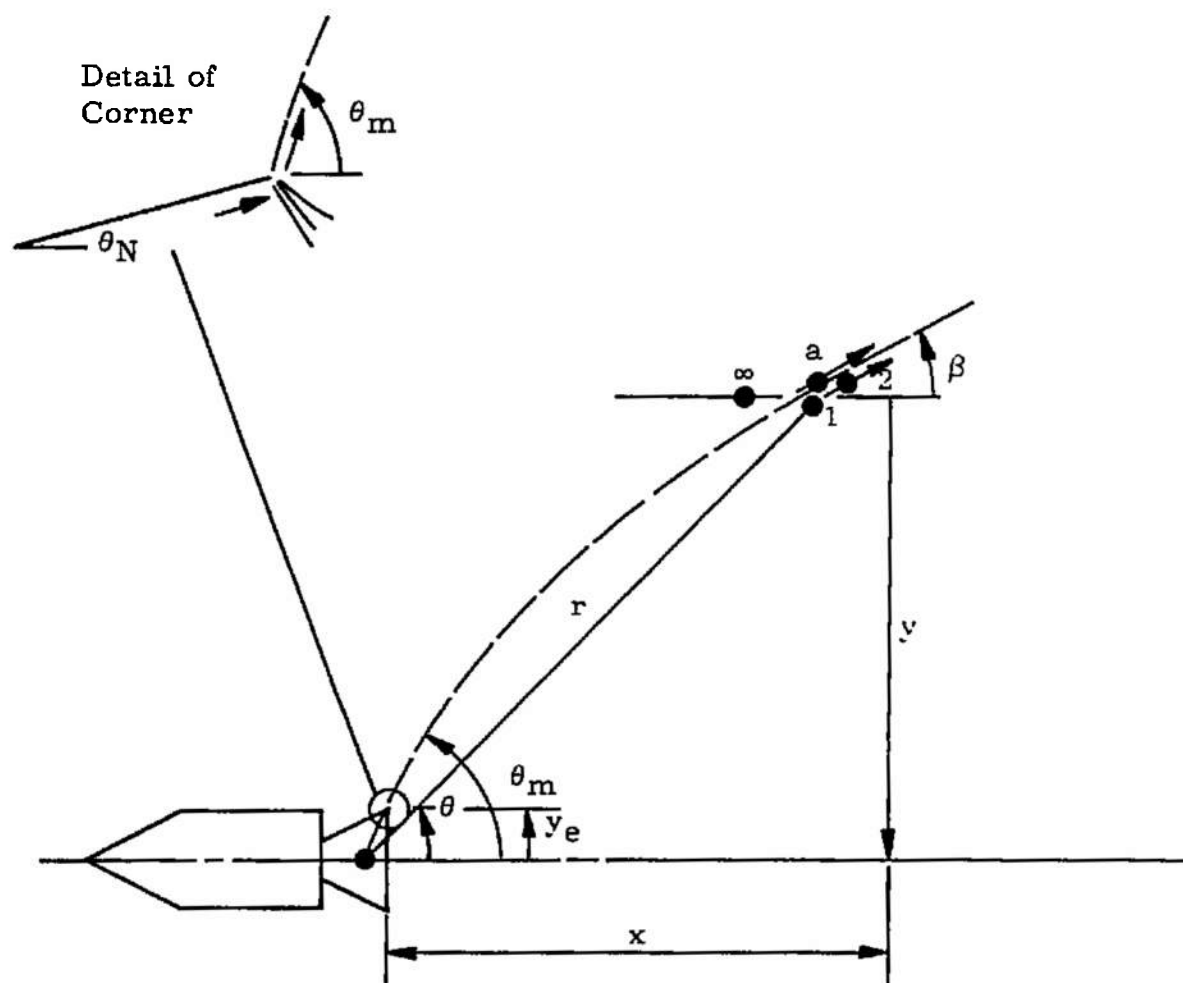
Fig. 4 Simplified Sketch of Plume Contact Surface

of the flow over the body on the plume may be neglected. Third, the simple Newtonian pressure law may be used. The equality of the pressures then leads to

$$p_\infty + \rho_\infty U_\infty^2 \sin^2\beta = p_1 + \rho_1 U_1^2 \sin^2(\theta - \beta) \tag{10}$$

The next assumption is that the distribution of Eq. (1) holds within the plume. This assumption is not a particularly good one, because, as mentioned above, the distribution given by Eq. (1) may not be accurate at the outer edges of the plume. Nonetheless, the result is used, because the purpose here is to develop the basic similarity variables, not determine the shape of the plume for specific cases. Thus

$$\rho_1 U_1^2 = \frac{K_1 f(\theta)}{r^2} \, U_{1im} \tag{11}$$

In addition, the pressure p_1 is neglected. By using

$$\sin\beta = \frac{\dfrac{dy}{d\theta}}{\sqrt{r^2 + \left(\dfrac{dr}{d\theta}\right)^2}}$$

and

$$\sin(\theta - \beta) = \frac{r}{\sqrt{r^2 + \left(\dfrac{dr}{d\theta}\right)^2}}$$

the result becomes

$$\left(\frac{1}{\gamma M_\infty^2}\left(r^2 + \left(\frac{dr}{d\theta}\right)^2\right)\right) + \left(\frac{dy}{d\theta}\right)^2 = \frac{C_{F_m} P_c}{2 q_\infty \sqrt{\pi}} \lambda r^{*2} \, f(\theta)$$

Now let

$$W = \frac{y}{r^*}\sqrt{\frac{1 + \gamma M_\infty^2 \sin^2\theta}{\gamma M_\infty^2 \sin^2\theta} \, \frac{q_\infty}{C_{F_m} P_c}}$$

$$= \frac{r}{r^*}\sqrt{\frac{1}{\gamma M_\infty^2}(1 + \gamma M_\infty^2 \sin^2\theta) \, \frac{q_\infty}{C_{F_m} P_c}} \tag{12}$$

and the result becomes

$$\left(\frac{dW}{d\theta}\right)^2 + \frac{1 + \gamma M_\infty^2}{(1 + \gamma M_\infty^2 \sin^2\theta)^2} \; W^2 = \frac{\lambda}{2\sqrt{\pi}} \; f(\theta) \tag{13}$$

The boundary conditions to be applied to this equation are

$$\text{at } \theta = \theta_m \quad W = \frac{y_e}{r^*}\sqrt{\frac{1 + \gamma M_\infty^2 \sin^2\theta_M}{\gamma M_\infty^2 \sin^2\theta_M}} \; \frac{q_\infty}{C_{F_m} P_c} \tag{14}$$

in which y_e is the exit radius of the nozzle. Note that the origin of the coordinate system has been located on the centerline at the intersection of the extension of the slope of the contact surface at the corner. This has been done to make the equations somewhat simpler, although in general the distance y_e is small in comparison with the plume size.

The maximum turning angle is established by a pressure balance at the corner. A sketch is shown in Fig. 4. The turning angle of the nozzle flow is $\theta_m - \theta_N$. The pressure is then obtained from the isentropic tables, i.e.,

$$p = \frac{p}{p_o} \; (\nu(M_e) + \theta_m - \theta_N) \; p_c$$

in which ν is the Prandtl-Meyer function. Setting this pressure equal to the pressure attributable to the free stream (and neglecting p_∞) gives

$$2 q_\infty \sin^2\theta_m = p_c \frac{p}{p_o} \; (\nu(M_e) + \theta_m - \theta_N)$$

or

$$\frac{\frac{p}{p_o} \; (\nu(M_e) + \theta_m - \theta_N)}{2 \sin^2\theta_m} = \frac{q_\infty}{p_c} \tag{15}$$

For a given nozzle, and given γ, the value of θ_m is therefore dependent upon the ratio of the chamber pressure to the free-stream dynamic pressure (the result can also be used for the case of no flow by setting the pressure equal to p_∞).

Combining Eqs. (12), (13), and (14) leads to

$$\frac{y - y_e}{r^*} = \sqrt{\frac{\gamma M_\infty^2 \sin^2\theta}{1 + \gamma M_\infty^2 \sin^2\theta}} \; \frac{C_{F_m} P_c}{q_\infty} \; W(\theta, \lambda, \theta_m, \gamma M_\infty^2)$$

in which θ_m is a function of p_0/q_∞. Usually the influence of θ_m is minor and may be neglected. Also, for simplicity, y_e may be neglected. Then

$$\sqrt{\frac{q_\infty}{C_{F_m} p_c}} \; \frac{y}{r^*} = \text{function } (\theta, \lambda, \gamma M_\infty^2) \qquad (16)$$

This yields the basic similarity parameters. The parameters q_∞, p_c, and r^* can be absorbed into a y scaling parameter, defined by

$$L = r^* \sqrt{\frac{C_{F_m} p_c}{q_\infty}} \qquad (17)$$

The primary remaining variables are λ and γM_∞^2. Of these, λ is of primary importance and γM_∞^2 of secondary importance. In fact, if

$$\gamma M_\infty^2 \sin^2 \theta \gg 1$$

then

$$\sqrt{\frac{q_\infty}{C_{F_m} p_c}} \; \frac{y - y_e}{r^*} = \left(\frac{\lambda}{2\sqrt{\pi}}\right)^{1/2} \int_\theta^{\theta_M} \sqrt{f(\theta)} \, d\theta \qquad (18)$$

The parameter λ should not be absorbed into the y scaling in this case, because the parameter λ also appears in the function $f(\theta)$, Eq. (1). The particular form of Eq. (1) is such that an analytical integration does not appear possible. However, if the approximation

$$1 - \cos \theta \approx \frac{2}{\pi} \theta$$

is made (see Fig. 5), then the result may be integrated to give

$$\sqrt{\frac{q_\infty}{C_{F_m} p_c}} \left(\frac{y - y_e}{r^*}\right) = \frac{\pi^{5/4}}{4\sqrt{\lambda}} \left[\text{erf} \left(\frac{\lambda}{\sqrt{2}} (1 - \cos \theta_m)\right) - \text{erf} \left(\frac{\lambda}{\sqrt{2}} (1 - \cos \theta)\right)\right]$$

or by setting the value of the first error function to unity, as done earlier, gives

$$\sqrt{\frac{q_\infty}{C_{F_m} p_c}} \left(\frac{y - y_e}{r^*}\right) = \frac{\pi^{5/4}}{4\sqrt{\lambda}} \left[1 - \text{erf} \left(\frac{\lambda}{2} (1 - \cos \theta)\right)\right] \qquad (19)$$

The value of Eq. (19) is not in the accuracy with which it represents more exact solutions, but it is the explicit form in which the basic scaling parameters appear. From this it can be seen that the main parameter is λ. Other parameters appear in groupings such that it is not necessary to match actual values, and ratios of parameters may be matched.
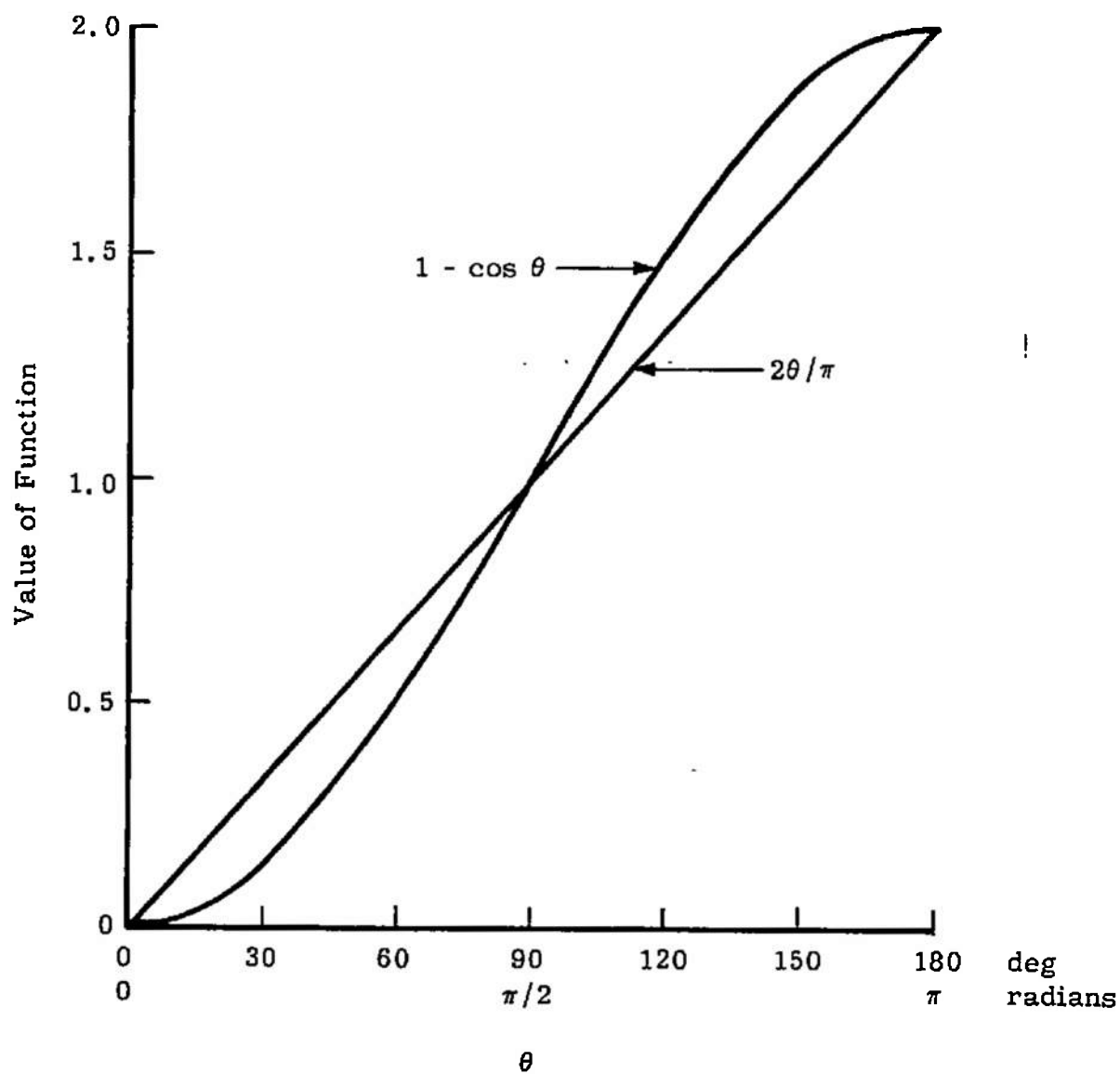
Fig. 5 Approximate Representation for 1 - cos θ

The scaling parameters considered up to this point have been established on the basis of inviscid continuum fluid mechanics. Some other factors of importance are associated with viscous effects and low density effects. These are important primarily in the mixing region. The simulation parameters of this region are considerably more complicated, and no attempt will be made here to establish the specific parameters. A preliminary look was obtained by testing at two different density levels by using two wind tunnels.

2.3 SELECTION OF TEST CONDITIONS

The tests were run in two VKF wind tunnels: Low Density Hypersonic Wind Tunnel (M) and Supersonic Wind Tunnel (D). Descriptions of these tunnels are given in Section III. The operating parameters of these tunnels established the test section conditions, as given in Table I, and the size of the plume simulator.

For a number of reasons it was desirable to use helium as the plume gas. The first of these was because of the suitability of helium for density measurements by use of the electron beam technique. The second was that helium has a very low condensation temperature and, therefore, is less likely to undergo condensation within the plume. Therefore, the helium nozzle was scaled to give the same value of λ as a real nozzle, for which a value of γ of 1.27 was selected.

For the full-scale flight nozzle, the following was assumed:

$$A_e/A^* = 25$$
$$\gamma = 1.27$$

Therefore,

$$\lambda = 4.7$$

For a helium exhaust from a model nozzle,

$$\gamma = 1.67$$

and for the same value of λ,

$$A_e/A^* = 1.61$$

The maximum feasible chamber pressure for Tunnel M was found to be 5 psi for the model tested. For the same value of θ_m the corresponding chamber pressure for flight is 440 psi.

TABLE I
SUMMARY OF TEST CONDITIONS

Condition	First Condition				Second Condition				
	Flight	IC5	IAB	IIB	Flight	IC2	IAC	IAA	IB
Tunnel		M	M	D		M	M	M	M
Free-stream Gas	Air	N_2	N_2	N_2	Air	N_2	N_2	N_2	N_2
Free-stream Conditions									
M_∞	18.00	18.15	18.15	5.0	10.00	18.15	18.15	18.15	18.15
P_∞, psi	1.5×10^{-4}	1.2×10^{-4}	1.2×10^{-4}	1.5×10^{-2}	1.5×10^{-4}	1.2×10^{-4}	1.2×10^{-4}	1.2×10^{-4}	1.2×10^{-4}
q_∞, psi	3.4×10^{-2}	2.7×10^{-2}	2.7×10^{-2}	2.6×10^{-1}	1.0×10^{-2}	2.7×10^{-2}	2.7×10^{-2}	2.7×10^{-2}	2.7×10^{-2}
Re_∞ per in.	200	1250	1250	2.9×10^5	125	1250	1250	1250	1250
λ_∞, in.	0.12	0.022	0.022	0.00021	0.12	0.022	0.022	0.022	0.022
$100\lambda_\infty/y_{max}$	0.024	0.022	0.022		0.039	0.022	0.022	0.022	0.022
Altitude, km	80	1.59	1.81	0.015	80	2.68	1.36	1.88	5.39
Nozzle									
Gas		He	CO_2	He		He	CO_2	CO_2	He
γ	1.27	1.67	1.27	1.67	1.27	1.67	1.27	1.27	1.67
A_e/A^*	25	1.61	25	1.61	25	1.61	25	25	25
M_e	4.26	2.07	4.26	2.07	4.26	2.07	4.26	4.26	7.09
d^*, in.	12.9	0.315	0.030	0.315	12.9	0.315	0.080	0.080	0.030
d_e, in.	64.7	0.40	0.15	0.40	64.7	0.40	0.40	0.40	0.40
P_c, psi	440	5	400	56	53	2	100	50	450
θ_m	41	42	43	42	36	37	36	32	22
λ_∞	4.7	4.5	4.7	4.5	4.7	4.5	4.7	4.7	33.5
$L = r^* \sqrt{C_{F_m} P_c / q_\infty}$	87 ft	2.7 in.	2.58 in.	2.94 in.	54 ft	1.70 in.	3.44 in.	2.43 in.	2.31 in.
Purpose		Basic data	Check simulation	Check λ_∞ effect		Basic data	Check simulation	Check P_c effect	Check γ effect
Data									
Impact Pressure		X	X	X		X	X	X	X
Electron Beam Photography		X	X			X	X	X	X
ρ, T		X				X			

The conditions are summarized in Table I. The symbolism for the conditions unfortunately underwent considerable alteration as modifications of the original test plan were found to be necessary, so that the final designations do not have the consistency that would be present if the designations had been made later. The designations have been preserved in the form used during the experimental portion of the program.

The first four columns list conditions for tests corresponding to one flight condition. Condition IC5 was the corresponding case in Tunnel M, using helium as the plume gas. Condition IAB was run in Tunnel M with CO_2 as the plume gas, in order to check the basic scaling parameters. Condition IIB was run in Tunnel D to check the effect of greater free-stream density.

The next three columns correspond to the first three, but with a reduced chamber pressure. The last two columns represent some extra conditions.

It was sometimes impossible to achieve the desired conditions in the tunnel. The reasons were various, but typically were the inability to pump the desired mass flow rate or the inability to achieve the desired maximum pressure. Therefore, there was not always obtained in practice the exact correspondence desired.

The various conditions are discussed in order in the following paragraphs. The first condition (see Table I) is for flight at an altitude of 80 km at a free-stream Mach number of 18, with the latter chosen to correspond to the test section Mach number of Tunnel M. The nozzle geometry was given earlier. The chamber pressure of 440 psi was selected to give the same value of θ_m as obtained in condition IC5.

Condition IC5 was run in Tunnel M with the helium nozzle. The chamber pressure was set at the maximum value that could be maintained without building up excessive backpressure in the system. The size of the nozzle was selected so that the maximum plume diameter would be about 8 in.

Condition IAB was run in Tunnel M with the small CO_2 nozzle. The intention was to set the chamber pressure to the same as the flight value (440 psi), but limitations on the system made it necessary to run at a slightly lower value.

Condition IIB was run in Tunnel D with the helium nozzle. The primary purpose for this test was to determine the rarefied flow effects.

The free-stream dynamic pressure in Tunnel D was approximately 10 times that in Tunnel M, and the nozzle chamber pressure was therefore also set at about 10 times the value for M. The mean free path in Tunnel D was 0.01 times that in Tunnel M, so that any rarefied flow effects would be considerably reduced.

The second condition was selected the same as IC5, but with a reduced chamber pressure of 2 psi, rather than 5 psi. Both the helium nozzle (condition IC2) and the large CO_2 nozzle (condition IAC) were used. The corresponding flight condition was a free-stream Mach number of 10 at 80 km.

Condition IAA was run with the CO_2 nozzle at a chamber pressure of 50 psi. Therefore, conditions IAA (50 psi), IAB (400 psi), and IAC (100 psi) allow direct comparisons to be made on the effect of pressure. Condition IB was run to get some direct information on the effect of γ. The condition was run with the same nozzle and chamber pressure as condition IAB, but with helium rather than CO_2 as the plume gas.

Characteristic solutions for some of these conditions are given in Figs. 6a through d.

SECTION III
## DESCRIPTION OF EQUIPMENT

3.1 TUNNEL M

The experimental work was performed in Tunnels M and D of the von Kármán Gas Dynamics Facility (VKF). Tunnel M, shown pictorially in Fig. 7a and schematically in Fig. 7b, is a continuous, arc-heated, low-density, hypersonic wind tunnel normally using nitrogen as the test gas. Pumping is provided by three stages of air ejectors in series which exhaust into the VKF main compressor system through the VKF Hypersonic Wind Tunnel (C) test section. This arrangement permits simultaneous operation of these two tunnels, or either can be operated alone. Tunnel M consists basically of the following major components, in streamwise order:

1. Rotating-arc-type d-c arc heater of VKF design with a power supply rated at 200 kw for continuous operation. Gas is injected into the arc heater tangentially.

2. Cylindrical settling chamber of 1.5-in. diameter and 3-in. length.

3. Axisymmetric, contoured aerodynamic nozzle with 0.181-in. throat diameter and 35.1-in. exit diameter. A 6- to 10-in.-diam, gradient-free test core extends from 25 in. upstream of the nozzle exit to 25 in. downstream of the exit. Table II gives the nominal Tunnel M operating conditions with the contoured nozzle.

4. Stationary bulkhead of 94-in. diameter which supports the nozzle, probe drive and support unit, pressure measuring system, and external force balance or model support base. The bulkhead contains eight 12-in.-diam ports.

5. Cylindrical 8-ft-diam test chamber which moves downstream to allow access to the test section, models, and probes.

6. Axisymmetric diffuser with convergent entrance, constant area throat, and divergent outlet. Interchangeable designs are available for different test configurations.

7. Downstream heat exchanger.

8. First air ejector stage.

9. Isolation valve.

10. Second and third air ejector stages.

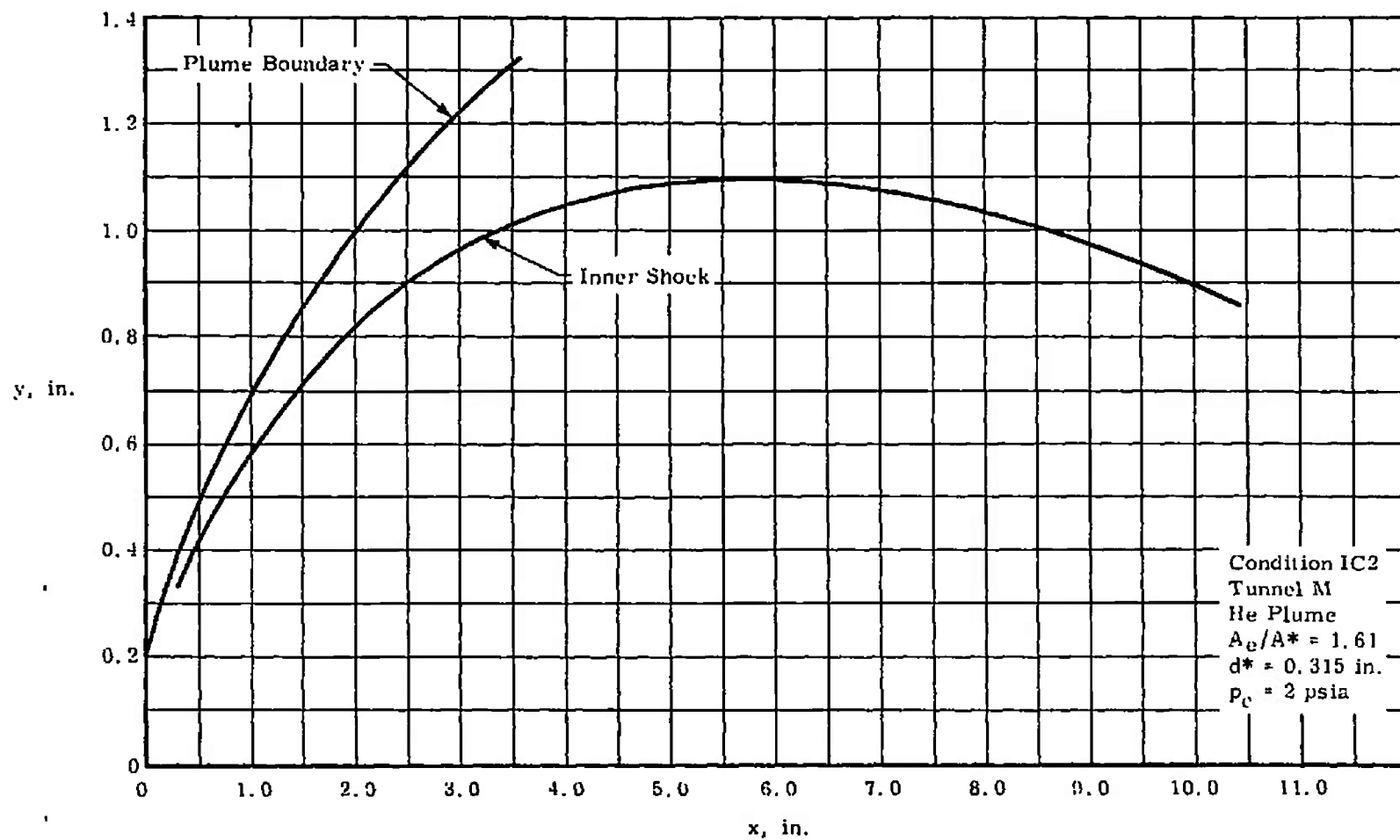11. Connection to the VKF Tunnel C test section.

Backside water cooling is used to protect the arc heater, settling chamber, nozzle, and diffuser.
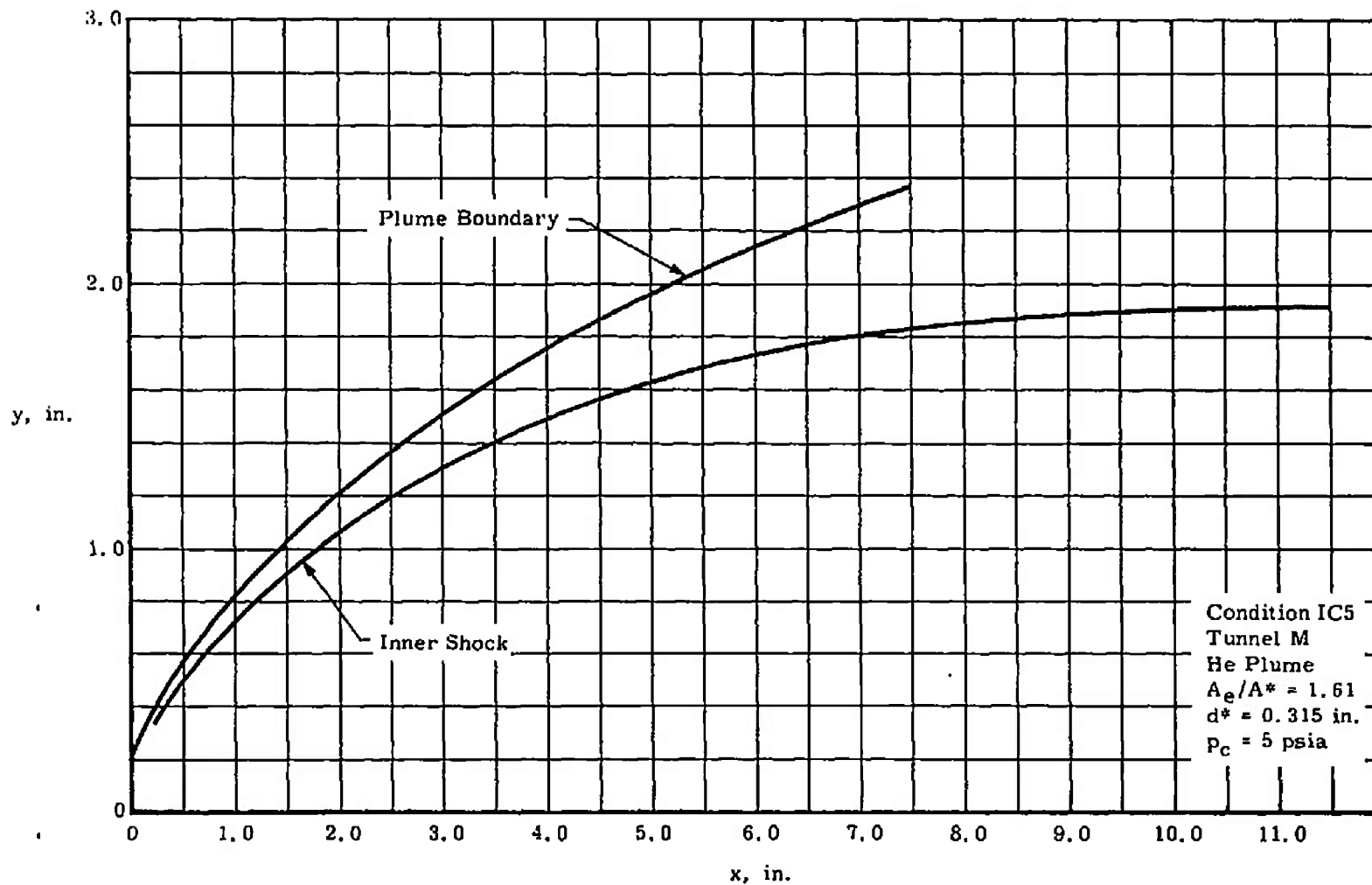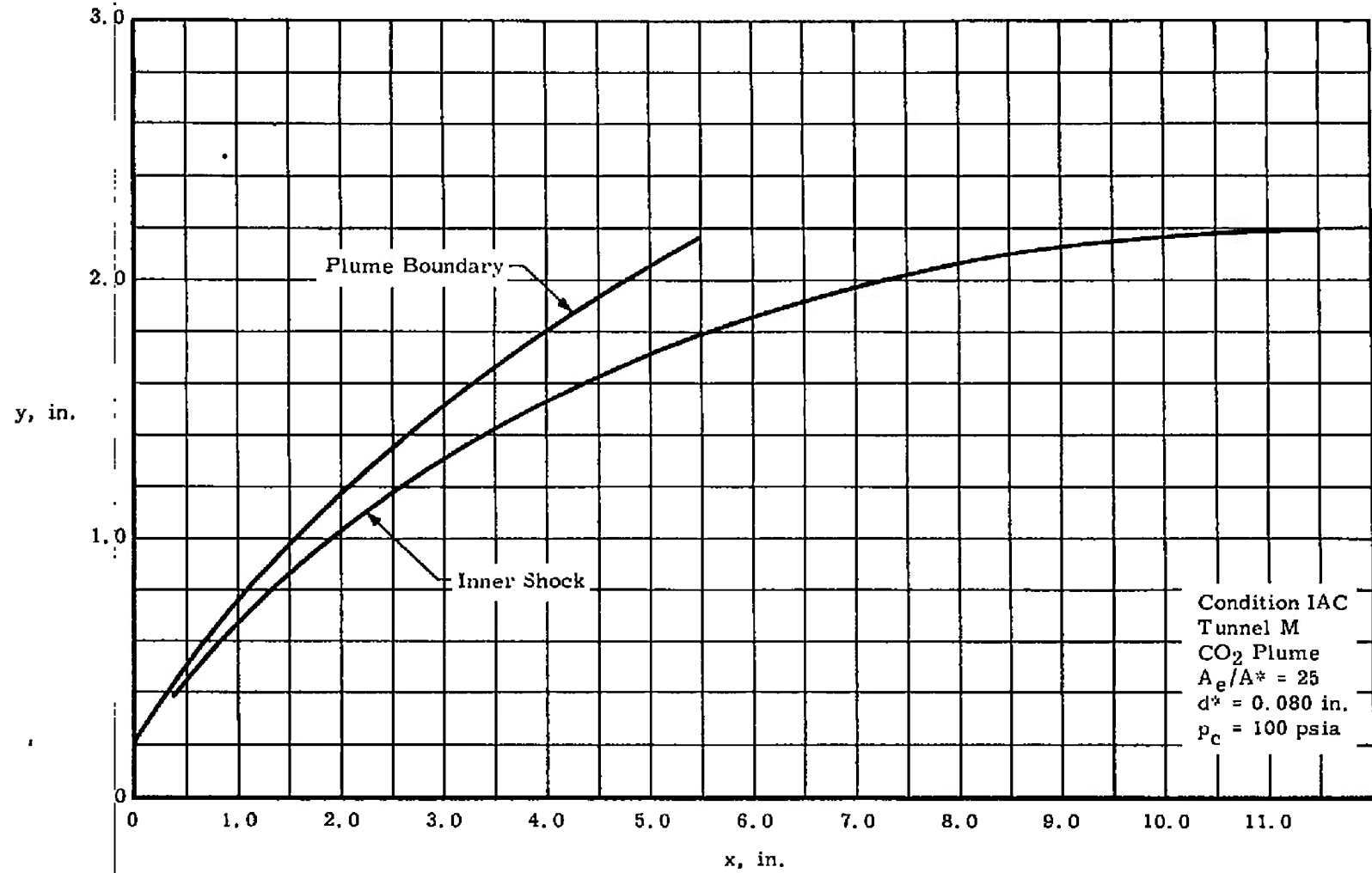
a. Condition IC5

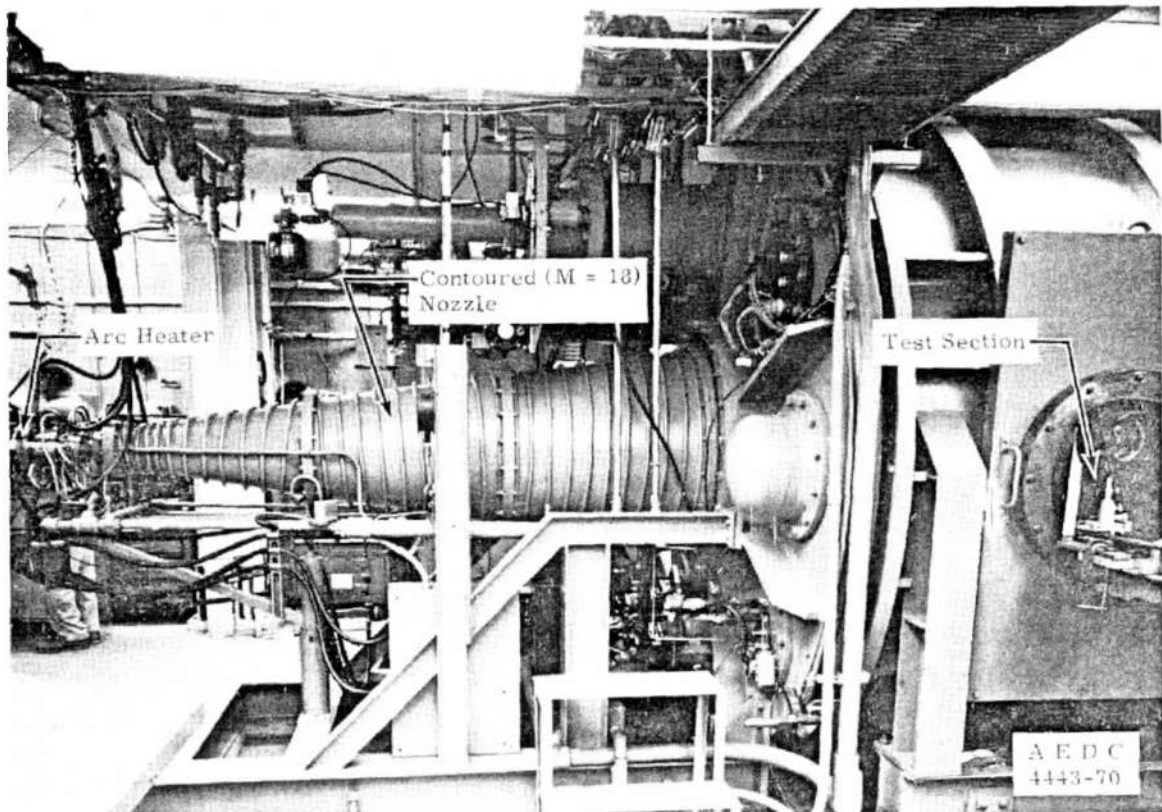Fig. 6 Characteristics Solutions
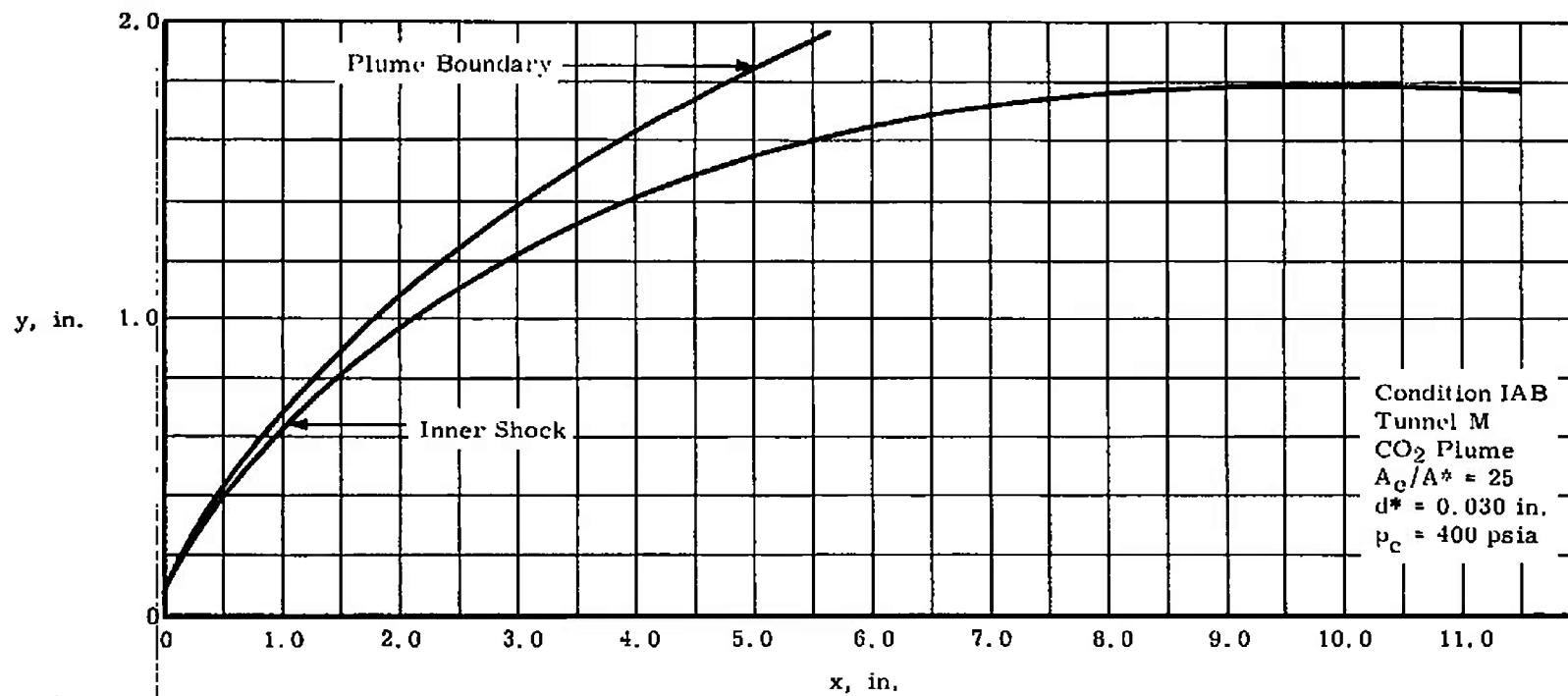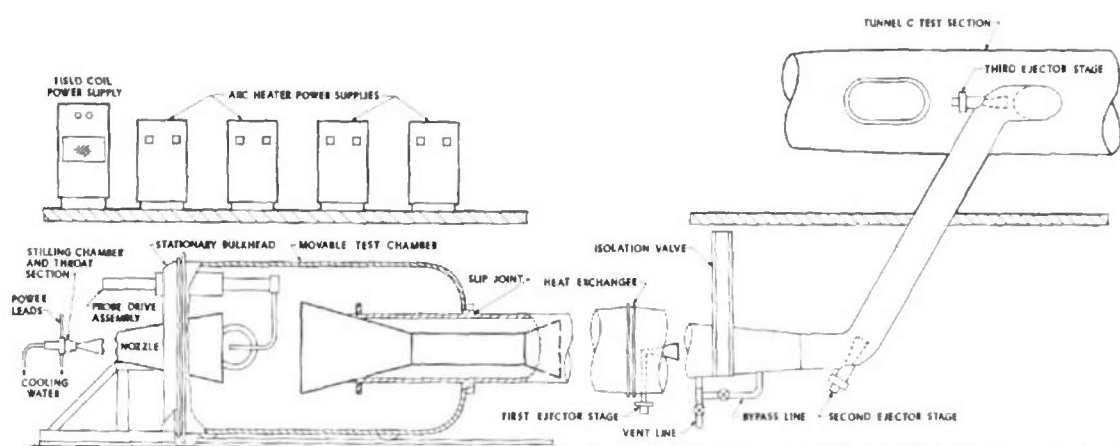
b. Condition IAB
Fig. 6 Continued

c. Condition IC2
Fig. 6 Continued

d. Condition IAC
Fig. 6 Concluded

a. Photograph

ELEVATION VIEW OF TUNNEL M

b. Elevation View
Fig. 7 Tunnel M

TABLE II
NOMINAL TUNNEL M NOZZLE 18N$_2$ OPERATING CONDITIONS

a. Customary Units

$\dot{m}$, lb_m/sec	0.0515
p_o, atm	19.0
T_o, °K	2900
h_o, Btu/lb_m	1500
p_o, mm Hg	2.55
M_∞	18.15
Re_∞, in.$^{-1}$	1250
p_∞, μ Hg	6.00
T_∞, °K	45.0
U_∞, ft/sec	8165
ρ_∞, lb_m/ft^3	3.73 x 10^{-6}
λ_∞, in.	0.022
q_∞, lb_f/ft^2	3.90
Re_2, in.$^{-1}$	45.0
Re_0, in.$^{-1}$	44.0

b. International System of Units

|	
$\dot{m}$, kg/sec	0.0233
p_o, N/m^2	1.925 x 10^6
T_o, °K	2900
h_o, J/kg	3.49 x 10^6
p_o, N/m^2	340
M_∞	18.15
Re_∞, m^{-1}	4.92 x 10^4
p_∞, N/m^2	0.800
T_∞, °K	45.0
U_∞, m/sec	2490
ρ_∞, kg/m^3	5.97 x 10^{-5}
λ_∞, m	5.59 x 10^{-4}
q_∞, N/m^2	187
Re_2, m^{-1}	1770
Re_0, m^{-1}	1730

3.2 TUNNEL D

Tunnel D is an intermittent, variable density wind tunnel with a manually adjusted, flexible-plate-type nozzle and a 12- by 12-in. test section. A picture is given in Fig. 8a and a schematic in Fig. 8b. The tunnel operates at Mach numbers from 1.5 to 5 at stagnation temperatures up to about 540°R.

3.3 PLUME GENERATION SYSTEM

Three rocket simulators, shown in Fig. 9, were used to generate the various plumes studied in Tunnel M. One of these ($d^* = 0.315$ in.) was used in Tunnel D. The 0.315-in.-throat-diam model had a nozzle expansion ratio of 1.6, whereas the 0.030- and 0.080-in.-throat-diam models had expansion ratios of 25. All had a 10-deg half-angle conical expansion. Dimensions, given in Table III, were kept as small as practicable to minimize the effect of the simulator itself on the free stream. The chamber diameter of the 0.315-in.-throat-diam model is of the same order as the throat diameter. Thus it was machined with a perforated conical baffle to promote flow uniformity entering the nozzle. A water-cooled strut, which supported the simulator in the test section, and gas supply and pressure lines extended up from the model support base and attached to the lower wall of the simulator chamber. A typical installation in Tunnel M with impact pressure probes is shown in Fig. 10a.

The plume-gas supply system is shown schematically in Fig. 11. Helium (99.995-percent purity) was supplied from a 41,000-ft^3 (standard temperature and pressure, STP) transport trailer initially at 2000 psi. The small quantity of argon used (99.99 + -percent purity) came from 2000 psi, 220-ft^3 (STP) cylinders. Carbon dioxide (99.5-percent minimum purity) was obtained as flash-off from a manifolded bank of nine 50-lb liquid CO_2 cylinders at 700 psi. A manually operated Hoke pressure regulator in series with two manual throttling valves was used to regulate gas flow to the heater and maintain the desired pressure in the rocket simulator chamber.

In Tunnel M the plume gas was heated to approximately two-thirds the desired chamber temperature by passing it through two parallel-connected, single-pass, hot-core, Kanthal®-element resistance heaters installed for these experiments. Final heating was provided by the tunnel flow (T_o = 2900°K) impinging on the simulator nose and supply tube. Desired chamber temperature was maintained by regulating the heater output by means of a manually operated control
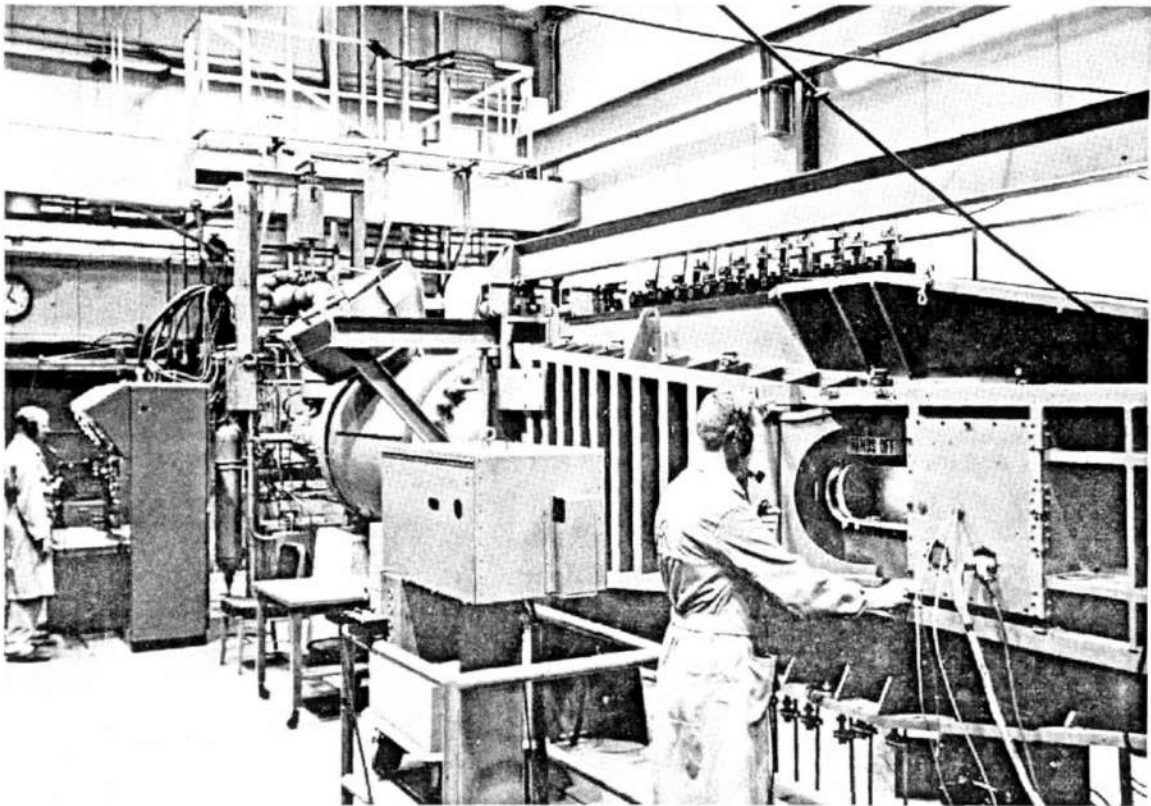
a. Photograph
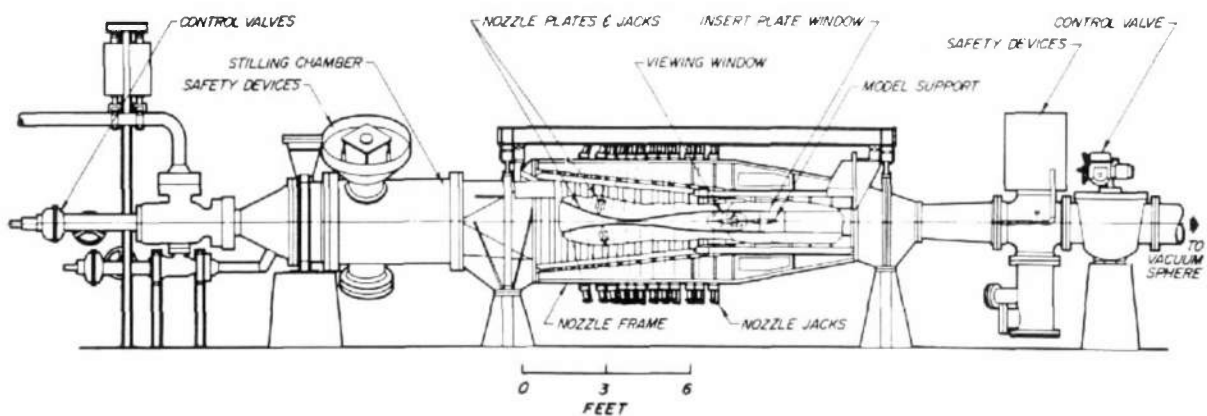
b. Schematic
Fig. 8 Tunnel D

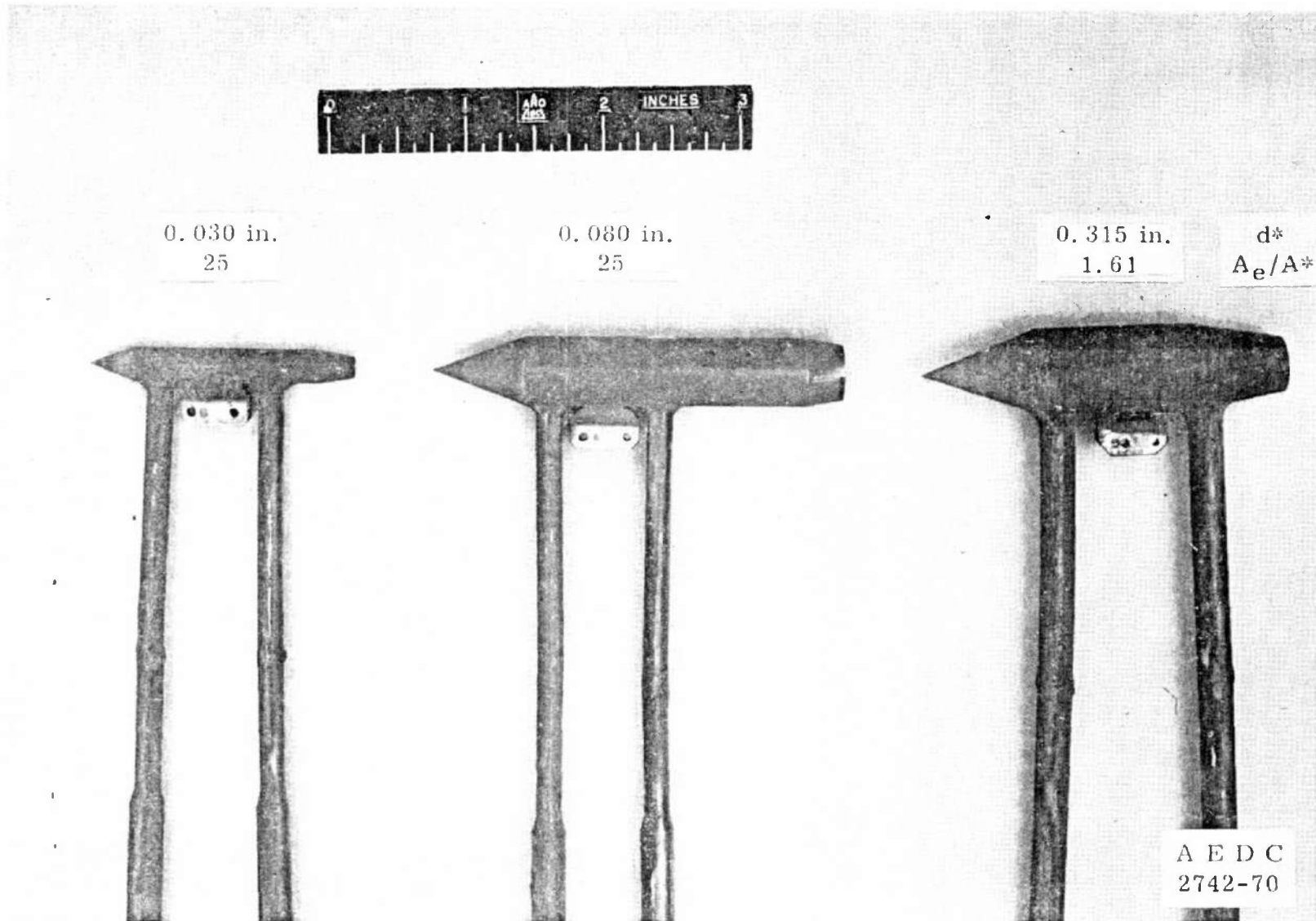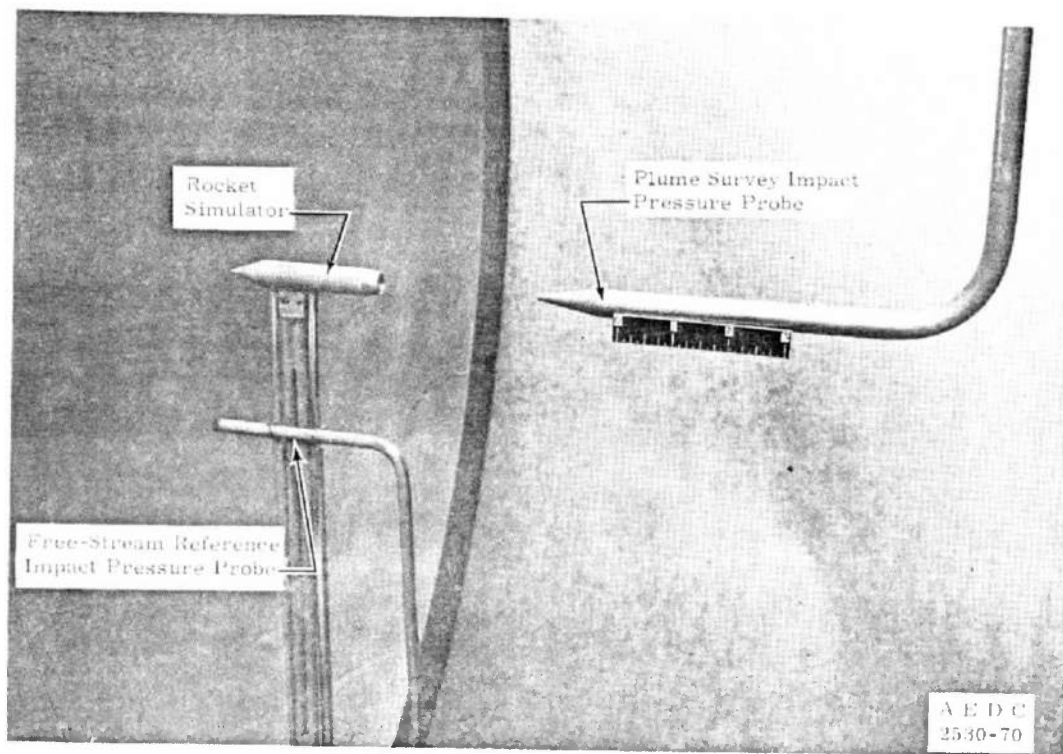| 0. 030 in. | 0. 080 in. | 0. 315 in. | d* |
| 25 | 25 | 1. 61 | $A_e/A*$ |

A E D C
2742-70
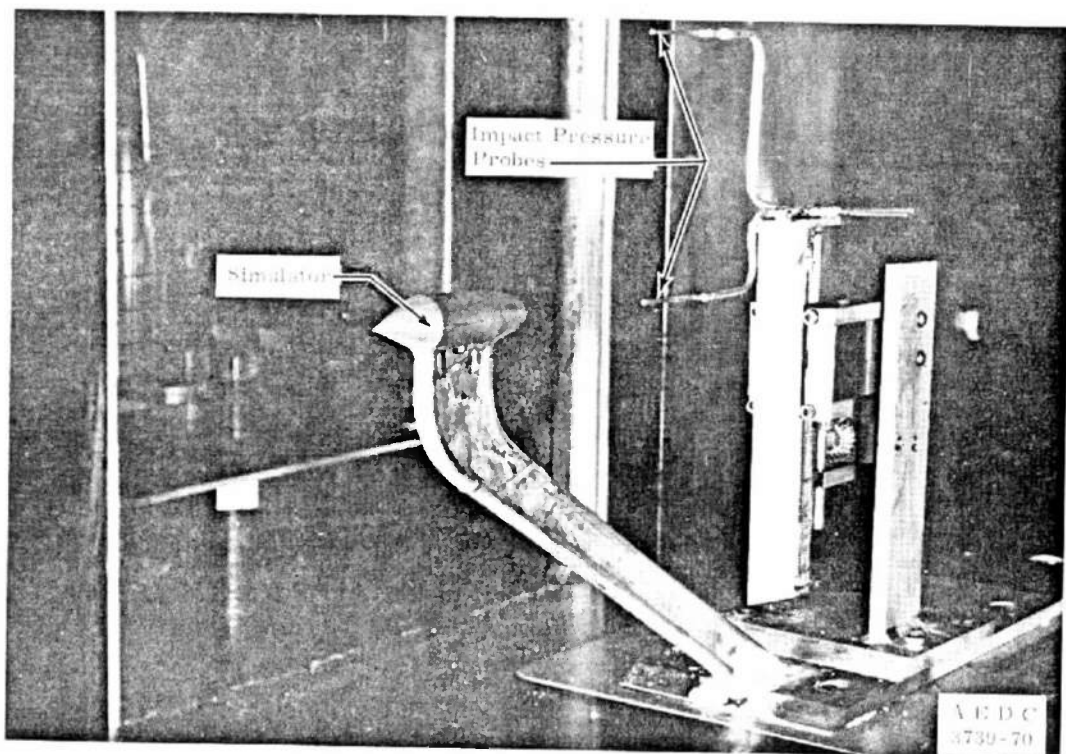
Fig. 9 Photograph of Plume Generators
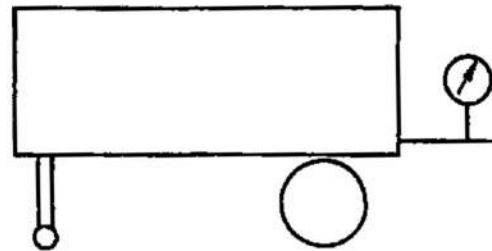
a. Tunnel M

b. Tunnel D
Fig. 10 Simulator and Impact Pressure Probe Installation

Helium Trailer
41,000 ft^3 (STP) at 2000 psi

Rocket
Simulator

PPB or Wiancko
Pressure Transducer

Temperature
Instrument

Hoke Regulator

Heater

Relief Valve
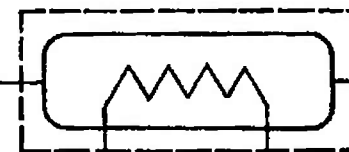
Control
Rheostat
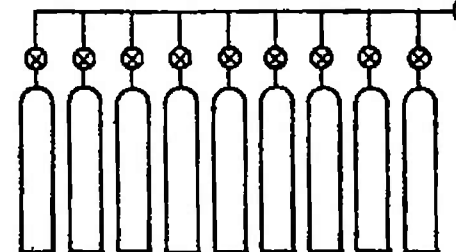
50-lb Liquid CO_2 Cylinders
at 700 psi

Fig. 11 Plume Gas Supply System

TABLE III
PLUME SIMULATOR DIMENSIONS

Throat Diameter, d^*, in.	Nozzle Diameter, d_1, in.	Chamber Diameter, d_2, in.	d_3, in.	L_1, in.	L_2, in.	L_3, in.
0.315	0.400	0.406	0.625	2.600	0.638	0.859
0.080	0.400	0.375	0.500	2.976	0.284	0.687
0.030	0.150	0.150	0.250	1.943	0.284	0.343

Heated Plume Gas In

Thermocouple

To Instrument for Measurement of T_{op}

To Pressure Transducer for Measurement of p_c
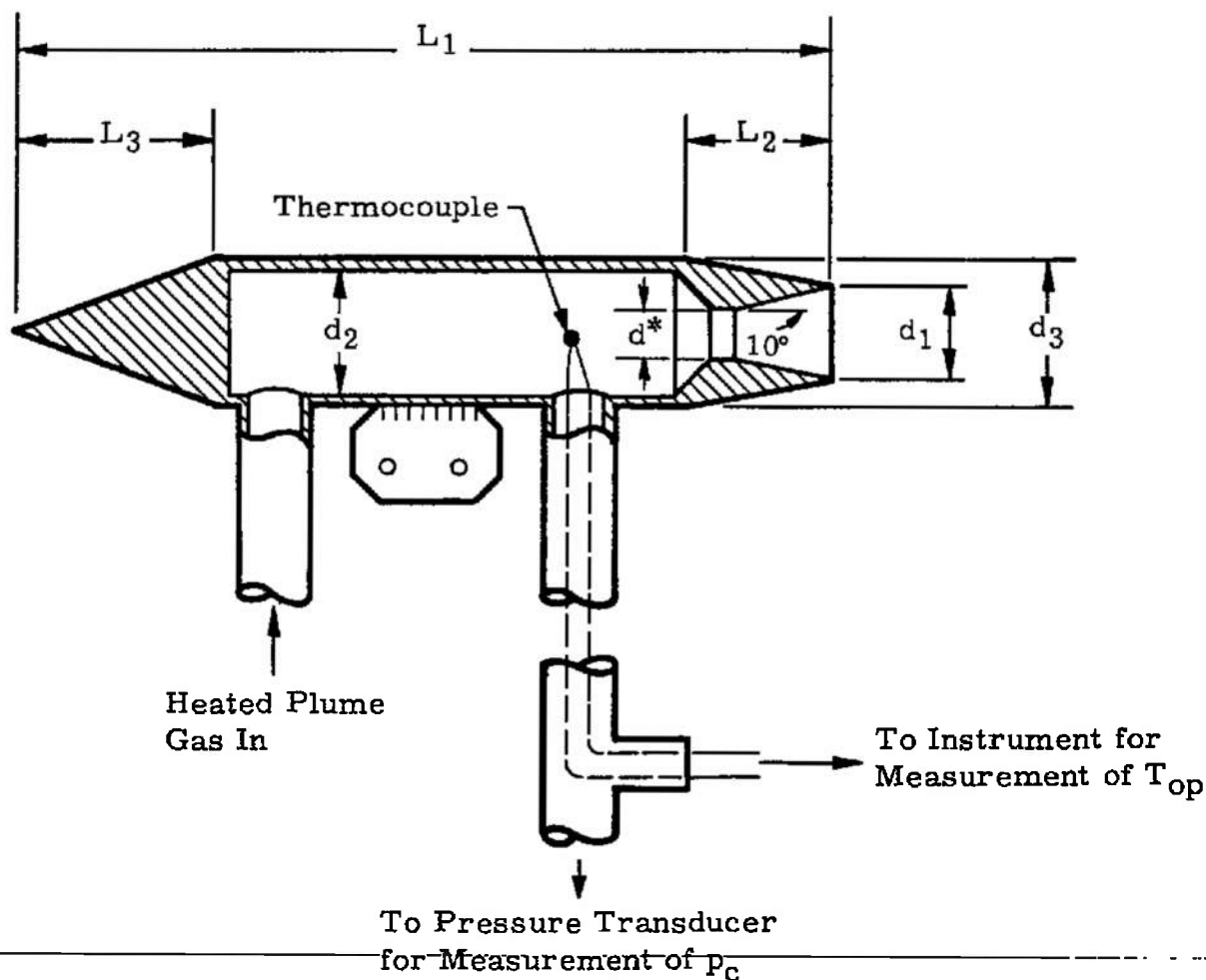
rheostat. For Tunnel D, no heater was used. Figure 10b shows the simulator and impact pressure probes installed in Tunnel D.

Estimates of the boundary-layer thickness at the exit plane of the simulator nozzles give values of about 0.030 in. for conditions IC2 and IAC. The corresponding value of δ^* is about 0.020 in. These values are felt to be sufficiently low that there should be no significant viscous effects.
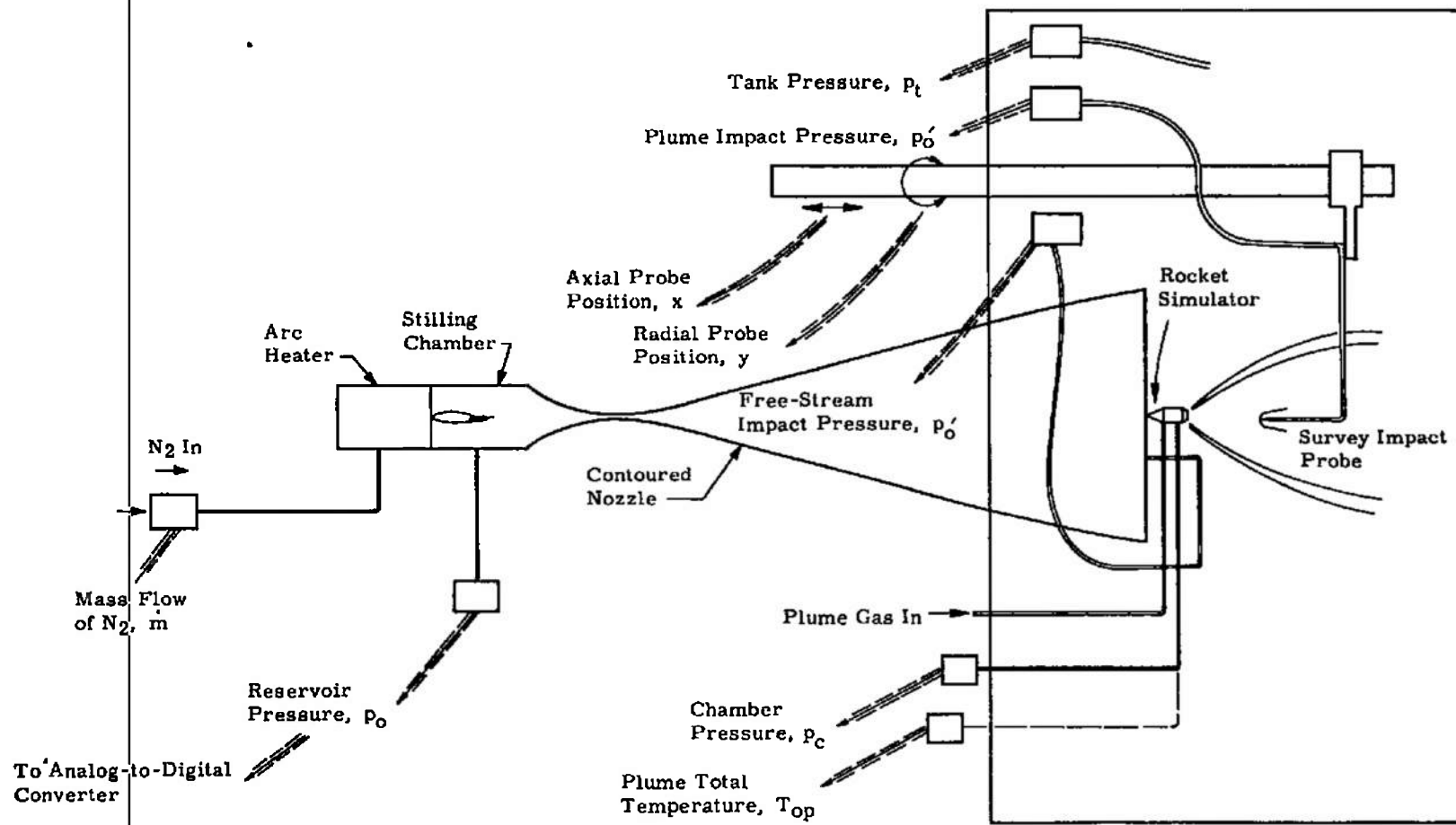
3.4 TUNNEL CONDITIONS AND PRESSURE MEASURING EQUIPMENT

The instrumentation apparatus is shown in Figs. 12a and b. The tunnel free-stream conditions were monitored from measurements of reservoir pressure and test section impact pressure. The third measurement was the reservoir temperature in Tunnel D, which was measured with a thermocouple, and the mass flow rate in Tunnel M, from which a reservoir temperature was determined.
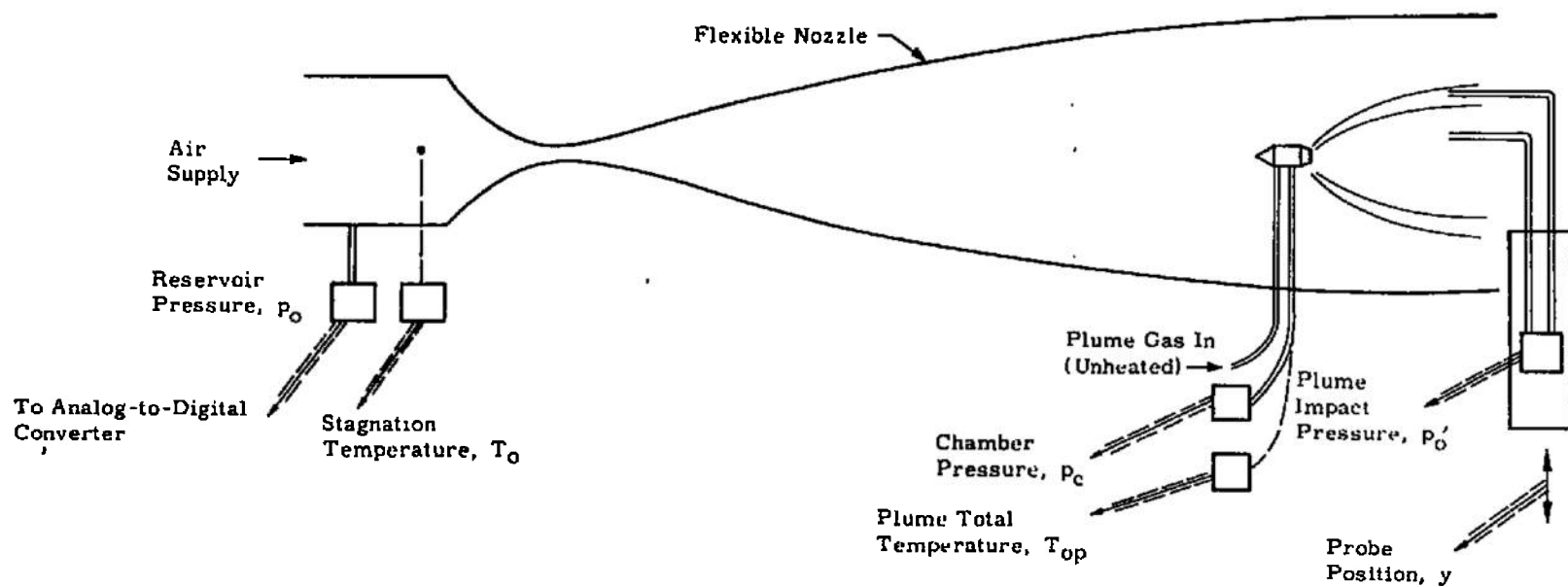
In Tunnel M impact pressures in the free stream and in the plume were measured with water-cooled probes connected, respectively, to 3- and 30-mm MKS Baratron® pressure meters. The flat-faced free-stream probe, located approximately even with the nose of the rocket simulator and 3 in. below the nozzle centerline, was 0.25-in. OD and had a 0.093-in.-ID pressure tube. The externally chamfered plume probe, with a 0.121-in.-diam nose and a 0.063-in.-diam orifice, was mounted on the probe carrier so that it could be traversed axially and radially through the plume flow field. Two 10-turn potentiometers were used to indicate probe position. The Baratron pressure meters were calibrated each day, using a precision oil micromanometer and a McLeod gage, under the same ambient conditions which they experienced during the test. All other pressure instruments were calibrated before the test.

Digital voltmeters plus various analog readout devices were used to monitor various parameters during the test. All analog data were fed into an analog-to-digital converter and then recorded on paper tape for subsequent computer processing.

In Tunnel D, two probes were attached to a common positioning mechanism (Fig. 13). One of these probes was angled to bring the probe in closer alignment with the plume flow. There was some overlap in the coverage of the plume by these two probes.

a. Tunnel M
Fig. 12 Instrumentation Schematic

Flexible Nozzle

Air
Supply

Reservoir
Pressure, p_o

To Analog-to-Digital
Converter

Stagnation
Temperature, T_o

Plume Gas In
(Unheated)

Plume
Impact
Pressure, p_o'

Chamber
Pressure, p_c

Plume Total
Temperature, T_{op}
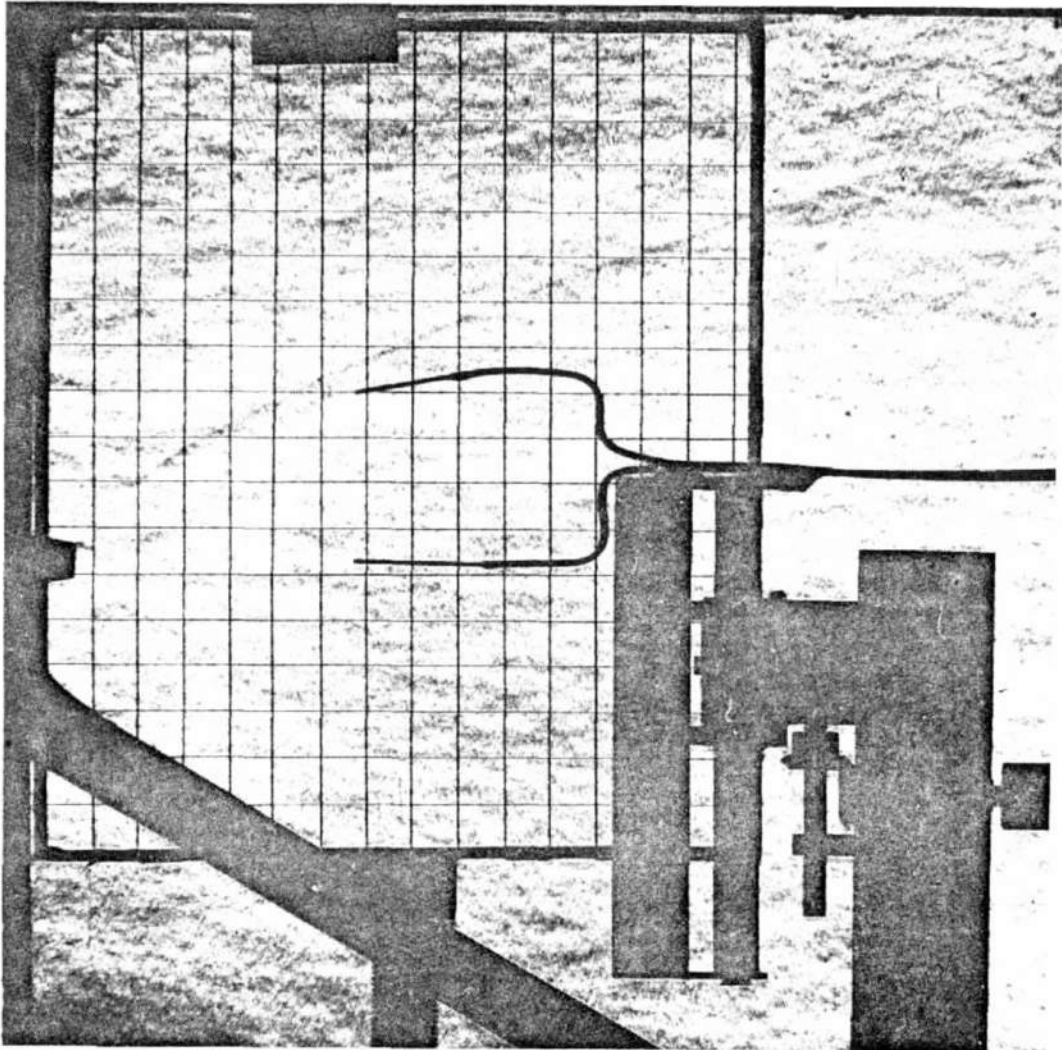
Probe
Position, y

b. Tunnel D
Fig. 12 Concluded

Fig. 13 Tunnel D Simulator and Impact Pressure Probes during Typical Run

The impact pressures in Tunnel D were measured on a Consolidated Electrodynamics Corporation (CEC) electromanometer pressure system using 15-psid precision pressure balances referenced to a vacuum.

The rocket simulator nozzle chamber pressure was measured on the same system using a 60-psid precision pressure balance referenced to a vacuum.

3.5 ELECTRON BEAM APPARATUS

Measurement of the rotational and vibrational temperatures of nitrogen and number density of both nitrogen and helium throughout the plume/free stream region was accomplished in Tunnel M using the electron beam fluorescence technique described in Appendix II. The apparatus required for injecting the high energy beam of electrons into the low density, hypersonic test gas is simple in nature, requiring only an electron source, power supply, and differential pumping system. A photograph of the electron beam apparatus installed in Tunnel M is shown in Fig. 14. The source of electrons was a GE Type 33 television-type electron gun, with an oxide-coated cathode, modified for 50-kv operation. The accelerator grid had an enlarged opening of approximately 3/16-in. diameter, allowing beam currents of up to 2 ma to be injected into the flow. The power supply for the filaments consisted of batteries, yielding 6 to 18 vdc. To obtain the required energy of approximately 20 kev, the anode of the gun was grounded and the cathode connected directly to the negative output of a 0- to 50-kv, 0- to 5-ma power supply. Both the grid and the preaccelerator bias voltages were supplied by batteries. Figure 15 shows the circuit diagram of the gun power supply. The gun itself was mounted within the tunnel in a leaktight insulated housing which was maintained at 1-atm pressure of air, as were the tubes leading the power supply cables into the tunnel; this arrangement prevented arcing to the tunnel wall. The beam was magnetically focused and deflected to coincide with an orifice of approximately 0.050-in. diameter opening into the test section containing the flow. To maintain the pressure within the electron gun at approximately 10^{-5} torr, as required for stable and long-life operation, a differential pumping system was employed. Referring to Fig. 16a, it can be seen that the electron gun was connected to the flow by a 24-in.-long stainless steel drift tube of 2-in. diameter; connected to this drift tube by means of a flexible bellows tube was a pumping line leading to a 4-in. diffusion pump located outside the tunnel (Fig. 16b). A solenoid-operated, 2-in. gate valve was located at the flow field end of the drift tube.

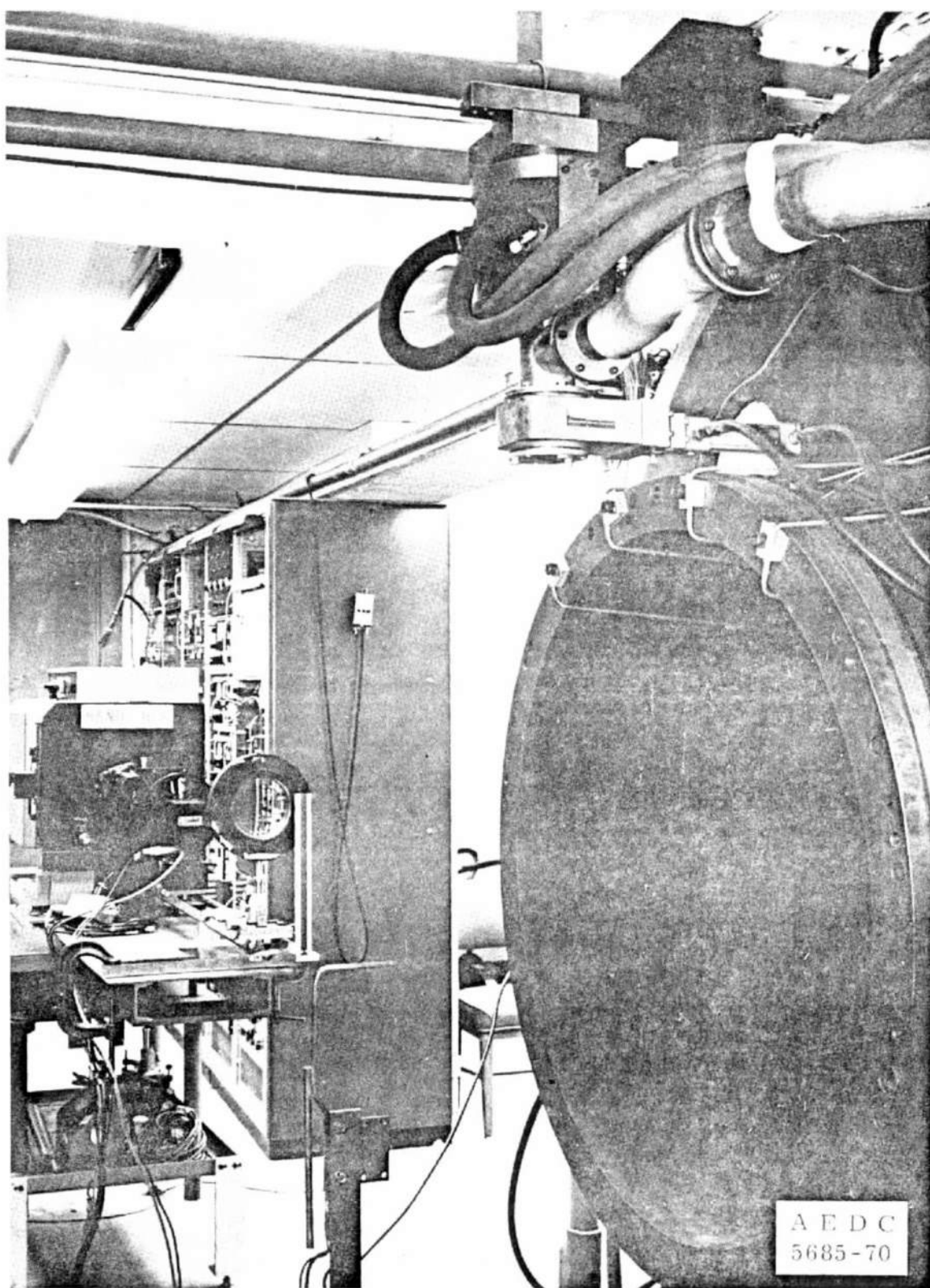Fig. 14 Photograph of Electron Beam Apparatus in Tunnel M
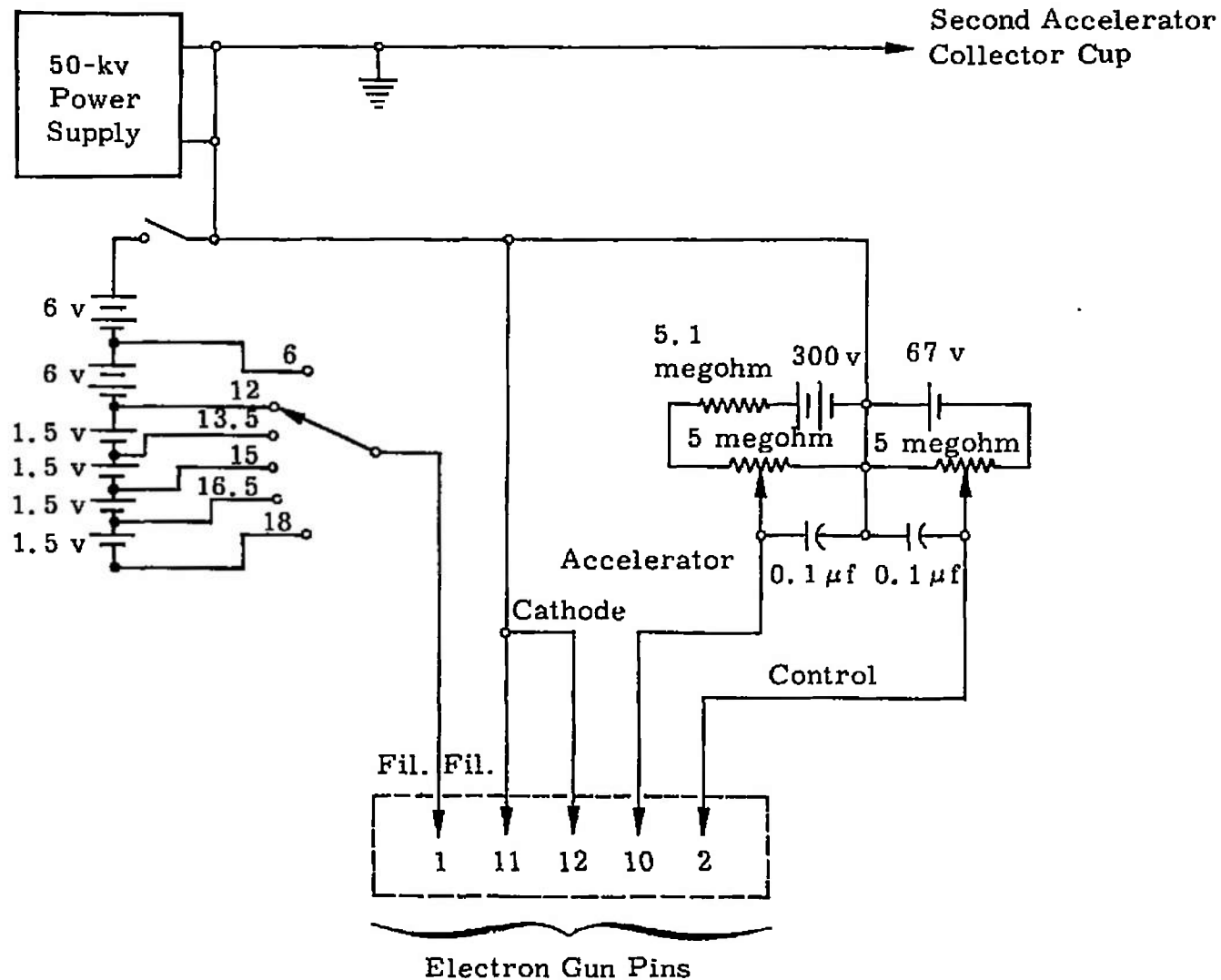
Fig. 15 Electron Gun Power Supply Schematic
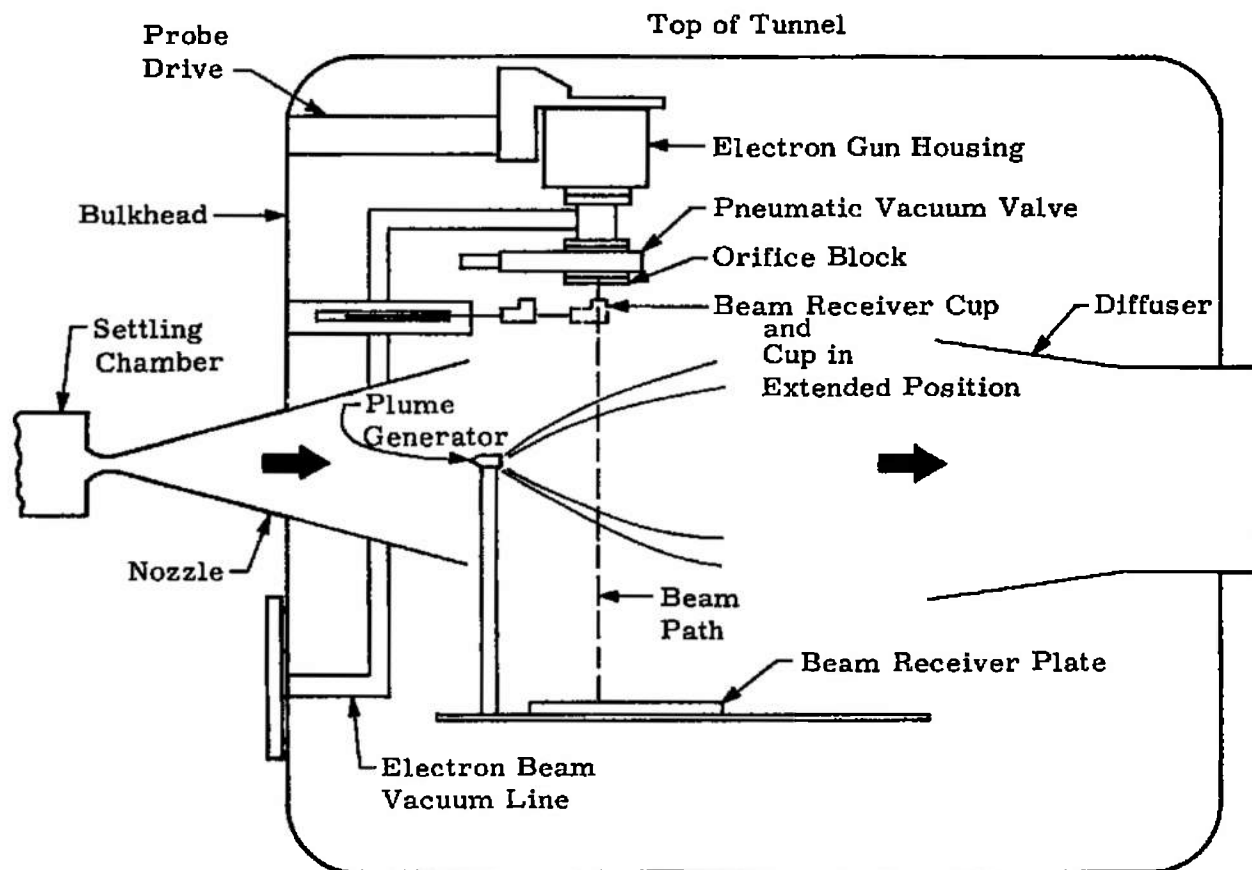
a. Tunnel M Installation
Fig. 16 Electron Beam Schematics

Tunnel M
Bulkhead

Ion Gage

To Reference Port of Equibar
Pressure Meter

Port

Hastings Gage

Vacuum Gate
Valve

Baffle

4-in. Oil
Diffusion Pump

Mechanical
Pump

Mechanical
Pump
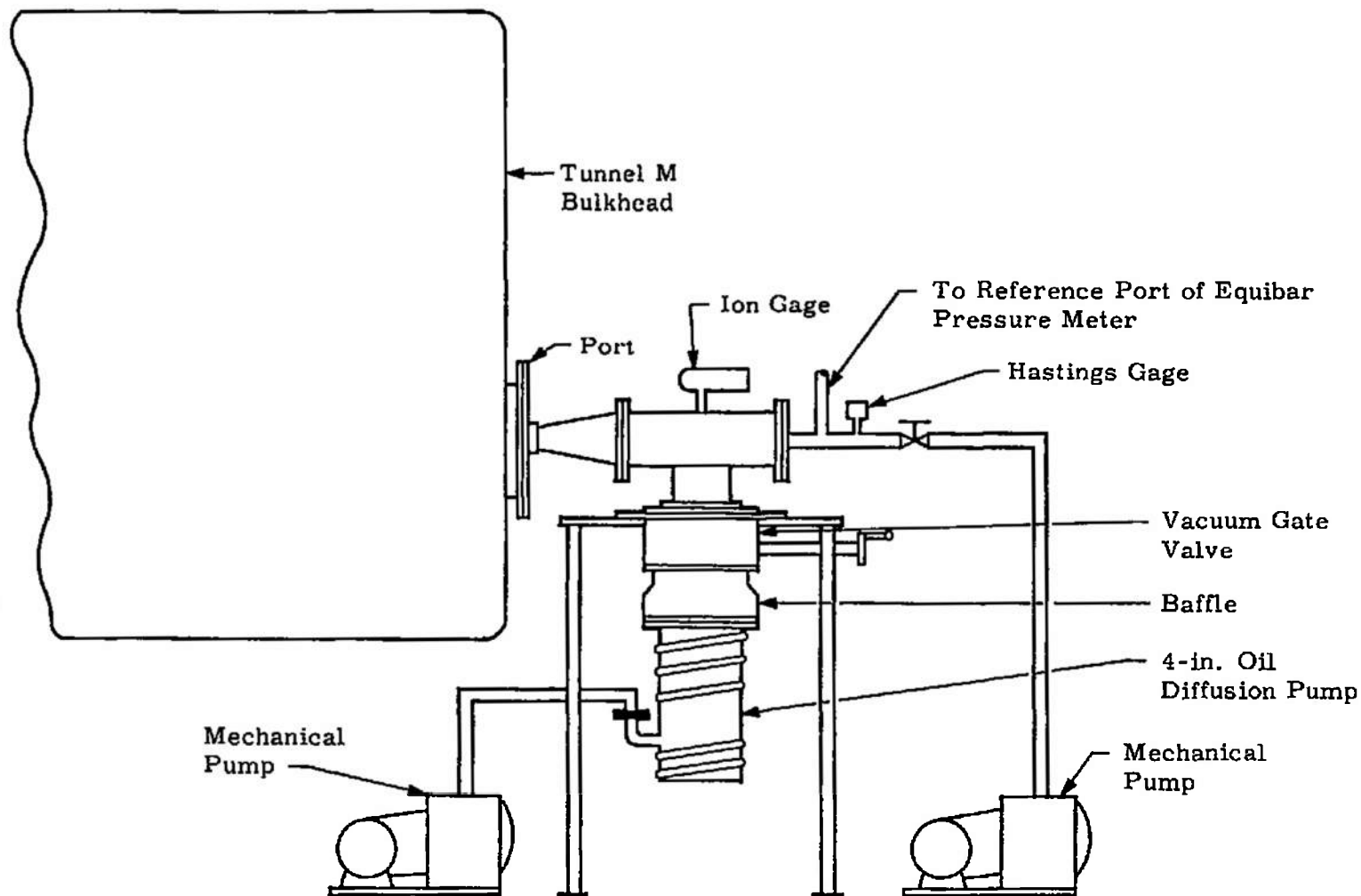
b. Electron Beam Vacuum Systems
Fig. 16 Concluded

Measurement of the beam current injected into the flow and the associated difficulties are described in Appendix II. For vibrational and rotational temperature measurements a precise value of the current is unimportant except for possible secondary effects which cannot at this time be included in the equations given in Appendix II. For this reason the value of current used for all temperature data was a nominal value as registered by an aluminum flat-plate collector of approximate dimensions 12 by 18 in. located on the tunnel floor approximately 4 ft from the orifice. The accuracy of such a measurement is indeed questionable because of both boundary layer and secondary ejected electron effects; however, the value of current was constantly monitored to ensure minimum current fluctuations and drift, thereby decreasing the imprecision of the temperature measurements. As can be seen from Eq. (II-2), knowledge of the value of the beam current is critical for an accurate density measurement; for that reason it was deemed essential that an additional current determination be made, specifically at the point of injection of the beam into the flow, thereby minimizing the errors attributable to beam spreading caused by elastic and inelastic scattering. To do this, a collector, to be described shortly, was mounted onto a traversing mechanism powered by a 24-vdc power supply. Before obtaining a density datum point, the auxiliary collector was traversed axially until it was located directly beneath the gun orifice (Fig. 16a). The current at the injection point was found, and the auxiliary collector was withdrawn to allow the traversal of the flow by the beam. Such a collector must meet one primary requirement, namely that it measure all current incident upon it. Shown in Fig. 17 is the geometrical configuration of the collector which was constructed of a 2-in. copper elbow with a reflecting plane soldered in place to give an effective increase in the length-to-diameter ratio, thereby minimizing the loss of ejected secondary electrons. The location of this current measurement site was approximately 24 in. above the tunnel center-line. The individual values of current from each of the two collectors were displayed and read from a digital voltmeter.

The optical radiation produced as a result of electron beam excitation was gathered by a 48-in.-focal-length lens which has an approximate f/number of 12 and was focused onto the slit of a Jarrell-Ash 1-meter scanning spectrometer of approximate f/8.6 as is shown in Figs. 18 and 19. The 102- by 102-mm diffraction grating used had 1180 grooves/mm and was blazed at 5000 Å. For the measurement of all quantities the object distance and the image distance to the lens were approximately 48 and 24 in., respectively, yielding a lens magnification factor of 1/2. Temperature measurements were performed with the spectrometer slit aligned parallel to the beam, and a dove prism was employed for the density measurements to rotate the beam.
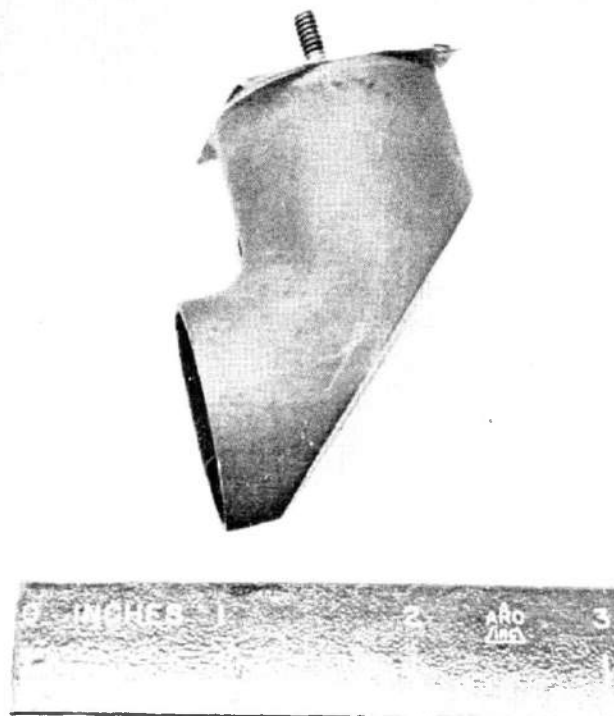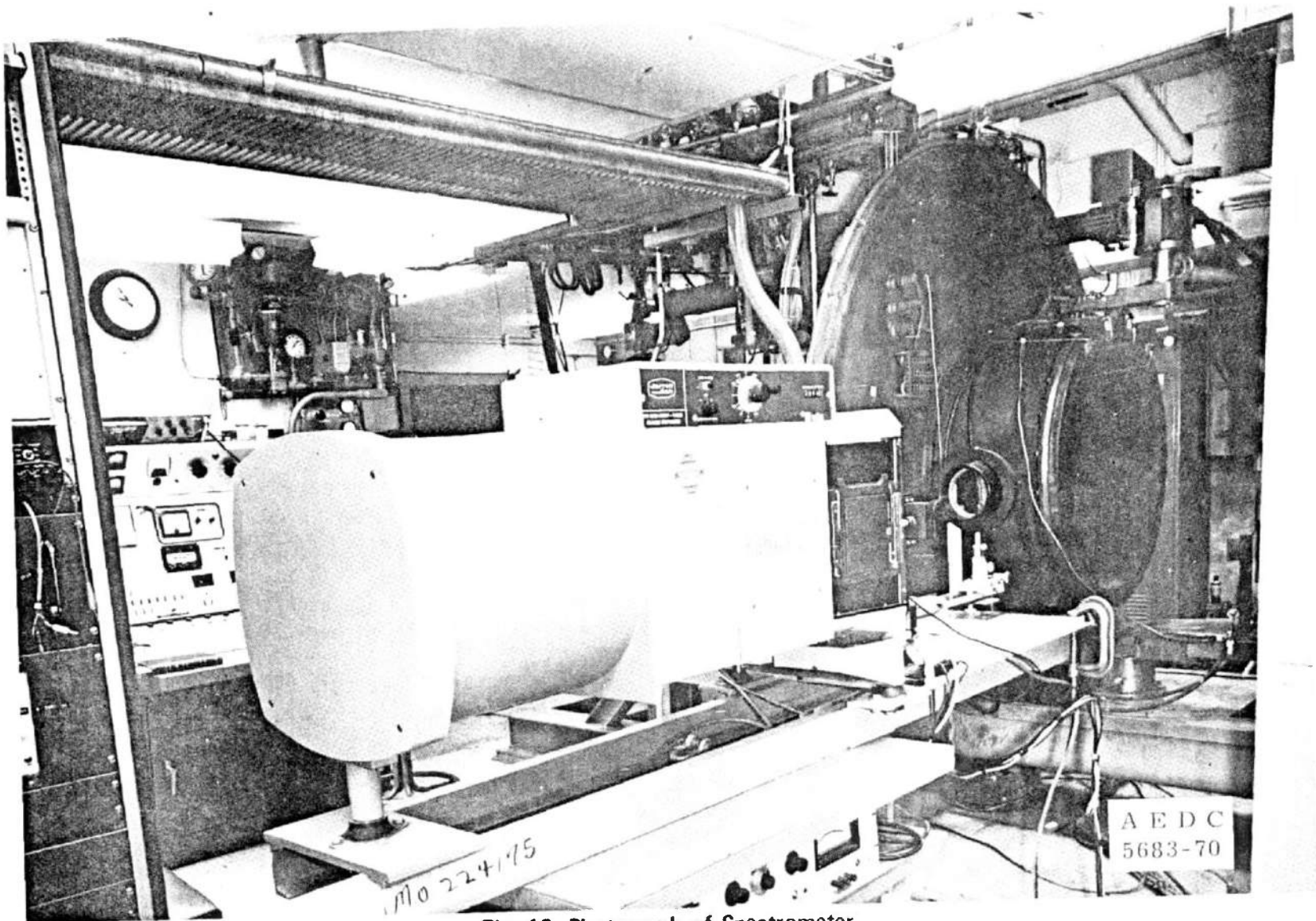
Fig. 17 Photograph of Current Collector
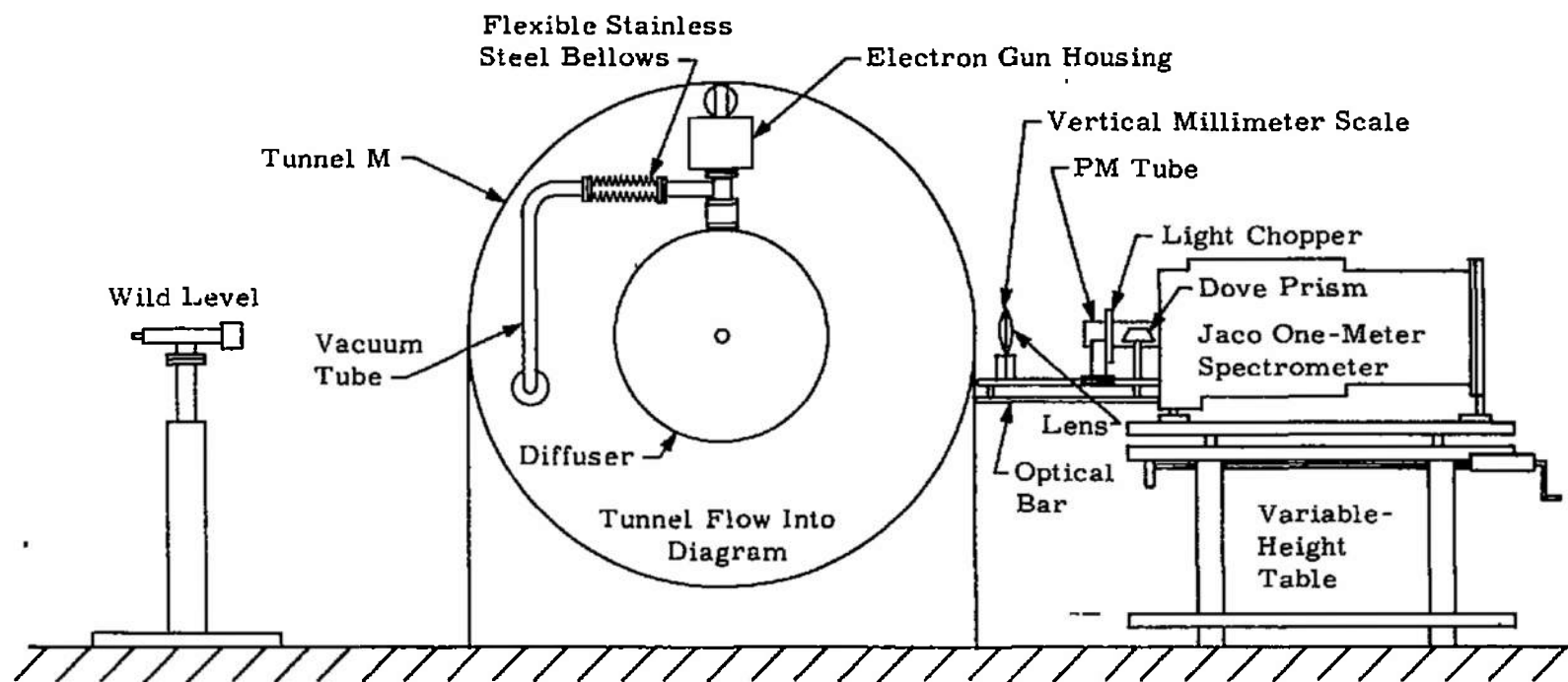
Fig. 18 Photograph of Spectrometer

Fig. 19 Downstream View of Electron Beam · Spectrometer·Telescope Setup

perpendicular to the slit. Detection was accomplished using an EMI 6256B photomultiplier tube with the output processed by a PAR HR-8 lock-in amplifier. The optical signal to the spectrometer was chopped by a PAR Model 125 chopping wheel at 340 Hz, and the reference signal to the lock-in amplifier was supplied by the chopping wheel assembly. Rotational temperature data were obtained by recording the lock-in output on a stripchart recorder. For both vibrational temperature and density measurements the output of the lock-in was fed to an active electronic integrator, the schematic of which is shown in Fig. 20, which had a time constant of 1 sec and an accuracy of ±1 percent for integration times less than or equal to 200 sec. The output of the integrator was then displayed on a digital voltmeter from which the final data were obtained. Necessary linearity checks of the system had been performed before the test.

To achieve the axial scanning capability required for high quality photography of the flow field as well as fine adjustment to the beam position, the entire electron gun housing was mounted on a probe carrier driven by a spline drive. The axial position of the beam was determined by displaying a potentiometric output on a digital voltmeter calibrated to give 3000 counts per 10 in. Rotation in the plane perpendicular to the axial direction was also possible and was used when aligning the beam. Radial scanning was performed by mounting the lens and spectrometer on a "welder's-table" which was capable of being raised or lowered by crank, thereby moving the spectrometer and optics system along the radial direction of the beam. To ensure that the electron beam (to first approximation) intersected the tunnel centerline, an object was located on the centerline and was focused into view using a levelling telescope on the side of the tunnel opposite the spectrometer (see Fig. 18). A plumb bob was then suspended from the electron beam orifice and the beam mount was traversed until the plumb bob intersected the centerline, which was also indicated by the image in the level. The lens was then adjusted until the entrance slit of the spectrometer came into focus with the level, and at that point it was certain that (1) the electron beam intersected the centerline and (2) the spectrometer entrance slit was focused onto the beam. After the magnetic field coil was turned on during tunnel operation a final adjustment of the axial and angular position of the beam was required, but the change was rather small and did not require refocusing. The radial position of observation was determined by mounting a scale on the spectrometer table; using the level, a centerline reference position was determined on the scale, which had a 1-mm least count, and the table was raised until, as observed through the level, a change of position of predetermined magnitude had occurred.
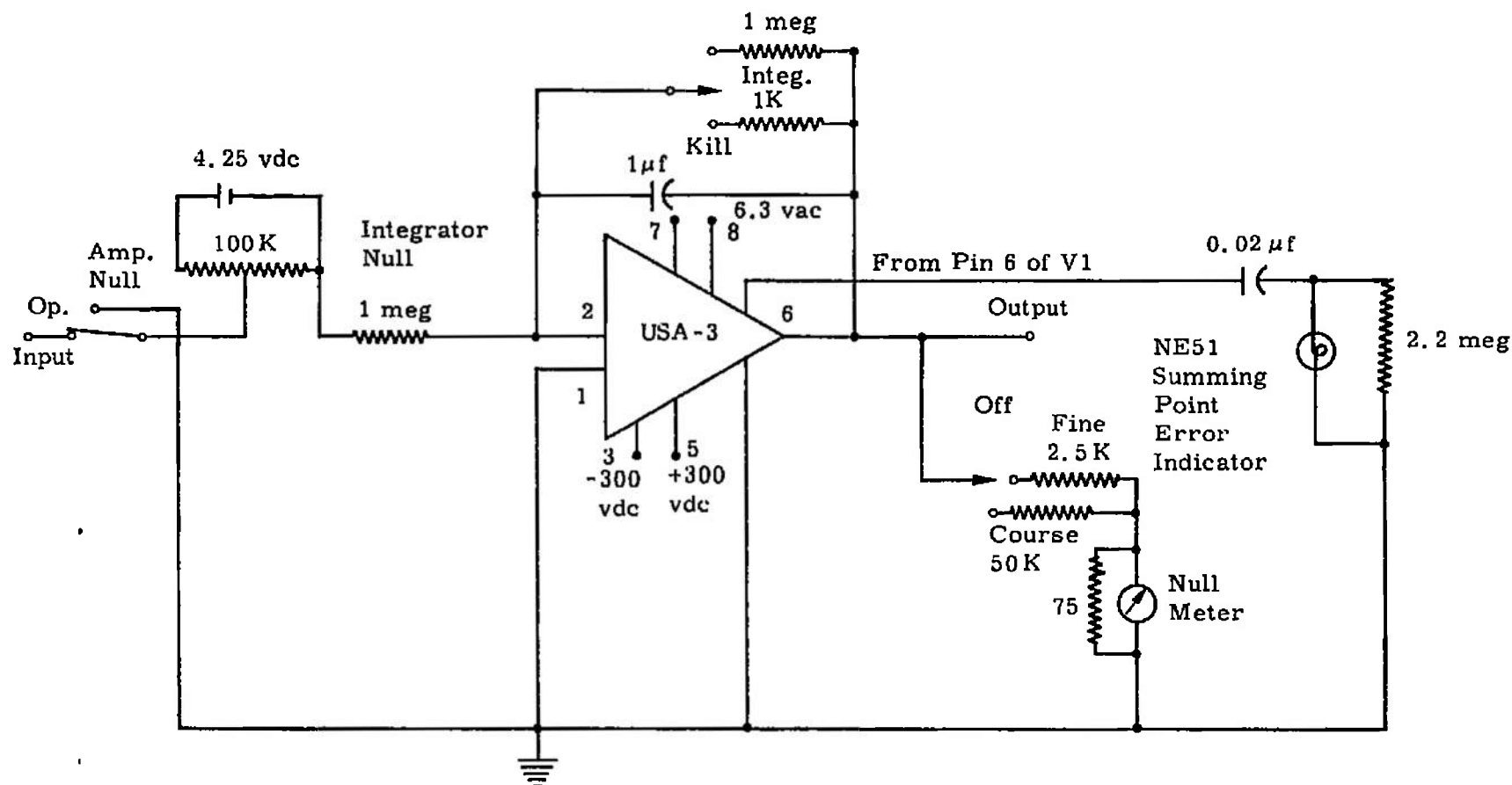
Fig. 20 Integrator Schematic

3.6 PHOTOGRAPHIC APPARATUS

For flow visualization photographs, a camera was mounted on the surveyor's stand that normally held the levelling telescope used for electron beam-spectrometer alignment. The camera was a Super Speed Graphic® with a 135-mm Graflex Optar® f/4.7 lens and a Graphex-Wollensak® shutter assembly.

For determination of proper film exposure time, Polaroid® Type 52 (black and white) and Polaroid Type 108 (color) were normally used. The film used for data point photographs was either Ektacolor® Type L or High Speed Ektachrome® B (processed as a negative).

Filters were frequently used with data point photographs to prevent the predominant radiation of some molecular species excited by the electron beam from exposing the film. Corning sharp cut 3-70 and 3-72 filters were used as well as a narrow-band filter ($\approx 50 \text{ Å/half-width}$, $\lambda_{peak} \approx 5015 \text{ Å}$). Transmission curves for the 3-70 and 3-72 filters are shown in Fig. 21a and the narrow-band filter curve is shown in Fig. 21b.

SECTION IV
DATA ACQUISITION AND REDUCTION TECHNIQUES

All test parameters were scanned in approximately 0.5 sec, thus providing essentially simultaneous reading of tunnel and plume conditions. These data were digitized, recorded on paper tape, and subsequently reduced on the VKF CDC 1604-B computer.

4.1 TUNNEL CONDITIONS

Test section flow conditions were determined from free-stream impact pressures and total pressure data by use of the normal shock relations. Pressure readings were correlated for orifice and probe effects as discussed in Appendix I. For Tunnel D, total temperature was measured with a thermocouple, and for Tunnel M was determined from measurements of mass flow rate, reservoir pressure, and geometric area of the sonic throat. Using calculations similar to those reported in Ref. 8, the flow was assumed to be in equilibrium upstream of the sonic throat and frozen downstream with a specific heat ratio of 1.4.
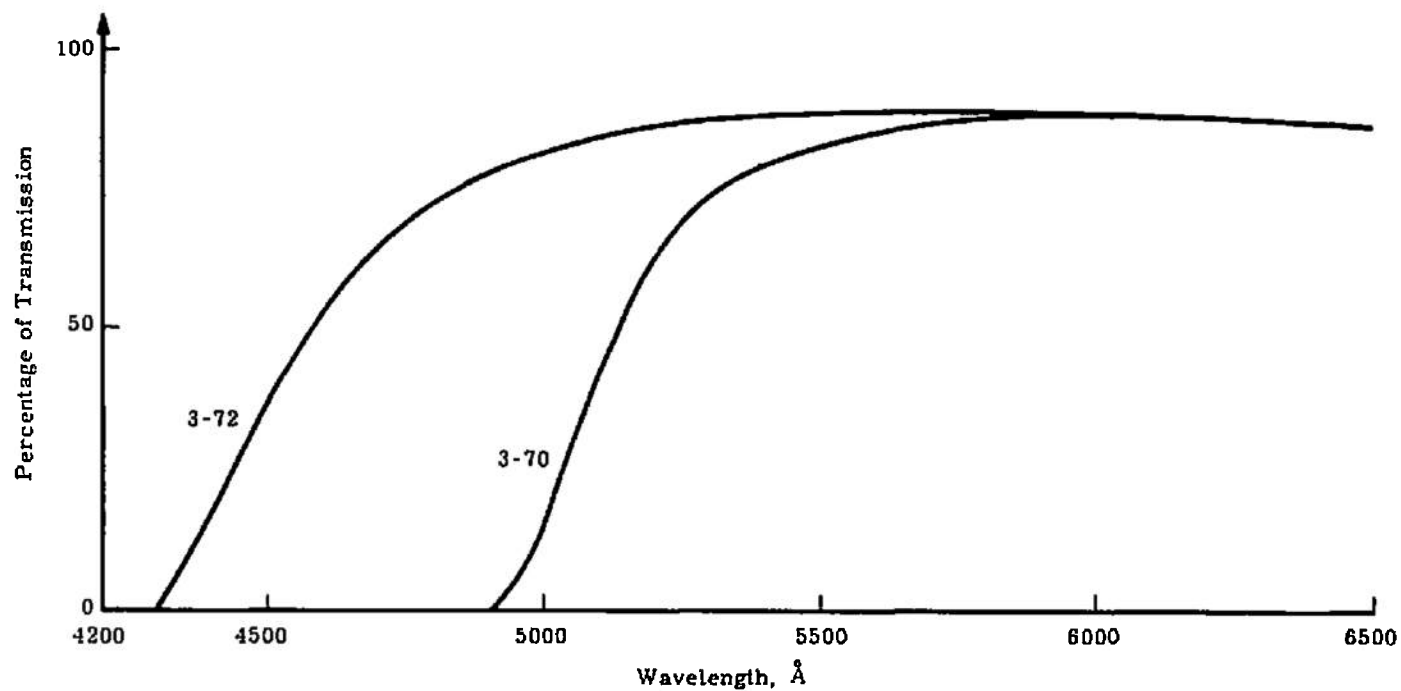
a. Color Filter
Fig. 21 Transmission Characteristics of Filters
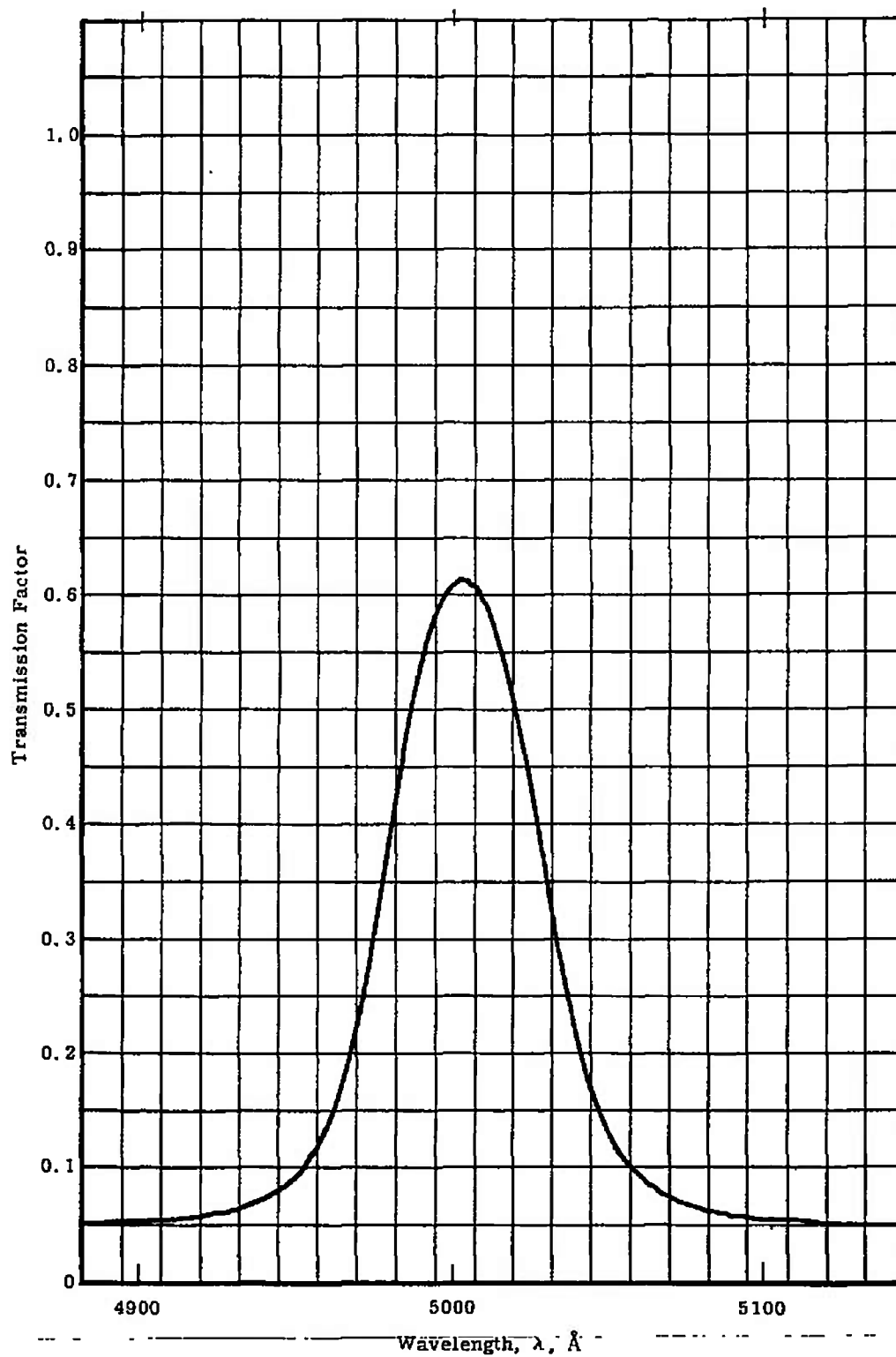
b. Helium Filter
Fig. 21 Concluded

48

4.2 PLUME SOURCE CONDITIONS

Total temperature in the rocket simulator chamber was measured by means of a thermocouple which passed through the pressure line and extended into the chamber (Table III). Chamber pressure was measured by means of a pressure tap in the chamber wall. For the 0.030- and 0.080-in.-throat-diam simulators, reservoir pressure could be taken equal to the static pressure. However, in the case of the 0.315-in.-throat-diam simulator with a chamber-to-throat area ratio of 1.61, the total-to-static pressure ratio was calculated to be 1.12 for the helium and argon involved and this correction was applied to the static measurement.

Average, plus maximum and minimum, values of total temperature and reservoir pressure in the simulator chamber are given in Table IV for the respective conditions.

4.3 PLUME IMPACT PRESSURE SURVEYS

An axial centerline impact pressure survey of the plume was made for each condition with measurements made at 1-in. intervals from the simulator nozzle exit plane ($x = 0$) to the Mach disk. Radial surveys extending from the centerline ($R = 0$) past the outer edge of the test core were made at $x = 3$ in and at axial stations 5 in. apart from $x = 5$ in. to the Mach disk. For the IC conditions, radial surveys were also made at $x = 1$ in. In the mixing region of the plume, measurements were generally made at nominal 1/8-in. radial intervals with 1/4- and 1/2-in. increments being used in regions of less steep gradients. During these surveys probe position was monitored on a digital voltmeter, and the probe was generally within ±0.025 in. of the nominal position. The nominal radial probe position was used in the tabulation and graphical presentation of impact pressure data for runs 1024 (condition IC5) and 1025 (condition IC2) and the 4000- and 5000-series of runs (conditions IB and IA, respectively) because excessive noise on that particular amplifier of the analog-to-digital converter was found to have rendered the recorded signal erratic.

Since the properties of the gas mixture in the plume mixing region were unknown, measured impact pressures were corrected for viscous and thermal effects as explained in Appendix I, assuming first that only nitrogen was present and then that only the plume gas was present. Although the former could be correct for points to the outside of the mixing region and the latter for points to the inside, within the mixing region the correct value should fall between the two values given.

TABLE IV
TEST SUMMARY

Condition	Plume Gas	Group Series	Test Activity	Chamber Conditions					
				T_{op}, °K			p_c, psia		
				avg	max	min	avg	max	min
IC5	Helium	1000	Impact Pressure Surveys	764	773	753	5.04	5.30	4.93
		1500	Flow Visualization .	777	791	762	4.95	5.20	4.78
		1700	Spectrometer Measurements	758	770	744	4.96	5.20	4.76
IAB	CO_2	5000	Impact Pressure Surveys	741	750	733	396	412	380
		5500	Flow Visualization	729	740	711	402	411	386
IIB	Helium	2	Impact Pressure Surveys	304	305	303	55.8	56.0	55.6
IC2	Helium	1000	Impact Pressure Surveys	711	722	696	2.03	2.10	1.91
		1500	Flow Visualization	704	721	693	1.86	2.14	1.66
		1700	Spectrometer Measurements	706	723	673	1.97	2.01	1.80
IAC	CO_2	5000	Impact Pressure Surveys	742	756	734	97.7	107.8	89.2
		5500	Flow Visualization	743	749	738	97.8	99.4	95.5
IAA	CO_2	5000	Impact Pressure Surveys	731	747	716	50.5	62.9	38.0
		5500	Flow Visualization	731	734	728	47.6	49.1	46.4
IB	Helium	4000	Impact Pressure Surveys	723	725	720	394	394	392
		4500	Flow Visualization	719	722	717	395	396	394
		4700	Spectrometer Measurements	713	721	691	398	399	396
	Argon	3500	Flow Visualization	551	553	547	2.94	3.16	2.80
			Flow Visualization	636	641	632	7.06	7.48	6.81
			Flow Visualization	725	728	721	8.00	8.04	7.95

4.4 ELECTRON BEAM

When making flow visualization photographs the tunnel and plume generator conditions were set at their desired values, and the electron gun housing was axially traversed until the electron beam was located in the plume generator nozzle exit plane. The digital voltmeter indicating the axial position of the beam was set to zero. Simultaneously, the camera shutter was opened and the electron beam was started on an axial traverse downstream. After the electron beam had moved approximately 16 in. downstream from the plume generator nozzle exit, the axial traverse was stopped and the camera shutter was closed. Tunnel data points were taken throughout the scan to monitor tunnel conditions and the exact length of axial traverse.

When filters were used, they were taped directly onto the camera lens mount. The 3-72 filter was normally used to reduce film exposure by $N_2^+(1^-)$ and $N_2(2^+)$ predominantly blue radiation yet pass the predominant radiation of helium at 5015-Å and argon at 4607-Å radiation. The 3-70 filter was used to block all radiation below 4900 Å. The narrow-band filter passed only the helium 5015-Å radiation; when it was used, several beam traverses had to be made to achieve adequate film exposure.

For rotational temperature measurements the spectrometer slits were set at 20 microns wide by 10 mm high. The rotational spectra scans were made at a scan speed of 2.5 Å/min with a lock-in time constant of 1 sec and using the 2- to 20-mv lock-in scales. For a given axial position and plume condition no more than two rotational spectra scans were made at a radial position.

A typical rotational spectra is shown in Fig. 22 (note that the R branch of the $N_2^+(1^-)(0,0)$ band was always used). From such a scan the peak heights of the spectral lines are measured. The peak heights are just the relative intensity values of the rotational lines $(I_{v'',K'-1}^{v',K'})$; using these values and the known values of $\lambda_{v'',K'-1}^{v',K'}$, Eq. (II-6) of Appendix II may be solved for rotational temperature by an iterative machine calculation. The data deck requires input data cards for the following: spectral scan number and designation, total number of spectral lines in a scan, and each line's relative intensity value.

Condition IC5
Tunnel M
He Plume
$A_e/A* = 1.61$
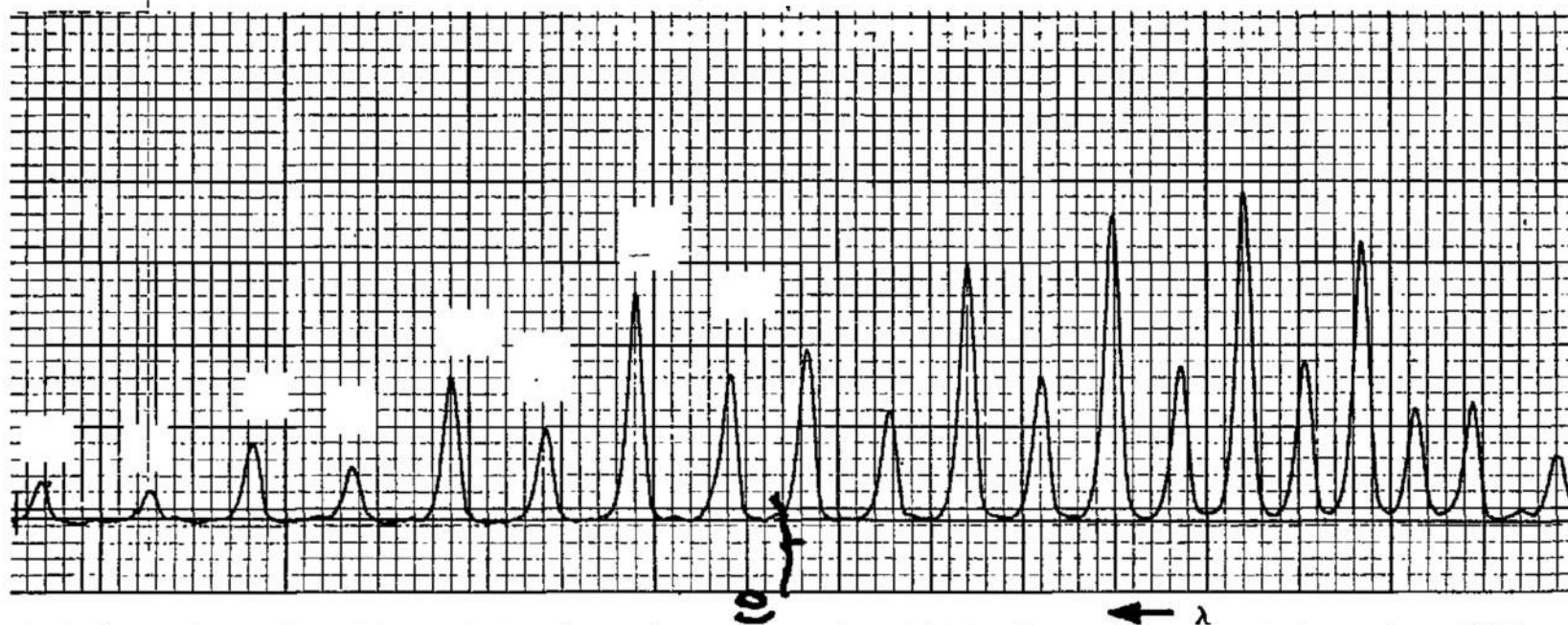$d* = 0.315$ in.
$P_c = 5$ psi
$x = 1$ in.
$y = 2.54$ in.

Fig. 22 Typical Rotational Spectra

The intensities of even numbered rotational lines ($K' = 2, 4, . . .$) are doubled before input to properly take account of the influence of nuclear statistics. Letting

$$y = \ln \frac{I_{v'', K'-1}^{v'', K'} \left(\lambda_{v'', K'-1}^{v'', K'}\right)^4}{[G]_o K'}$$

and $x = K'(K'+1)$, the machine calculation performs a least-squares fit of the y values to the straight line given by Eq. (II-6)(Fig. 23). As shown from Eq. (II-6) the slope of the stright line is

$$\frac{hc\, B_o}{k\, T_R}$$

hence, a rotational temperature can be calculated from the slope of the straight line. A temperature of 200°K is always assumed in the first step of the iteration process. Using 200°K, the values of $[G]_o$ may be calculated and a straight line is then fit to the y values. From the slope of the line, a temperature is calculated. If this calculated value of rotational temperature is not within 0.01 percent of the assumed value of rotational temperature, then the calculated value is used as the next assumed value of temperature and the calculation is repeated.

As observed by Williams (Ref. II-9) and Ashkenas (Ref. 9) only for temperatures near 200°K (pure gas, equilibrium conditions) is the plot of y values versus $x = K'(K'+1)$ a good straight line; that is, the temperature determined from the slope of the line is a function of the number of rotational lines used. For this reason a temperature defined by the maximum number of spectral lines is first calculated by the iterative procedure described in the preceding paragraph. Then the entire process is repeated for $K'_{max}-1$ lines, and this gives another rotational temperature. This process is repeated i times through $K'_{max}-i+1=6$. Only if the variation of temperature with the number of rotational lines used is fairly small can a single, well-defined temperature be obtained.

As shown in Appendix II (Eq. (II-8)), a calculation of band intensity ratios as a function of vibrational temperature can be made. With these calculations a measurement of band intensity ratios will yield the vibrational temperature. For band intensity measurements the dove prism was placed in the optical system, and the spectrometer slits were normally set 100 to 400 microns wide by 20 mm high. The output of the lock-in amplifier was fed into the integrator (Fig. 19),
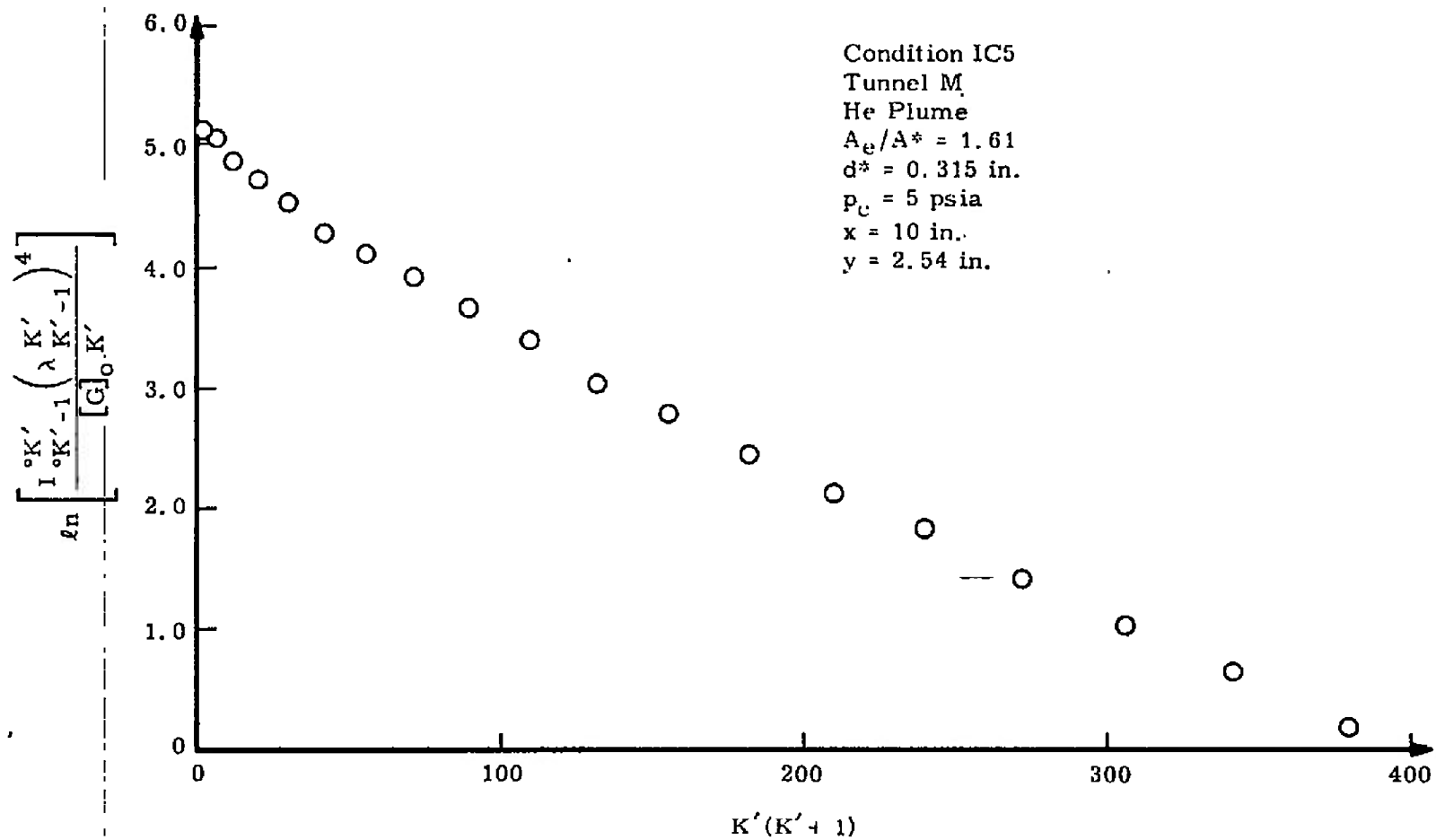
Fig. 23 Boltzmann Plot, DWM 0020

The plot shows the y-axis labeled:

$$\ln\left[\frac{I^{o}_{K'}}{I^{o}_{K'-1}}\left(\frac{\lambda_{K'}}{\lambda_{K'-1}}\right)^{4}\frac{1}{[G]_{o}K'}\right]$$

with values from 0 to 6.0, and the x-axis labeled $K'(K'+1)$ from 0 to 400.

Condition IC5
Tunnel M
He Plume
$A_e/A^* = 1.61$
$d^* = 0.315$ in.
$p_c = 5$ psia
$x = 10$ in.
$y = 2.54$ in.

and the output of the integrator was displayed by a digital voltmeter. Before a scan of a vibrational band the light from the electron beam was blocked off, and the integrator null was adjusted such that the integrator output was constant in time. The integrator output was then set to zero with the "kill" switch (Fig. 19). The spectrometer was started in its scan of the band (at a rate of 25 Å/min), and the integrator was placed into the integrate mode. The display of the digital voltmeter was observed, and the reading was recorded after the band was completely scanned. Beam current was kept constant during the integration of the two bands to be used for the intensity ratio.

The nitrogen number density was determined by integration of the $N_2^+(1^-)(0,0)$ band. The integration technique was the same as for vibrational temperature determination. Spectrometer slits were 60 microns wide by 20 mm high, and the dove prism was used. At the end of each $(0,0)$ band integration the beam current was measured at both the flat-plate collector on the tunnel floor and at the auxiliary collector (extended position) located directly beneath the gun orifice. The ratio of band intensity to beam current (auxiliary collector value used) then gave a relative value of nitrogen number density, as shown by Eq. (II-13), assuming T_V to have the same value in the plume region as in the free-stream region. Absolute nitrogen number densities are then obtained by relating these relative values to the band intensity-beam current ratio obtained from centerline free-stream measurements and the Tunnel M data reduction program calculation of free-stream nitrogen density (Appendix II).

The determination of helium number density was obtained by the integration of the He 5015-Å line. The integration technique was the same as that for nitrogen number density determination. Spectrometer slits were 60 microns wide by 20 mm high, and the dove prism was used. Again, beam current was measured at both positions at the end of each integration. The ratio of line intensity to beam current (auxiliary collector value used) then gave a relative value of helium number density, as shown by Eq. (II-1). Absolute helium number density values were then obtained using the calibration of the ratio of line intensity to beam current versus helium number density (Appendix II).

SECTION V
EXPERIMENTAL RESULTS

5.1 PHOTOGRAPHS

Color still photographs were taken for all conditions in Tunnel M using the electron beam as the source of excitation. Photographs were

taken with and without filters, as discussed in Section 4.4. Photographs taken with the filters showed considerably more detail than those without filters. Photographs taken with the various filters were usually quite similar, differing only in details of coloring which could be altered in processing. As far as revealing the basic structure of the flow field in the photography, the specific filter used was found to be of minor importance.

Selected photographs are given in Figs. 24 through 28. The first three of these are for helium plumes and are for conditions IC5, IC2, and IB. The fourth is for a CO_2 plume, condition IAB, and the fifth is of an argon plume.

Figure 24 gives the photograph for Group 1517, condition IC5, using the 3-70 filter. In the coloring of this particular photograph nitrogen appears as red and helium as green. The outer shock appears quite prominently as the line dividing the bright red region from the background. The nitrogen shock layer appears as the red region. In the region near the nozzle exhaust, the inner shock appears as the line dividing the bright green region from the inner dark green background. The dividing line between the nitrogen and helium is quite distinct.

As one moves farther downstream, the inner shock becomes less distinct because the density is low. It is not clear whether the shock is becoming thicker as one moves downstream or the densities are so low that the photographs do not register the small difference in density across the shock. The contact region, which begins as a thin line near the exit plane, becomes very thick. The outer limits of the helium and the inner limit of the nitrogen can be picked off the photograph as the limit of the appropriate color.

The large thickness of the mixing region would not be anticipated on the basis of experience under lower altitude conditions. Farther downstream, the thickness of the mixing region is several times that of the nitrogen shock layer.

Figure 25 is a photograph for condition IC2, which is identical to condition IC5 except for the chamber pressure, which is 2 psi rather than 5 psi. Although the photograph is in every way similar, a large relative plume length is shown. The closing of the inner shock is faintly visible.

Figure 26 is for condition IB, which is for a high chamber pressure (450 psi) and the large area ratio nozzle. The inner shock is considerably more distinct than in the two previous photographs because of the
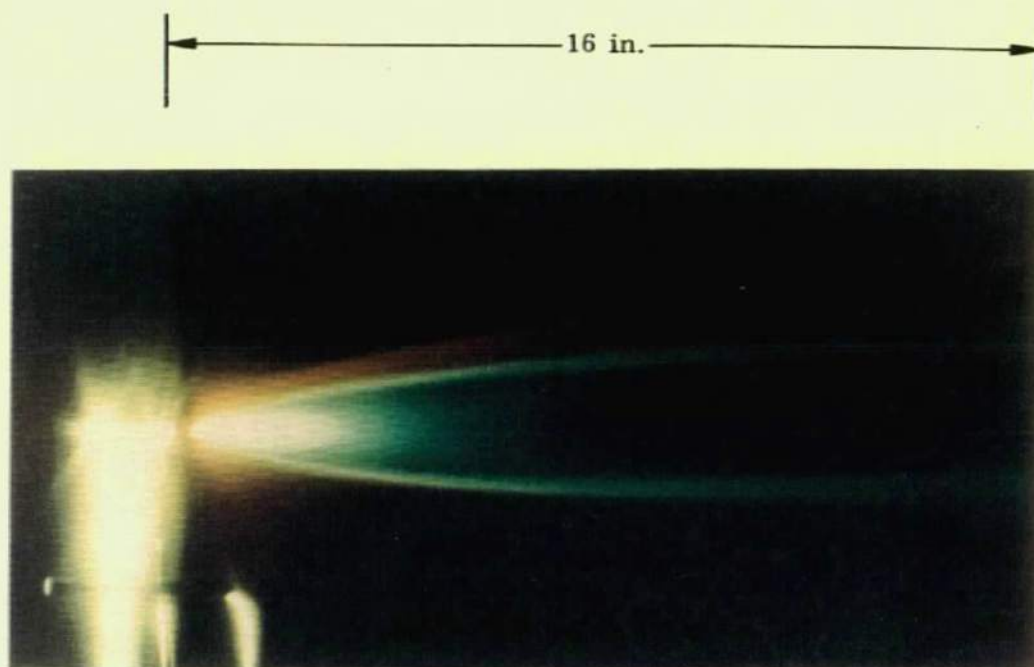
16 in.

Fig. 26 Photograph of Plume for Condition IB, Tunnel M, He Plume, $A_e/A^* = 25$, $d^* = 0.030$ in., and $p_c = 450$ psia

Fig. 27 Photograph of Plume for Condition IAB, Tunnel M, CO_2 Plume, $A_e/A^* = 25$, $d^* = 0.030$ in., and $p_c = 400$ psia
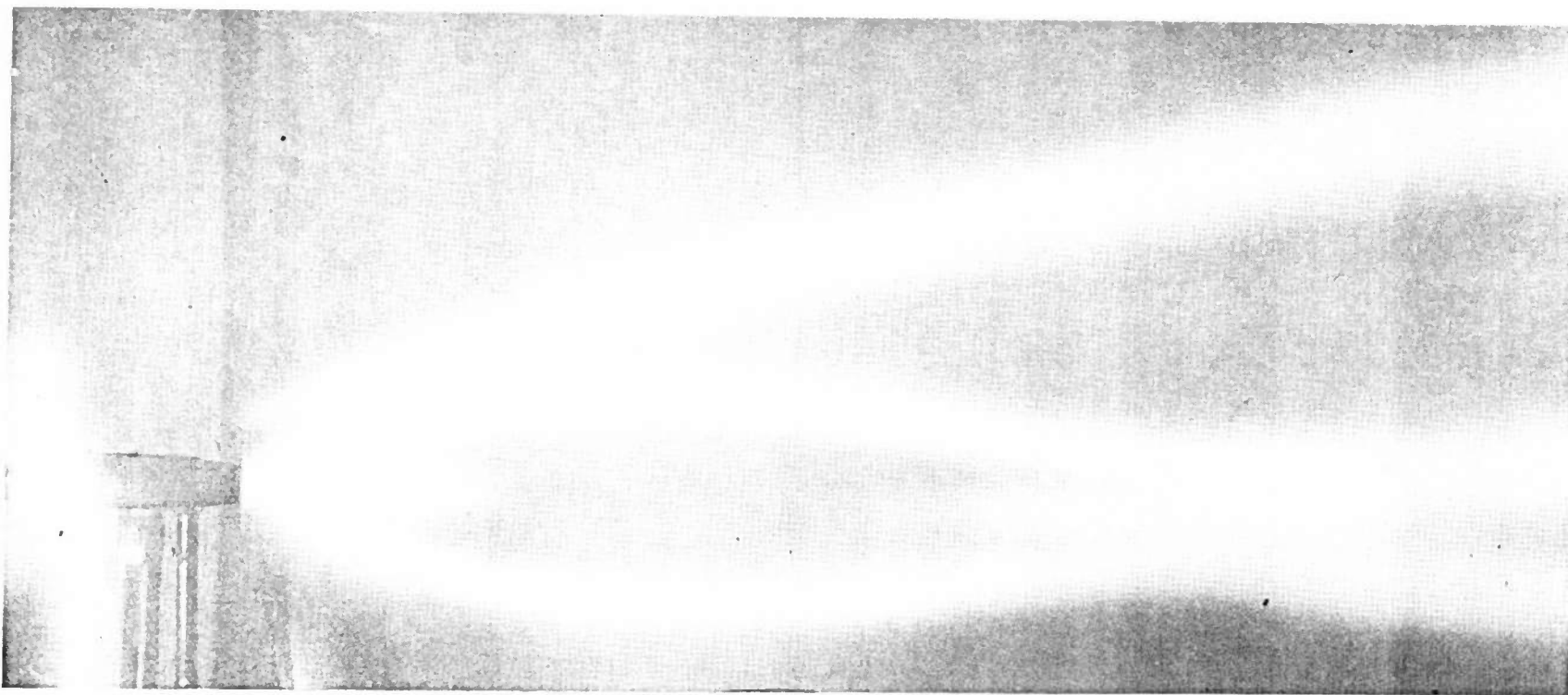
58

Fig. 28 Photograph of Argon Plume, Tunnel M, $A_e/A^* = 1.6$, $d^* = 0.315$, and $p_c = 3$ psia

considerably higher density. The mixing region is still relatively large. The long slender nature of this plume is appropriate for the large value of λ for this particular combination of nozzle area ratio and γ.

Figure 27 is for the condition IAB, which is a CO_2 plume with conditions chosen to match condition IC5. Because of the differences in d^* and p_c, direct comparison of physical lengths on the corresponding photographs (Figs. 24 through 27) should not be made.

Figure 28 is for a condition similar to IC2 except with argon as the plume gas. This particular condition was run in an unsuccessful attempt to evaluate effects of condensation. The photograph is included because it shows a larger extent of the inner plume than any of the others. In particular, regions around the Mach disk are shown. It is not possible, however, to pick out a distinct line corresponding to the Mach disk.

No worthwhile photographic data were retained from Tunnel D. Color schlieren photographs were taken, but were too faint to be of value. The installation photograph (Fig. 13) was actually taken during a run, and it is obvious that little flow information can be drawn from the photograph.

5.2 IMPACT PRESSURE SURVEYS

The corrected impact pressure data for the various conditions are given in the series of figures from Fig. 29 to Fig. 35. For the data taken in Tunnel M, the pressure data have been corrected for orifice and probe effects (Appendix I). In the outer flow the raw data have been corrected using values for nitrogen, whereas, for the inner flow, values appropriate for the plume gas have been used. In the mixing region values are given for both gases.

For each condition tested in Tunnel M the (a) part of the figure gives an axial centerline traverse, and the succeeding parts give results for radial surveys at various axial locations.

For the axial surveys the most striking feature is the minimum in the value of impact pressure. This minimum is assumed to occur at the location of the Mach disk. Table V summarizes the results for the location of the Mach disk. Also shown is the Mach disk location normalized with the scaling parameters of Eq. (19). For the first condition of Table I (conditions IC5 and IAB), the agreement is adequate, but for
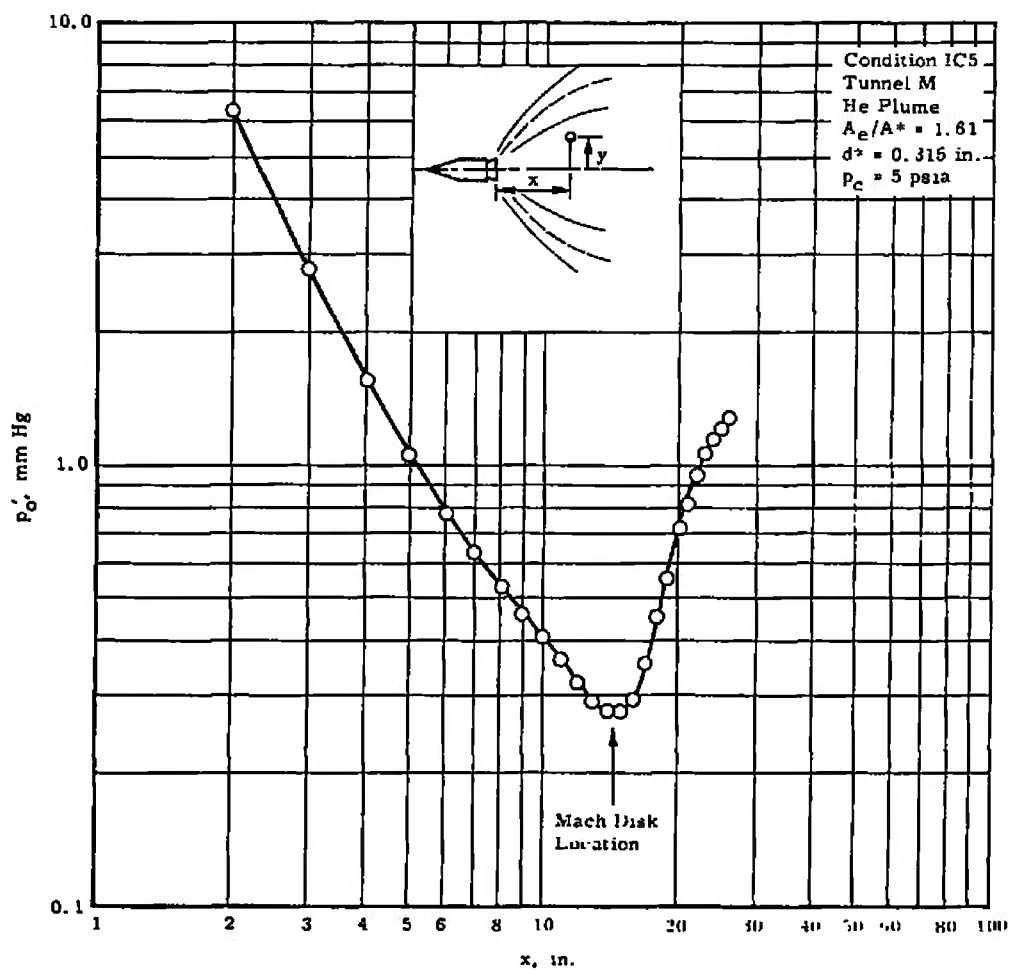
a. Axial Centerline Corrected Impact Pressure Survey
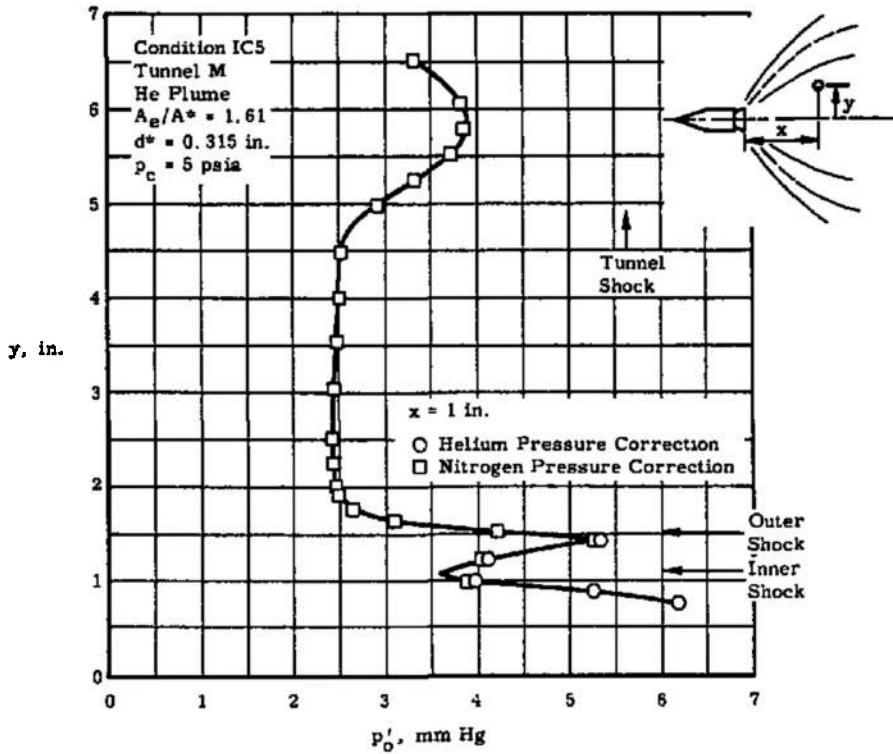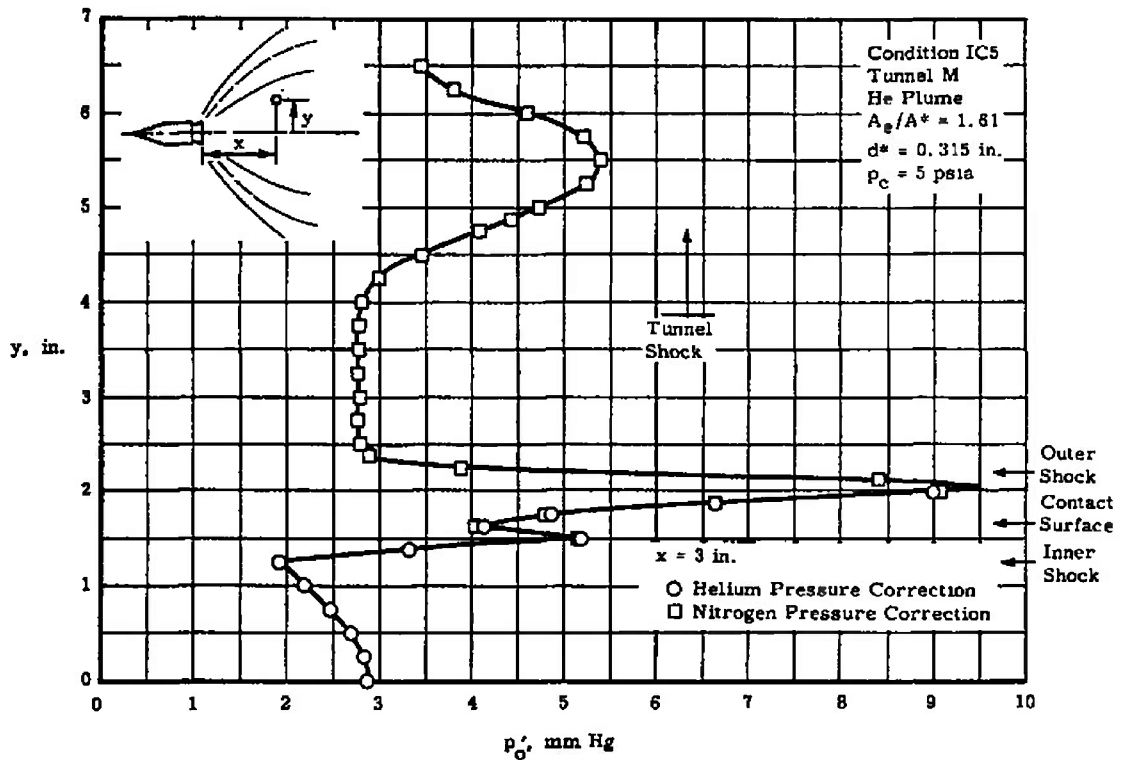Fig. 29 Impact Pressure Surveys for Condition IC5

b. Radial Corrected Impact Pressure Survey (x = 1 in.)

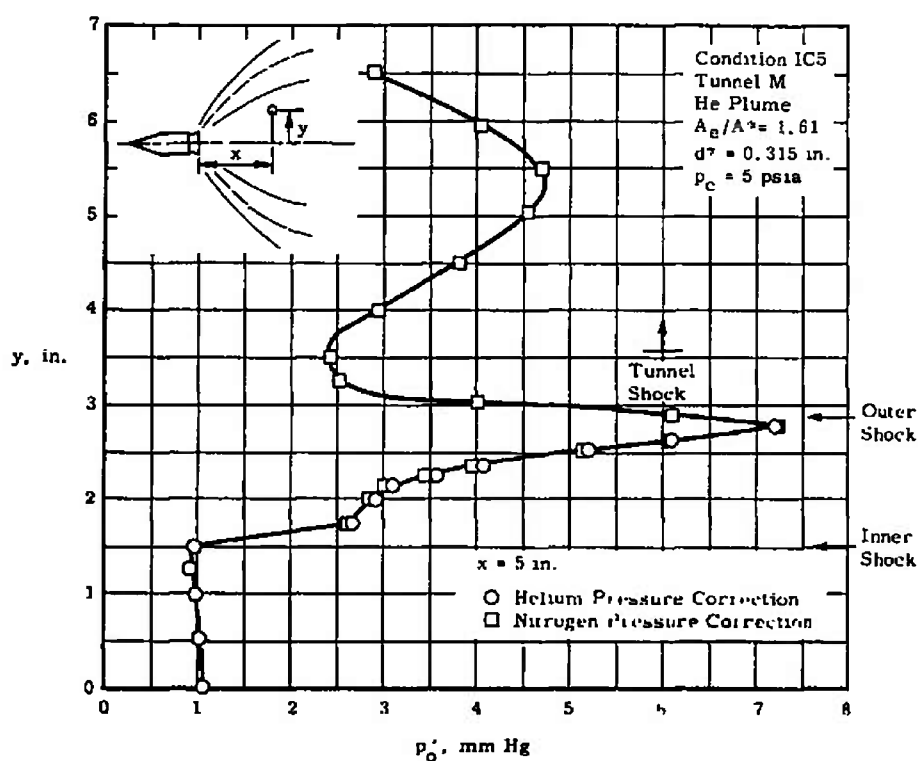c. Radial Corrected Impact Pressure Survey (x = 3 in.)
Fig. 29 Continued
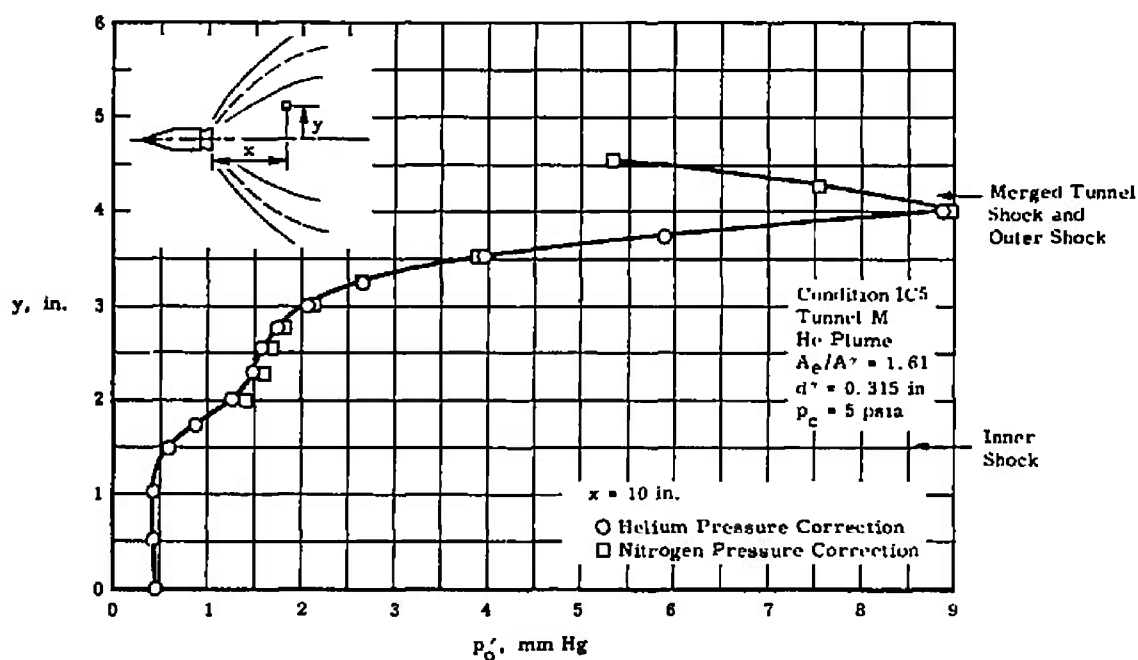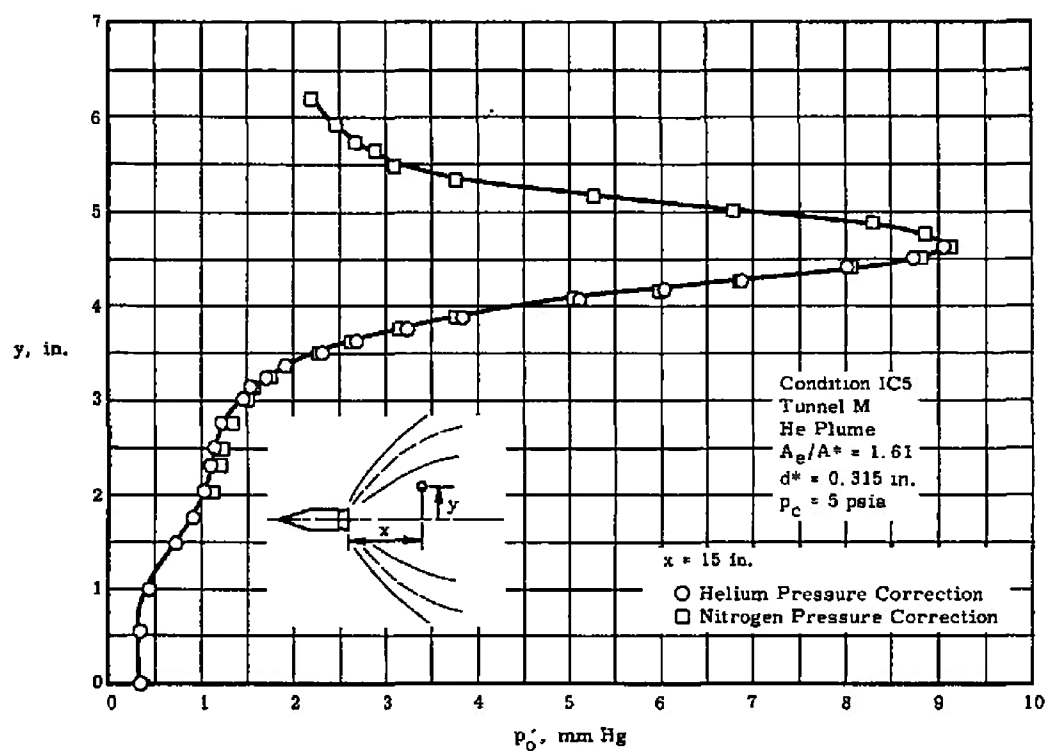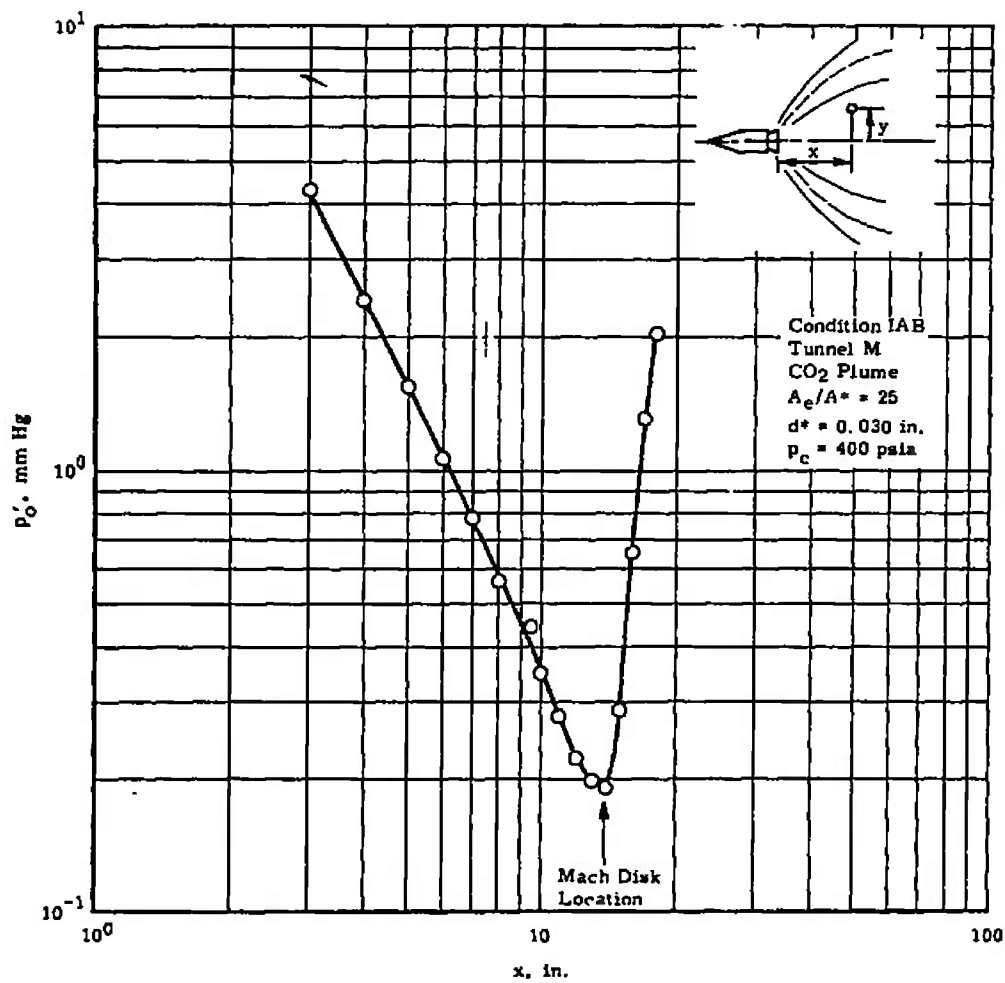
d. Radial Corrected Impact Pressure Survey (x = 5 in.)

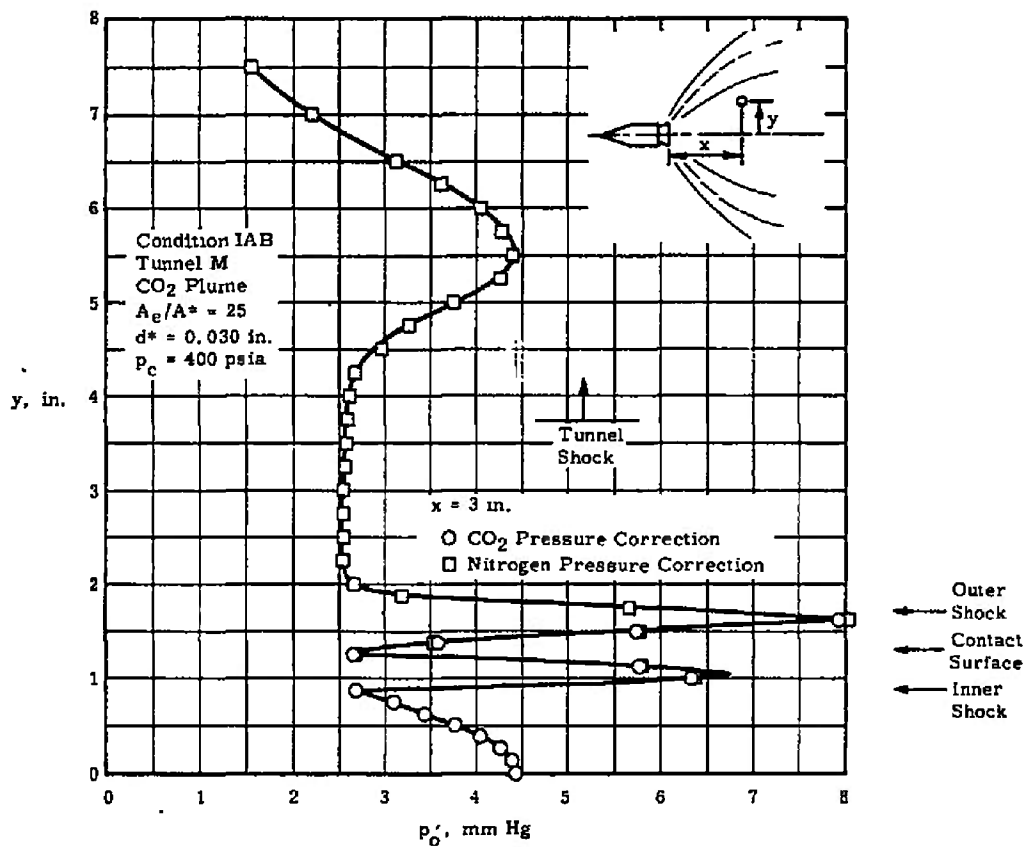e. Radial Corrected Impact Pressure Survey (x = 10 in.) -
Fig. 29 Continued

f. Radial Corrected Impact Pressure Survey (x = 15 in.)
Fig. 29 Concluded

a. Axial Centerline Corrected Impact Pressure Survey
Fig. 30 Impact Pressure Surveys for Condition IAB

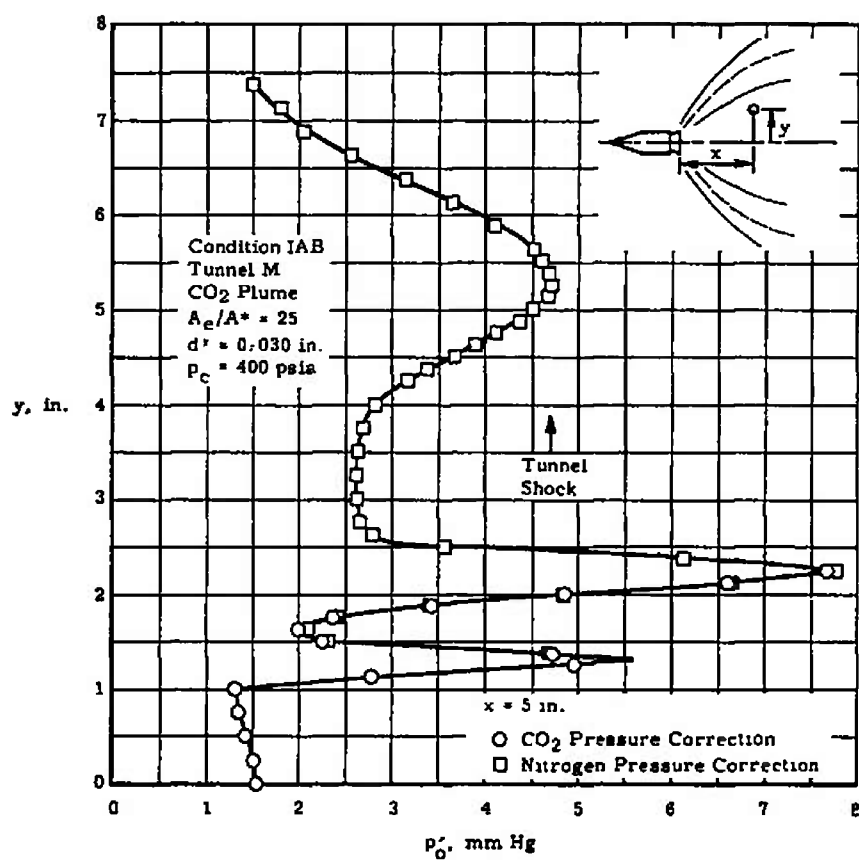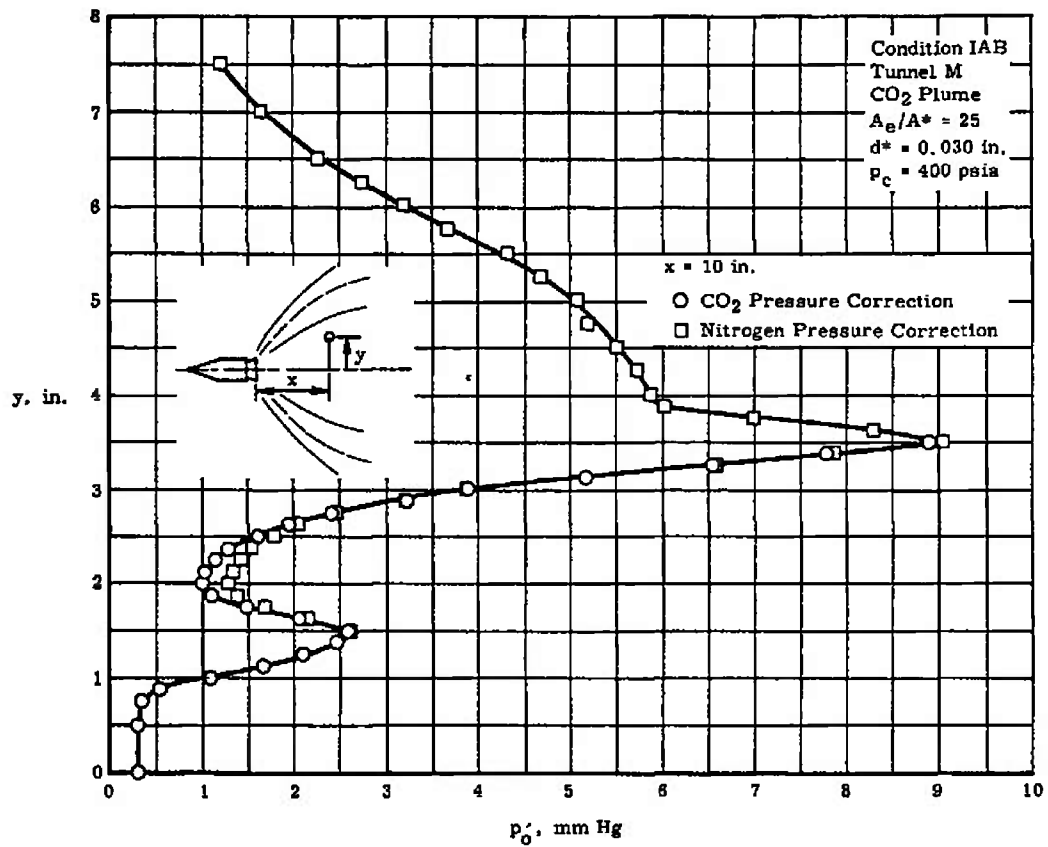b. Radial Corrected Impact Pressure Survey (x = 3 in.)
Fig. 30 Continued

Condition IAB
Tunnel M
CO_2 Plume
$A_e/A^* = 25$
$d^* = 0.030$ in.
$P_c = 400$ psia

Tunnel
Shock

$x = 5$ in.

O CO_2 Pressure Correction
□ Nitrogen Pressure Correction

y, in.

P_o', mm Hg

c. Radial Corrected Impact Pressure Survey (x = 5 in.)
Fig. 30 Continued

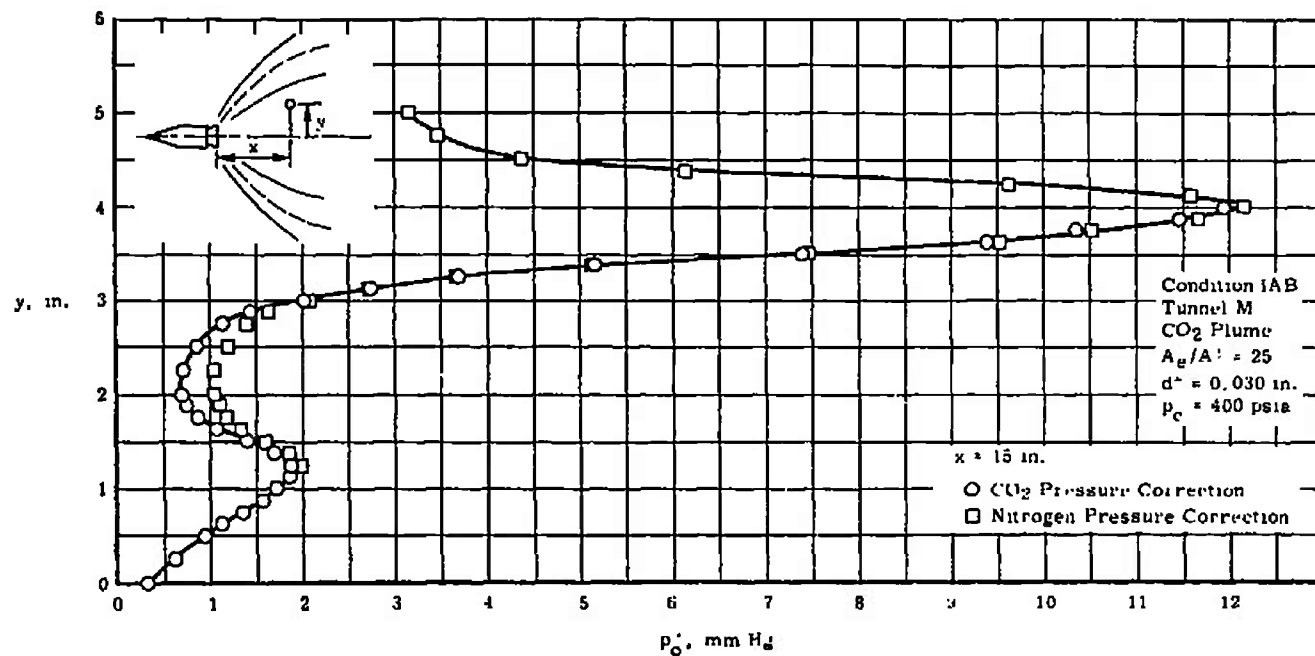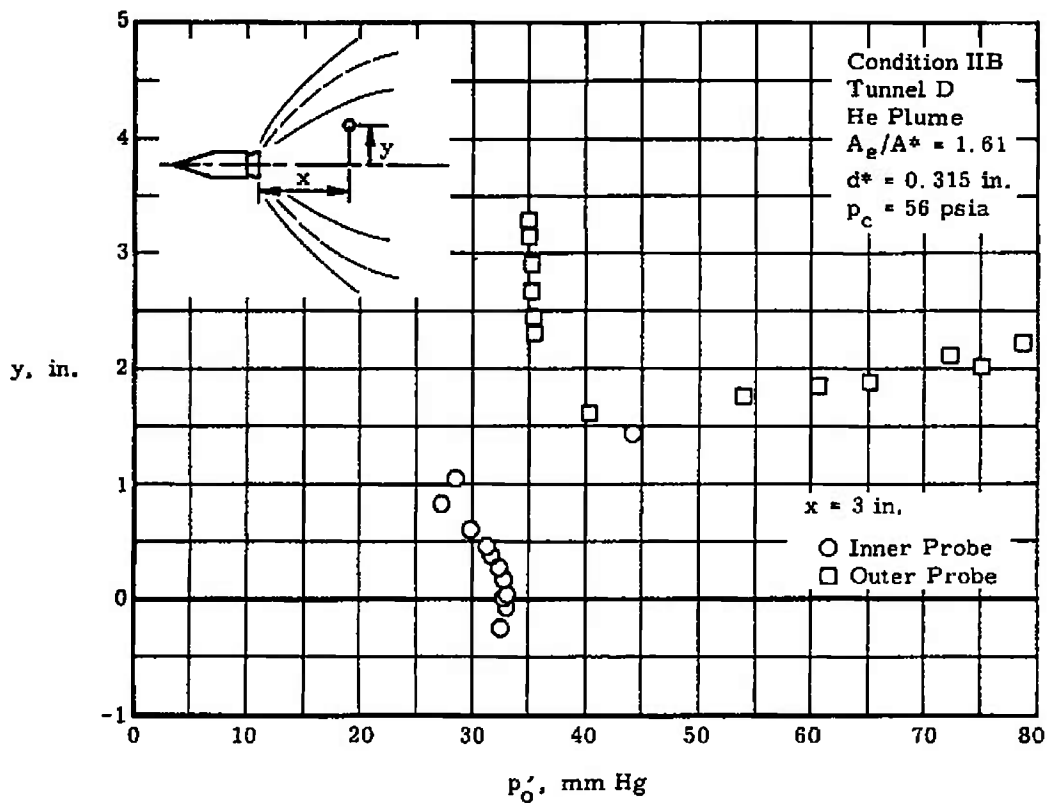d. Radial Corrected Impact Pressure Survey (x = 10 in.)
Fig. 30 Continued

e. Radial Corrected Impact Pressure Survey (x = 15 in.)

Fig. 30 Concluded

a. Radial Impact Pressure Survey (x = 3 in.)
Fig. 31 Impact Pressure Surveys for Condition IIB

b. Radial Impact Pressure Survey (x = 5 in.)
Fig. 31 Continued

c. Radial Impact Pressure Survey (x = 10 in.)
Fig. 31 Concluded

a. Axial Centerline Corrected Impact Pressure Survey
Fig. 32 Impact Pressure Surveys for Condition IC2

b. Radial Corrected Impact Pressure Survey (x = 1 in.)

c. Radial Corrected Impact Pressure Survey (x = 3 in.)
Fig. 32 Continued

d. Radial Corrected Impact Pressure Survey (x = 5 in.)

e. Radial Corrected Impact Pressure Survey (x = 10 in.)
Fig. 32 Concluded

a. Axial Centerline Corrected Impact Pressure Survey
Fig. 33 Impact Pressure Surveys for Condition IAC

b. Radial Corrected Impact Pressure Survey (x = 3 in.)
Fig. 33 Continued

c. Radial Corrected Impact Pressure Survey (x = 5 in.)
Fig. 33 Continued
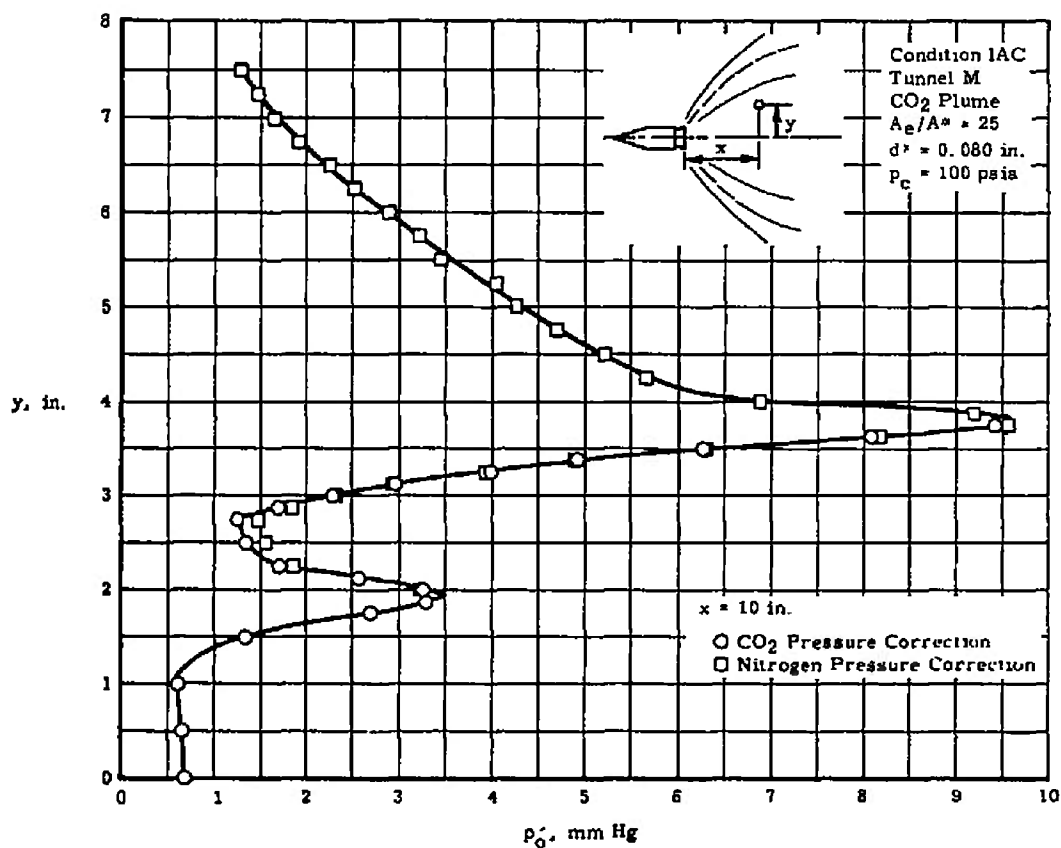
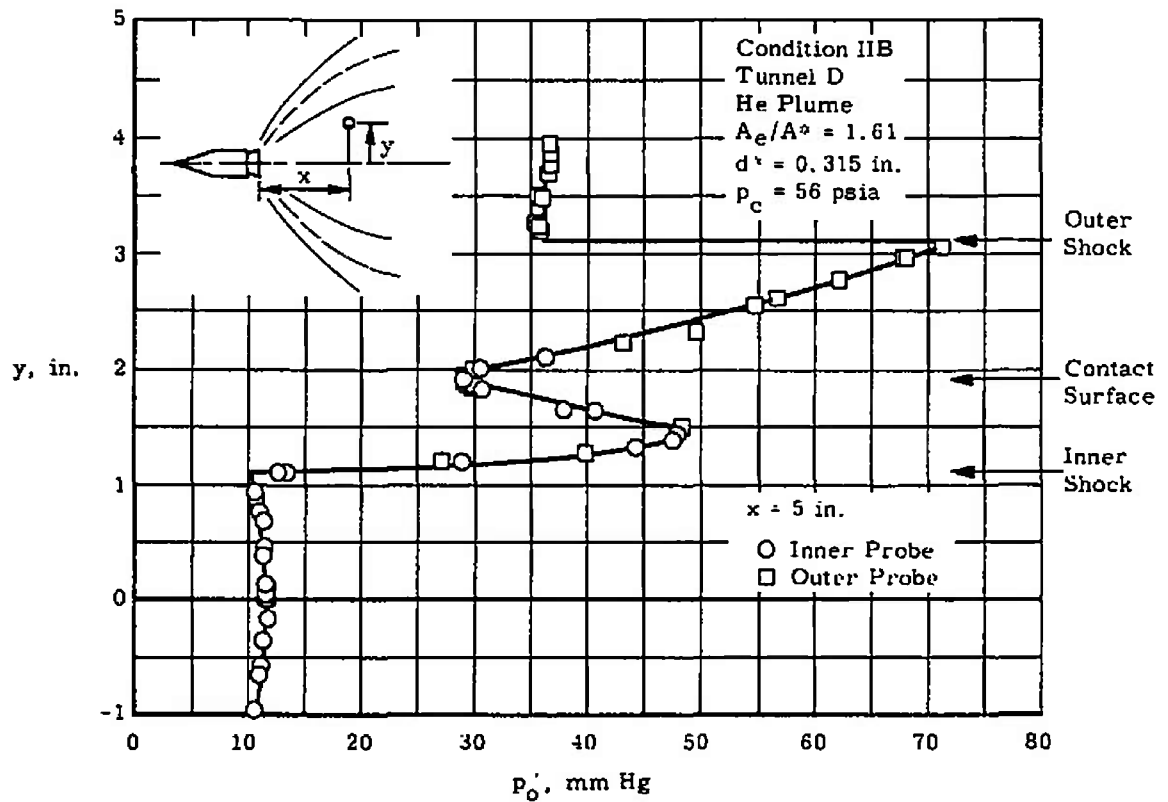d. Radial Corrected Impact Pressure Survey (x = 10 in.)
Fig. 33 Continued
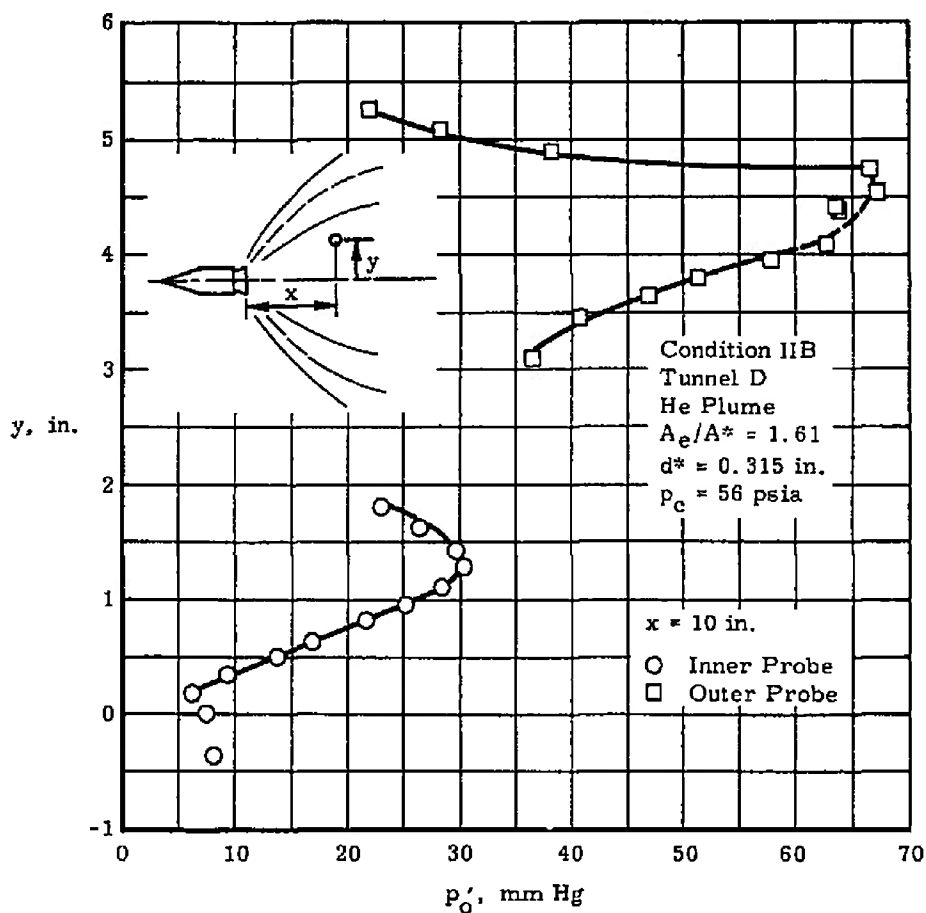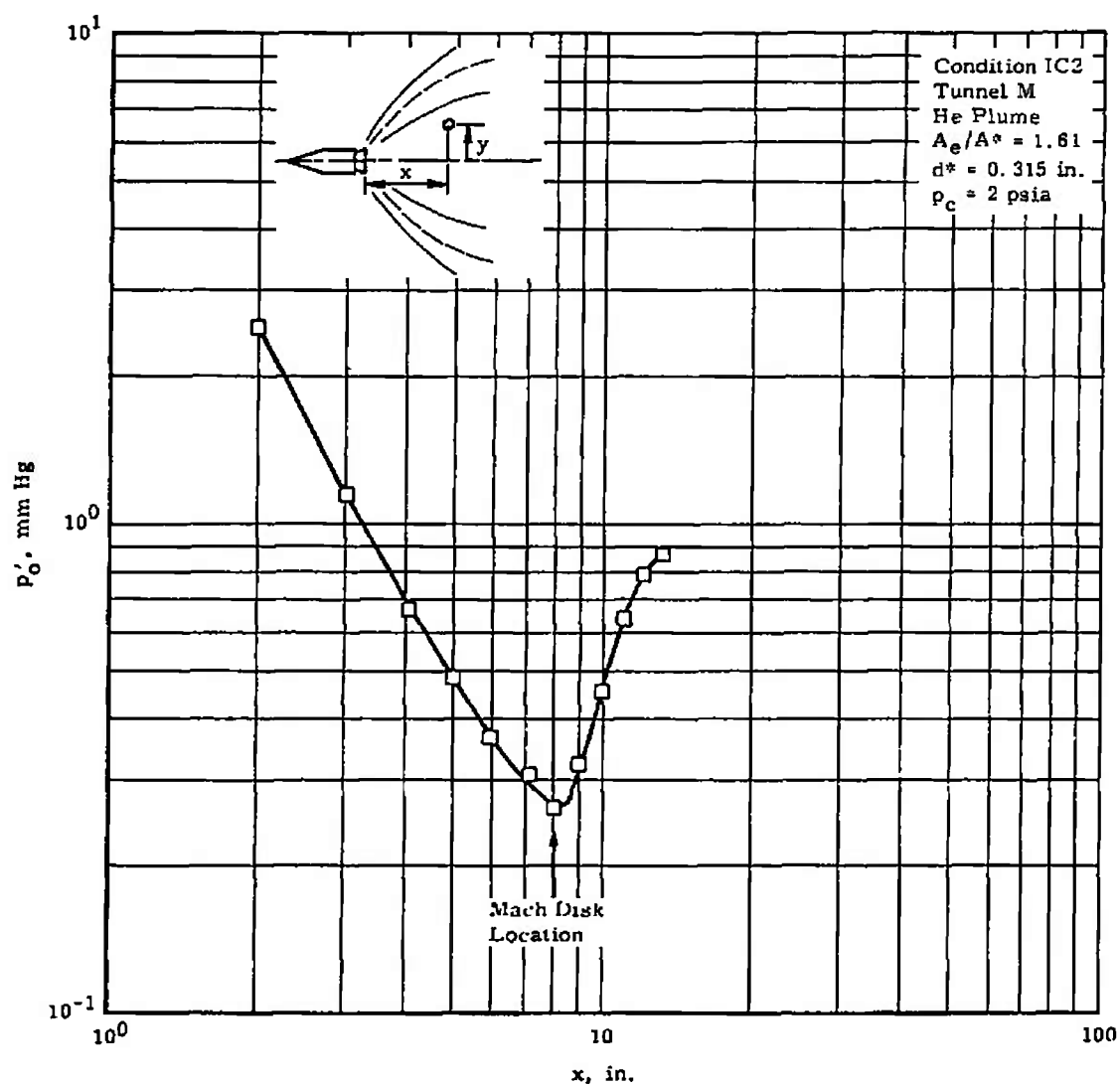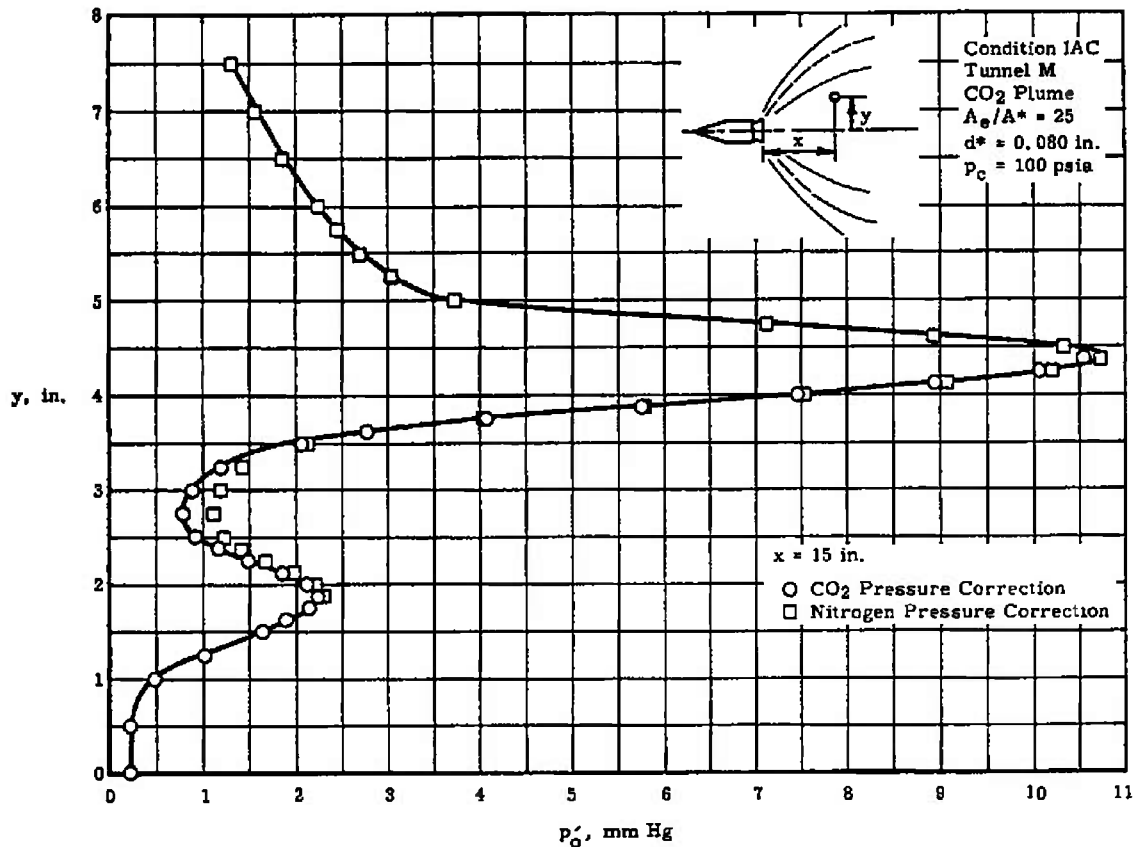
e. Radial Corrected Impact Pressure Survey (x = 15 in.)
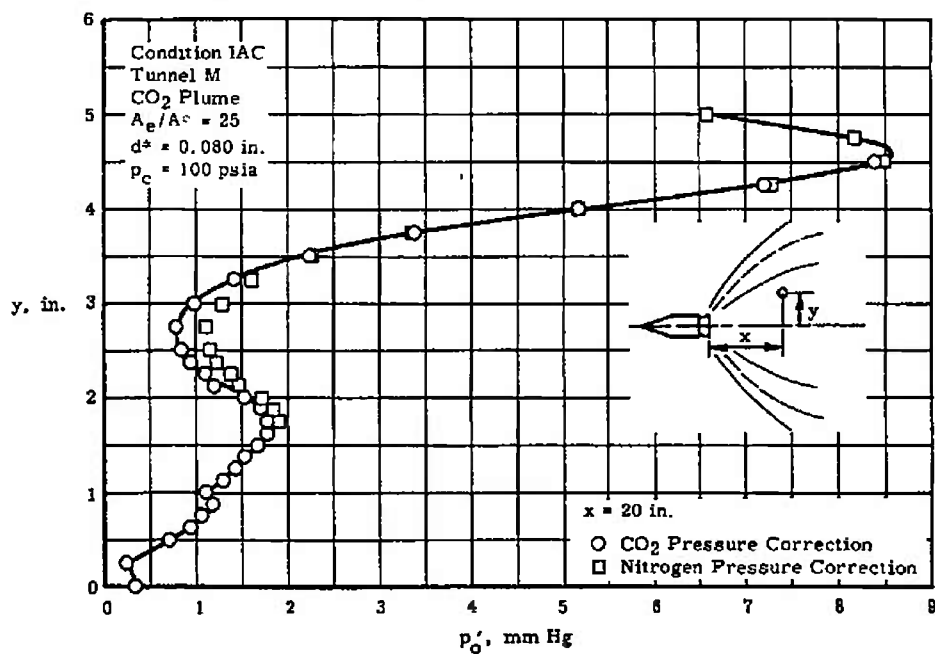
f. Radial Corrected Impact Pressure Survey (x = -20 in.)
Fig. 33 Concluded
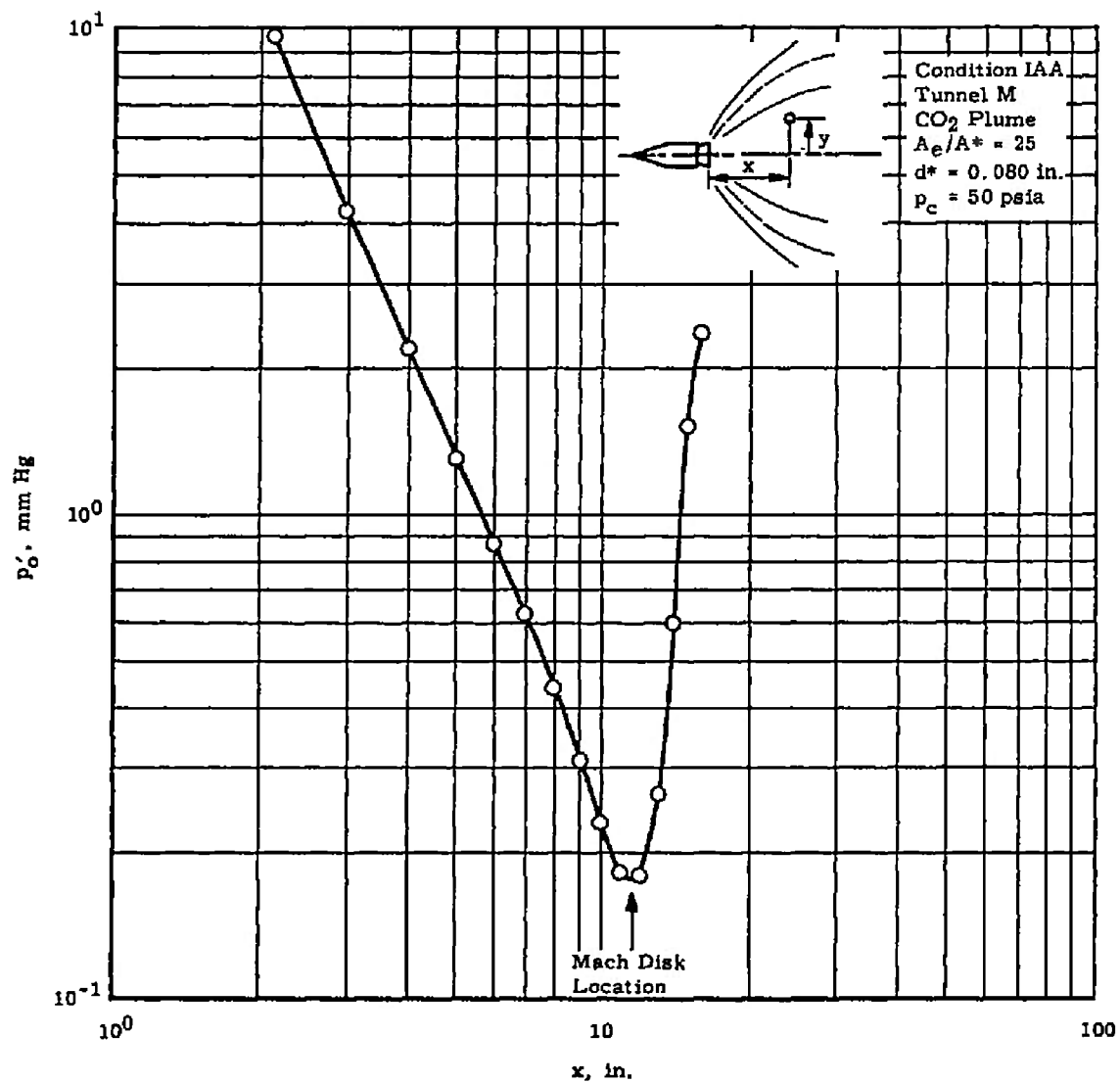
a. Axial Centerline Corrected Impact Pressure Survey
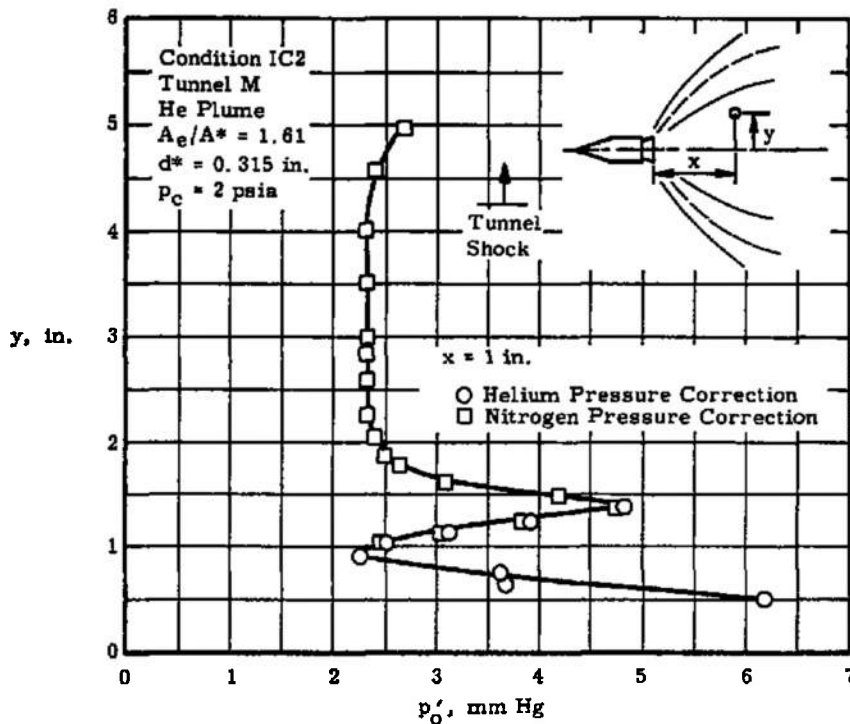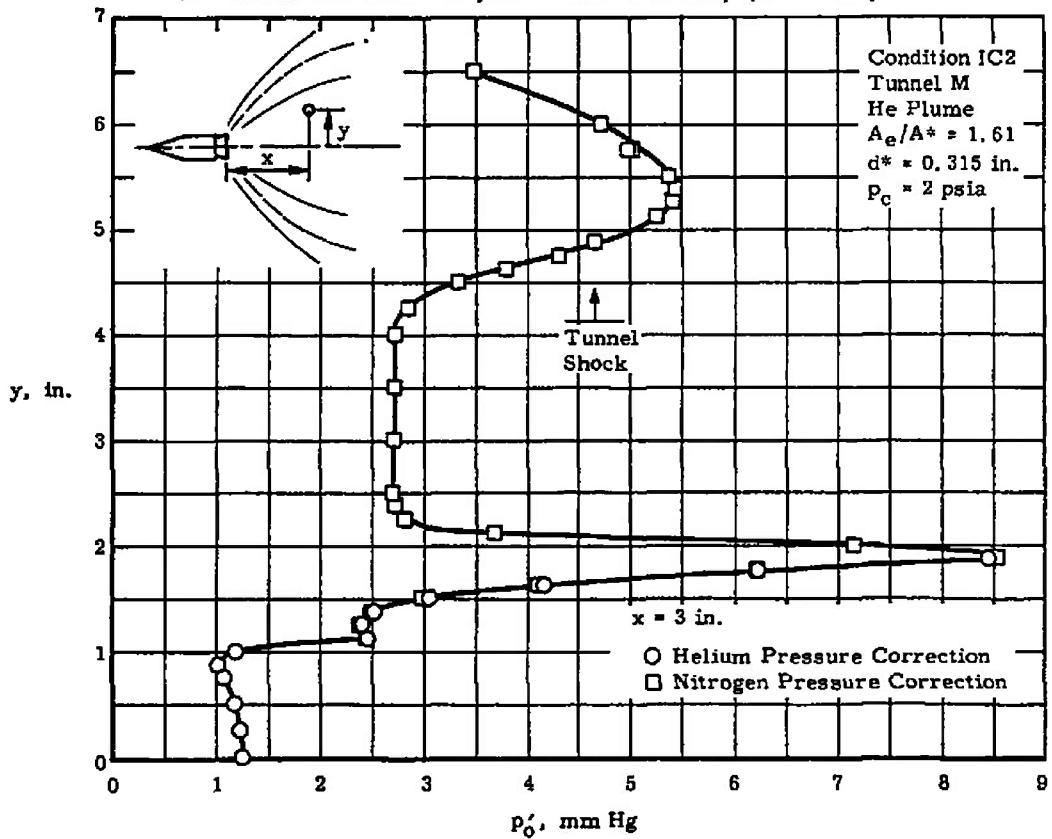Fig. 34 Impact Pressure Surveys for Condition IAA
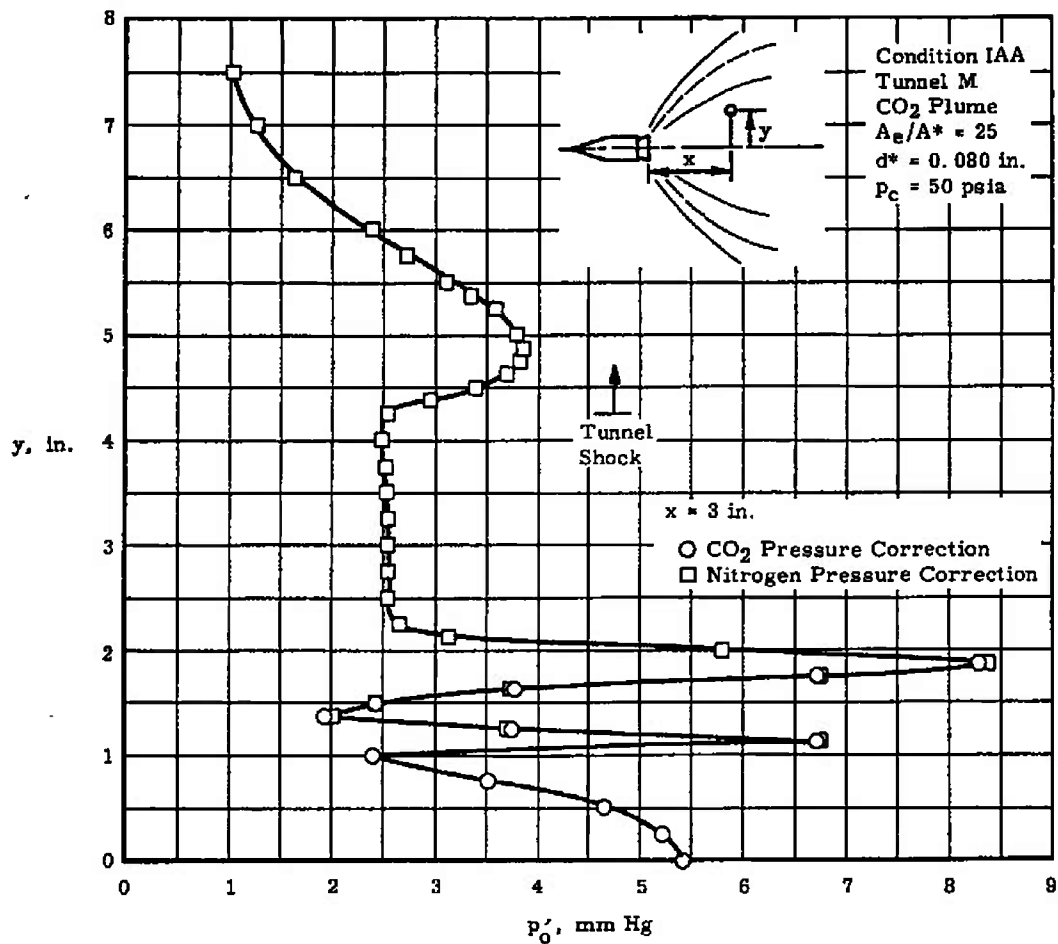
b. Radial Corrected Impact Pressure Survey (x = 3 in.)
Fig. 34 Continued
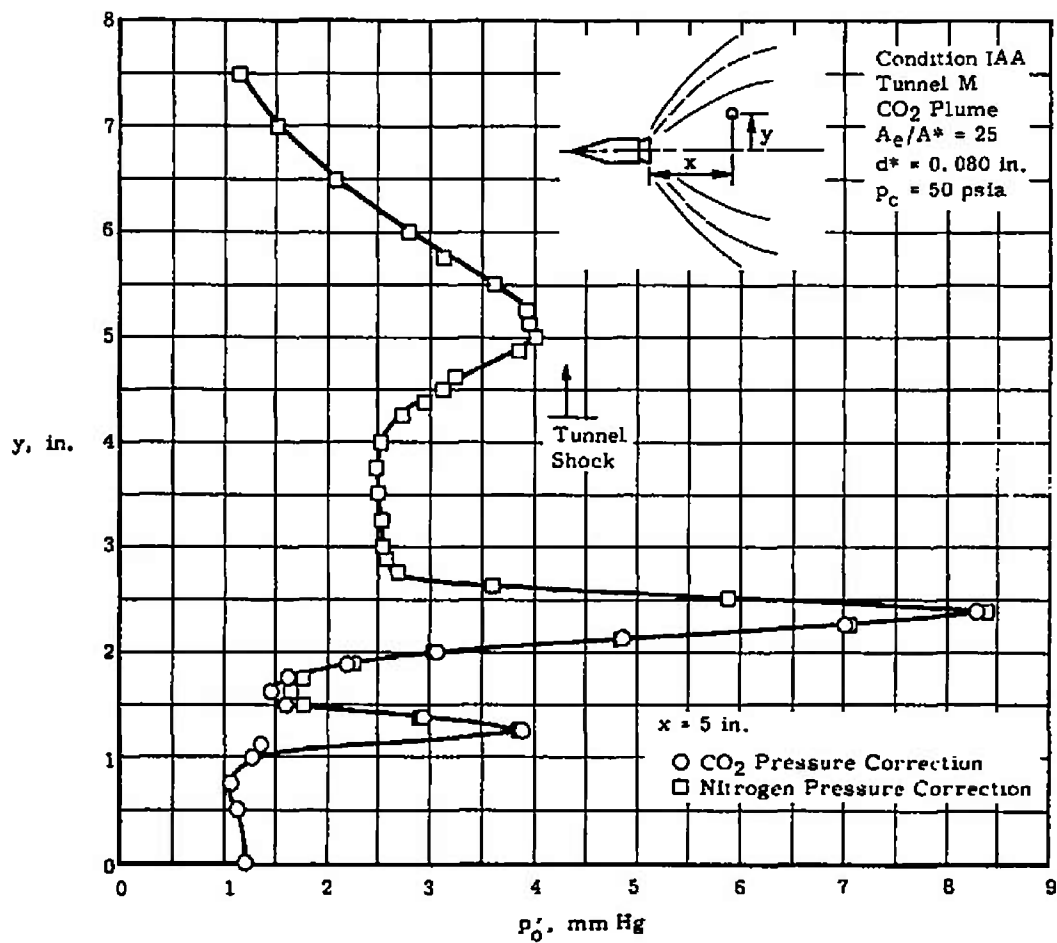
c. Radial Corrected Impact Pressure Survey (x = 5 in.)
Fig. 34 Continued

Condition IAA
Tunnel M
CO_2 Plume
$A_e/A^* = 25$
$d^* = 0.080$ in.
$p_c = 50$ psia

x = 10 in.

O CO_2 Pressure Correction
□ Nitrogen Pressure Correction

y, in.

p_o', mm Hg
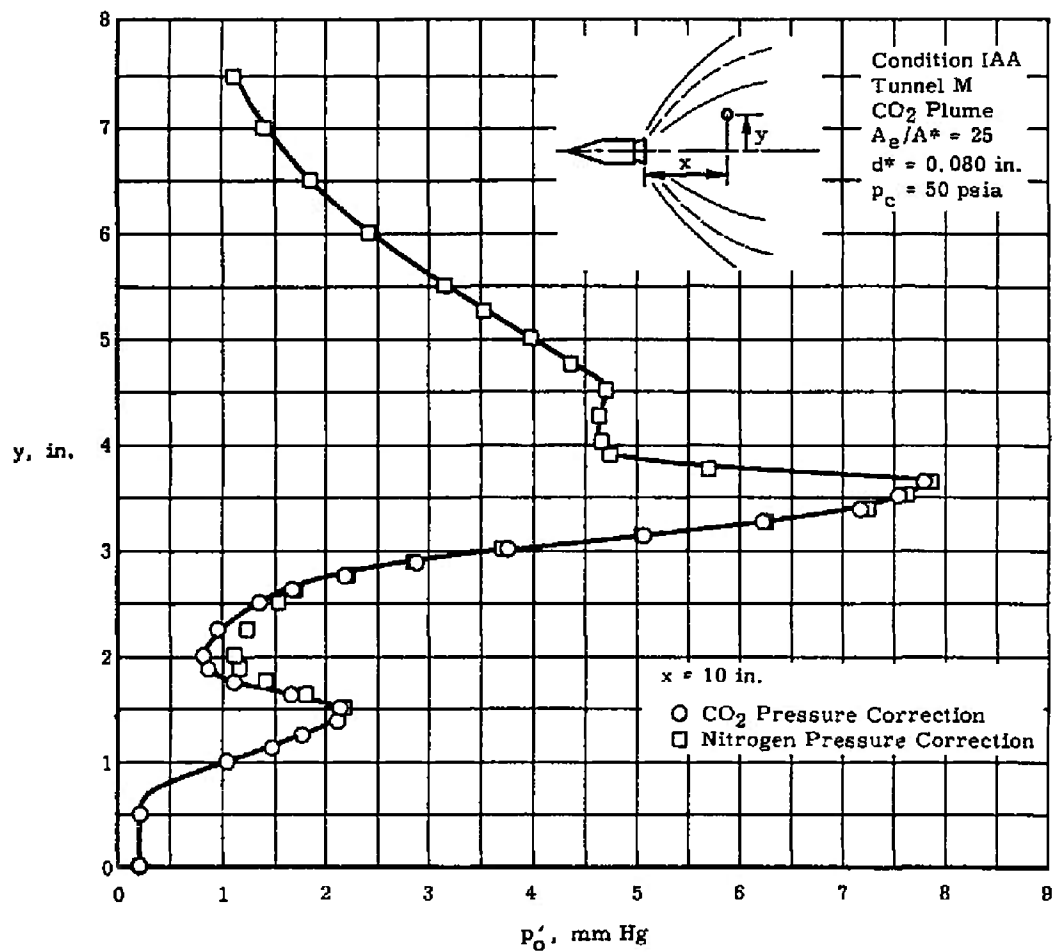
d. Radial Corrected Impact Pressure Survey (x = 10 in.)
Fig. 34 Continued
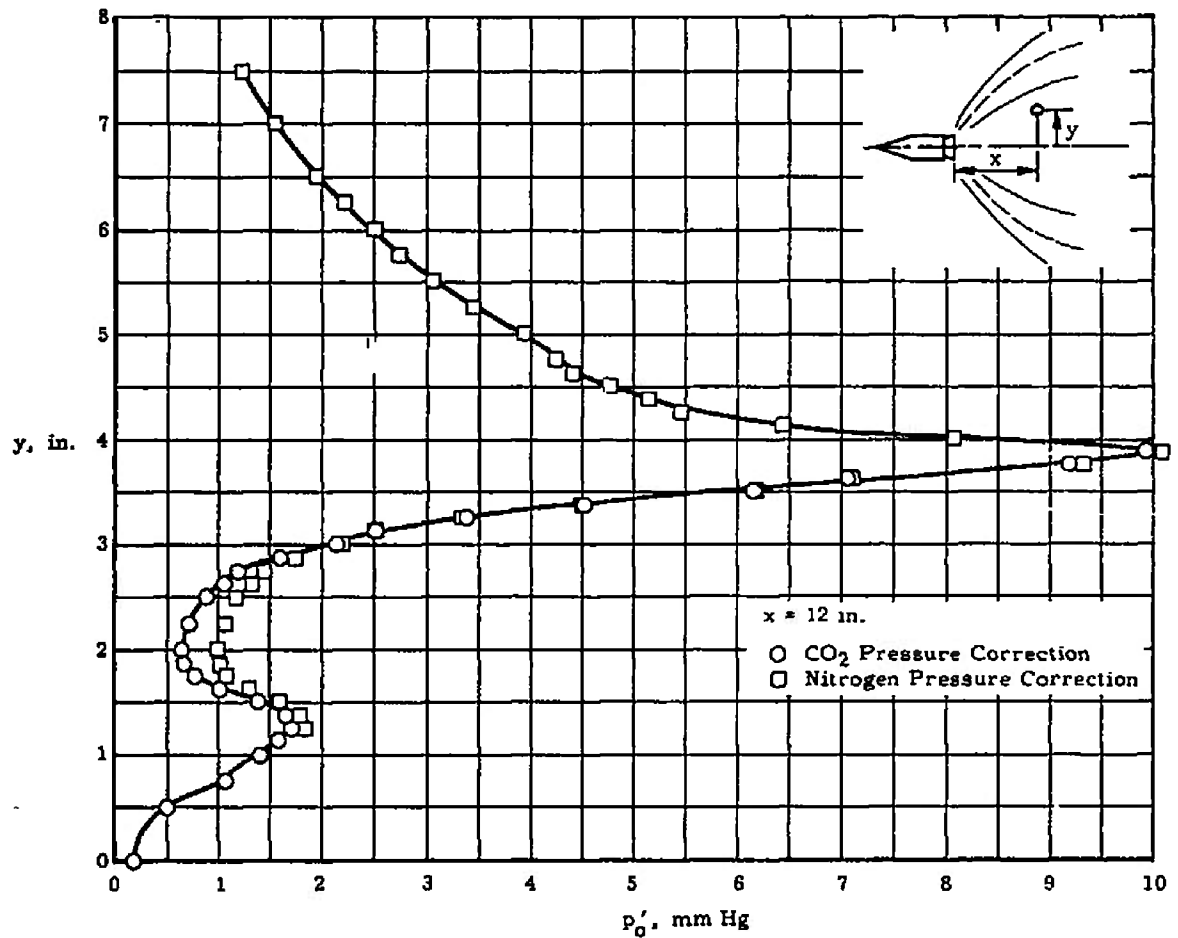
e. Radial Corrected Impact Pressure Survey (x = 12 in.)
Fig. 34 Concluded

85
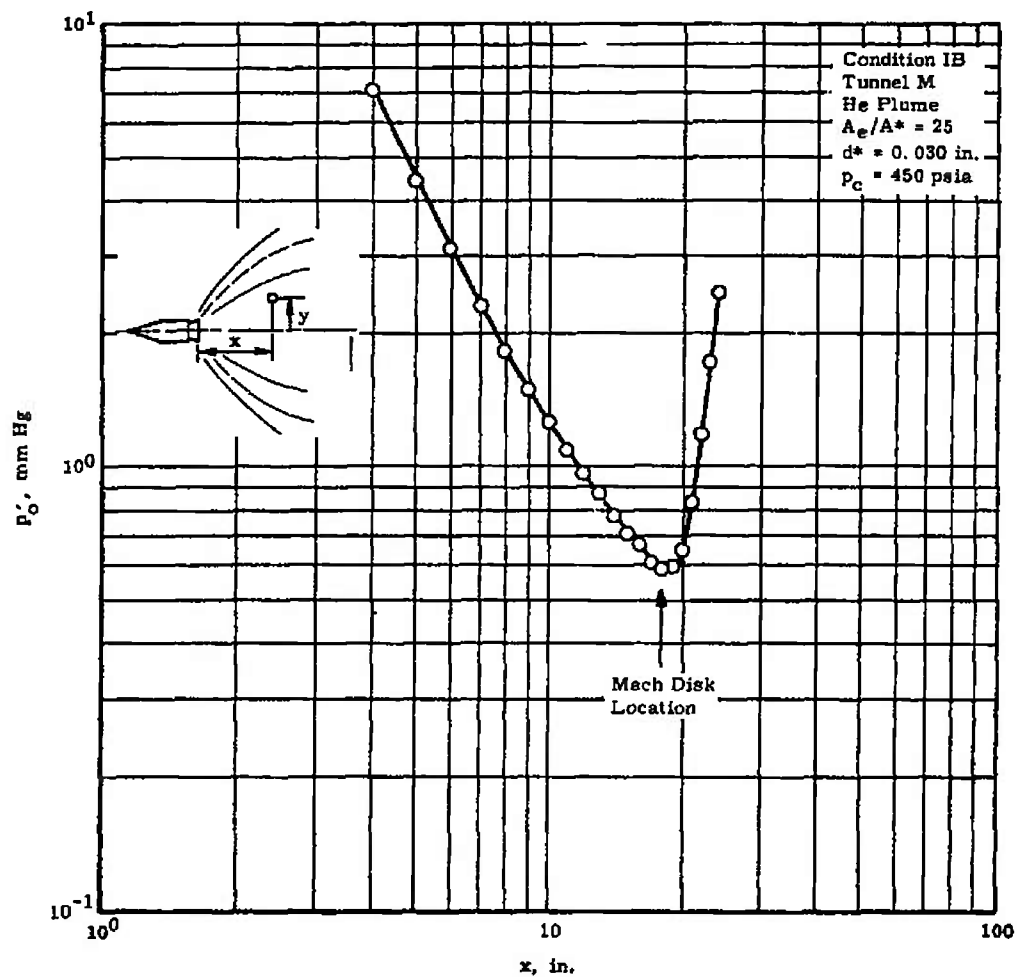
a. Axial Centerline Corrected Impact Pressure Survey
Fig. 35 Impact Pressure Surveys for Condition IB

86
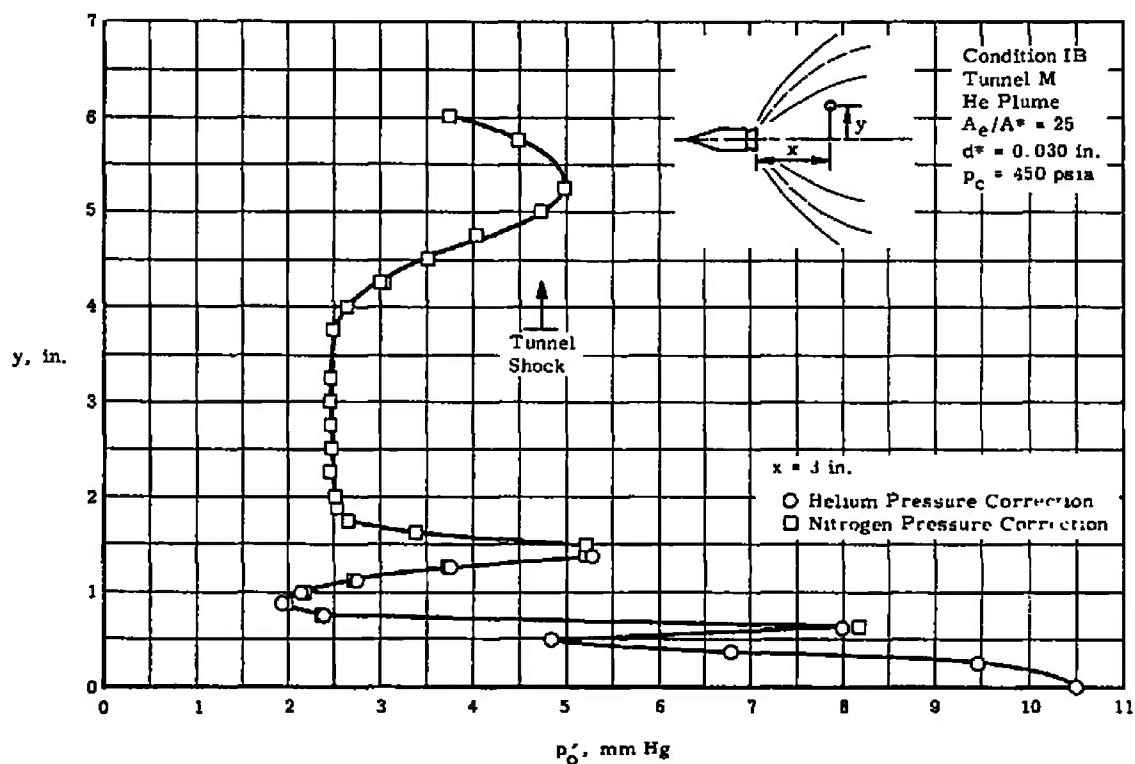
b. Radial Corrected Impact Pressure Survey (x = 3 in.)
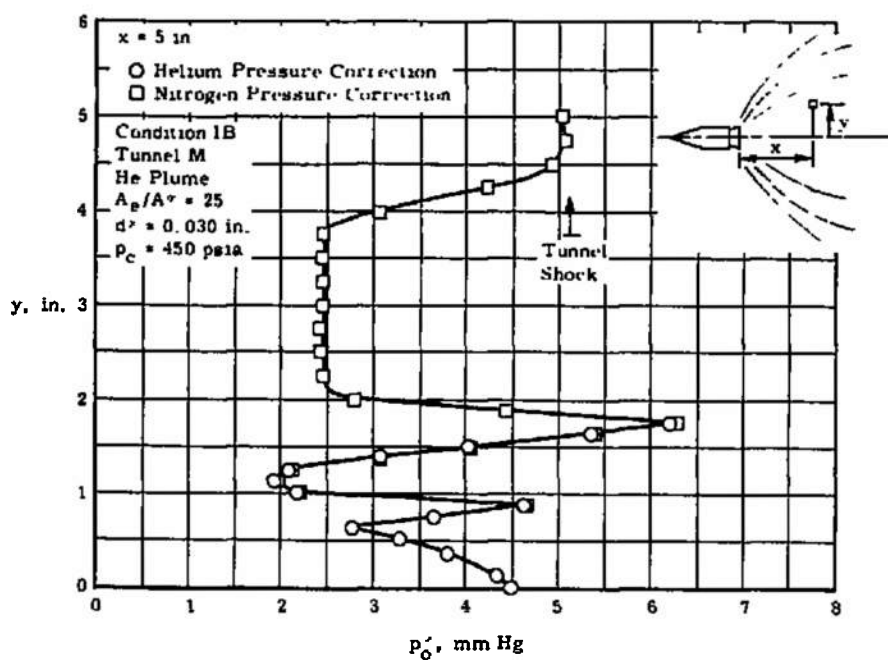
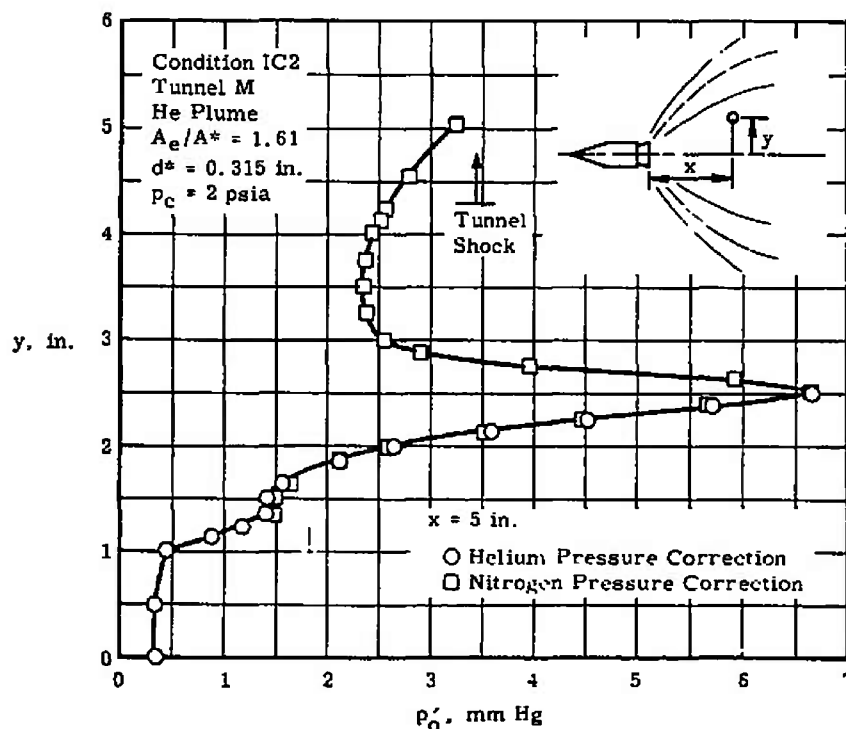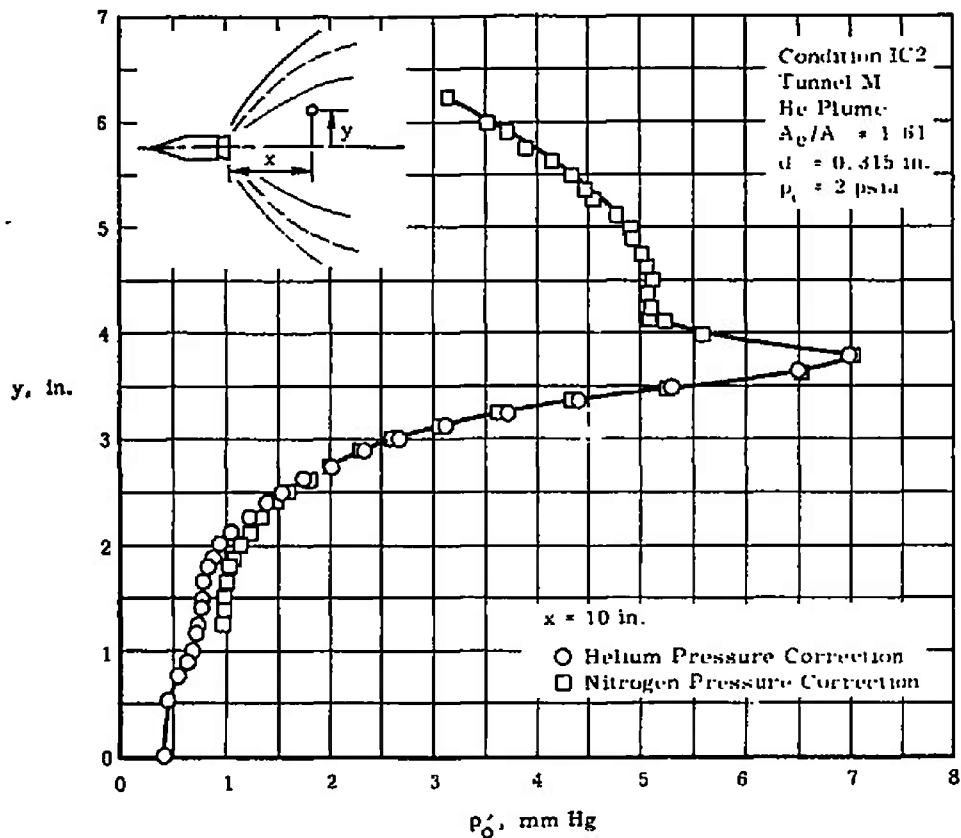c. Radial Corrected Impact Pressure Survey (x = 5 in.) -
Fig. 35 Continued

87
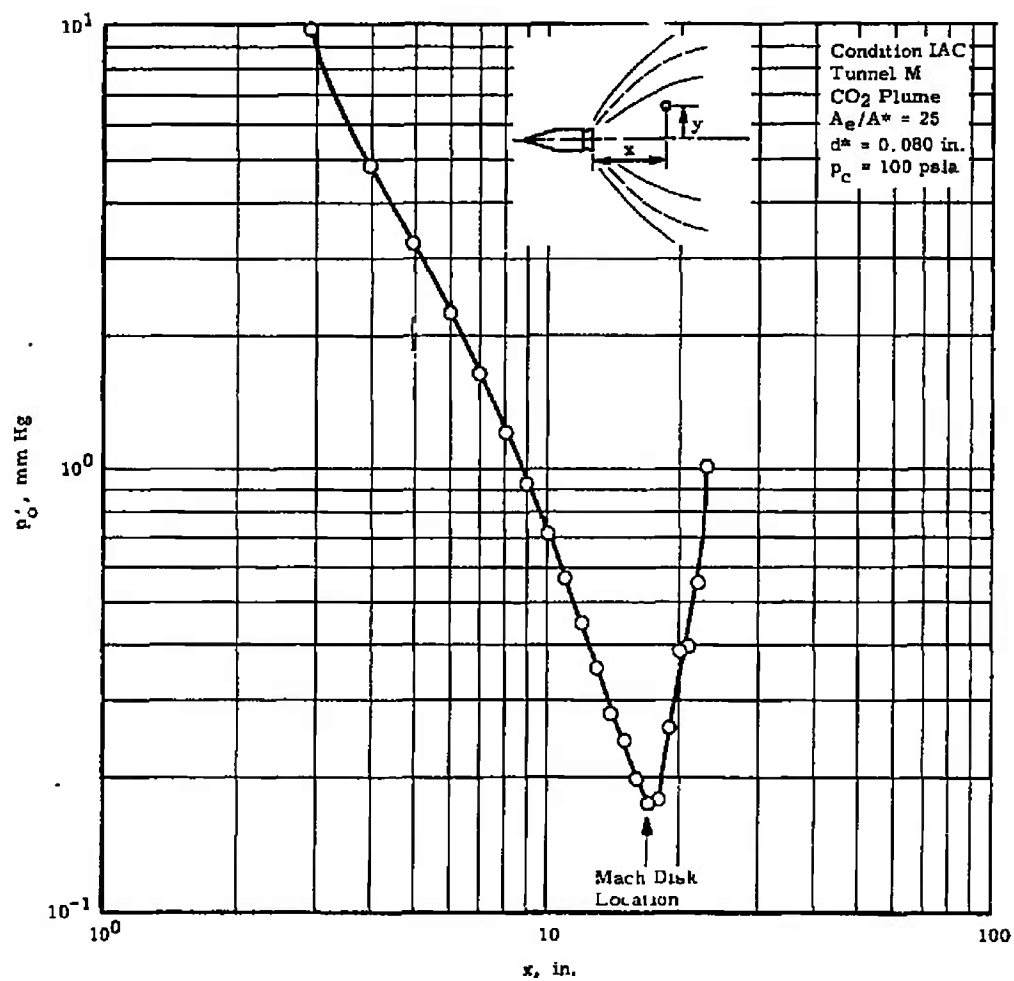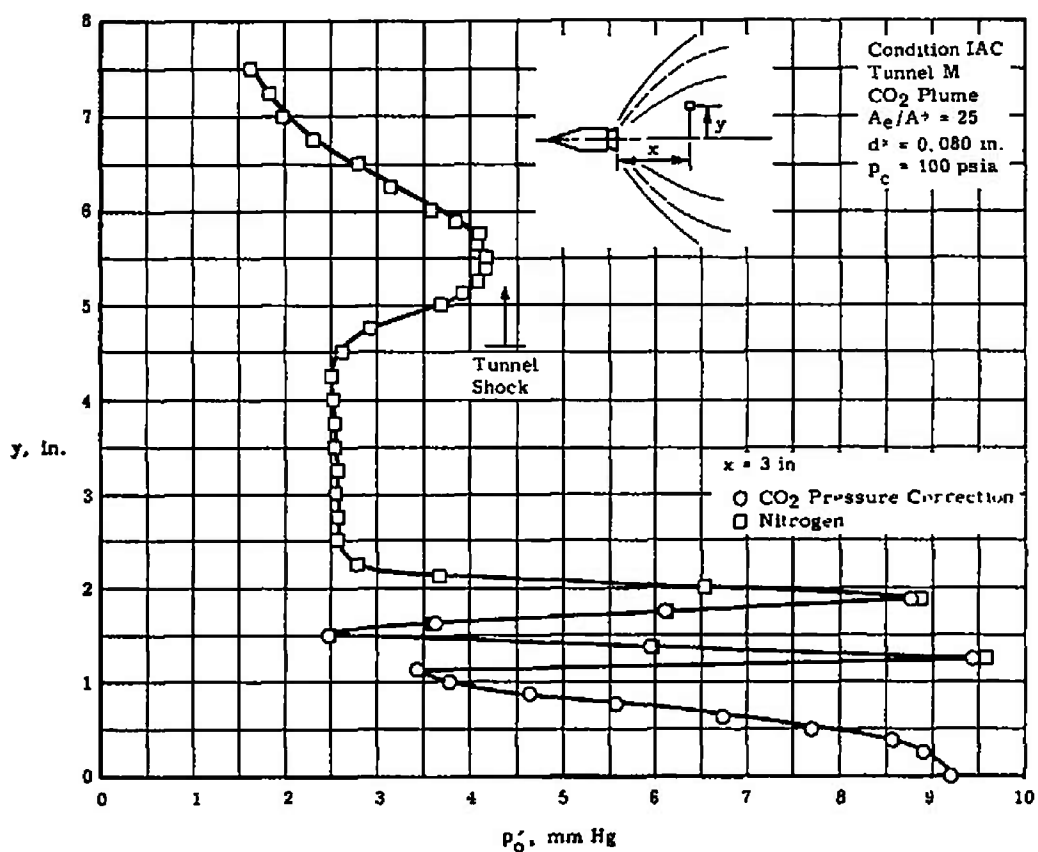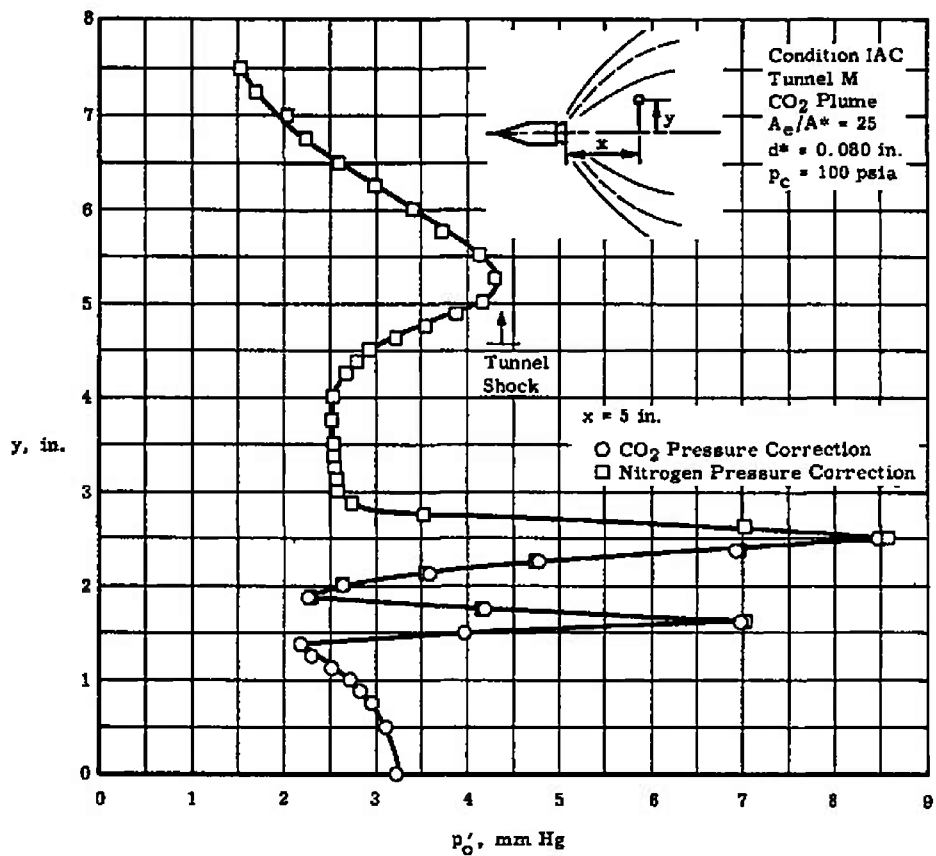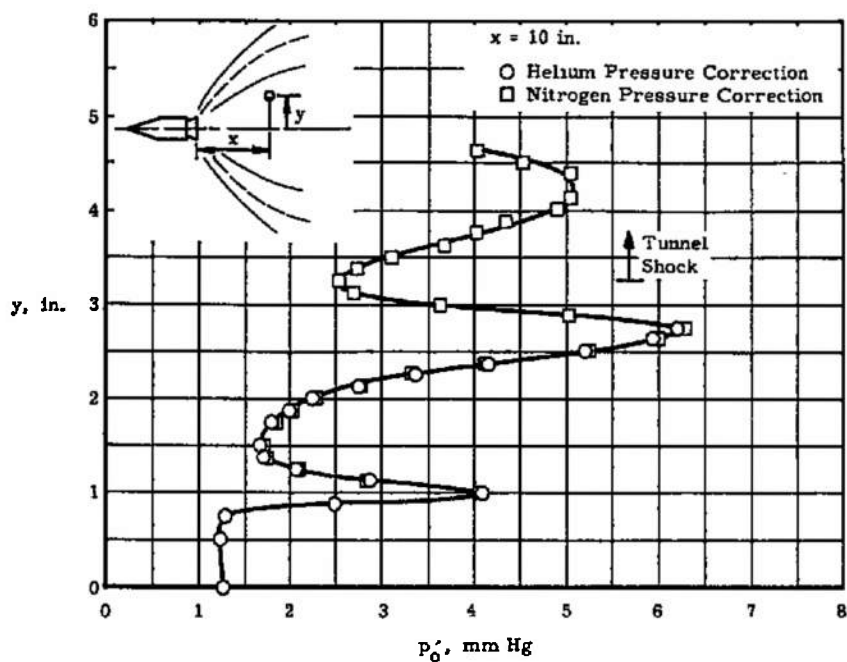
d. Radial Corrected Impact Pressure Survey (x = 10 in.)
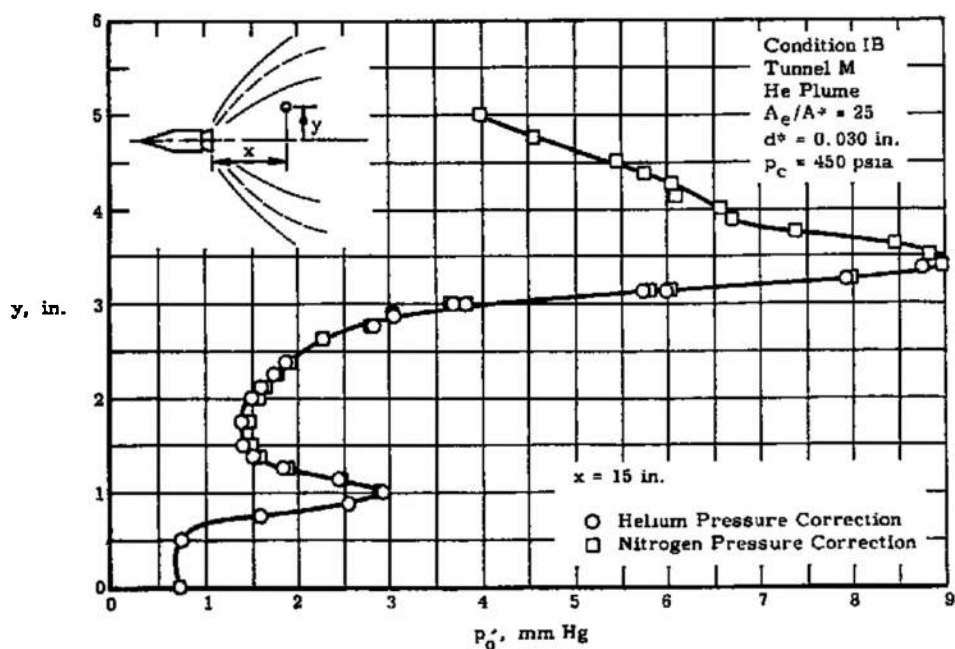
e. Radial Corrected Impact Pressure Survey (x = 15 in.)
Fig. 35 Concluded

TABLE V
EXPERIMENTAL DATA ON MACH DISK LOCATION
AS DETERMINED BY IMPACT PRESSURE SURVEYS

Condition	d^*, in.	x Mach Disk, in.	λ	$\dfrac{x}{r^*}\sqrt{\dfrac{q_\infty}{p_c\,C_{F_m}}}$
IC5	0.315	15.0	4.5	5.55
IAB	0.030	14.0	4.7	5.41
IC2	0.315	8.0	4.5	4.70
IAC	0.080	17.0	4.7	4.95
IAA	0.080	11.5	4.7	4.74
IB	0.030	18.0	33.5	7.79

the second base condition of Table I (conditions IC2, IAC, and IAA), the agreement is reasonable. Although there are differences in the values for the two sets of data for $\lambda_\infty \approx 4.6$, the average of all values of $(x/r^*) \sqrt{(q_\infty/(p_c \, C_{F_m})}$ at $\lambda_\infty \approx 4.6$ is 5.07 ± 0.42. About half of this spread could be caused by variations in effective r^* attributable to low Reynolds numbers in the rocket simulator throats, and the remainder could be brought about by other nonuniform flow conditions in the small nozzles. External low density flow phenomena cannot be ruled out either.

The radial pressure surveys of Fig. 29 are typical of the other surveys in terms of gross details. Figure 29b gives data taken in the plane 1 in. from the exit plane. In this figure the prominent features are the inner shock, the outer shock, and the tunnel shock. These can be noted in the photograph of Fig. 24. The (c) part of the figure gives similar results, with the inner shock and the outer shock displaced farther from centerline and the tunnel shock closer. There is an indication of what could be the contact surface. In the (d) part of the figure, there is no indication of the contact surface. In Fig. 29e the inner shock appears as a smeared region, rather than a discontinuity. The tunnel shock and the outer shock have merged. This merger does not appear at this location in the photograph (Fig. 24) because the tunnel shock intersects the centerline nearer the exit with the probe in the tunnel because of a higher tank pressure caused by the probe blockage effect. In the (f) part of the figure everything has smeared out. This location is close to the Mach disk location (Fig. 29a). The results for the remaining figures are, in general, similar to those of Fig. 29.

5.3 DENSITY AND TEMPERATURE MEASUREMENTS

5.3.1 Density

Using the electron beam flourescence technique in Tunnel M, the radial profiles of the number density of neutral ground state atomic helium and molecular nitrogen were determined at the axial positions located 3, 5, and 10 in. downstream of the exit plane of the plume nozzle for plume conditions IC2 and IC5, and similar data were obtained 3 in. from the exit plane of the plume nozzle for condition IB.

Absolute number density data were obtained in the manner described in Appendix II with the experimental apparatus discussed in Section 3.5, using the raw intensity data of the atomic and molecular radiation and measured beam current. Figures 36a, b, and c present the radial profiles of the absolute number densities for condition IC5; Figs. 37a, b, and c for condition IC2; and Fig. 38 for condition IB. The data given in
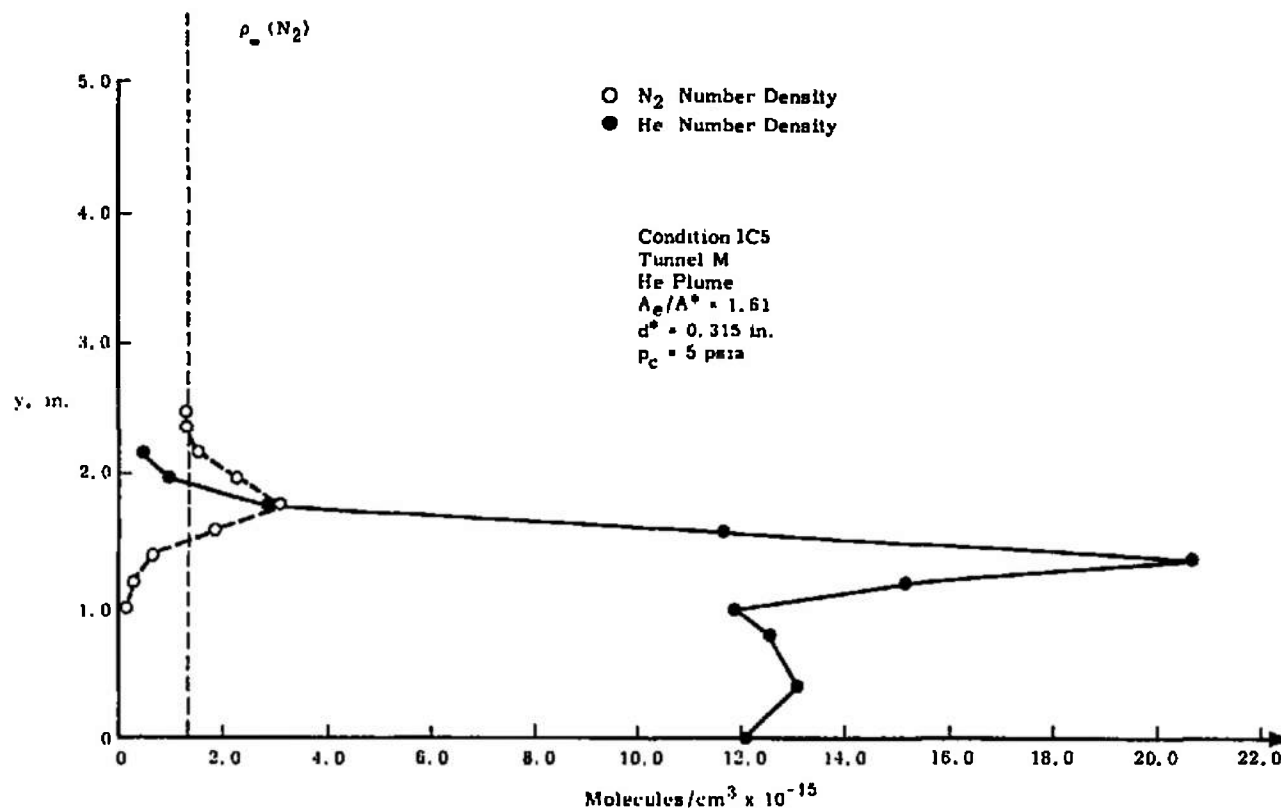
a. x = 3 in.

Fig. 36 Electron Beam Number Densities for Condition IC5
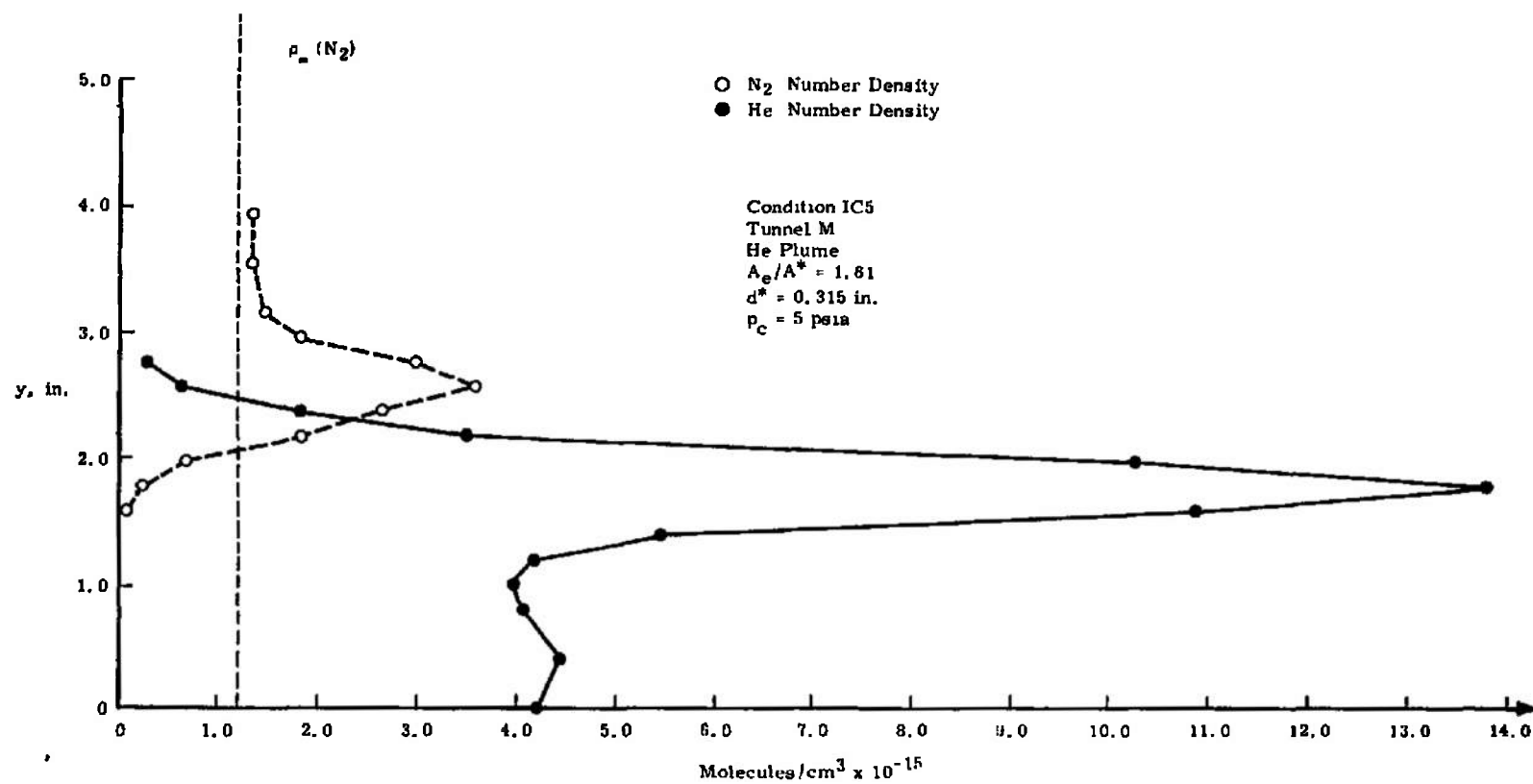
b. x = 5 in.
Fig. 36 Continued
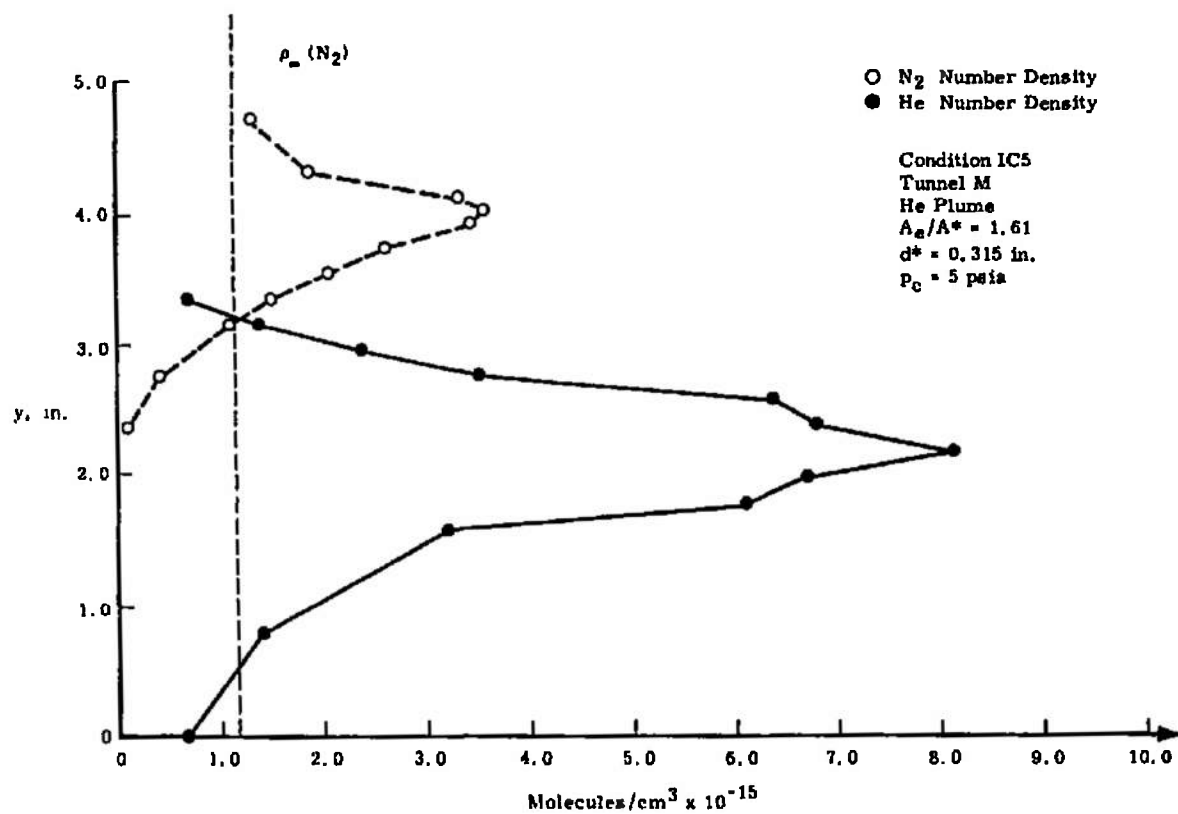
c. x = 10 in.

Fig. 36 Concluded
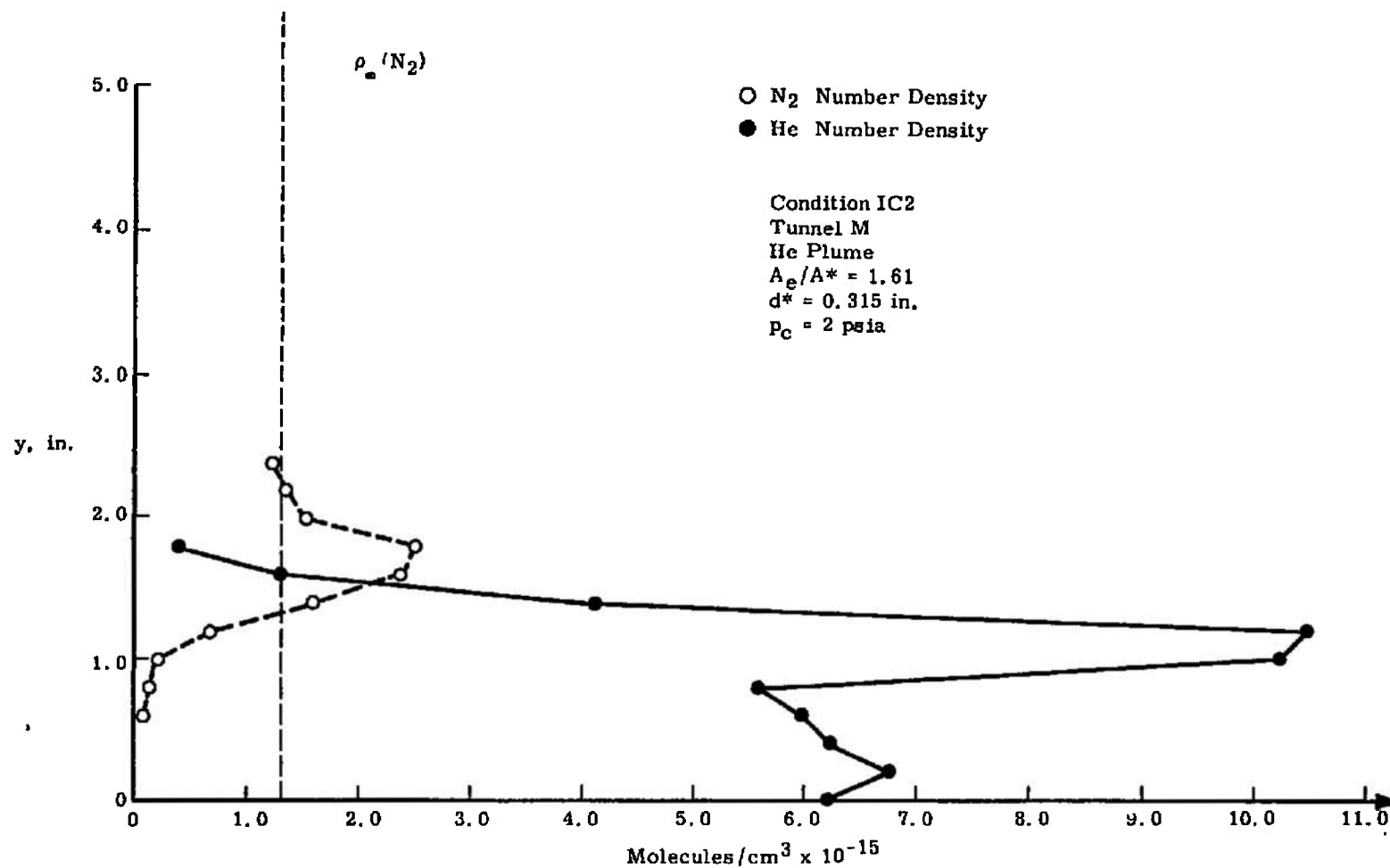
a. x = 3 in.

Fig. 37 Electron Beam Number Densities for Condition IC2

$\rho_\infty(N_2)$

O N$_2$ Number Density
● He Number Density

Condition IC2
Tunnel M
He Plume
$A_e/A^* = 1.61$
$d^* = 0.315$ in.
$p_c = 2$ psia

y, in.

Molecules/cm^3 x 10^{-15}

b. x = 5 in.
Fig. 37 Continued

ρ_∞ (N_2)

O N_2 Number Density
● He Number Density

Condition IC2—
Tunnel M
He Plume
$A_e/A* = 1.61$
$d* = 0.315$ in.
$p_c = 2$ psia

y, in.

Molecules/cm^3 x 10^{-15}
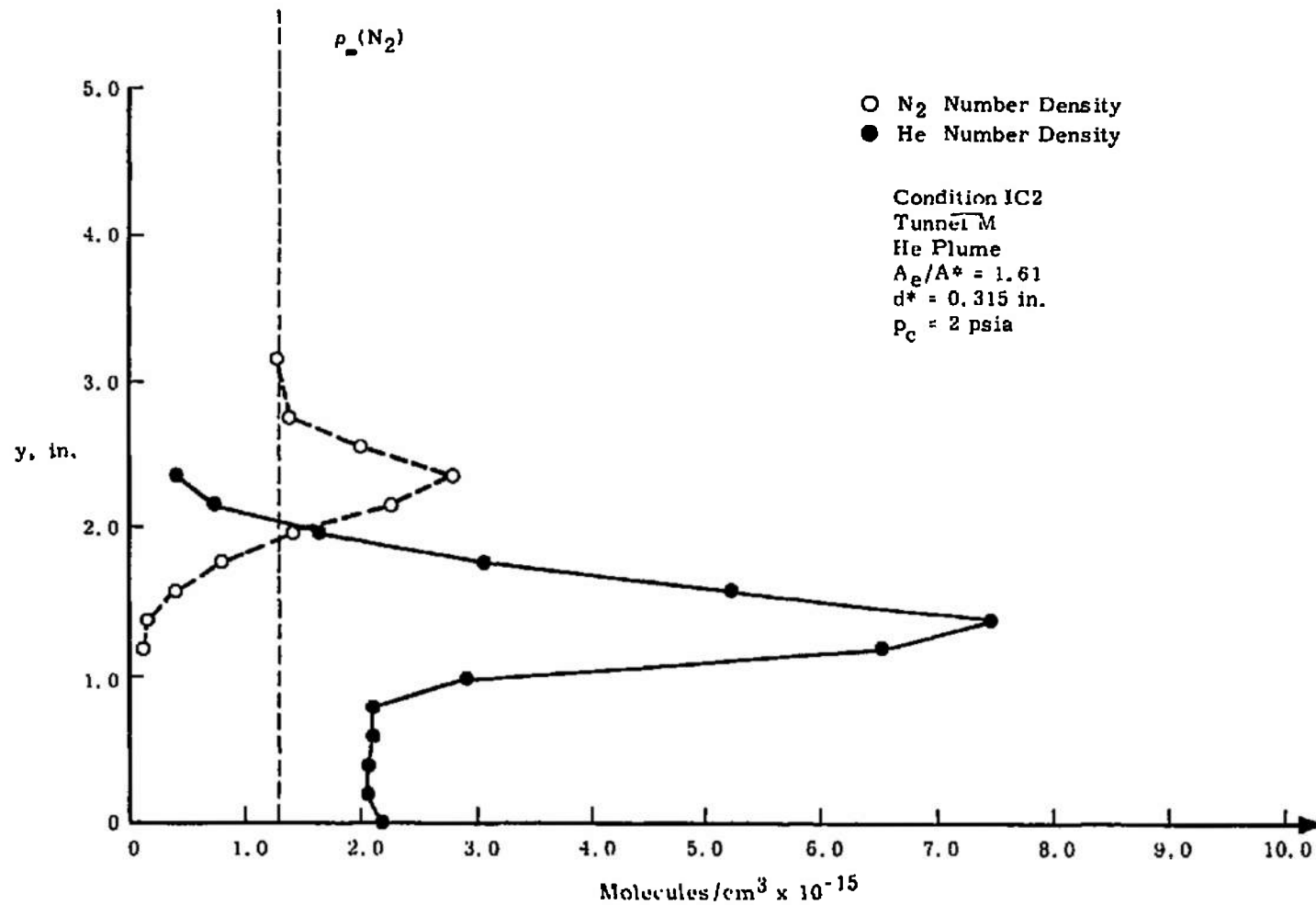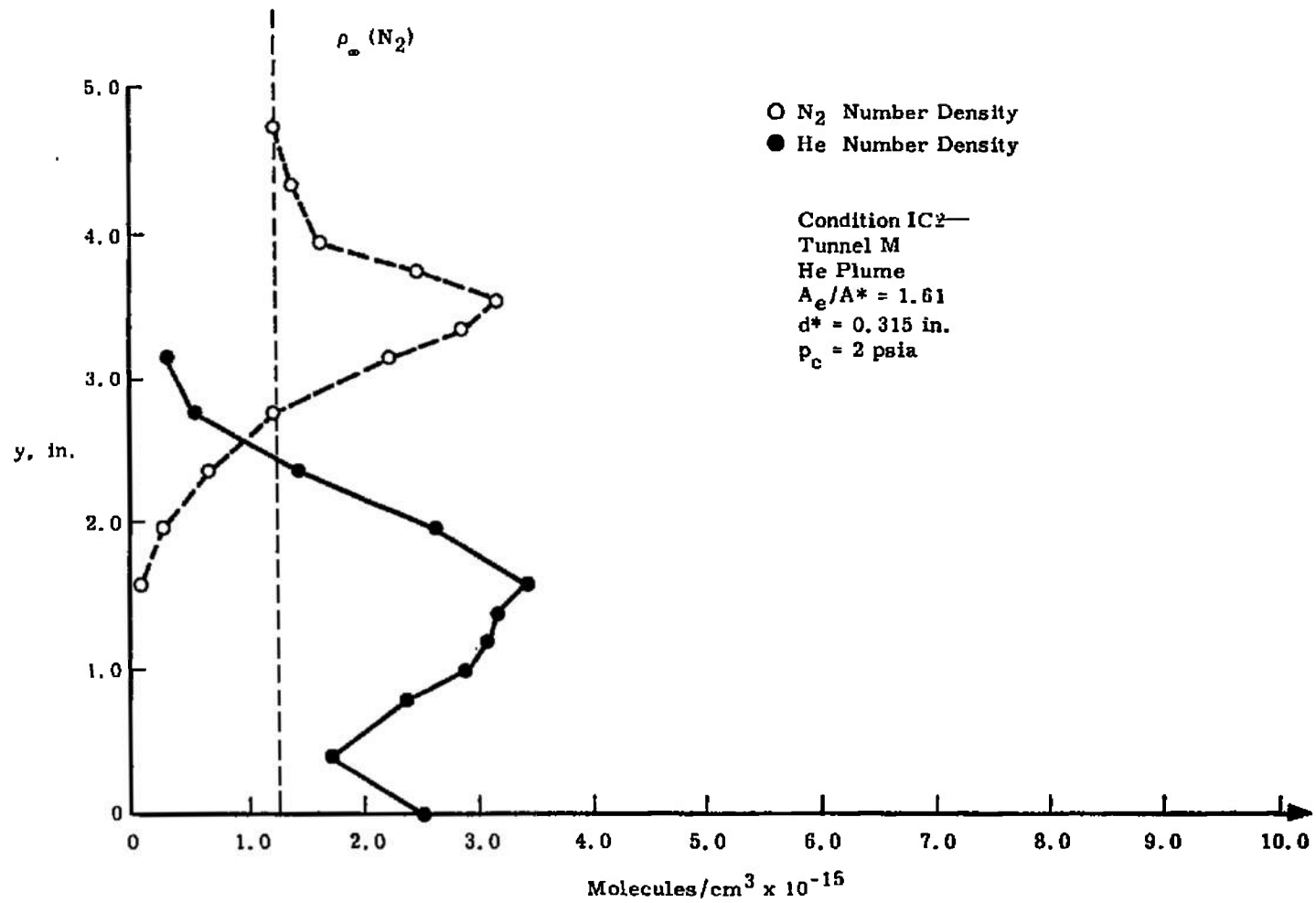
c. x = 10 in.
Fig. 37 Concluded
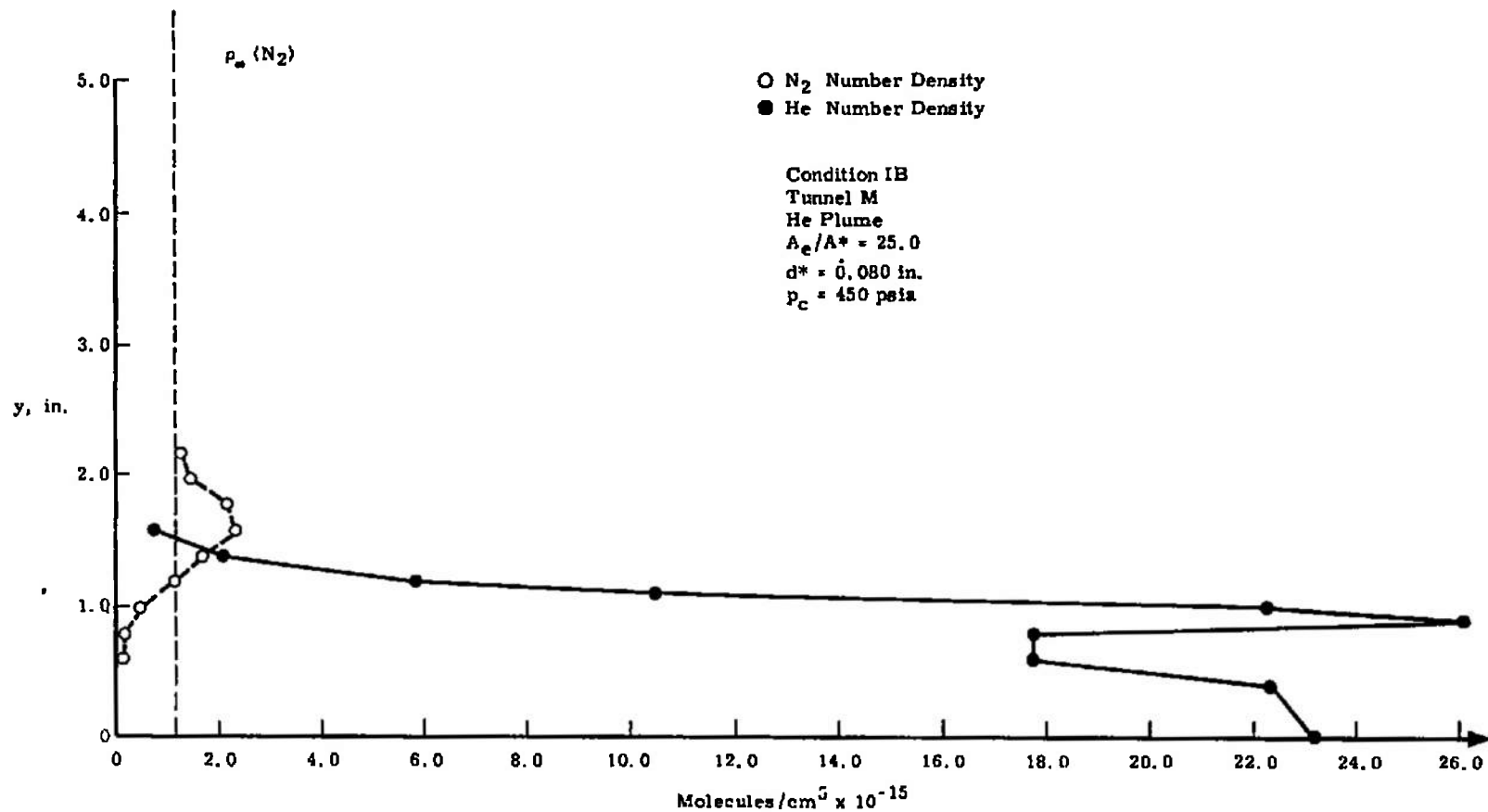
Fig. 38 Electron Beam Number Densities for Condition IB (x = 3 in.)

these figures were obtained assuming the line or band intensity to be a linear function of number density; i.e., no allowance has been made for collisional quenching effects. Figures 39 through 41 exhibit the same experimental data where collisional quenching effects are estimated using the quenching ratio constants listed in Table II-III, Appendix II. It should be noted that until low temperature rate constants are experimentally determined, Figs. 39 through 41 indicate only an estimate of the effect of collisions.

Listed in Table VI and shown in Fig. 42 are the locations of the maxima of the number density in the radial direction as a function of axial position for all plume conditions investigated.

Figures 43a and b present the centerline values of helium number density as a function of the inverse square of the axial position.

5.3.2 Rotational Temperature

Radial profiles of the rotational temperatures of the ground state neutral nitrogen molecule were determined in Tunnel M using the (0,0) band of the first negative system of N_2^+ as described in Appendix II for the IC2 and IC5 conditions at the axial position 10 in. downstream from the plume nozzle exit plane and for the IC5 condition at the 5-in. axial position. These data are shown in Figs. 44a, b, and c, where the rotational temperatures obtained from iterated computer calculations described in Appendix II are plotted as a function of the number K' of spectral lines employed for the determination. If a rotational temperature, T_R, is defined, the T_R variation with K' should exhibit a zero slope, whereas a finite slope is indicative of the non-Boltzmann nature of the radiating species and can, in all probability, be attributed to both secondary electrons and collisional processes of extremely large cross sections. Since these cross sections, or rate constants, are presently unknown, no density corrections have been applied to the data.

The rotational temperature obtained using ten spectral lines, serving only to show the gross character of rotational energy distribution throughout the plume, is shown in Fig. 45 as a function of the radial position for the IC2 and IC5 conditions at the 10-in. axial position, and these values, as well as the IC5 data at 5 in., are listed in Table VII.

5.3.3 Vibrational Temperature

Using the (0,1) and (1,2) bands of the first negative system of N_2^+, electronically integrated vibrational band intensity ratios were obtained for both the IC2 and IC5 conditions at the 3- and 5-in. axial positions.

○ N$_2$ Number Density, Corrected
● He Number Density, Corrected

Condition IC5
Tunnel M
He Plume
A$_e$/A* = 1.61
d* = 0.315 in.
p$_c$ = 5 psia

y, in.

Molecules/cm^3 x 10^{-15}
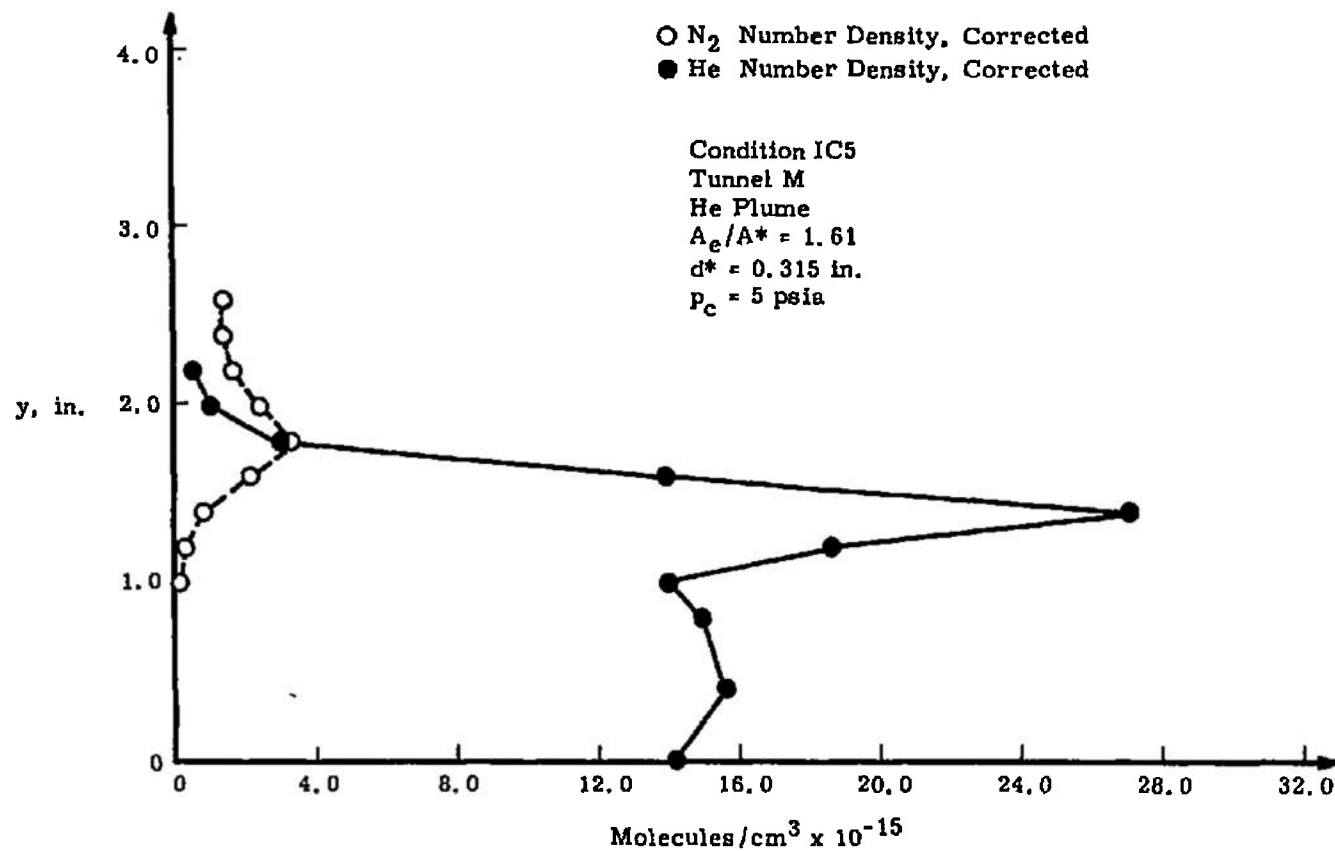
a. x = 3 in.

Fig. 39 Electron Beam Number Densities with Collisional Quenching Effects for Condition IC5

O N$_2$ Number Density, Corrected
● He Number Density, Corrected

Condition IC5
Tunnel M
He Plume
A$_e$/A* = 1.61
d* = 0.315 in.
p$_c$ = 5 psia

y, in.

Molecules/cm^3 x 10^{-15}

b. x = 5 in.
Fig. 39 Continued

O N$_2$ Number Density, Corrected
● He Number Density, Corrected

Condition IC5
Tunnel M
He Plume
A$_e$/A* = 1.61
d* = 0.315 in.
p$_c$ = 5 psia

y, in.

Molecules/cm^3 x 10^{-15}
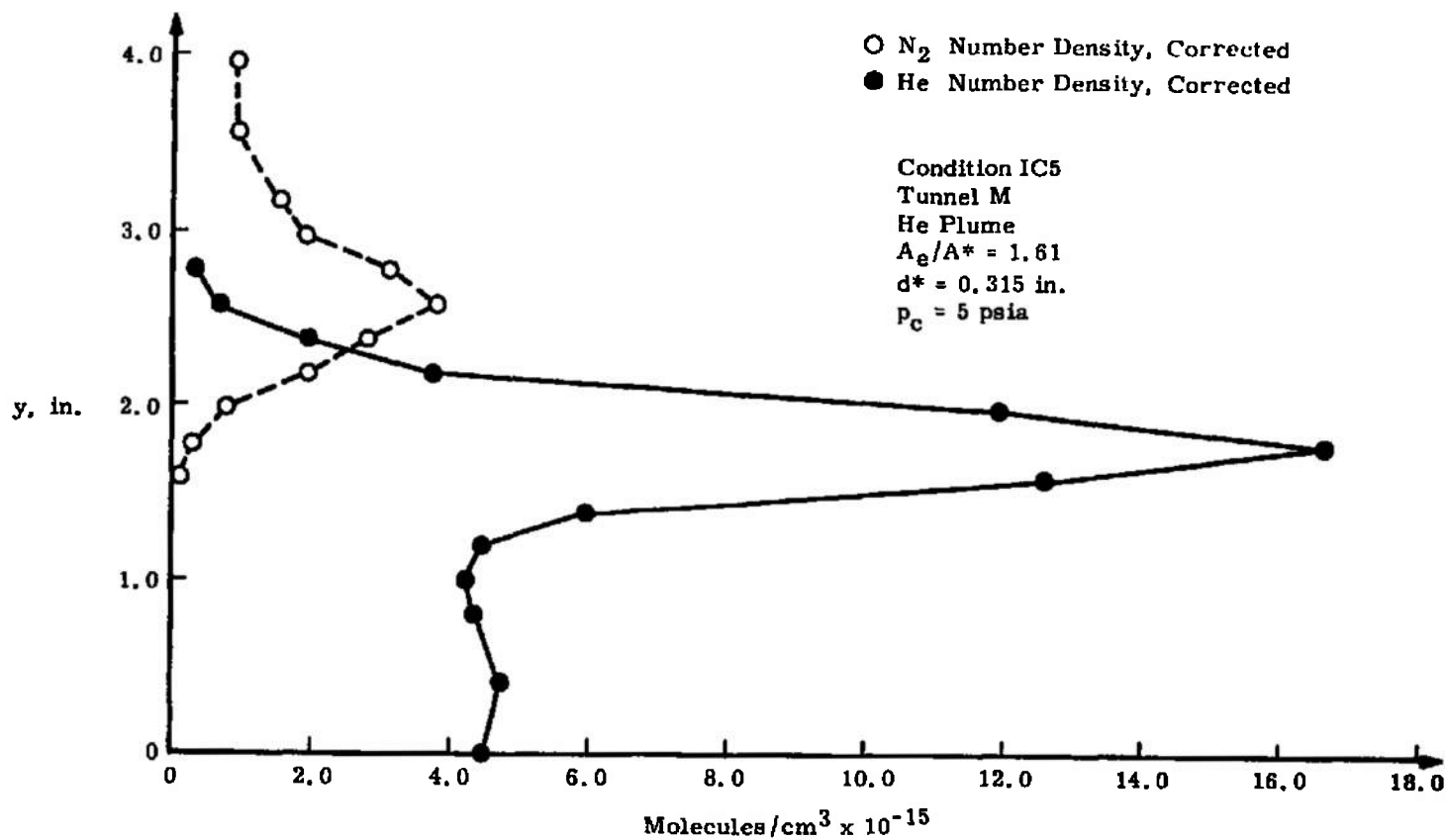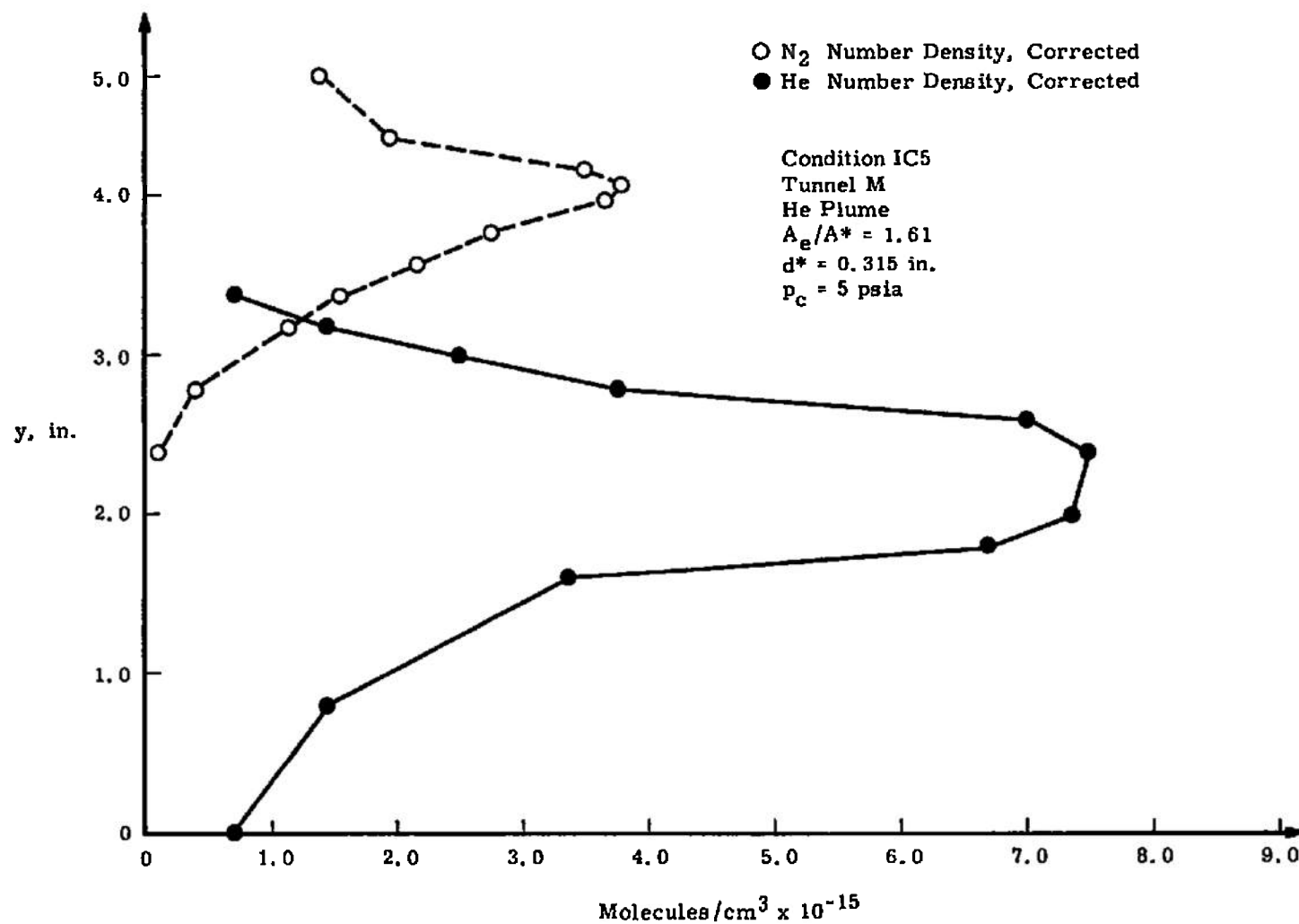
c. x = 10 in.
Fig. 39 Concluded
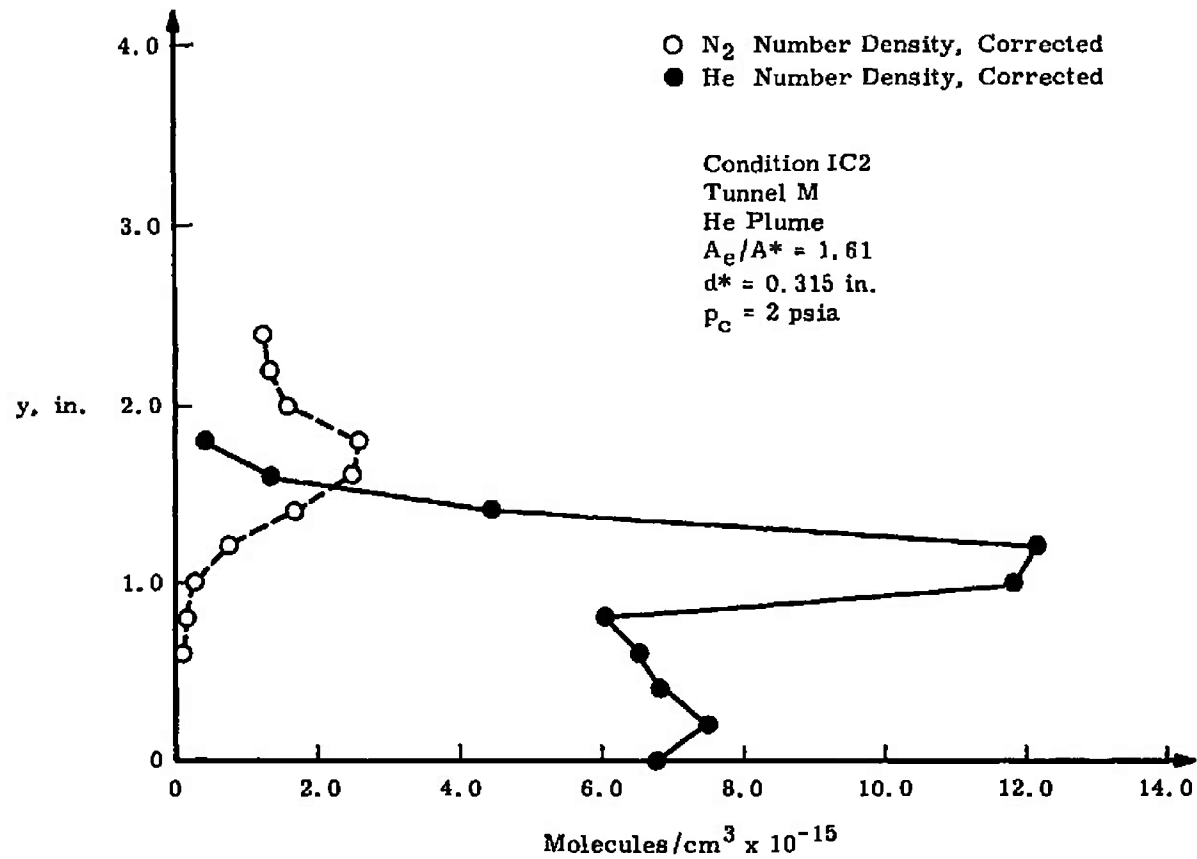
a. x = 3 in.

Fig. 40 Electron Beam Number Densities with Collisional Quenching Effects for Condition IC2

b. x = 5 in.
Fig. 40 Continued

○ N₂ Number Density, Corrected
● He Number Density, Corrected

Condition IC2
Tunnel M
He Plume
$A_e/A^* = 1.61$
$d^* = 0.315$ in.
$p_c = 2$ psia

y, in.

Molecules/cm³ x 10⁻¹⁵
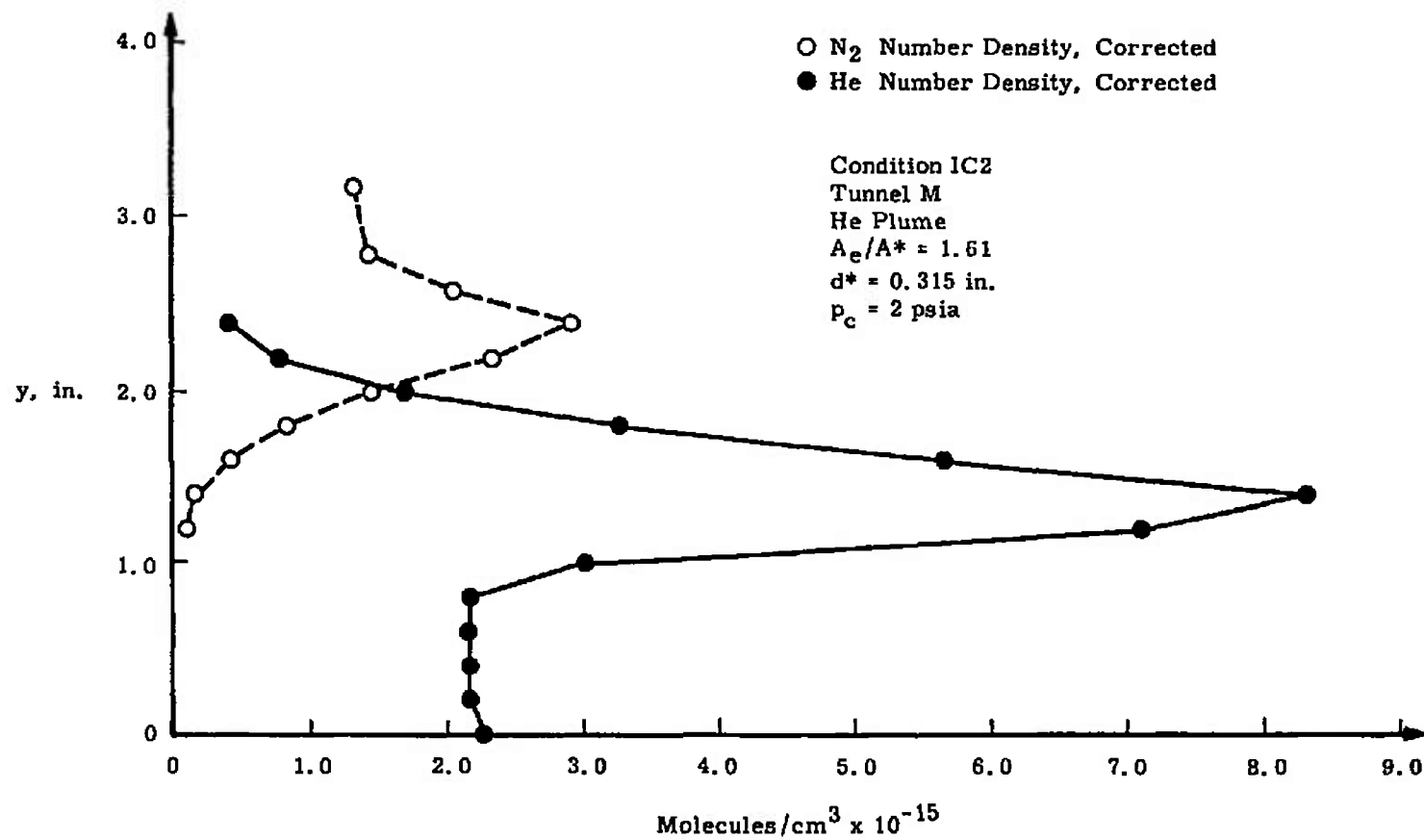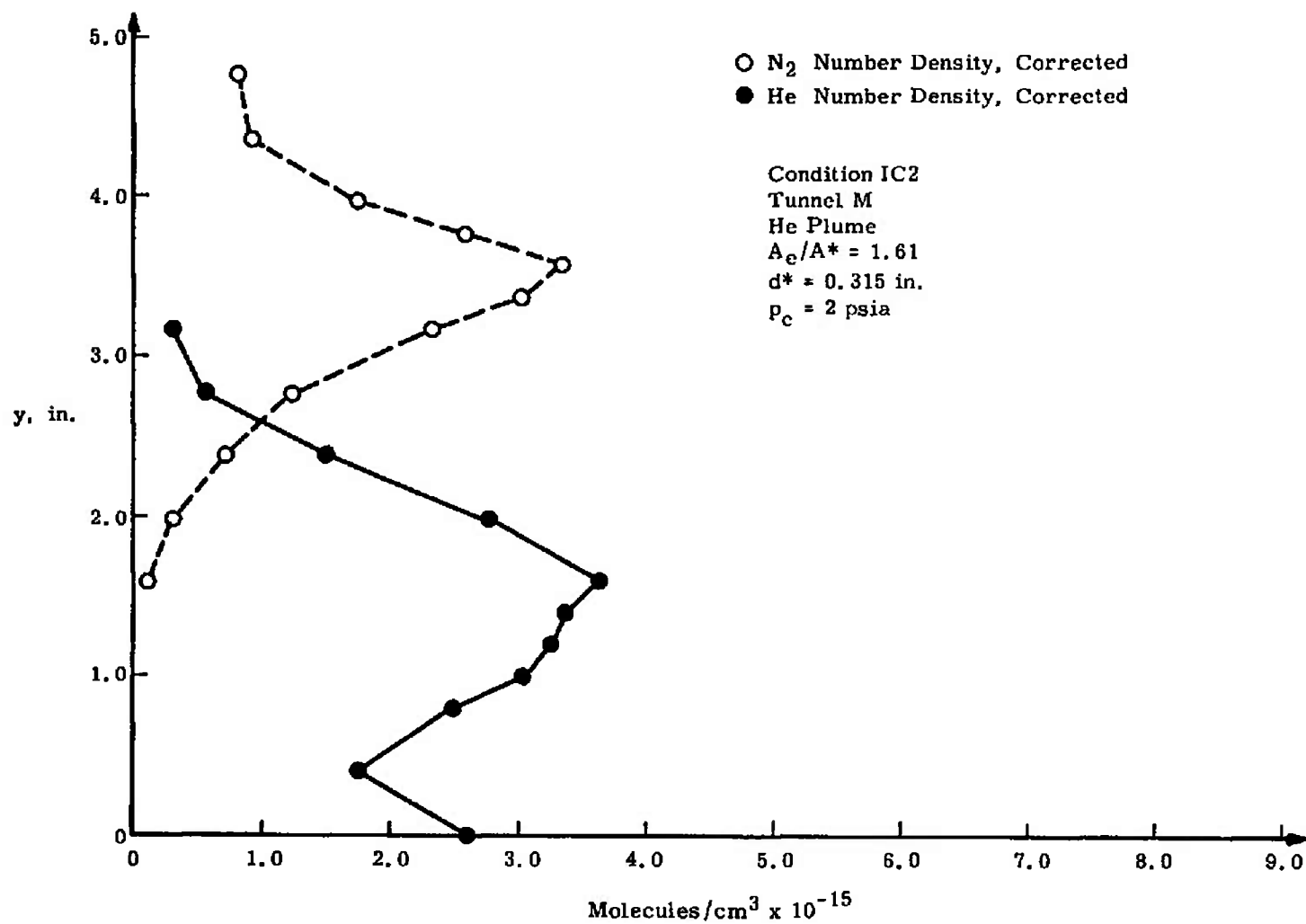
c. x = 10 in.
Fig. 40 Concluded
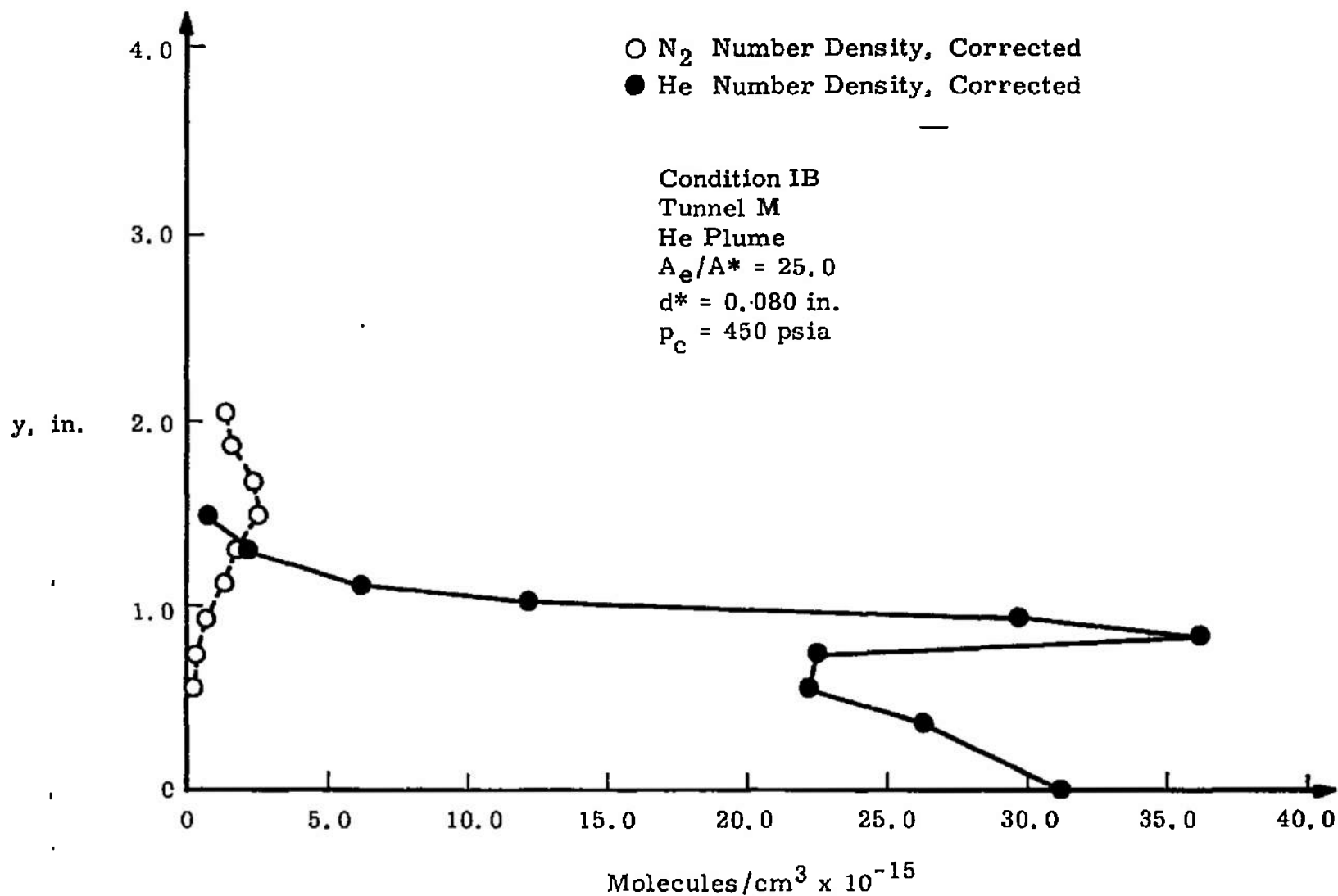
Fig. 41 Electron Beam Number Densities with Collisional Quenching Effects for Condition IB (x = 3 in.)
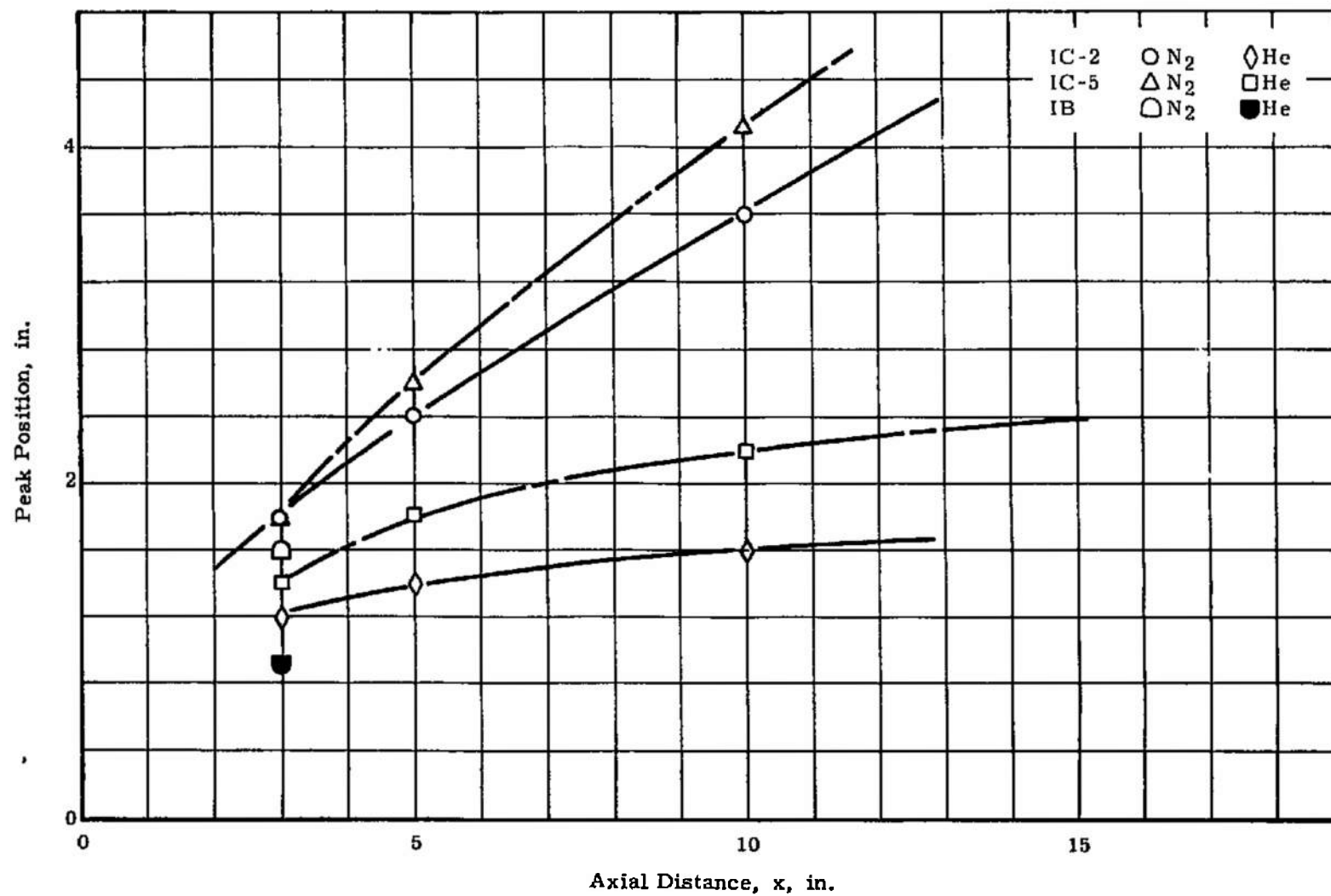
Fig. 42 Locations of the Maxima of the He and N_2 Number Densities

TABLE VI
ELECTRON BEAM RESULTS

Location of Peaks y, in.

x, in.	IC2		IC5		IB	
	N_2	He	N_2	He	N_2	He
3	1.8	1.2	1.8	1.0	1.6	0.9
5	2.4	1.4	2.6	1.8		
10	3.5	1.6	4.1	2.2		

Condition IC5
Tunnel M
He Plume
$A_e/A^* = 1.61$
$d^* = 0.315$ in.
$p_c = 5$ psia
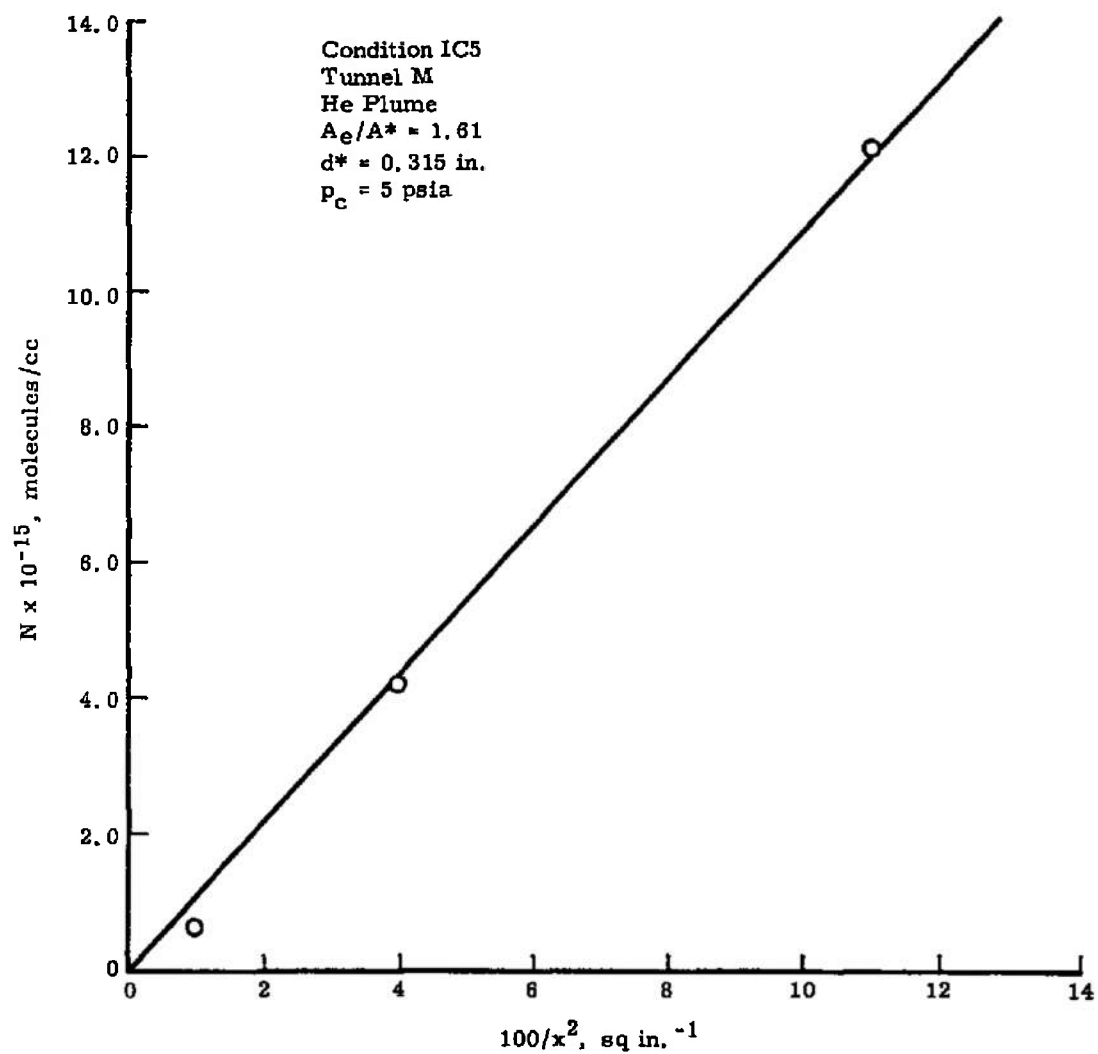
a. Condition IC5
Fig. 43 Centerline Number Density of He versus Inverse Square of Axial Distance

Condition IC2
Tunnel M
He Plume
$A_e/A* = 1.61$
$d* = 0.315$ in.
$P_c = 2$ psia
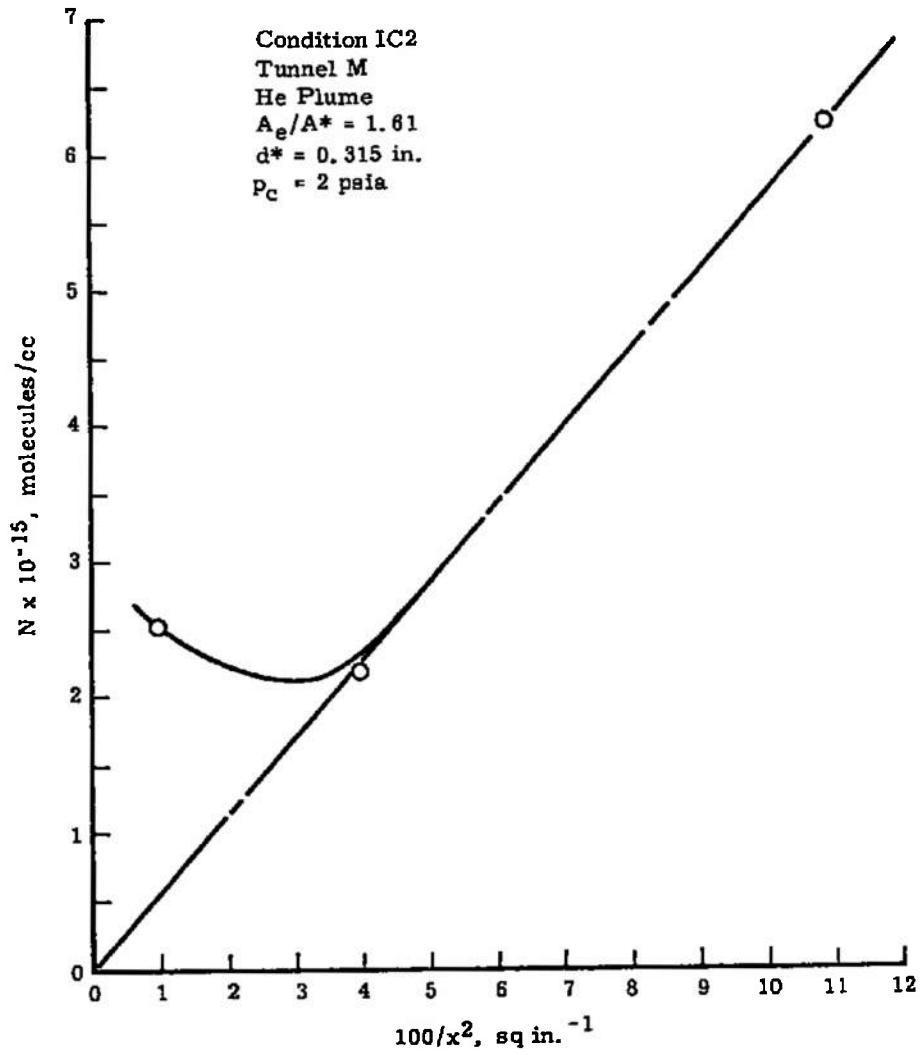
b. Condition IC2
Fig. 43 Concluded
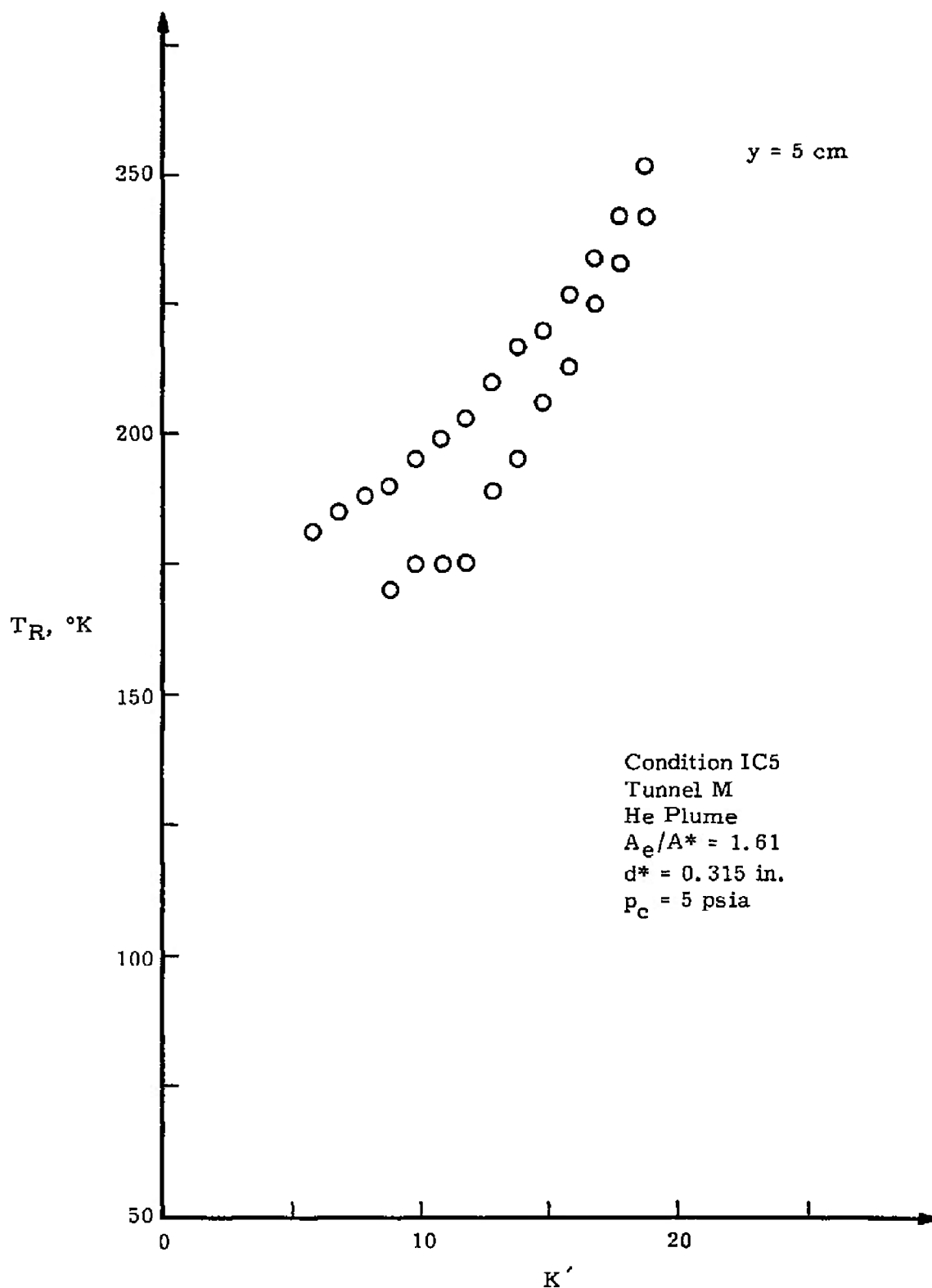
a. Condition IC5, x = 5 in.
Fig. 44 Rotational Temperature of N_2 as a Function of the
Number of Spectral Lines Used
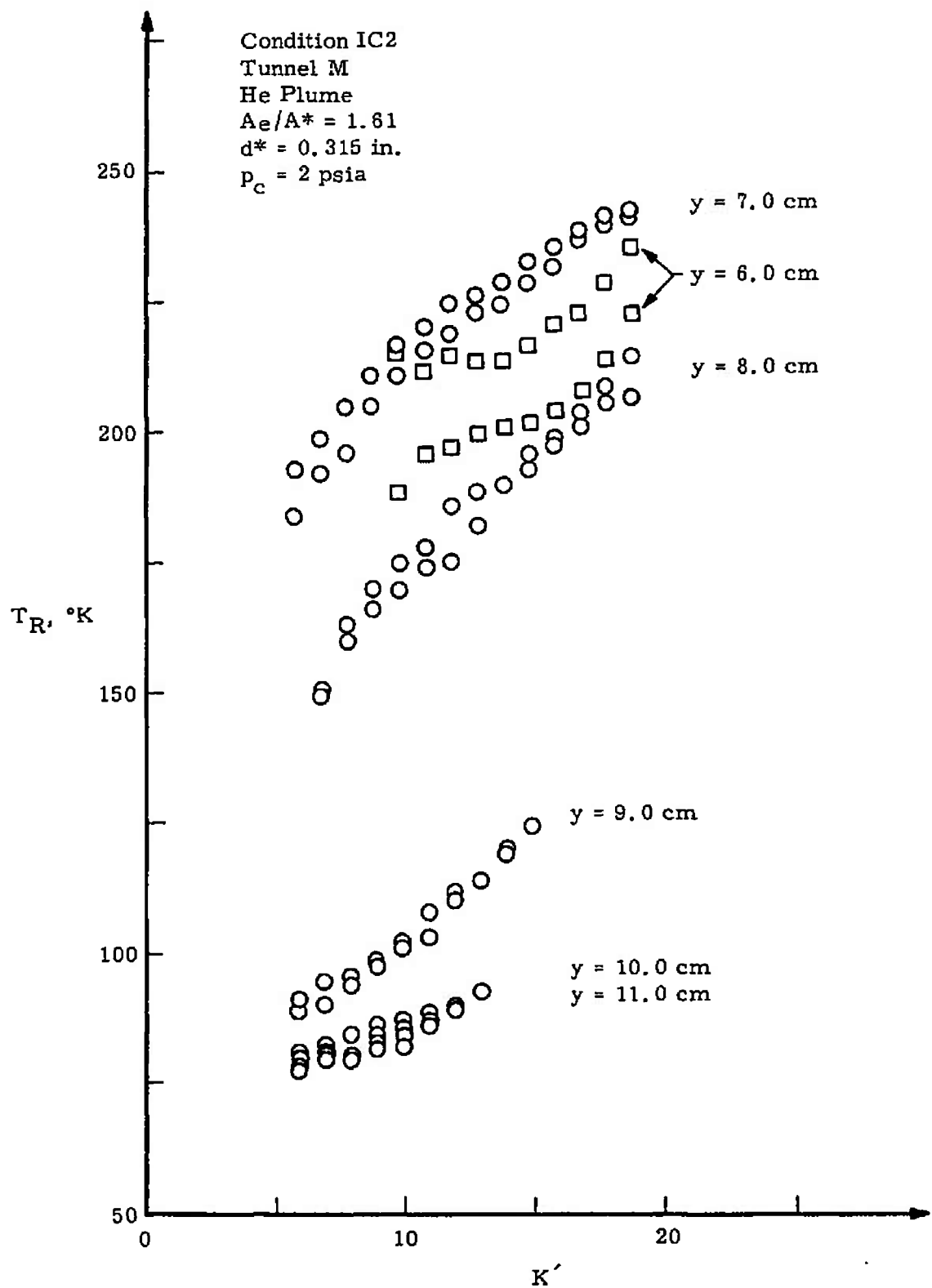
b. Condition IC2, x = 10 in.
Fig. 44 Continued
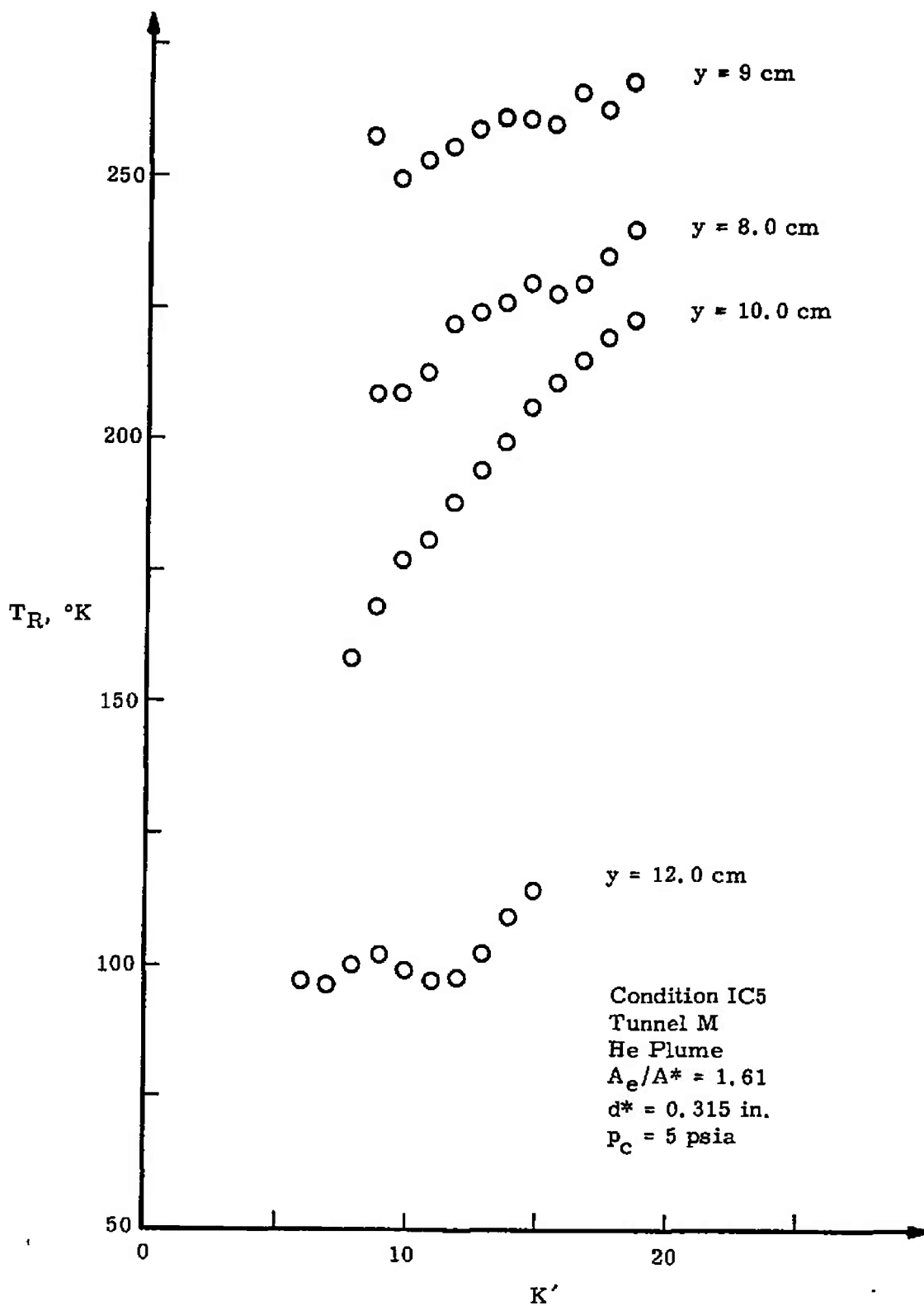
c. Condition IC5, x = 10 in.
Fig. 44 Concluded
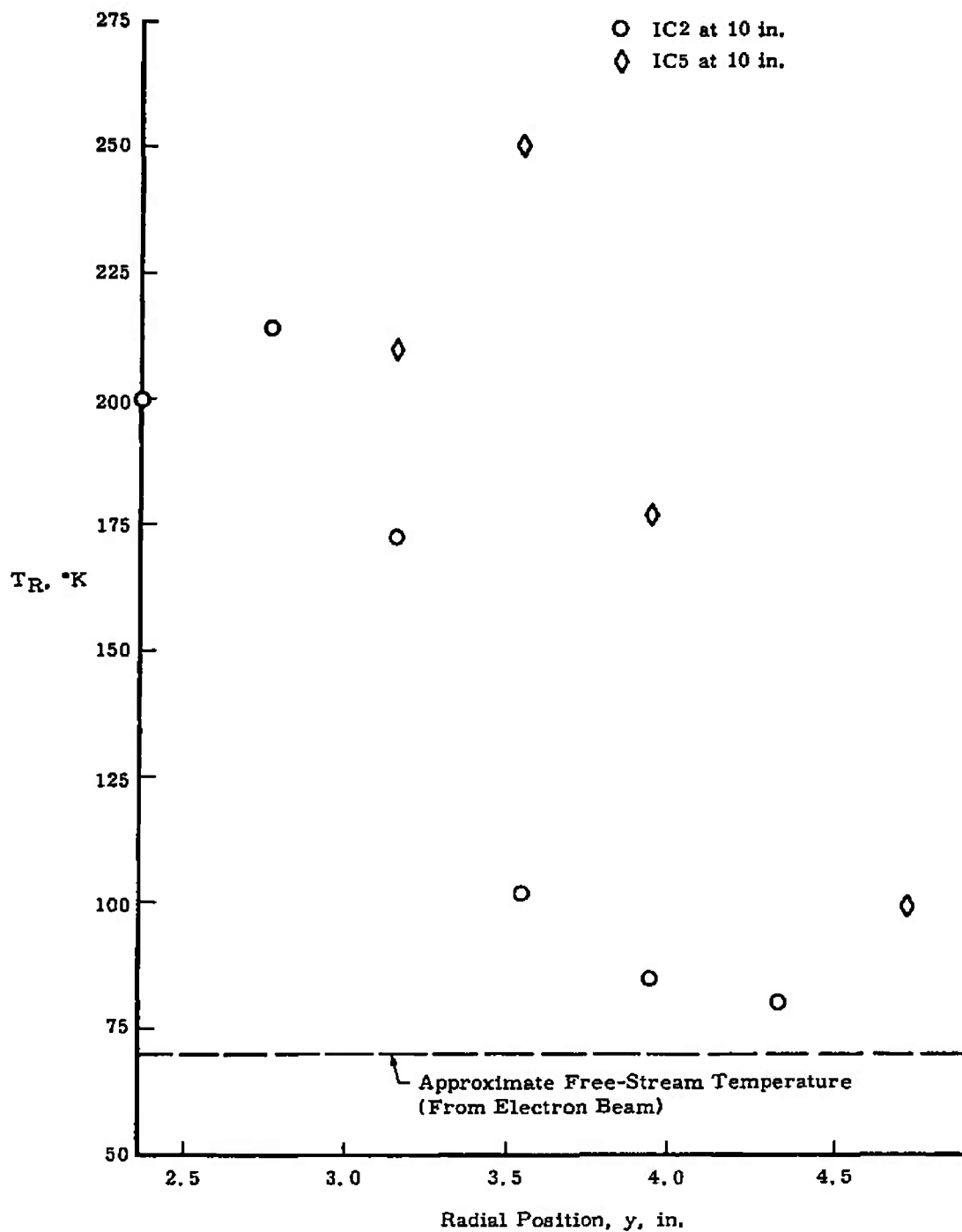
Fig. 45 N$_2$ Rotational Temperature versus Radial Position Using
Ten Spectral Lines

TABLE VII
TEN SPECTRAL LINE T_R AS FUNCTION OF RADIAL POSITION

Plume Condition:	IC5					
Axial Position:	5 in.					
y, in.	1.97					
T_R, °K	185					

Plume Condition:	IC2					
Axial Position:	10 in.					
y, in.	2.37	2.76	3.16	3.55	3.95	4.35
T_R, °K	200	214	172	102	85	80

Plume Conditions:	IC5			
Axial Position:	10 in.			
y, in.	3.16	3.55	3.95	4.74
T_R, °K	209	250	177	99

The band intensity ratio yielded the vibrational temperature by use of
Fig. II-6 of Appendix II. Density corrections based on rate constants
experimentally obtained at 300°K and estimated when unknown show
that the density correction to T_v is approximately 3 percent; the
smallness of the correction is caused primarily by the assumed
equality of $k_1(N_2^-, He)$ and $k_0(N_2^+, He)$, defined in Appendix II, and
this assumption is made solely because of ignorance of the correct
values. Consequently, no density correction has been applied to the
data.

Table VIII lists the average band intensity ratios and the corre-
sponding vibrational temperatures as a function of the radial position
for the various conditions investigated, and these results are presented
in Figs. 46 and 47. Also listed in Table VII is the parameter ΔT_v
which is a measure of the repeatibility of the result when more than one
value of the ratio was obtained.

5.4 COMPARISON OF RESULTS

Two types of comparisons of results are made. The first is the
comparison of results from different techniques for the same condition,
and the second is comparison of results for different conditions in terms
of the scaling parameters.

5.4.1 Results from Different Techniques

These comparisons are made of the tests in Tunnel M using re-
sults from impact pressure surveys, density measurements by the
electron beam technique, and photographs. Figure 48 gives compari-
sons for condition IC. Figure 48a is at the x location of 3 in. Impact
pressures are from Fig. 29c, and the helium and nitrogen densities
are from Fig. 36a. The photographic results from Fig. 24 are shown
as bars - a solid bar for bright and a dashed one for what appears as
the mixing region. Figure 48b is for x = 5 in. and Fig. 48c for 10 in.

It appears as if the peak in the impact pressure, the peak in the
nitrogen density, and the outer edge of the bright brown region are at
about the same distance from the centerline. This location may then
be properly identified with the outer edge of the shock.

The peak in the helium density does not seem to coincide exactly
with any other measurement. Figure 48d summarizes the results for
condition IC5, Figs. 49a through d are analogous to Figs. 48a through d
for IC2, and Fig. 50 is for condition IB at x = 3 cm. Photographic
information has not been included on this figure because the plume is so
thin (Fig. 28).
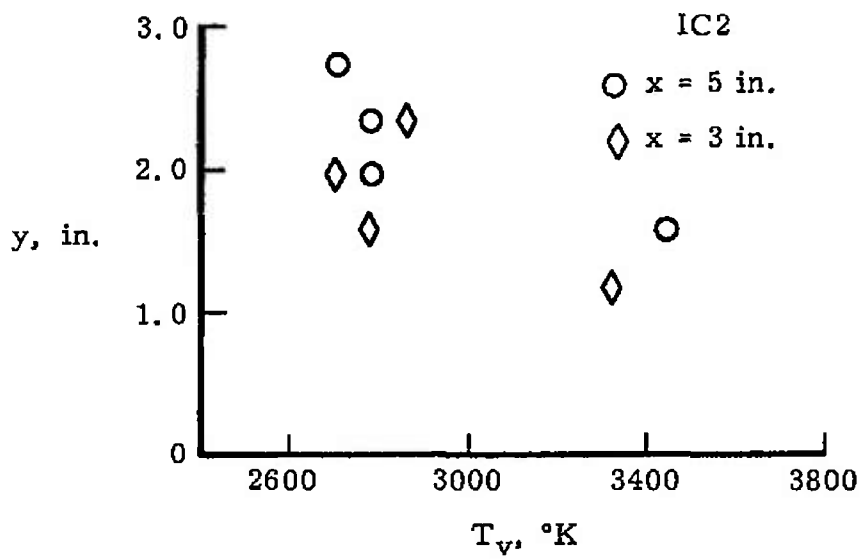
Fig. 46 N$_2$ Vibrational Temperature versus Radial Position for Condition IC2
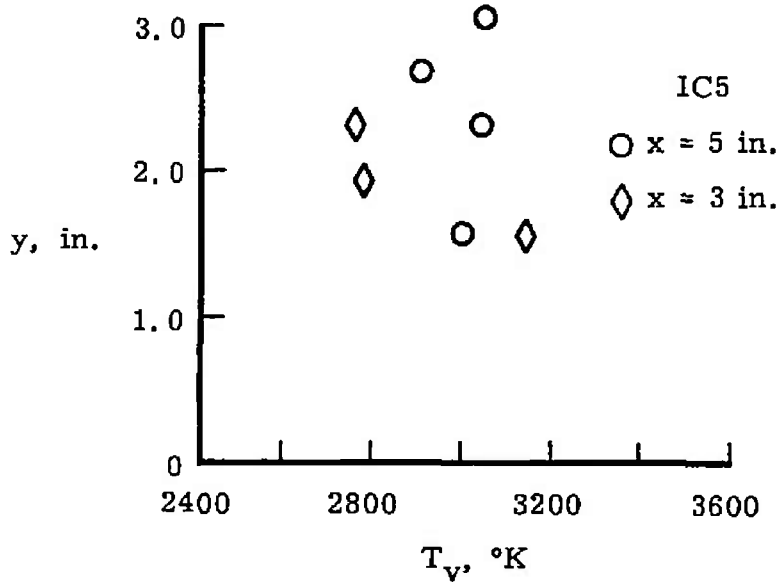
Fig. 47 N$_2$ Vibrational Temperature versus Radial Position for Condition IC5

TABLE VIII
VIBRATIONAL TEMPERATURE AS A FUNCTION OF RADIAL POSITION

Plume Condition IC2

Radial Position y, in.	Axial Position, in.					
	3			5		
	Ratio	T_v, °K	ΔT_v, °K	Ratio	T_v, °K	ΔT_v, °K
1.18	2.06	3320	60	---	----	---
1.58	2.37	2780	40	2.08	3440	---
1.97	2.42	2700	20	2.37	2780	---
2.37	2.32	2860	40	2.37	2780	---
2.76	---	---	---	2.42	2700	40

Plume Condition IC5

Radial Position y, in.	Axial Position, in.					
	3			5		
	Ratio	T_v, °K	ΔT_v, °K	Ratio	T_v, °K	ΔT_v, °K
1.58	2.15	3140	0	2.24	3000	60
1.97	2.37	2780	---	---	---	---
2.37	2.38	2760	20	2.22	3040	20
2.77	---	---	---	2.28	2900	40
3.16	---	---	---	2.20	3050	20
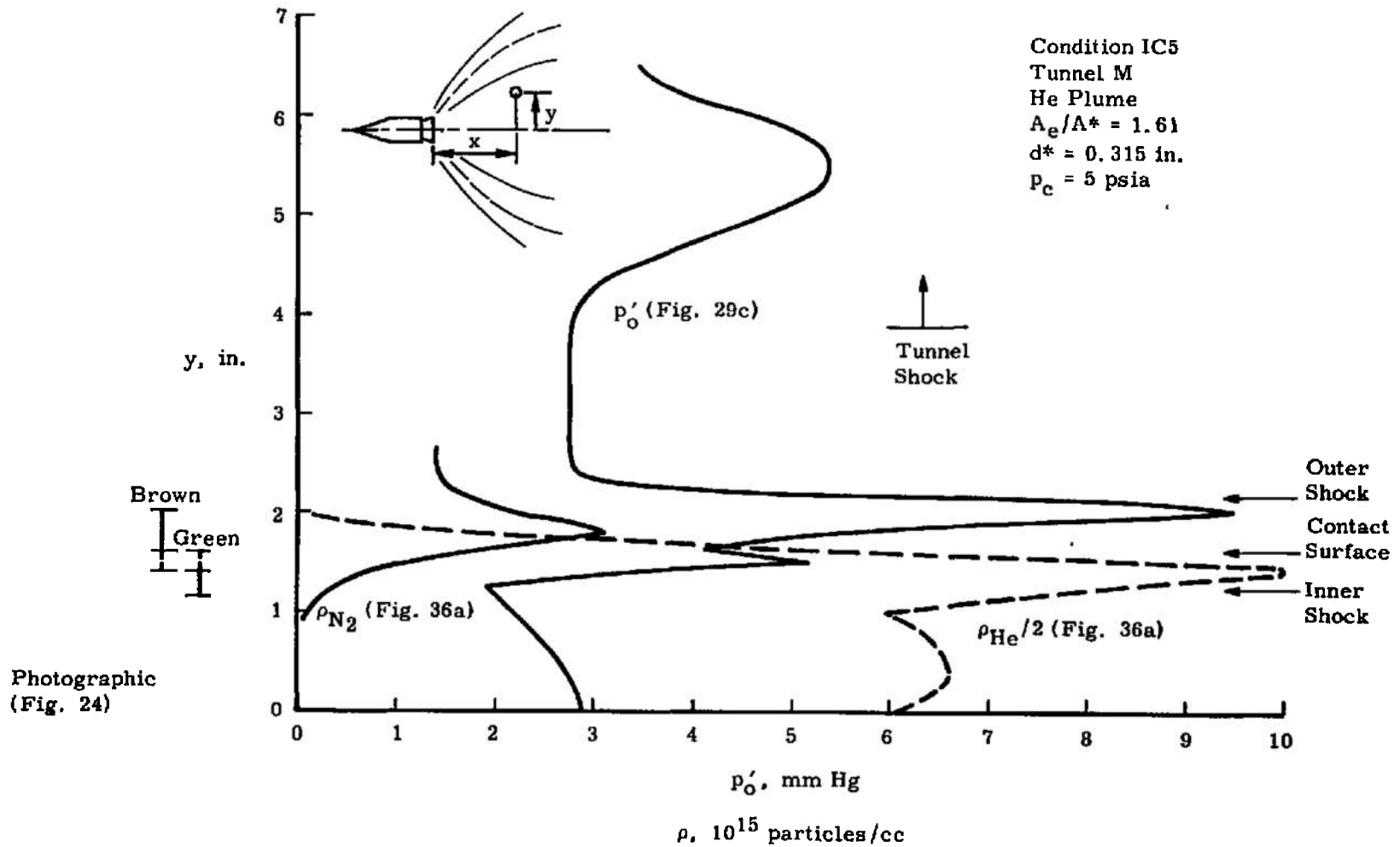
a. x = 3 in.

Fig. 48 Comparison of Results for Condition IC5
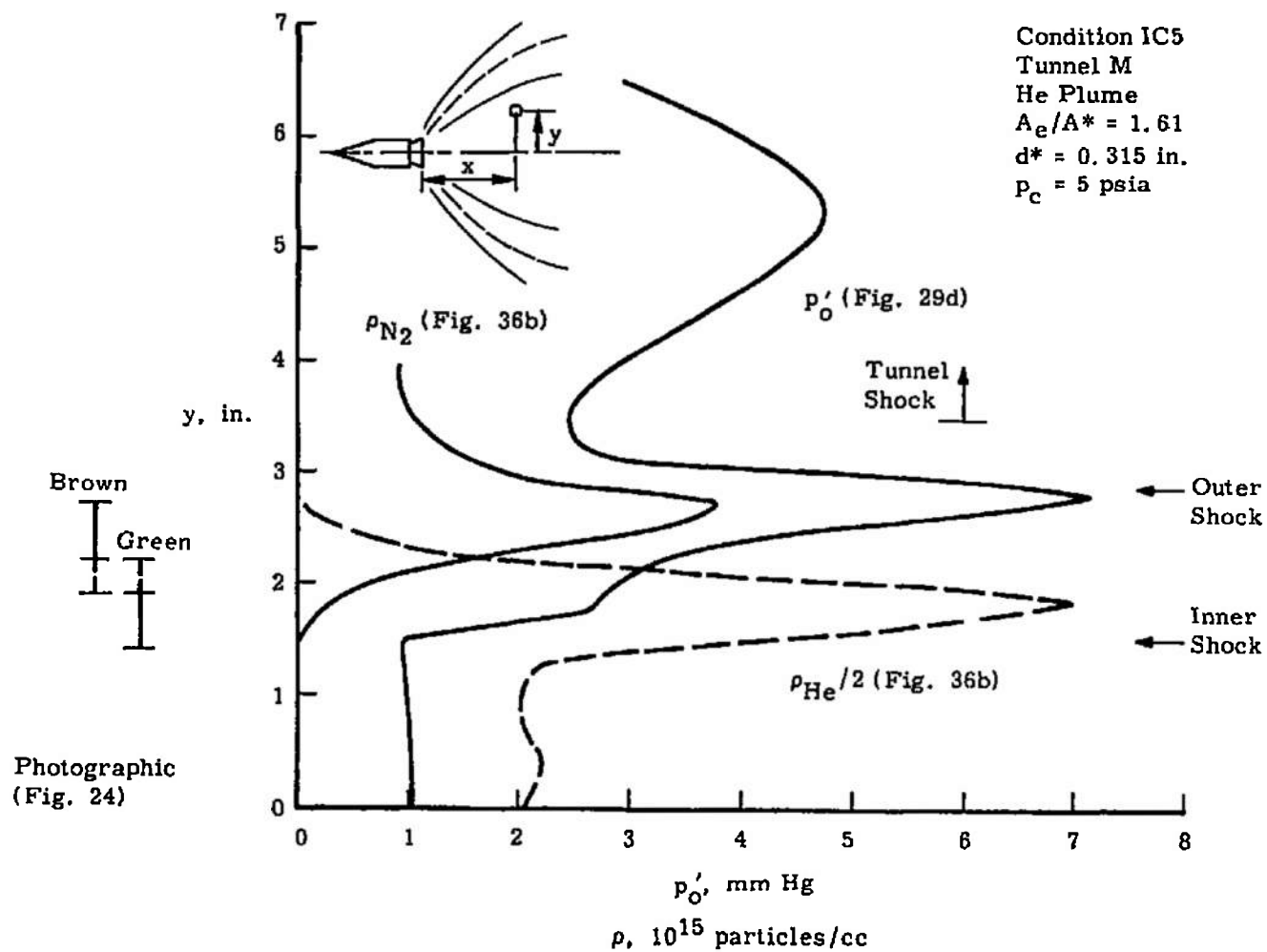
Condition IC5
Tunnel M
He Plume
$A_e/A^* = 1.61$
$d^* = 0.315$ in.
$P_c = 5$ psia

ρ_{N_2} (Fig. 36b)

P_o' (Fig. 29d)

Tunnel Shock

Outer Shock

Inner Shock

$\rho_{He}/2$ (Fig. 36b)

Brown

Green

Photographic (Fig. 24)

y, in.

P_o', mm Hg

ρ, 10^{15} particles/cc

b. x = 5 in.
Fig. 48 Continued

Condition IC5
Tunnel M
He Plume
$A_e/A^* = 1.61$
$d^* = 0.315$ in.
$p_c = 5$ psia

ρ_{N_2} (Fig. 36c)

Brown

Green

y, in.

Merged Tunnel
Shock and
Outer Shock

p_o' (Fig. 29e)

ρ_{He} (Fig. 36c)

Inner
Shock

Photographic
(Fig. 24)

p_o', mm Hg

ρ, 10^{15} particles/cc
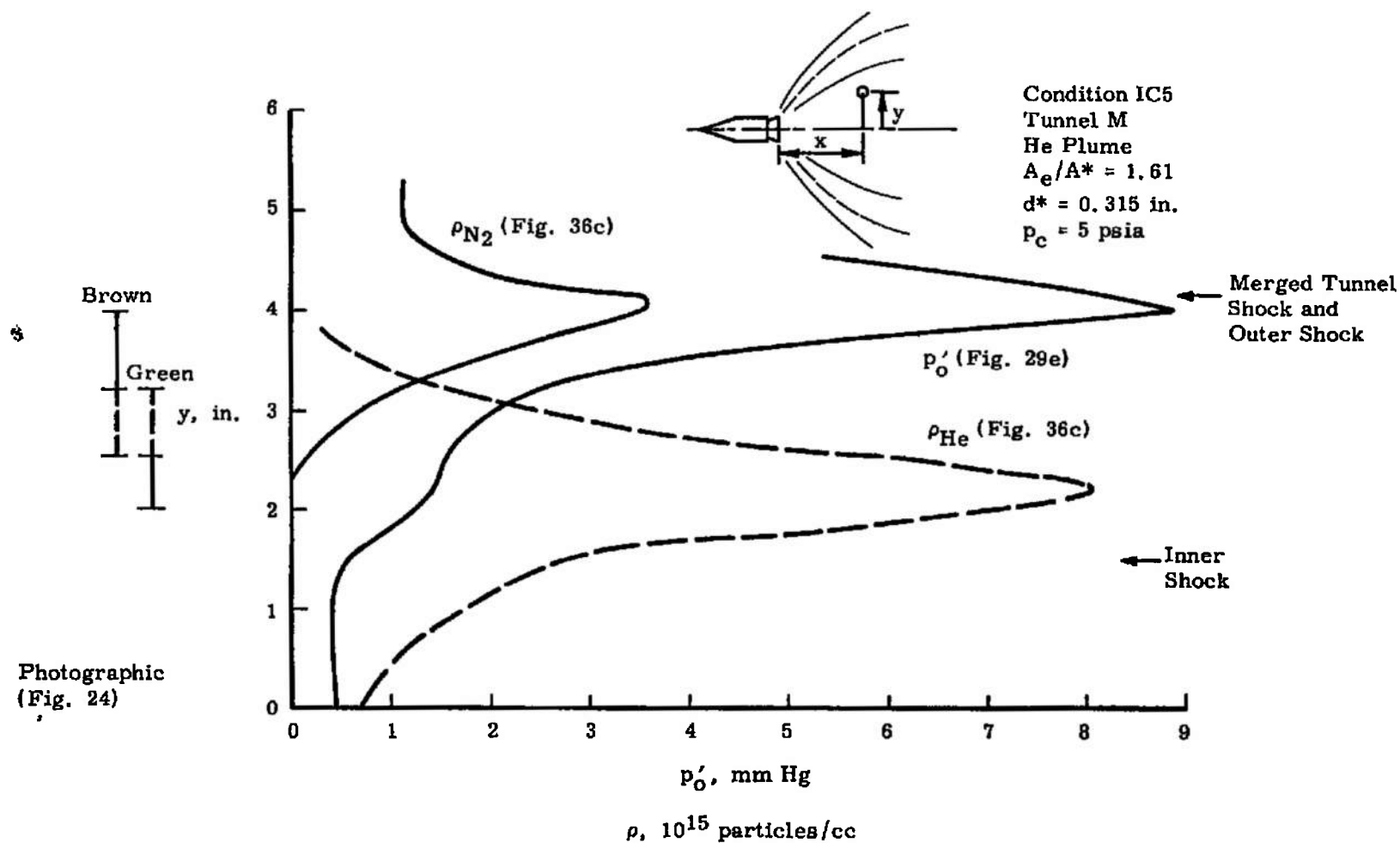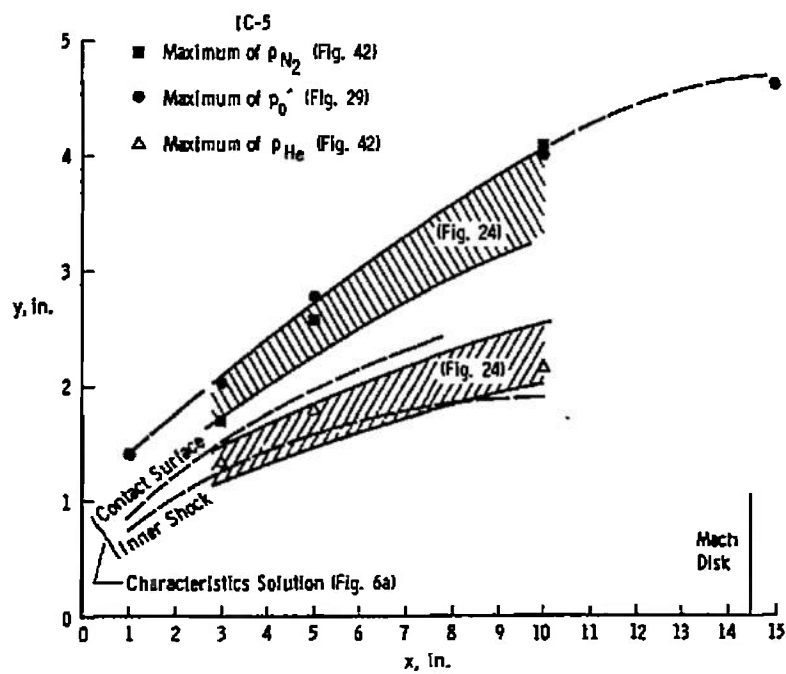
c. x = 10 in.
Fig. 48 Continued

d. Summary
Fig. 48 Concluded
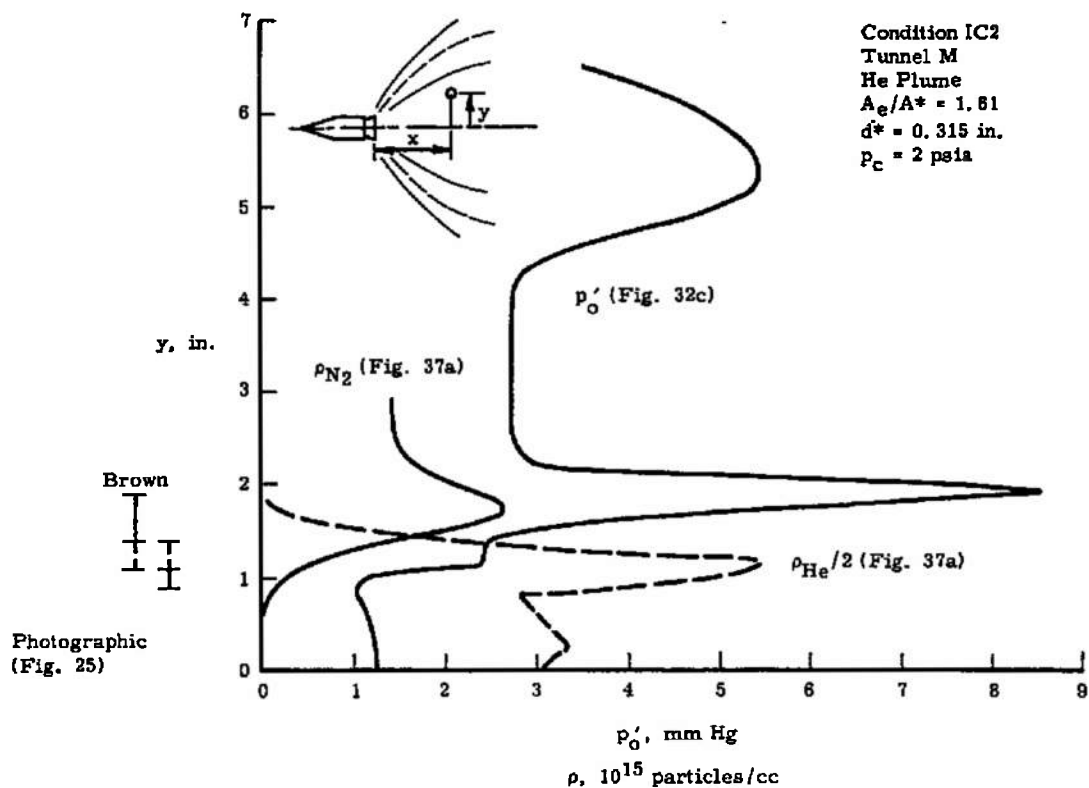
a. x = 3 in.
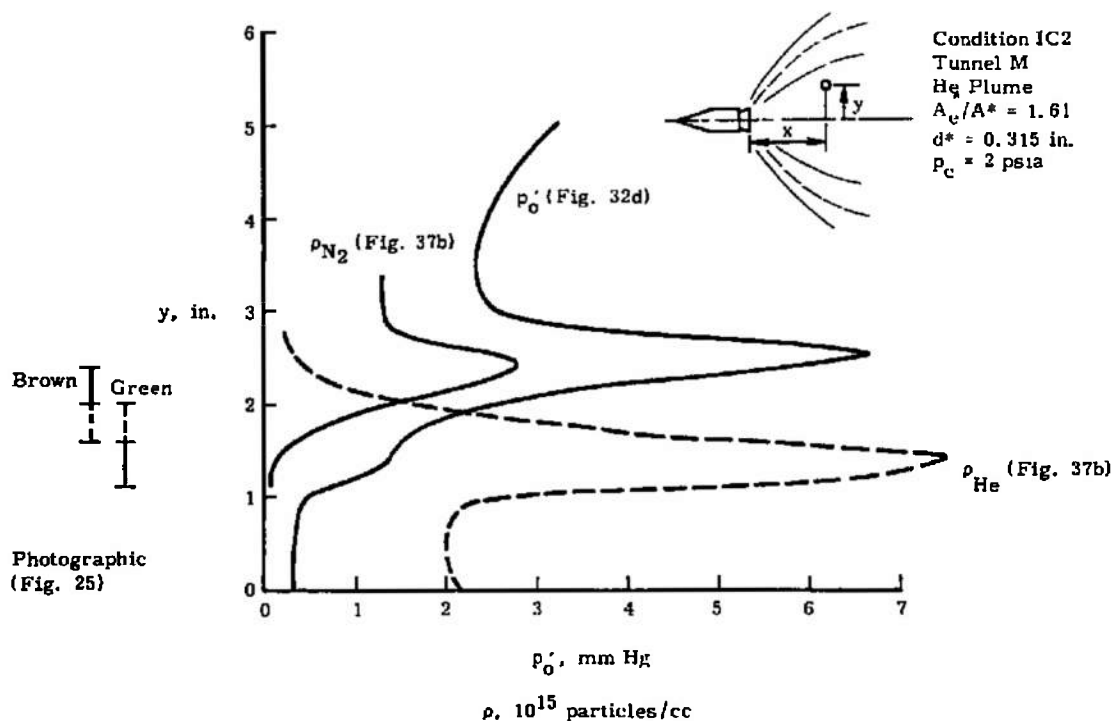
b. x = 5 in.

Fig. 49 Comparison of Results for Condition IC2

122

Condition IC2
Tunnel M
He Plume
$A_e/A* = 1.61$
$d* = 0.315$ in.
$p_c = 2$ psia

ρ_{N_2} (Fig. 37c)

p_o' (Fig. 32e)

ρ_{He} (Fig. 37c)

Brown

Green

Photographic
(Fig. 25)

p_o', mm Hg

ρ, 10^{15} particles/cc

c. x = 10 in.

IC2
■ Maximum of ρ_{N_2} (Fig. 42)
● Maximum of p_o' (Fig. 32)
△ Maximum of ρ_{He} (Fig. 42)

(Fig. 25)

(Fig. 25)

Contact
Surface

Inner Shock

Characteristics Solution (Fig. 6c)

Mach
Disk
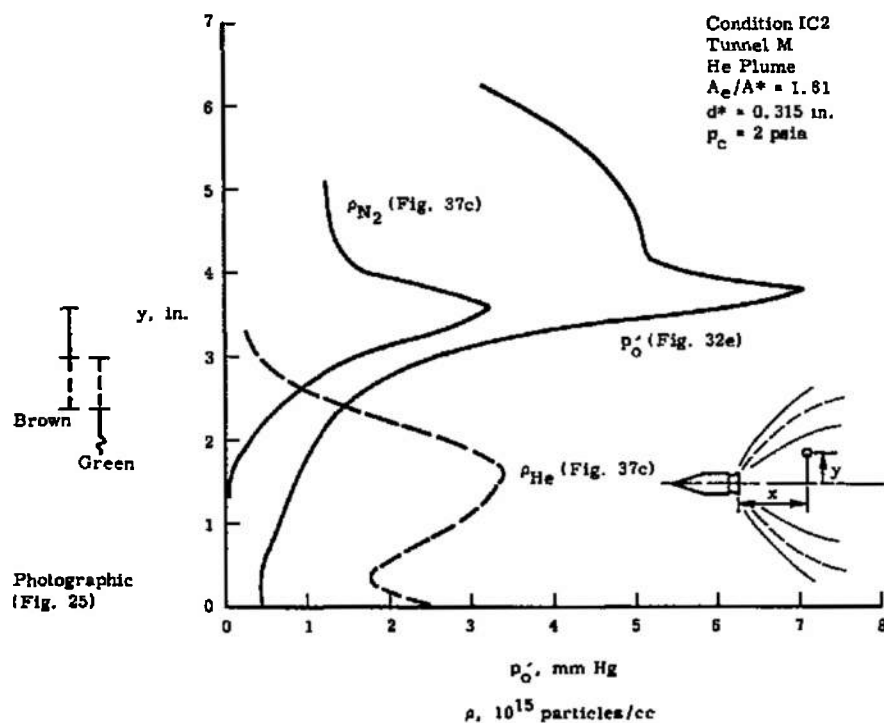
x, in.
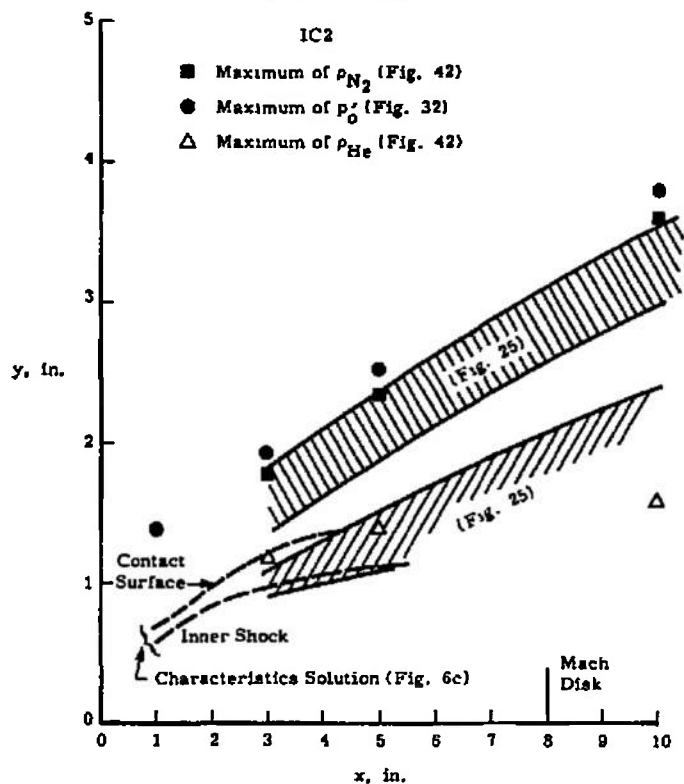
d. Summary
Fig. 49 · Concluded

Condition IB
Tunnel M
He Plume
$A_e/A* = 25$
$d* = 0.030$ in.
$p_c = 450$ psia

p_0' (Fig. 33)

ρ_{N_2} (Fig. 38)

$\rho_{He}/10$ (Fig. 38)

y, in.

p_0', mm Hg

ρ, 10^{15} particles/cc
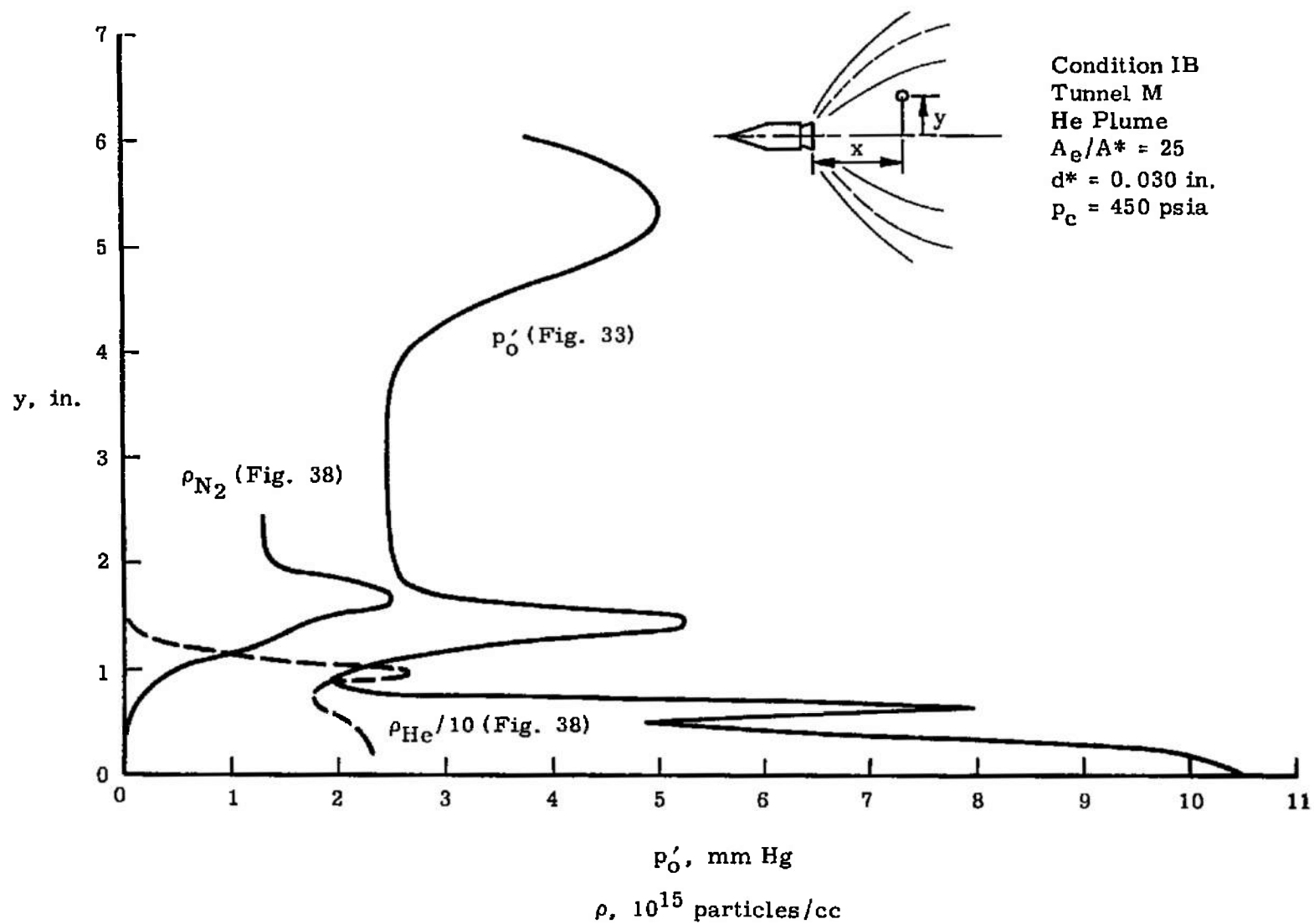
Fig. 50 Comparison of Results for Condition IB (x = 3 in.)

Figure 51 gives a comparison of the shock locations for various conditions and gases, with the distances normalized by the scale length, L (Eq. (17)). The values for helium seem to correlate fairly well, as do those for CO_2. However, the locations for the CO_2 are about 20 percent less than those for helium. The reason for this has not been explained.
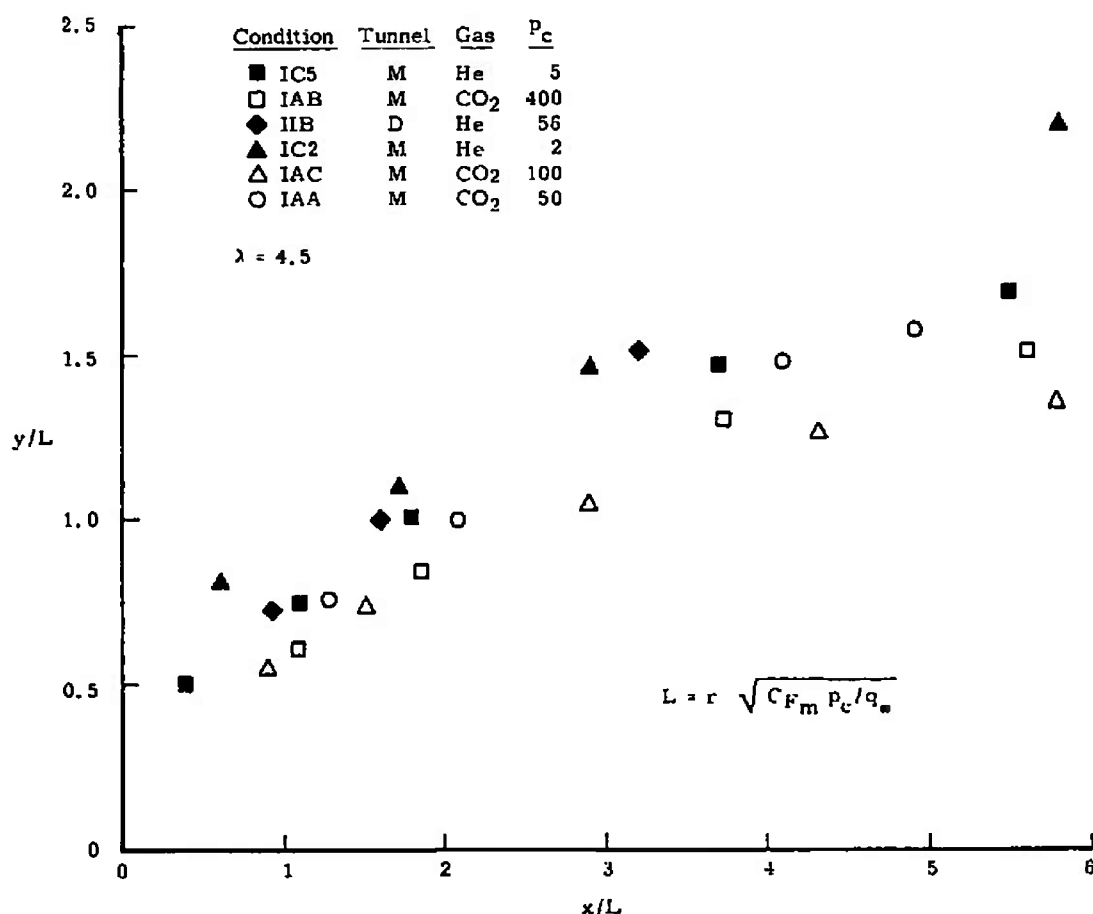
Fig. 51 Normalized Location of Maximum Impact Pressure

SECTION VI
SUMMARY AND CONCLUSIONS

Scaling parameters for rocket exhaust plumes were determined on the basis of a simplified inviscid theory. These parameters were used to determine test conditions for the simulation of the flight of a typical rocket through the atmosphere at an altitude of 80 km at Mach numbers

of 18 and 10. For the test, CO_2 and He were chosen for the exhaust gases of the models; CO_2 was chosen because its properties closely matched those of the actual rocket plume, and He was chosen because of the suitability for density and temperature surveys with the electron beam.

Models with three different geometries and with the two exhaust gases were tested in two different wind tunnels (M and D). Rocket chamber conditions also were varied to enable determining plume properties under a variety of conditions. Pitot pressure surveys were made at all test conditions; photographs were taken in Tunnel M using the electron beam for flow visualization; and densities and temperatures were determined during the helium rocket exhaust test in Tunnel M using radiation measurements from the electron beam excited flow.

The shocks were found to be somewhat diffuse and thick, and it is believed that there were rarefaction effects on plume size and shape (characteristics solutions for the exact conditions would be necessary to establish this). Density measurements of the free-stream and plume gases demonstrated that significant mixing of the two gases had occurred across the interface. The test produced useful detailed data on simulated rocket exhaust plumes interacting with a rarefied hypersonic gas stream.

REFERENCES

1. Prozan, R. J. "Development of a Method of Characteristics Solution for Supersonic Flow of an Ideal, Frozen, or Equilibrium Reacting Gas Mixture." Lockheed Report No. HREC A782535, April 1966.

2. Jarvinen, Phillip O., Hill, Jacques A. F., Draper, James Starkey, and Good, R. Earl. "High Altitude Rocket Plumes." AFCRL 66-656, June 1966.

3. Alden, R. L., and Habert, R. H. "Gas Dynamics of High Altitude Rocket Plumes." MITHRAS Report MC 63-80-R1, July 1964.

4. Hill, Jacques A. F. and Habert, Roger H. "Gasdynamics of High-Altitude Missile Trails." MITHRAS Report No. MC-61-18-R1, January 1963.

5. Adamson, Thomas C., Jr. "The Structure of the Rocket Exhaust Plume without Reaction at Various Altitudes." University of Michigan Report No. 4613-45-T, June 1963.

6. Barthel, J. R., et al. "High Altitude Rocket Plume Structure."
    General Dynamics Convair Report No. DBE65-023,
    September 1965.

7. Muntz, E. P., Hamel, B. B. and Maguire, B. L. "Exhaust
    Plume Rarefaction." General Electric Report No. 685D288,
    July 1968.

8. Kinslow, Max and Miller, John T. "Nonequilibrium Expansion
    of a Diatomic Gas through a Convergent-Divergent Nozzle."
    Physics of Fluids, Vol. 9, No. 9, September 1966.

9. Ashkenas, H. "On Rotational Temperatures Measurements in
    Electron-Beam Excited Nitrogen." Physics of Fluids,
    Vol. 10, No. 12, December 1967.

APPENDIXES
I. CORRECTION OF PRESSURE MEASUREMENTS
FOR ORIFICE AND PROBE EFFECTS
II. FLOW DIAGNOSTICS USING EXCITATION
BY AN ELECTRON BEAM

APPENDIX I
CORRECTION OF PRESSURE MEASUREMENTS
FOR ORIFICE AND PROBE EFFECTS

Under rarefied flow conditions impact pressure probes may not indicate the ideal impact pressure because of viscous and transitional flow phenomena. The viscous effects are attributable to the thickening of the boundary layer and shock and their eventual merging. At lower Reynolds numbers the shock becomes more diffuse and the flow departs further from equilibrium as free molecular conditions are approached. In the present report, all free molecular conditions are based on equations from Ref. I-1. The specific effects considered are the external or probe effect which was reported by Potter and Bailey (Ref. I-2), and the orifice effect discussed first by Potter, Kinslow, and Boylan (Ref. I-3) for a nonequilibrium state attributable to a flux of energy at a surface. The ideal impact pressure is needed in order to determine conditions in the free stream, so that the measured values must be corrected for the probe and orifice effects.

Various papers have been written on the probe effect, showing first, as one proceeds toward more rarefied flow, a small decrease in the measured impact pressure below the ideal and then a larger pressure rise as near-free molecule conditions are encountered.

The interpretation of impact probe measurements is further complicated by the orifice effect. This effect is manifested by an inequality between the pressure sensed by an orifice and the pressure existing at the surface containing the orifice in the presence of a flux of energy or momentum. The orifice effect was reported in Ref. I-3 for the case of the energy flux to a surface.

The method used to correct pitot probe measurements for the probe and the orifice effect to obtain the true impact pressure follows.

Probe Effect

A study of impact probes under conditions similar to those in Tunnel M was reported by Daun, et al. (Ref. I-4). An empirical fit to the Daun data and to data from Tunnel M resulted in the following equations for flat-faced probes.

$$\frac{p_w}{p_o'} = \frac{\dfrac{91.4}{(p_w/p_o')_{fm}} + Re_{2,r_p}^2 \, (p_2/p_\infty)}{\dfrac{91.4}{(p_w/p_o')_{fm}^2} + 1.5 \, Re_{2,r_p} \sqrt{p_2/p_\infty} + Re_{2,r_p}^2 \, (p_2/p_\infty)} \qquad \text{(I-1)}$$

in which p_w is the pressure at the face of the probe, obtained from the indicated pressure by applying the orifice correction, and p_o' is the ideal impact pressure.

The free molecule limit of p_w/p_o' for large Mach numbers is

$$\left(\frac{p_w}{p_o'}\right)_{fm} = \left(\frac{2}{\gamma+1}\right)^{\frac{\gamma+1}{\gamma-1}} \gamma^{\frac{\gamma}{\gamma-1}}\left(1 + \sqrt{\frac{\pi}{2\gamma}\frac{T_w}{T_\infty}}\frac{1}{M_\infty}\right) \qquad (I\text{-}2)$$

In order to evaluate these equations an iteration scheme was necessary since M_∞, T_∞, $Re_{2,r}$, and ρ_2/ρ_∞ require the knowledge of p_o'. The numerical solution is discussed below.

Orifice Effect

This effect, attributable to the nonequilibrium state of the gas at the solid boundary, when a flux of energy is present, causes the pressure sensed by an orifice to deviate from the force per unit area on the surface. The amount of deviation is expressed in terms of a dimensionless pressure parameter, $\bar{p}$, defined by

$$\bar{p} = (p_i - p_{i_{fm}})/(p_w - p_{i_{fm}}) \qquad (I\text{-}3)$$

where

p_i is the pressure inside the orifice cavity,

$p_{i_{fm}}$ is the value of p_i for a free molecule orifice, and

p_w is the true wall pressure in the absence of the orifice.

In Refs. I-3 and I-5, $\bar{p}$ was shown to be a function of the Knudsen number based on the orifice diameter, d, the wall temperature, T_w, and p_i. However, recent measurements of the orifice effect in Tunnel M and data from Cornell Aeronautical Laboratory (Ref. I-6) show that the results of the correlation parameter used in Refs. I-3 and I-5 are inadequate for higher enthalpy flows. The method of correcting for the orifice effect in this test is based upon a paper presented at the Seventh International Symposium on Rarefied Gas Dynamics at Pisa, Italy, June 30, 1970 (Ref. I-7).

The relation between $\bar{p}$ and a Knudsen number, $\widetilde{Kn}$, based upon orifice diameter, p_w, and a reference temperature T_r that was used is,

$$\bar{p} = Z/(1 + Z) \qquad (I\text{-}4)$$

in which

$$Z = \frac{0.394}{\sqrt{\tilde{K}n}} + \frac{0.282}{\tilde{K}n} + \frac{0.038}{\tilde{K}n^2}$$

$p_{i_{fm}}$ and T_r are both functions of κ, the dimensionless heat-transfer rate parameter, and α, the thermal accommodation coefficient. $p_{i_{fm}}/p_w$ and T_r/T_w are given by:

$$\frac{p_{i_{fm}}}{p_w} = \frac{\sqrt{2\pi}\left(\frac{2-\alpha}{\alpha}\right)\kappa + \sqrt{\frac{8\pi\kappa^2(1-\alpha)}{\alpha^2} + 4}}{2 - \pi\kappa^2} \tag{I-5}$$

and

$$\frac{T_r}{T_w} = 1 + 2\pi\kappa^2\left(\frac{2-\alpha}{\alpha}\right) - \frac{2\kappa}{\alpha^2}\sqrt{2\pi\left[2\pi\kappa^2(1-\alpha) + \alpha^2\right]} \tag{I-6}$$

where

$$\kappa = \frac{\dot{q}(\gamma - 1)}{p_w(\gamma + 1)\sqrt{RT_w}} \tag{I-7}$$

An iteration scheme is required to solve for p_w. The thermal accommodation coefficient, α, was presumed to be 0.79 for N_2, 0.8 for CO_2 and 0.51 for He. The values for helium and nitrogen are those used in Ref. I-5 and close to those obtained in Ref. I-8. The carbon dioxide value was obtained from a consideration of molecular weight.

Based on limited heat-transfer data from Tunnel M for flat-faced bodies, the following equation was used to calculate the stagnation point heat transfer

$$\dot{q} = \frac{\dot{q}_{fm}}{\left[\left(\frac{\dot{q}_{fm}}{\dot{q}_{FR}}\right)^5 + 1\right]^{1/5}} \tag{I-8}$$

where $\dot{q}_{fm}$ is the free molecule heat-transfer rate and $\dot{q}_{FR}$ is from the continuum Fay-Riddell equation (Ref. I-9). This experession gives the correct free molecule heat-transfer rate and approaches the Fay-Riddell theory for higher Reynolds numbers.

The equations used for $\dot{q}_{fm}$ and $\dot{q}_{FR}$ for higher Mach numbers are

$$\dot{q}_{fm} = -\alpha p_\infty\sqrt{RT_\infty}\left[\left\{\frac{\gamma}{2}M_\infty^2 + \frac{\gamma}{\gamma-1} - \frac{(\gamma+1)}{2(\gamma-1)}\frac{T_w}{T_\infty}\right\}\sqrt{2\pi\gamma}\,M_\infty\right] \tag{I-9}$$

and based upon Ref. I-9, the heat-transfer rate to a flat-faced probe of radius r is

$$\dot{q}_{FR} = -0.54\sqrt{2}\left(\frac{T_o}{T_w}\frac{\mu_w}{\mu_o}\right)^{0.1}\sqrt{\frac{\mu_o p_o'}{RT_o}}\sqrt{\frac{4U_\infty}{3\pi r_p}\sqrt{2\frac{\rho_\infty}{\rho_2}\left(1-\frac{1}{2}\frac{\rho_\infty}{\rho_2}\right)}}\left(\frac{h_o - h_w}{(P_r)^{0.6}}\right)$$

(I-10)

based upon the results of Ref. I-9. Heat-transfer rate is negative for "cold wall" conditions.

If free-stream properties are known then Eqs. (I-1) through (I-10) can be solved to permit the correction of data for the orifice and probe effects. However, since free-stream conditions are known only after applying the correction, an iteration scheme was used. The numerical method for correcting the pitot data is described briefly below.

Iteration Procedure

An iteration procedure was used to obtain the ideal impact pressure, p_o', from the indicated pressure, p_i. An initial approximation was made equating p_o' to p_i. Using the reservoir stagnation pressure, flow properties, such as $Re_{2,r}$, ρ_2/ρ_∞, M_∞, T_∞, p_∞, and U_∞ were obtained using isentropic flow equations along with the value for p_o'. The stagnation point heat transfer was obtained using Eqs. (I-8), (I-9), and (I-10). The p_w was assumed equal to p_i, thereby permitting the solution κ from Eq. (I-7). Equations (I-3) through (I-6) were solved for $\bar{p}$ yielding p_w which was substituted in Eq. (I-7) giving a new κ. Equations (I-3) through (I-6) were repeatedly solved until p_w did not change from one iteration to the next. Using the obtained value of p_w in Eqs. (I-1) and (I-2), p_o' was obtained and used to repeat the above procedures until the value of p_o' was constant for successive iterations. The final value of p_o' is the ideal impact pressure which can be used to obtain the corrected free-stream properties.

REFERENCES

I-1. Schaaf, S. A. and Chambre, P. L. "Flow of Rarefied Gases." Fundamentals of Gas Dynamics, Section H. Edited by H. W. Emmons, pp. 687-739.

I-2. Potter, J. Leith, and Bailey, Allen B. "Pressures in the Stagnation Regions of Blunt Bodies in the Viscous-Layers to Merged-Layer Regimes of Rarefied Flow." AEDC-TDR-63-138 (AD411624), September 1963.

I-3. Potter, J. L., Kinslow, M., and Boylan, D. E. "An Influence of the Orifice on Measured Pressures in Rarefied Flow." Rarefied Gas Dynamics. Edited by J. H. deLeeuw. Vol. 2, Academic Press, New York, 1966, pp. 175-194.

I-4. Daum, Fred L. Rarefied Effects on Impact Pressure Probes in Hypersonic Flow." ARL-65-176, September 1965.

I-5. Kinslow, Max, and Arney, G. D., Jr. "Thermo-Molecular Pressure Effects in Tubes and at Orifices." AGARDograph 119, August 1967.

I-6. Bartz, John D., and Vidal, Robert J. "Experimental Study of Pseudo Transpiration at an Orifice in Rarefied Flow." CAL No. AF-2041-A-3, September 1968.

I-7. Kinslow, Max, and Potter, J. Leith. "Reevaluation of Parameters Relative to the Orifice Effect." Presented at the 7th International Symposium on Rarefied Gas Dynamics, University of Pisa, Pisa, Italy, June 29 to July 3, 1970.

I-8. Teagan, W. P. and Springer, G. S. "Heat Transfer and Density Distribution Measurements between Parallel Plates in the Transition Regime." The Physics of Fluids, Vol. 11, No. 3, March 1968, p. 497.

I-9. Fay, J. A. and Riddell, F. R. Journal of Aeronautical Sciences, Vol. 25, 1958, pp. 73-85.

APPENDIX II
FLOW DIAGNOSTICS USING EXCITATION BY AN ELECTRON BEAM

THEORY OF THE ELECTRON BEAM FLUORESCENCE METHOD OF FLOW DIAGNOSTICS

In well-documented papers (Refs. II-1 and II-2), Muntz has presented in detail the theory underlying the excitation of a low density gas by an electron beam and use of the induced fluorescence to determine rotational and vibrational temperatures and atomic and molecular specie concentrations. Therefore, only a brief summary of the technique as applied to helium (He) and nitrogen (N_2) is presented here.

It is well known that the interaction of an electron beam of energy of approximately 20 kv with a low density gas can be characterized by descriptions of two general collisional processes: elastic scattering and inelastic scattering. Elastic scattering is descriptive of the deviation of the path of the beam of electrons attributable to close encounters with the target nuclei and involves no excitation of the gas atoms. The major effect of elastic scattering is the spreading of the beam, leading to the necessity of the determination of the diameter of the beam at the point of observation, thereby influencing both the method of current measurement as well as the technique of optical detection. The results of Center (Ref. II-3) were influential in selection of the current measurement method, and the results of Maguire (Ref. II-4) were helpful in selecting parameters for the optical measurement technique for the present study. Details of these methods of measurement are discussed in Section 3.5 of this report.

The occurrence of inelastic scattering is the more significant process of the two for the purpose of flow diagnostic measurements, for as a result of this process the emission of radiation results which can, in principle, be related to gas density and temperature. Figure II-1 shows a sketch of two possible types of inelastic collisions, namely ionizing and nonionizing collisions, each occurring to the extent determined by its partial cross section. One of the results of the inelastic collision can be excitation of the atom or molecule to a particular level of an excited state from which it decays by emission of radiant energy; intuitively, one expects the intensity of this emission to be related directly to the gas density, thereby affording a nonperturbative optical method of density measurement. To allow use of such a method, two major criteria must be met: (1) the excitation process must be direct, i.e., free from secondary production sources such as low energy electrons and cascading transitions, and (2) the radiative lifetime, τ_r,

136

$\overline{e}_p$

He

He*

He

hν

Nonionizing

$\overline{e}_p$

$\overline{e}_s$

He

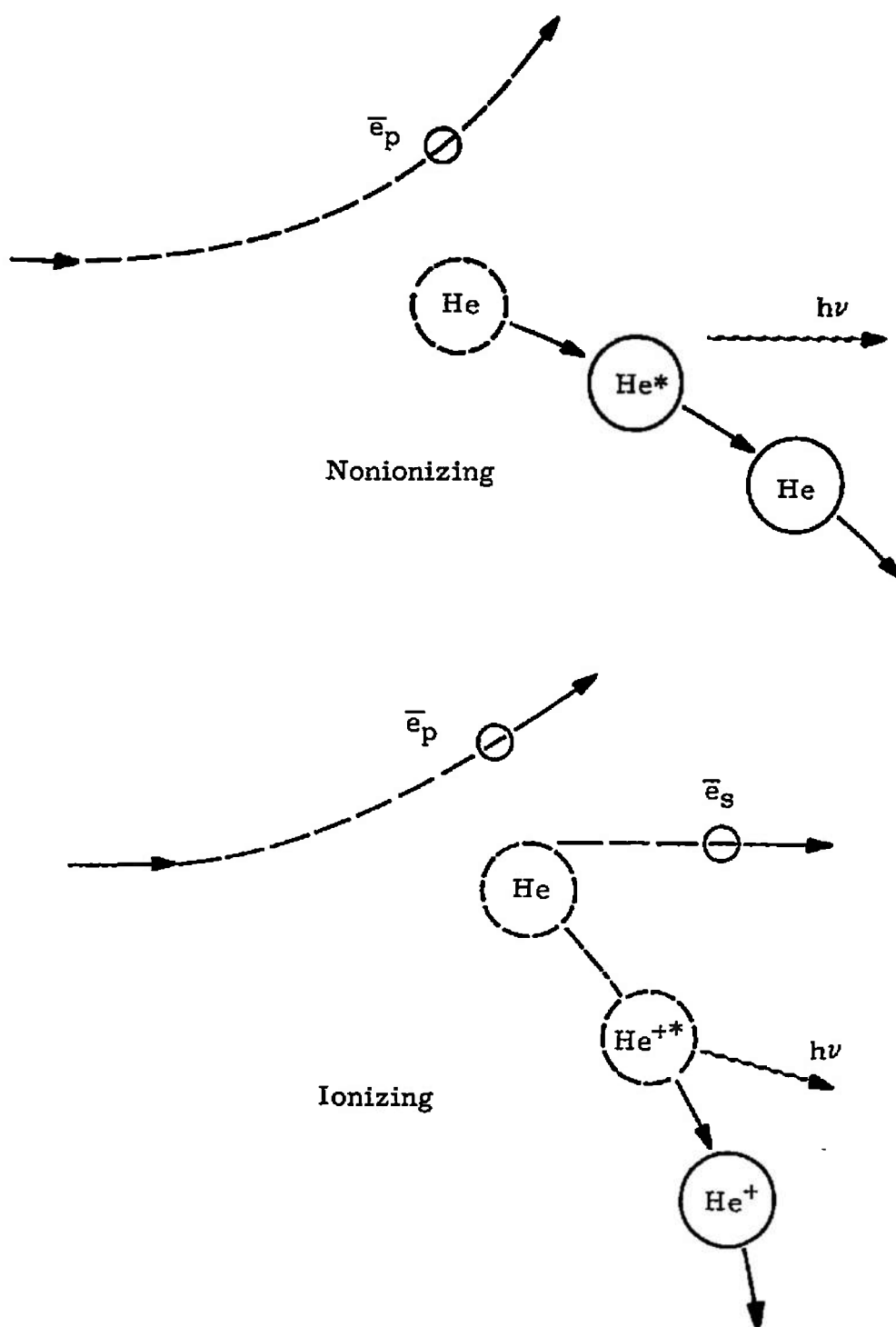He^{+*}

hν

He$^+$

Ionizing

Fig. II-1 Schematics of Ionizing and Nonionizing Collisions

must be sufficiently short that effects attributable to collisions and flow speed are negligible. For the typical hypersonic flow field environment this requires τ_r to be less than approximately 10^{-7} sec.

Particularizing the discussion to He, the HeI transition of $3^1P \rightarrow 2^1S$ at 5016 Å, sketched in Fig. II-2, satisfies both these criteria and was selected for use in this test for the purpose of performing a measurement of He density. It is now necessary to cast into quantitative form the intuitive feeling of the relationship of radiant intensity and He density. For sufficiently low gas density, for which one can neglect collisional effects, it is shown in Ref. II-2 that the steady-state intensity per unit volume is given by

$$I(5016) = \frac{C_o \, A(5016) \, h \, c \, j \, N(He)}{\lambda(5016) \, \tau_r(3^1P)} \qquad \text{(II-1)}$$

where

$A(5016)$ = Einstein spontaneous emission coefficient

h = Planck's constant

c = Speed of light

j = Electron beam current density

$\lambda(5016)$ = Wavelength of 5016-Å line

$\tau_r(3^1P)$ = Radiative lifetime of 3^1P state

C_o = Constant independent of temperature and density

and

$N(He)$ = Number density of ground state ^1S_o He atoms.

Equation II-1 shows the intensity I to be directly proportional to the number density of the ground-state helium atoms, and, therefore, a measurement of I will yield $N(He)$ if by calibration the multiplication factor of $N(He)$ is determined. If this is done Eq. (II-1) becomes

$$I(5016) = C_1 j N(He) \qquad \text{(II-2)}$$

where C_1 is ideally independent of both temperature and density. Details of the calibration required to determine C_1 are given in a following section.

Referring to Fig. II-2, it is shown that excited, neutral He atoms in the 3^1P_1 level not only radiatively decay by the transition $3^1P_1 \rightarrow 2^1S_0$ but also by the emission of an ultraviolet photon of wavelength equal to 537Å in the transition $3^1P_1 \rightarrow 1^1S_0$, returning the atom to the electronic ground state. Since the ultraviolet (uv) photon emitted is in resonance with the reverse transition $1^1S_0 \rightarrow 3^1P_1$, there exists a significant absorption coefficient at this wavelength, once again returning the atom to the 3^1P_1 state from which it can once more radiatively decay by emitting a photon of wavelength of either 5016Å or 537Å. This has the effect of increasing the radiative lifetime $\tau_r(3^1P)$ as well as broadening the beam by diffusive spreading. From the results of both Maguire (Ref. II-4) and Phelps (Ref. II-5), for the majority of density values encountered in the test the effect was to broaden the beam of He emission species to approximately eight "current beam diameters," and allowance was made for this effect by adjustment of the spectrometer slit height to ensure complete imaging of the beam.

For gas density values such that the collision time τ_c is not much larger than τ_r, one must alter Eqs. (II-1) and (II-2) to allow for collision decay channels for excited HeI 3^1P atoms; this is shown diagrammatically in Fig. II-3 where the density-dependent rate constant k is expressed in units of cm^3/sec. For the simple phenomenological model of that figure one can show that the intensity-density relationship now becomes

$$I(5016) = \frac{C_2 \, j \, N(He)}{1 + k \, \tau_r(3^1P) \, N(He)} \tag{II-3}$$

where C_2 is a factor independent of temperature and, because of the imprisonment of radiation, is dependent on the number density N(He) to a slight degree. For the range of values of N(He) encountered during this test, this dependence was neglected. It has been assumed, as before, that only helium is present, and the more general case of a binary mixture is considered in a following section.

As shown by the results presented in Fig. II-13, the nonlinearity predicted by Eq. (II-3) becomes significant only at the higher density values encountered. For values of N(He) in the region of $10^{16}/cm^3$, $\tau_r(3^1P)$ is known to be approximately 7.3×10^{-8} sec; from previous measurements of k performed locally under laboratory conditions, the quenching constant at 300°K has been found to be 2.0×10^{-10} cm^3/sec. From Eq. (II-3) it can be seen that at 300°K quenching becomes significant for values of N(He) such that $k \cdot \tau_r(3^1P_1) \times N(He) = 0.1$ or for N(He) values on the order of $10^{16}/cm^3$. If one assumes hard
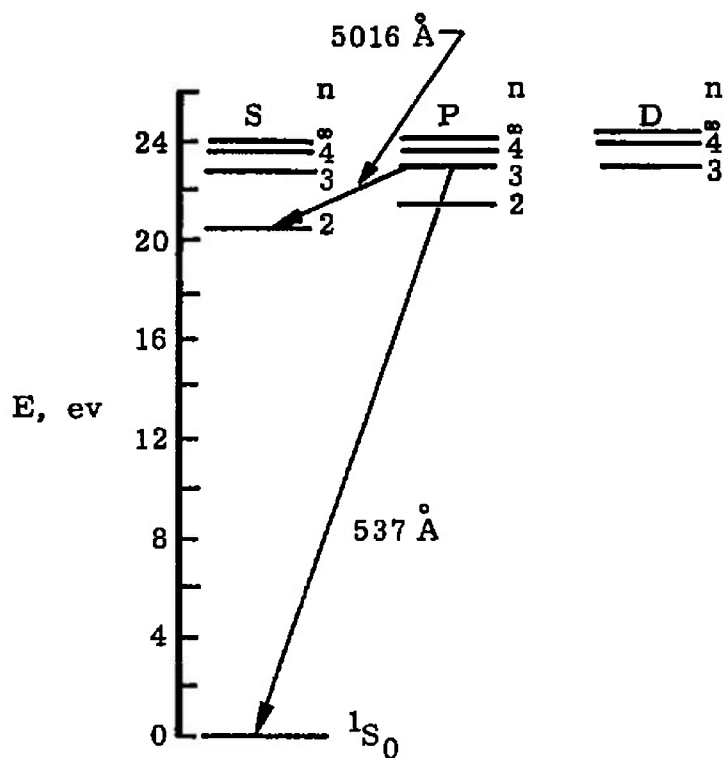
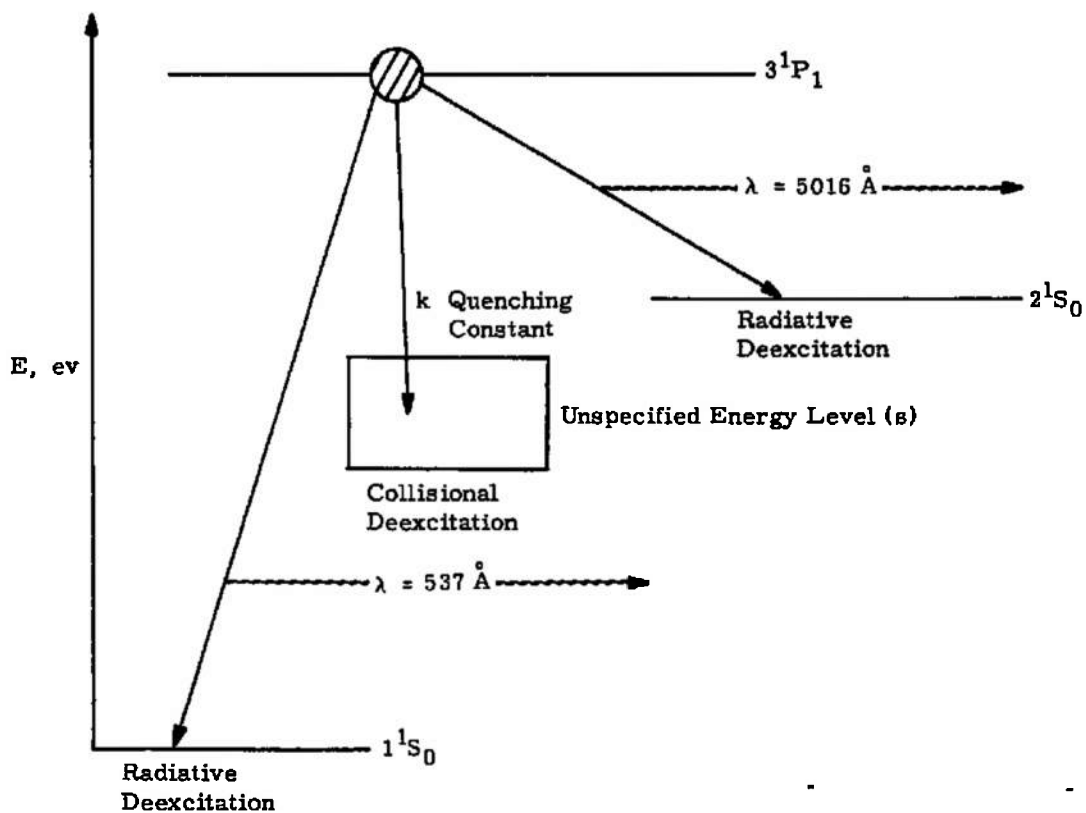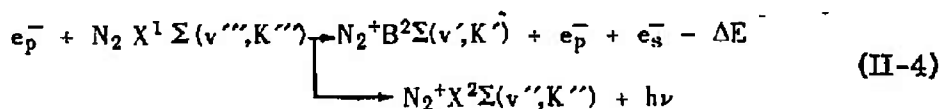Fig. II-2 Partial Energy Level Diagram for Helium

Fig. II-3 Phenomenological Quenching Radiative Decay Model

sphere collision theory to be appropriate for the description of the quenching process, it is found that k varies as $\sqrt{T}$, and is, therefore, of less consequence as the temperature is lowered from 300°K to those values encountered in the test. However, it is difficult at this time to believe that k behaves in this manner because the amount of energy transferred by the quenching process $3^1P_1 \rightarrow {}^1S_0$ is quite sizable, as Fig. II-3 shows, since the energy separation is equivalent to a photon with a wavelength of 537Å which is approximately 23 ev; collisions involving such a large transfer of energy are quite inefficient. More likely, it is expected that a quasi-resonance transfer is the mechanism responsible. The temperature dependence of such a process varies as $1/T$, becoming more important as the temperature is lowered, but only further experiments will decide the form and magnitude of the correction to be applied, because such data are not in hand at present. However, one may appreciate the magnitude of the possible correction attributable to variation of k with temperature if one assumes k to vary as $1/T$. From Eq. (II-3) it can be seen that the denominator of the right-hand side at 300°K is approximately 1.14 at N(He) equal to $10^{16}/cm^3$; at 60°K, for the same number density, the denominator is approximately equal to 1.70, thereby giving approximately a 30-percent difference in density values.

EXCITATION OF GASEOUS MOLECULAR NITROGEN BY ELECTRONS

Excitation of the first negative system of N_2^+ by impact of high energy electrons upon neutral nitrogen molecules has received extensive treatment in the literature following the initial report of Muntz (Ref. II-1) in 1961, and two of the authors of this report have published results of an investigation of the appropriateness of the Muntz model of excitation as well as an extension of those equations for vibrational temperature measurements at higher density (Refs. II-6 and 7). Reference will be frequently made to these works for detailed derivations of the equations which are to follow.

Figure II-4 shows some of the energy levels of N_2 and N_2^+ molecules along with the designation of the radiative molecular band system denoted as the N_2^+ first negative, or $N_2^+ (1-)_{v'v''}$, in which the subscripts v'v'' are used to designate the upper and lower vibrational states, respectively. Shown in Fig. II-5 is an enlarged diagram of the excitation emission process caused by the inelastic collision between a primary electron e_p^- and a neutral nitrogen molecule; i.e.

$$e_p^- + N_2 X^1\Sigma(v''',K'') \rightarrow N_2^+B^2\Sigma(v',K') + e_p^- + e_s^- - \Delta E$$
$$\hookrightarrow N_2^+X^2\Sigma(v'',K'') + h\nu \qquad\qquad \text{(II-4)}$$
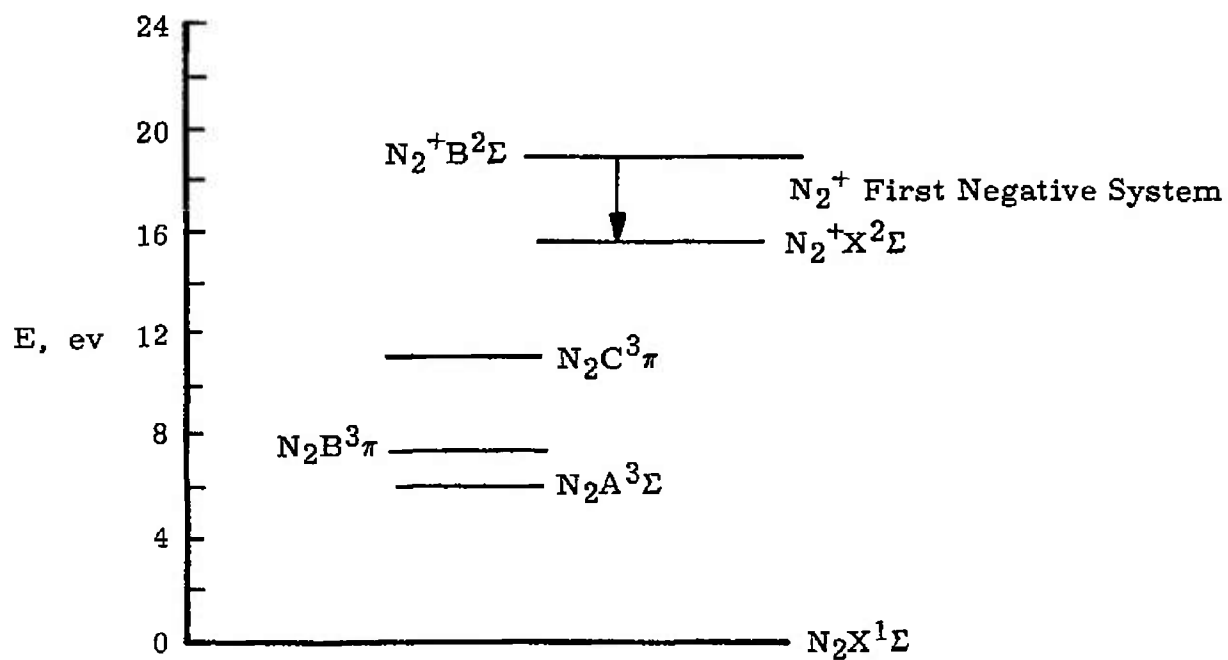
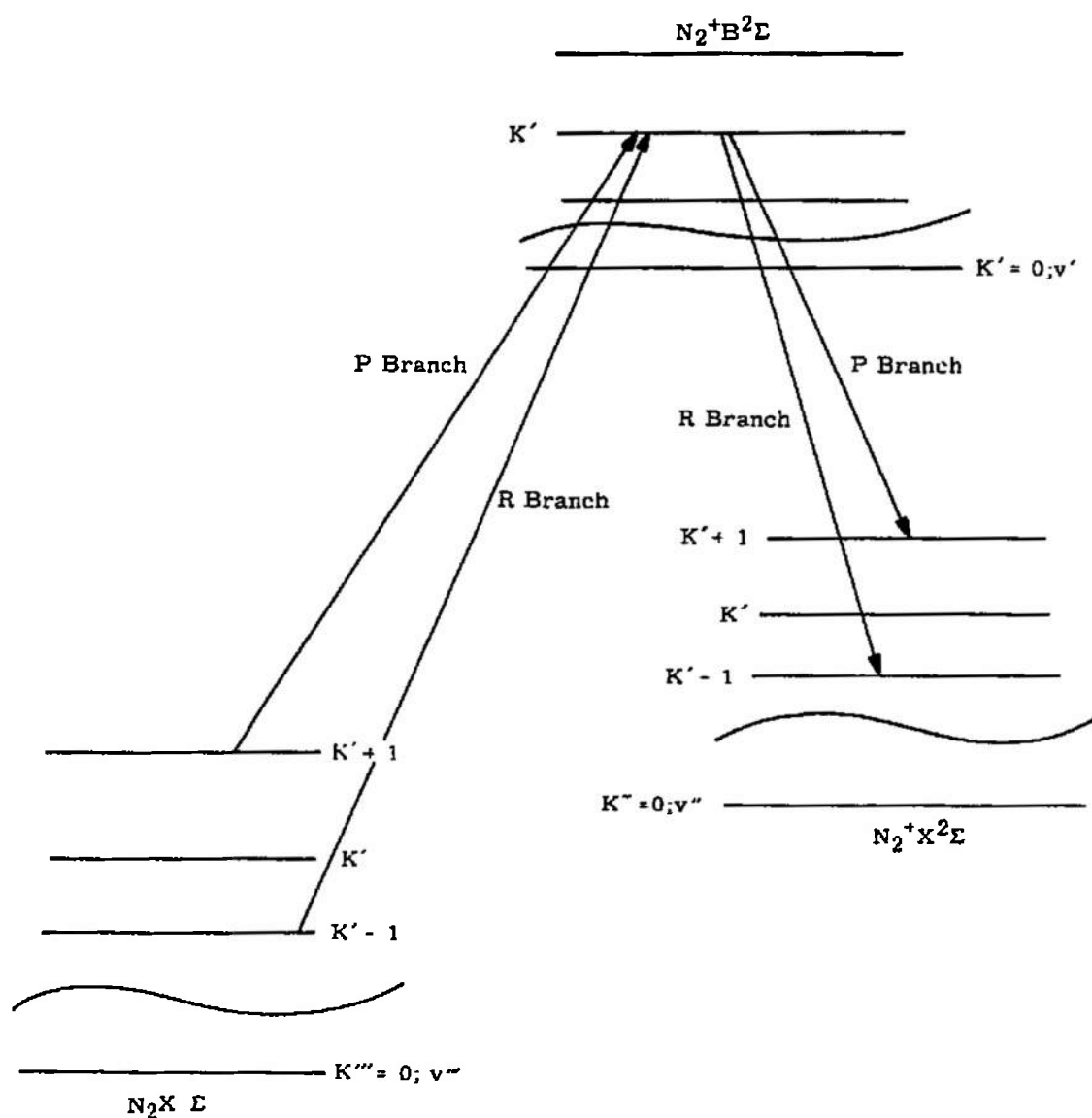Fig. II-4 Partial Energy Level Diagram of Nitrogen

Fig. II-5 Excitation-Emission Diagram

where K denotes the rotational quantum number of the molecule, and it is to be noted that dipole excitations, $\Delta K = \pm 1$, are assumed to be the production mechanism and dipole emission the process of radiative decay. With these assumptions, and further assuming the negligibility of collisional deexcitation and excitation by the secondary electrons, designated in Eq. (II-4) by $e_{\bar{s}}$, one finds the steady-state intensity $I_{v''K'-1}^{v'K'}$ of an emission line for the R branch transition

$$N_2^+ B^2\Sigma(v',K'') \rightarrow N_2^+ X^2\Sigma(v'',K' = K''-1)$$
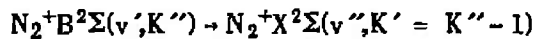
$$\frac{I_{v''K'-1}^{v'K'}\left[\lambda_{v''K'-1}^{v'K'}\right]}{K'[G]_{v'=0}} = \frac{C\,j\,N(N_2)}{(p.f.)_T} \cdot e^{-B_o K'(K'+1)hc/kT_R} \qquad (\text{II-5})$$

where

C = constant

$N(N_2)$ = total $N_2 X^1 \Sigma$ number density

B_o = rotational constant for the $v''' = 0$ state of $N_2\ X^1\Sigma$

k = Boltzmann's constant

T_R = rotational temperature

$(p.f.)_T$ = total partition function of $N_2 X^1\Sigma$ which possesses a vibrational temperature T_v and a rotational temperature T_R

$\lambda_{v''K'-1}^{v'K'}$ = wavelength of the emission line

$$[G]_o = \frac{(K'+1)e^{-2B_o(K'+1)hc/kT_R} + K'\,e^{+2B_o K'hc/kT_R}}{2K'+1}$$

and $[G]_o$ is known as the Muntz G factor, or simply as the G factor. Taking the natural logarithm of both sides one finds

$$\ell n \left\{\frac{I_{v''K'-1}^{v'K'}\left(\lambda_{v''K'-1}^{v'K'}\right)^4}{[G]_o \cdot K'}\right\} = \ell n \left[\frac{C\,j\,N(N_2)}{(p.f.)_T}\right] - B_o K'(K'+1)\frac{hc}{kT_R} \qquad (\text{II-6})$$

which shows that the experimental intensity data, when cast in the form of the left-hand side of the equation and plotted versus $K'(K'+1)$ in principle yield a straight line whose slope equals $-B_o hc/h\,T_R$, thereby giving T_R. Since $[G]_o$ contains T_R, Eq. (II-3) must be solved by iteration, but in practice convergence is rapid.

Performing a summation, either mathematically or, in practice, electronically, of the rotational line intensity values over the vibrational band $v'v''$ one obtains the vibrational band intensity

$$I_{v''}^{v'} = I_{v'v''} = \frac{C_1\, N(N_2)\, j\, p(v'v'') \sum_{v'''=0}^{\infty} \bar{p}(v',v''')e^{-\hat{G}(v''')hc/kT_v}}{(p.f.)_{v'''}\,\lambda_{v'v''}^4 \sum_{v''=0}^{\infty}[p(v',v'')/\lambda_{v'v''}^3]} \quad (II-7)$$

where

$(p.f.)_{v'''}$ = vibrational position function of the $N_2\ X^1\Sigma$ molecule

$\lambda_{v'v''}$ = average wavelength of the vibrational band

$G(v''')$ = vibrational constant of the $N_2 X^1\Sigma$ molecule

$p(v'v'')$ = vibrational band strength for emission

$\tilde{p}(v'v''')$ = vibrational band strength for excitation

If one now obtains the ratio of two vibrational bands originating from different upper-state vibrational levels i and k, respectively, and terminating in levels j and l, respectively, one finds

$$\frac{I_{ij}}{I_{kl}} = \left(\frac{\lambda_{kl}}{\lambda_{ij}}\right)^4 \frac{p(ij)}{p(kl)} \frac{\sum_{s=0}^{\infty}\tilde{p}(is)\,e^{-\hat{G}(s)hc/kT_v}}{\sum_{s=0}^{\infty}\tilde{p}(ks)\,e^{-\hat{G}(s)hc/kT_v}} \frac{\tau_r(i)}{\tau_r(k)} \quad (II-8)$$

where $\tau_r(i) = 1/\sum_{s=0} p(is)/\lambda^3_{is} \equiv$ radiative lifetime of level i.

It is well known that the vibrational band strength p (i j), for example, can be written as

$$p(ij) = R_e^2\,(\bar{r}_{ij})\, q(ij) \quad (II-9)$$

where q(i j) is the calculable Franck-Condon or overlap factor for the $i \rightarrow j$ transition and is given in terms of the vibrational configurations by

$$q(ij) = |\langle i|j\rangle|^2 \quad (II-10)$$

where $|i\rangle$ denotes the appropriate vibrational eigenket vector.

Also,

$$R_e^2(\bar{r}_{ij}) = |<i| R_e(r) |j>|^2 \qquad (II-11)$$

where $R_e(r) = < \eta|\sum\limits_{i=1}^{Z} r_e|\mu>$ electronic transition moment. The terms $|\eta>$ and $|\mu>$ represent the final and initial electronic state eigenkets, respectively, and r_{ie} is the displacement vector relative to the origin of the ith electron.

The electronic transition moment is calculable only for the simplest molecules and, as a result, must be experimentally determined for the $N_2^+(1-)$ system.

The r-centroid $\bar{r}_{ij}$ is defined by

$$\bar{r}_{ij} = <i|r||j>, <i||j> \qquad (II-12)$$

and represents an "average" internuclear distance r for the transition.

Table II-1 lists the calculated values of $q(ij)$ and $\bar{r}_{ij}$ as well as experimentally determined values of $p(ij)$. It is noted that for three bands for which $i-j = k-1 = \Delta_v$ and $i \neq k$, the values of the first r-centroids are very nearly equal, as are the wavelengths λ_{ij} and λ_{k1}. Since the r-centroids are very nearly equal, then $R_e(\bar{r}_{ij}) \cong R_e(\bar{r}_{k1})$ and

$$\frac{p(ij)}{p(kl)} \cong \frac{q(ij)}{q(kl)}$$

showing that use of the two bands ij and kl has the results of minimizing the inaccuracy of a vibrational temperature measurement, since $R_e(\bar{r}_{ij})$ usually has large errors associated with it. Additionally, since $\lambda_{ij} \cong \lambda_{kl}$ for $i-j = k - 1$, selection of these two band systems will minimize the error associated with making spectral sensitivity corrections. For these two reasons, the band pairs (01), (12), and (02), (13) were used for vibrational temperature measurements using the $N_2^+ (1-)$ system.

One should note that Eq. (II-8) contains not only emission band strengths, p_{ij}, but also excitation band strengths, $\tilde{p}$ (is), which have the same mathematical basis as the emission band strengths; unfortunately, no work has been performed to determine their values. Because of this ignorance, and with no other justification, excitation Franck-Condon factors, $\tilde{q}$ (is), are used in their stead, and these parameters are listed in Table II-2.

TABLE II-1
EMISSION FRANCK-CONDON FACTORS, BAND STRENGTHS AND r-CENTROIDS

v'	v''	$q(v'v'')$	$p(v',v'')$	$r(v'v'')$
0	0	0.6570	0.6364	1.0995
0	1	0.2982	0.2611	1.1523
1	0	0.2546	0.2693	1.0512
1	1	0.2316	0.2189	1.1124
2	0	0.0686	0.0776	1.0227
2	1	0.2838	0.2971	1.0572
3	0	0.0157	0.0189	0.9543
3	1	0.1299	0.1458	1.0177
4	0	0.0033	0.0004	0.8923
4	1	0.0418	0.0498	0.9832

TABLE II-2
EXCITATION FRANCK-CONDON FACTORS $q(v',v'')$

v'	v''	$q(v'v'')$
0	0	0.8794
0	1	0.1184
1	0	0.1063
1	1	0.6874
2	0	0.0128
2	1	0.1606
3	0	0.0014
3	1	0.0290

147

The radiative lifetimes $\tau_r(0)$ and $\tau_r(1)$ are required to evaluate Eq. (II-8), and for this purpose the value of $\tau_r(0) = 6.58 \times 10^{-8}$ reported by Bennett and Dalby (Ref. II-8) is used. Using results of experimental intensity data $\tau_r(1)$ was found to be 6.50×10^{-8} sec. With these values the ratio of intensities of the two just-mentioned band pairs are shown in Fig. II-6 as a function of T_v; with these curves measured ratios of band intensity can be related directly to the vibrational temperature.

Returning to Eq. (II-7), one sees that the band intensity $I_{v'v''}$ can be written as

$$I_{v'v''} = C_2 \, j \, N(N_2) \, \frac{\sum\limits_{v'''=0}^{\infty} \bar{p}(v',v''') e^{-\hat{G}(v''')hc/kT_v}}{\sum\limits_{v'''=0}^{\infty} e^{-\hat{G}(v''')hc/kT_v}} \qquad (II-13)$$

where C_2 is a constant, thereby enabling one to make a determination of the neutral nitrogen number density $N(N_2)$ by simply measuring the integrated band intensity, so long as T_v is known.

Selecting the most intense vibrational band $v' = v'' = 0$ for use in Eq. (II-13) and the measurement of $N(N_2)$, Fig. II-7, shows I_{00} as a function of $N(N_2)$ for various values of T_v, thereby demonstrating not only the linear dependence of I_{00} on $N(N_2)$ but also the errors to be encountered by an ignorance of T_v.

In the event the density $N(N_2)$ is sufficiently large that $k\tau_r N(N_2)$ becomes significant relative to unity, as with He, effects attributable to addition of collision decay channels must be considered. Figure II-8 shows a phenomenological model of the radiative and collisional deexcitation processes for the vibrational levels 0 and 1 of the $N_2^+ B^2 \Sigma$ state where $k_0(N_2^+, N_2)$ and $k_1(N_2^+, N_2)$ represent the density-dependent rate constants for N_2 collision quenching of the $v = 0$ and 1 levels, respectively. With this model one can easily show that the intensity of the $v' = 0$, $v'' = 0$ band can be written as

$$I_{00} = I_{00}^o \cdot (N(N_2)/[1 + k_0(N_2^+, N_2) \, r(0) \, N(N_2)]) \qquad (II-14)$$

where the vibrational-temperature-dependent quantity I_{00}^o is the limit of I_{00} as $N(N_2)$ approaches zero.

Values of $k_0(N_2^+, N_2)$ and $k_1(N_2^+, N_2)$ have been estimated to be 2.1×10^{-10} cm^3/sec and 3.1×10^{-10} cm^3/sec, respectively, at 300°K. With the same qualifications for the temperature dependence of the quenching constants as stated for He, one can now employ Eq. (II-14) for a measurement of $N(N_2)$ for those regions of $N(N_2)$ for which collisional effects are important, the upper $N(N_2)$ limit being determined by the decreasing slope of I_{00} versus $N(N_2)$ and the slope finally approaching zero at several torr at room temperature.
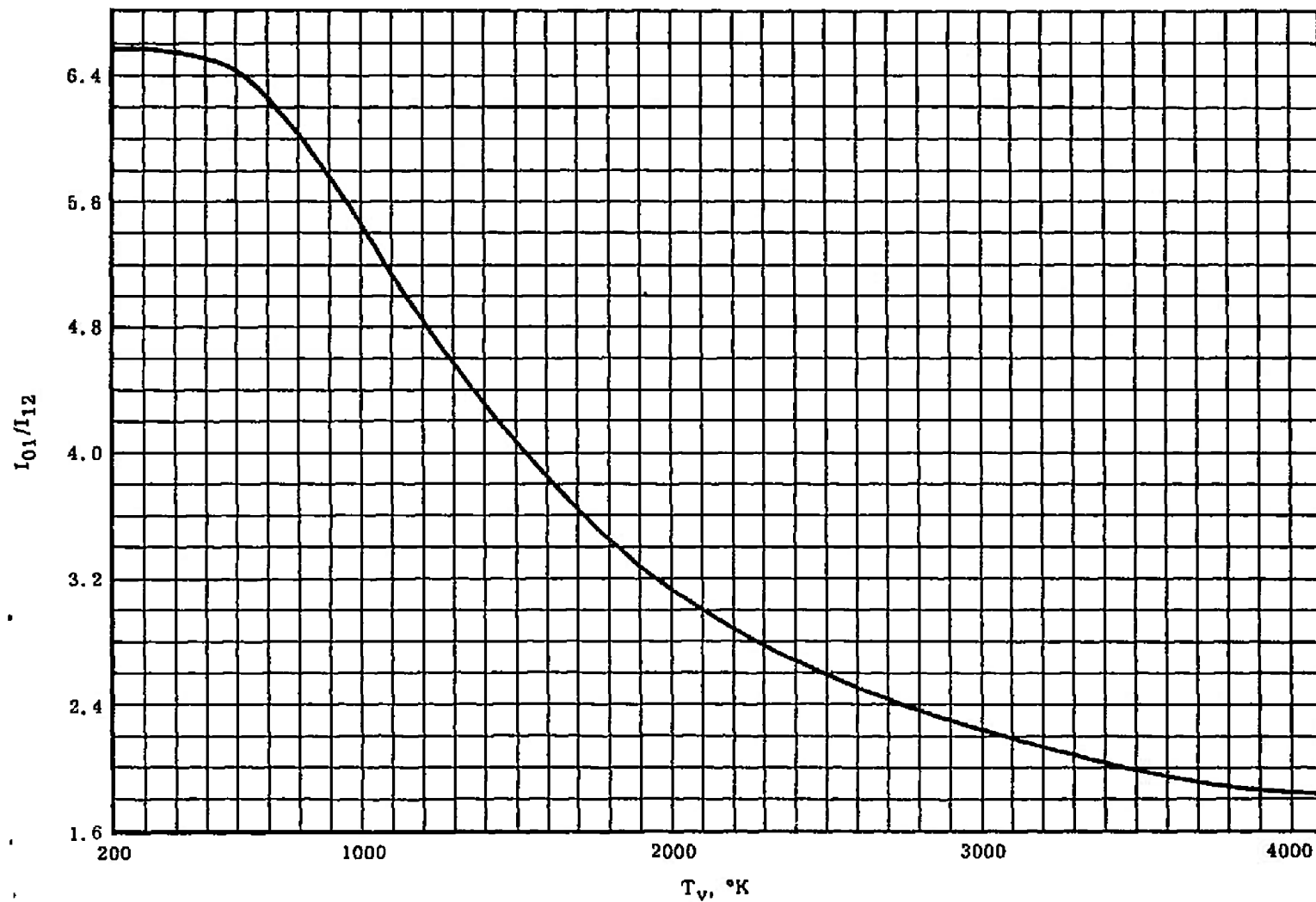
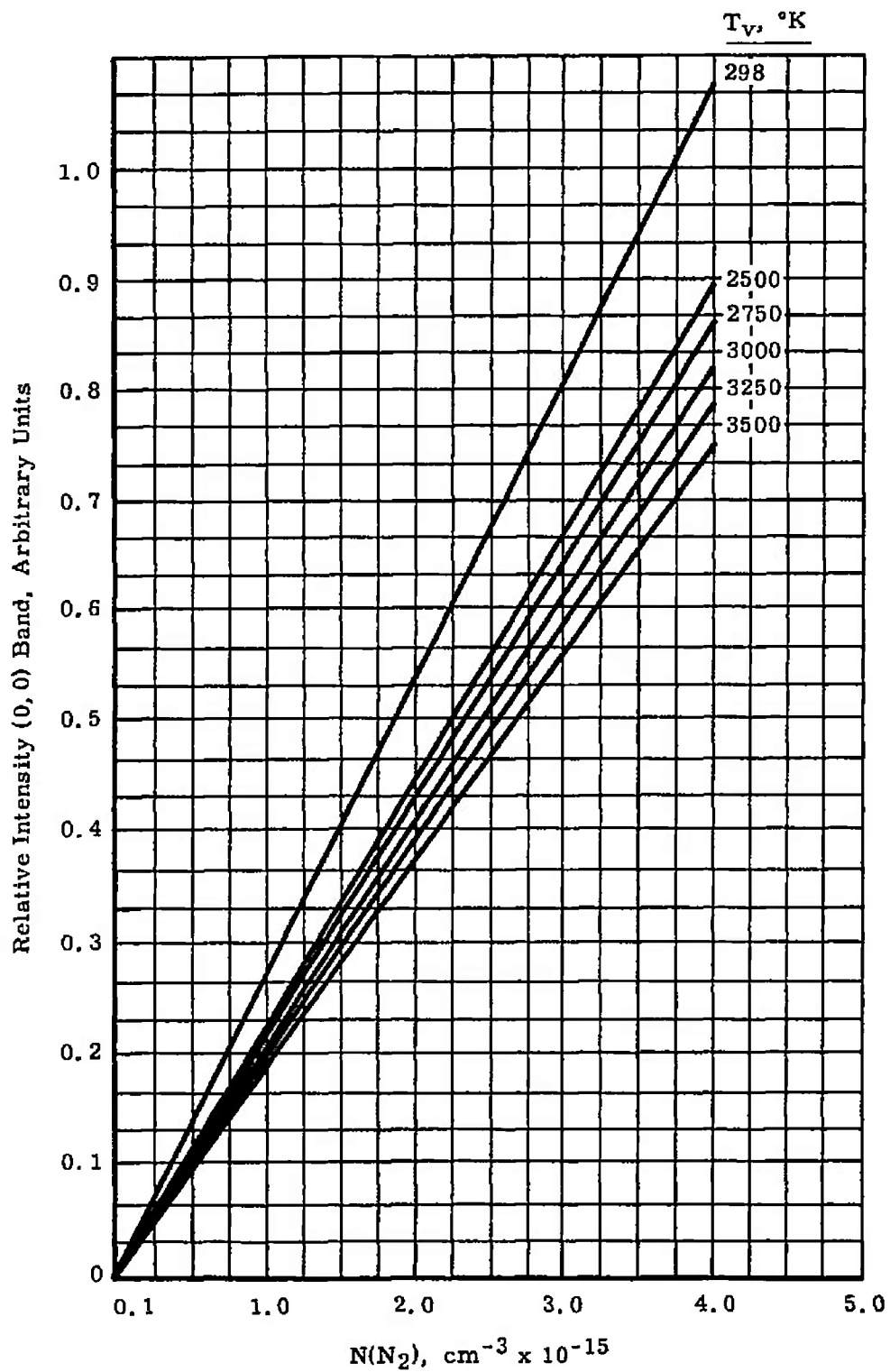Fig. II-6 Band Intensity Ratio I_{01}/I_{12} versus Vibrational Temperature

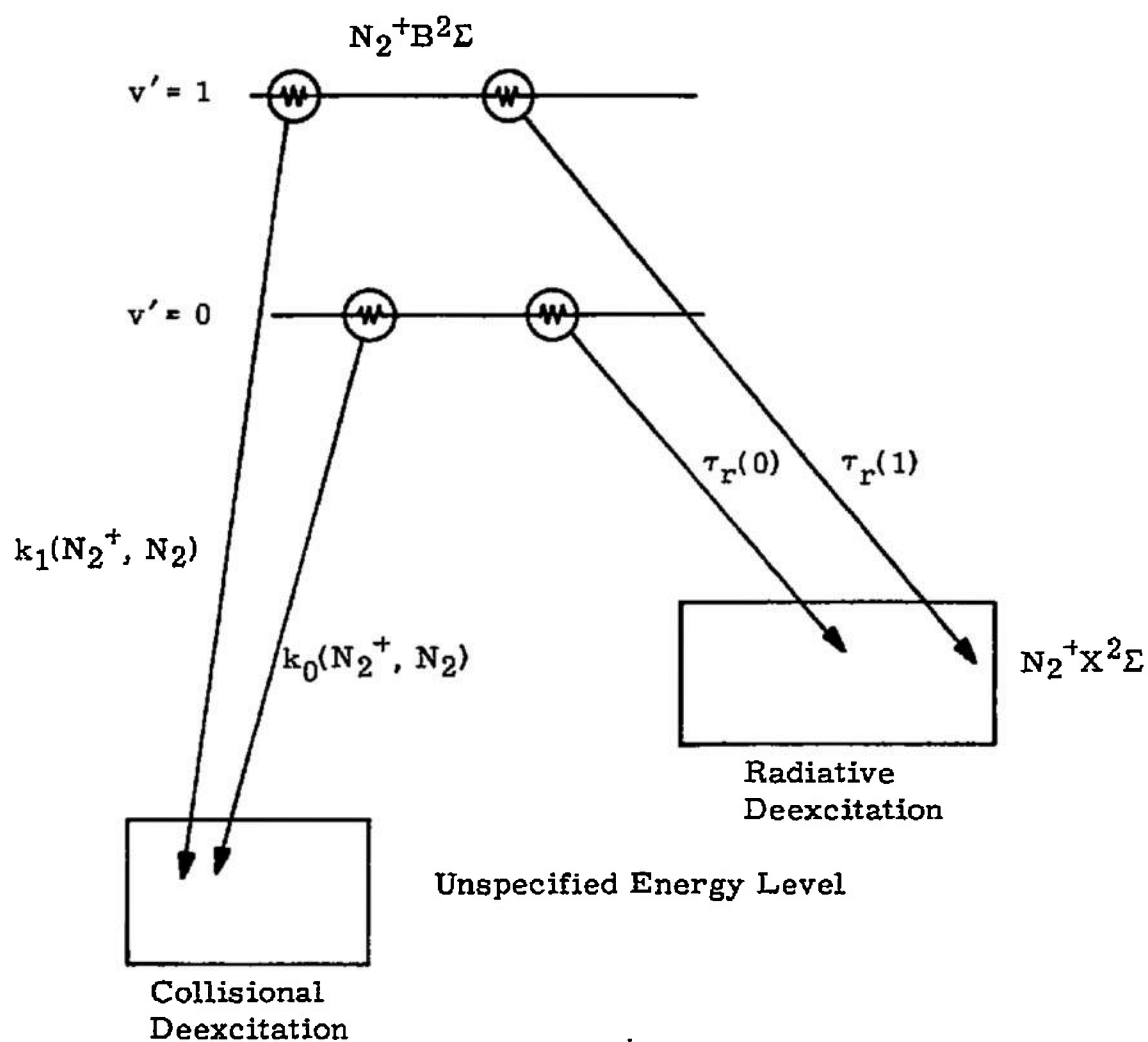Fig. II-7 Relative Intensity 10.0 Band (Arbitrary Units)

Fig. II-8 Phenomenological Collisional-Radiative Decay Scheme of $N_2^+B^2\Sigma$.

To conclude remarks concerning pure nitrogen, the effects of collisions upon the vibrational temperature determination are obtained by generalizing Eq. (II-8) using Eq. (II-14) to yield

$$\frac{I_{oj}}{I_{11}} = \left(\frac{I_{oj}}{I_{11}}\right)^o X \frac{[1 + k_1(N_2^+, N_2) \, \tau_r(1) \, N(N_2)]}{[1 + k_o(N_2^+, N_2) \, \tau_r(0) \, N(N_2)]} \tag{II-15}$$

where $\left(\dfrac{I_{oj}}{I_{11}}\right)^o$ is the low density limit of Eq. (II-15) and is identical with the right-hand side of Eq. (II-8). It is emphasized that dependence of Eq. (II-15) upon the kinetic temperature, T_∞, is at present unknown, and when employed, it must be done with caution.

EXCITATION OF A BINARY MIXTURE OF HELIUM AND NITROGEN

In the event the gas sample is a binary mixture of He and N_2, the preceding equations, notably Eqs. (II-2), (II-6), (II-8), and (II-13), are valid as long as collisional effects are negligible. Over the density regime for which collisional effects first become discernible, one expects Eqs. (II-3), (II-14), and (II-15) to serve adequately as first-order approximations. However, for sufficiently high values of density the above equations must be replaced by expressions in accord with the approximate model as shown in Figs. II-9 and II-10. These appropriate equations are

$$I(5016) = \frac{C_2 \cdot j \cdot N(He)}{1 + [k(He, He) N(He) + k(He, N_2) N(N_2)] \tau(3^1 P)} \tag{II-16}$$

$$I_{oo} = I_{oo}^o N(N_2) / [1 + k_o(N_2^+, N_2) N(N_2) + k_o(N_2^+, He) N(He)] \cdot \tau_r(0) \tag{II-17}$$

$$\frac{I_{oj}}{I_{11}} = \left(\frac{I_{oj}}{I_{11}}\right)^o \frac{\{1 + [k_1(N_2^+, N_2) N(N_2) + k_1(N_2^+, He) N(He)] \tau_r(1)}{\{1 + [k_o(N_2^+, N_2) N(N_2) + k_1(N_2^+, He) N(He)] \tau_r(0)} \tag{II-18}$$

Of the quenching constants found in the preceding three equations, $k_o(N_2^+, He)$, $k_1(N_2^+, He)$, and $k(He, N_2)$ are unknown at present and can only be estimated if needed. Table II-3 lists the values of those rate constants that were previously mentioned as having been obtained at 300°K and also shows values of those unknown quenching rates that are estimated using elastic scattering collision rates of charged-uncharged pairs of species (Ref. II-9).

Rewriting Eq. (II-18) as

$$\frac{I_{oj}}{I_{11}} = \left(\frac{I_{oj}}{I_{11}}\right)^o \cdot R \tag{II-19}$$
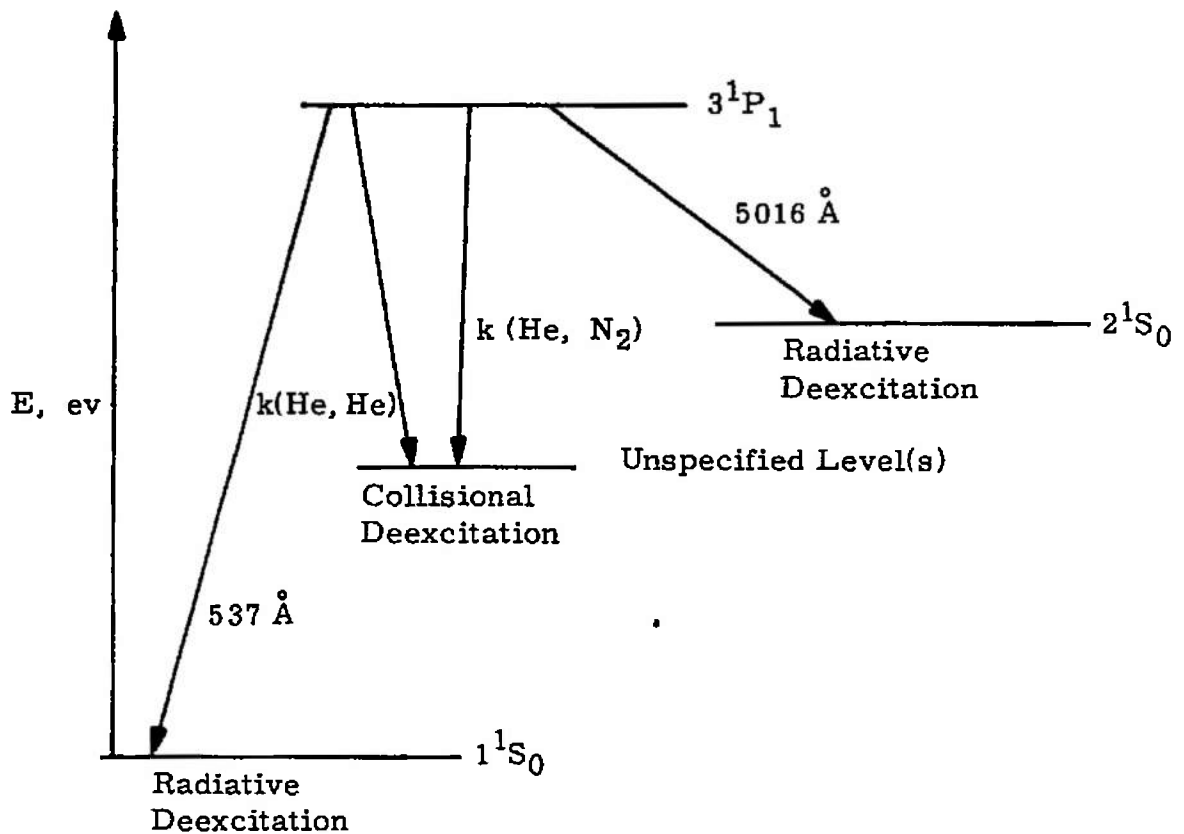
a. Phenomenological Model of Collision
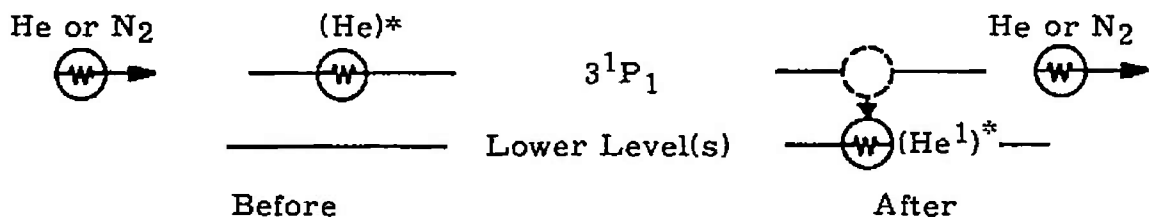
b. Schematic of Collision Process

Fig. II-9 Collisional-Radiative Deexcitation Model of HeI
(3^1P_1) in Mixture of Nitrogen and Helium

$$N_2{}^+B^2\Sigma$$

v' = 1

v' = 0

E, ev

$k_0(N_2{}^+, N_2)$

$k_1(N_2{}^+, N_2)$

$k_0(N_2{}^+, He)$

$k_1(N_2{}^+, He)$

$\tau_r(1)$

$\tau_r(0)$

$N_2{}^+X^2\Sigma$

Unspecified Energy Level

a. Phenomenological Model of Collision

He or N_2

$N_2{}^+$

He or N_2

Lower Level(s)

$N_2{}^+$
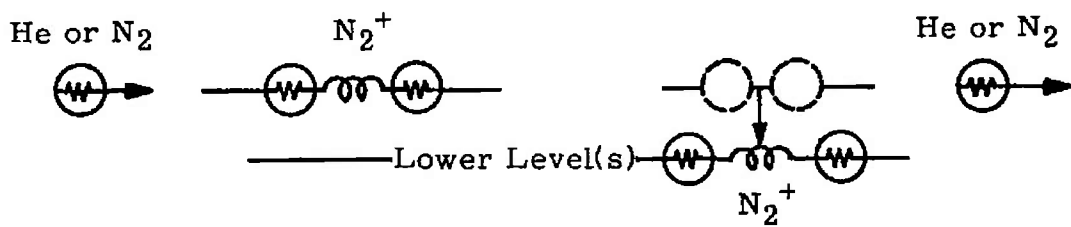
b. Schematic of Collision Process
Fig. II-10 Collisional-Radiative Decay Scheme of $N_2{}^+B^2\Sigma$
in a Mixture of Nitrogen and Helium

TABLE II-3
QUENCHING RATE CONSTANTS

Rate Constant	T, °K	Magnitude, cm^3/sec
$k(He, He)$	300	1.98×10^{-10}
$k_0(N_2^+, N_2)$	300	2.1×10^{-10}
$k_1(N_2^+, N_2)$	300	3.1×10^{-10}
$k(He, N_2^+)$		$(10^{-10})*$
$k_0(N_2^+, He)$		$(10^{-10})*$
$k_1(N_2^+, He)$		$(10^{-10})*$

*   Estimated

where R is the density-dependent factor of Eq. (II-18), one sees that, using the estimated rate constants of Table II-3

$$R = \frac{1 + 0.02015\ N(N_2) + 0.0065\ N(He)}{1 + 0.01382\ N(N_2) + 0.0066\ N(He)} \tag{II-20}$$

where the number densities are expressed in units of $10^{15}/cm^3$. Figure II-11 shows R as a function of the nitrogen number density $N(N_2)$, assuming $N(He)$ is zero. For the range of $N(He)$ values encountered in the test, the correction attributable to quenching collisions with helium atoms is negligible—a result which was ensured by assuming the equality of values of $k_0(N_2^+, He)$ and $k_1(N_2^+, He)$.

The density correction for the rotational temperature data has not been discussed because none of the quenching constants for the individual rotational levels are at present known. If sufficient interest and requirements exist, this determination is straightforward.

CALIBRATION OF ELECTRON BEAM

HELIUM NUMBER DENSITY CALIBRATION

Calibration of the device consists of determining the constant C in Eq. (II-2) which relates the intensity of the 5016-Å line to the current density and helium number density. The calibration was performed statically in the tunnel using the system shown in Fig. II-12. The system consists of an electron drift tube extension, test chamber, vacuum pumps and valves, bleed valve, helium supply, Equibar pressure meter, and retractable beam receiver cup. The drift tube and test chamber were bolted to the orifice plate of the electron gun system. Test chamber pressure was measured with the Equibar pressure meter (a portable, differential, variable-capacitance micromanometer). Reference pressure for the pressure meter was the electron gun section pressure (less than 1×10^{-4} torr). Beam current was read with a digital voltmeter.

The calibration system (with helium supply valve closed) was first evacuated to a pressure of approximately 0.2 torr. The bleed valve was then closed, and the helium supply valve opened. A pressure of 40 psia was then set on the high pressure side of the bleed valve. The vent valve on the high pressure side of the bleed valve was opened for approximately 1 min to further purify the helium to be leaked into the test chamber. With the bleed valve closed, the remainder of the calibration system was pumped down to less than 5×10^{-4} torr with a leak rate of less than 1×10^{-4} torr/min. Helium was then leaked into the
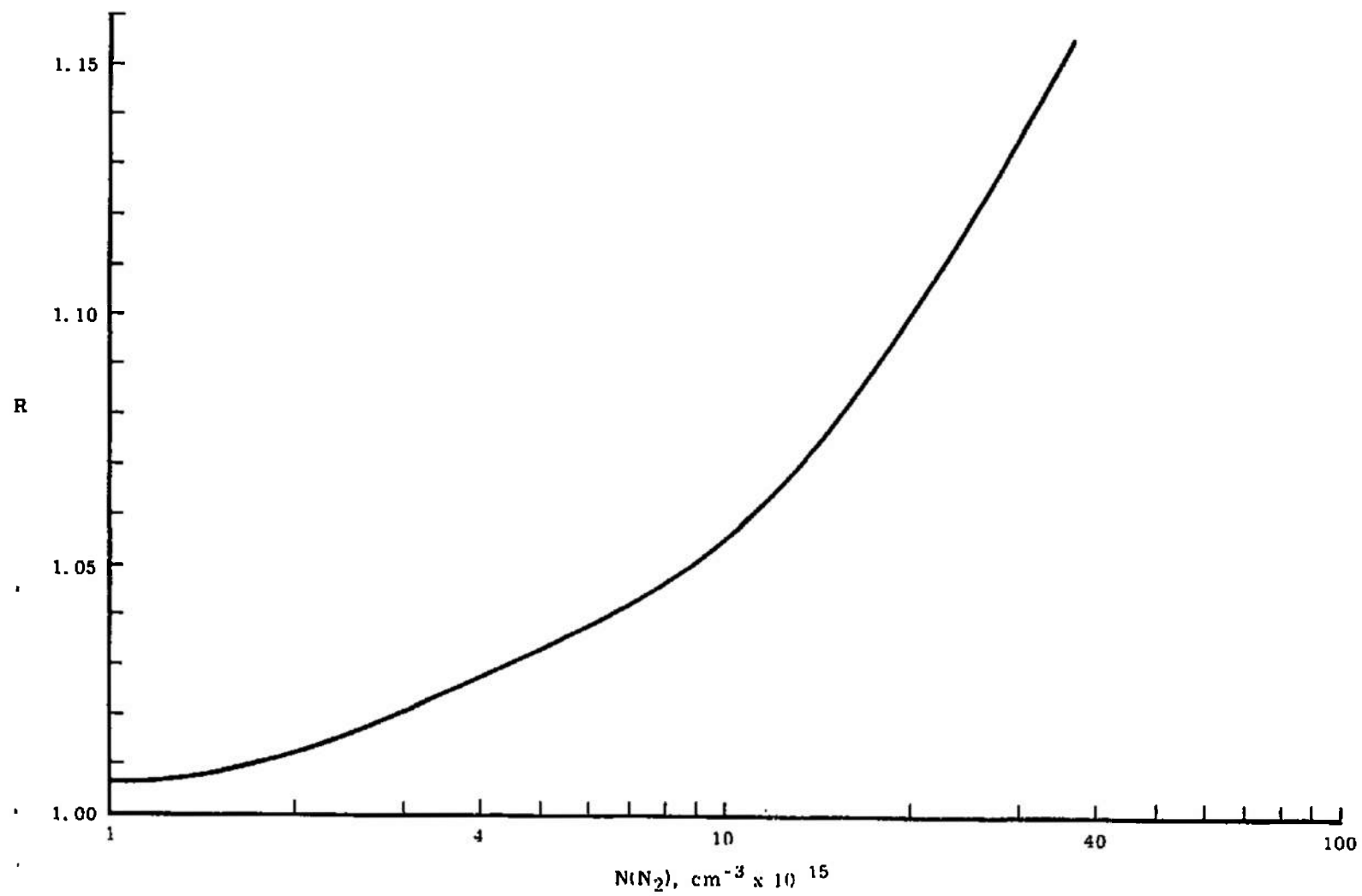
Fig. II-11 R as a Function of Nitrogen Number Density

Top of Tunnel

Probe Drive

Electron Gun Housing

Bulkhead

Pneumatic Vacuum Valve

Orifice Block

Diffuser

Settling Chamber

Drift Tube Extension

Valve

Test Chamber View Port

To Rough Pump

Retractable Receiver Cup

To Equibar

Valve

Nozzle

2-in. Oil Diffusion Pump

Helium Supply Valve

To Forepump

Beam Receiver Plate

Bleed Valve

Regulator

Vent

Electron Beam Vacuum Line

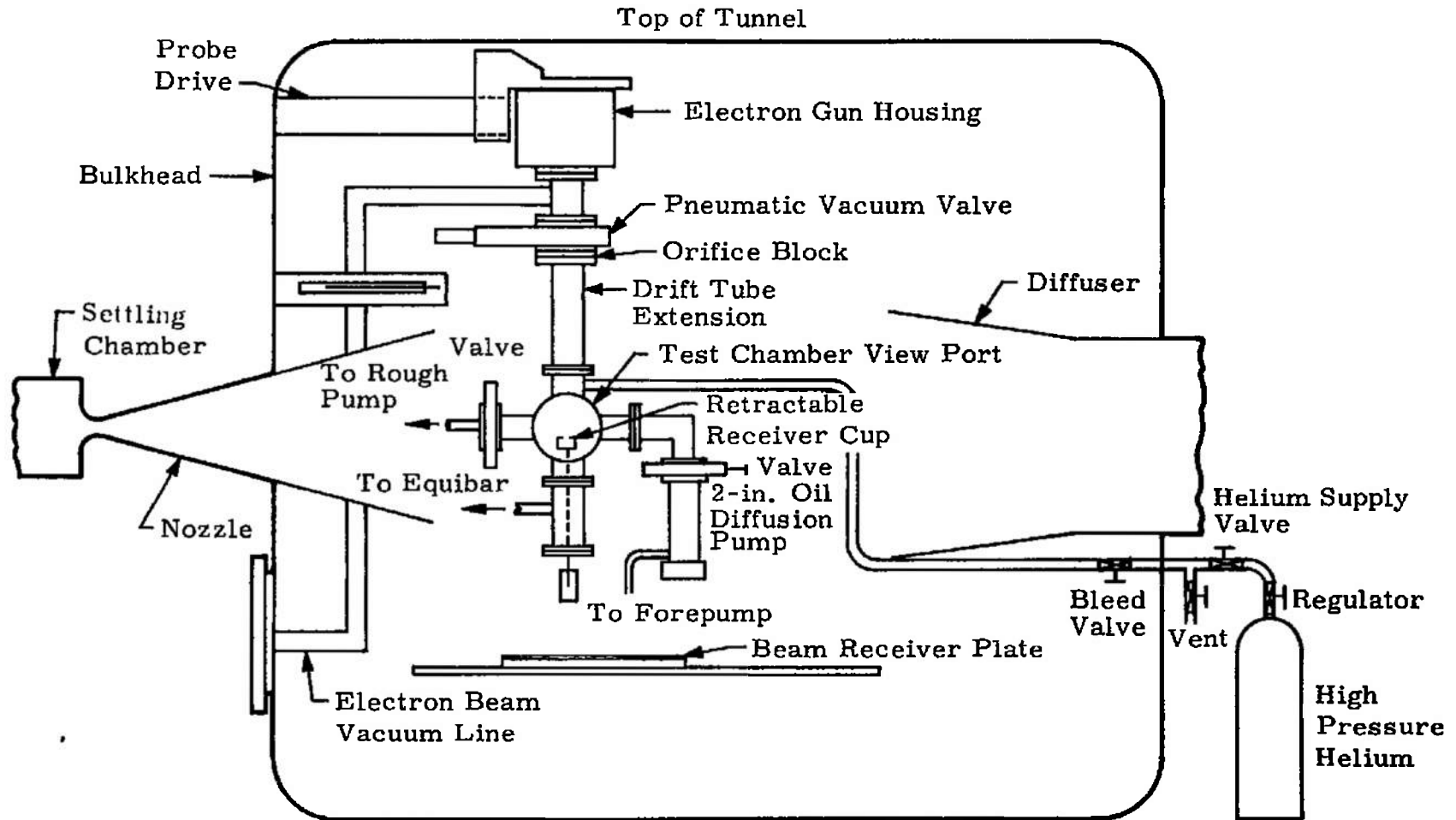High Pressure Helium

Fig. II-12 Schematic Drawing of Tunnel M Electron Beam Installation and Helium Calibration System

test chamber through the bleed valve until the desired test chamber pressure was achieved. The electron beam was then injected into the chamber. The intensity of the 5016-Å line was measured using the integration technique described in Section 3.5. For each pressure setting the line intensity was measured twice, and the beam current was measured with the retractable receiver cup positioned at the point along the electron beam that was focussed on the spectrometer slit. There was a small difference in beam area distribution between the test chamber and actual plume conditions. However, from the data of Center (Ref. II-3), for a number density of $1.5 \times 10^{15}/cm^3$, the beam diameter is approximately 15 mm. Since the magnification factor for the optical system was 1/2, this gave an effective diameter of 7.5 mm which was easily collected by the 20-mm-high spectrometer slit.

Two helium calibrations were made and are shown in Fig. II-13. The calibrations are plotted as the ratio of 5016-Å intensity to beam current versus helium pressure at 300°K. This ratio is a fairly linear function of helium density as it should be over the calibration density range in Fig. II-13.

NITROGEN NUMBER DENSITY CALIBRATION

Nitrogen number densities are related to the intensity through Eq. (II-13). The reference density was taken as the Tunnel M center-line free-stream density. The $N_2^+[1-]$ (0,0) band intensity was measured using the band integration technique, and beam current was measured at both the auxiliary and flat-plate positions. With each measurement of band intensity and current, readings of the tunnel conditions were made. Normally three of four band measurements were made to give an average ratio of band intensity to beam current, and the tunnel data reduction program provided a calculation of nitrogen number density. With the valid assumption that the relation of band intensity to N_2 number density was linear for the number density range in this test, this single-point calibration technique provided the necessary calibration of band intensity versus number density. This calibration procedure was repeated each time that nitrogen number density measurements were made in the plume. Slit settings, photomultiplier supply voltage, and lock-in amplifier scales were kept the same during tunnel measurements as they were during the calibration.

SPECTRAL SENSITIVITY CALIBRATION

In order to check the relative spectral sensitivity of the optical system, a calibrated, tungsten-ribbon, standard lamp was set inside Tunnel M. With the lamp turned on, the test section was closed and
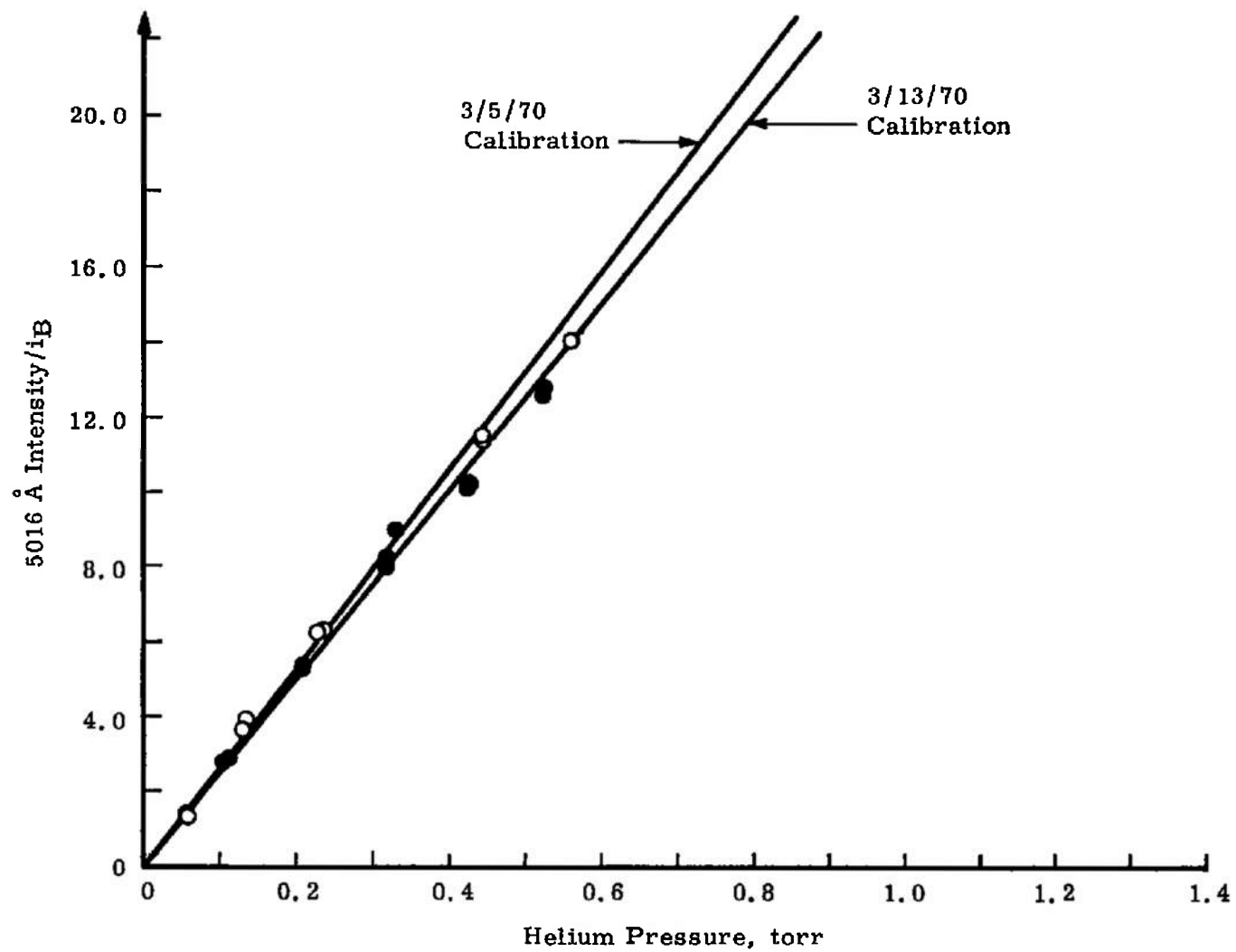
Fig. II-13 Helium Calibrations

PM: EMI-6256B
PMV: 1780 v
Optics: Dove Prism, Lens,
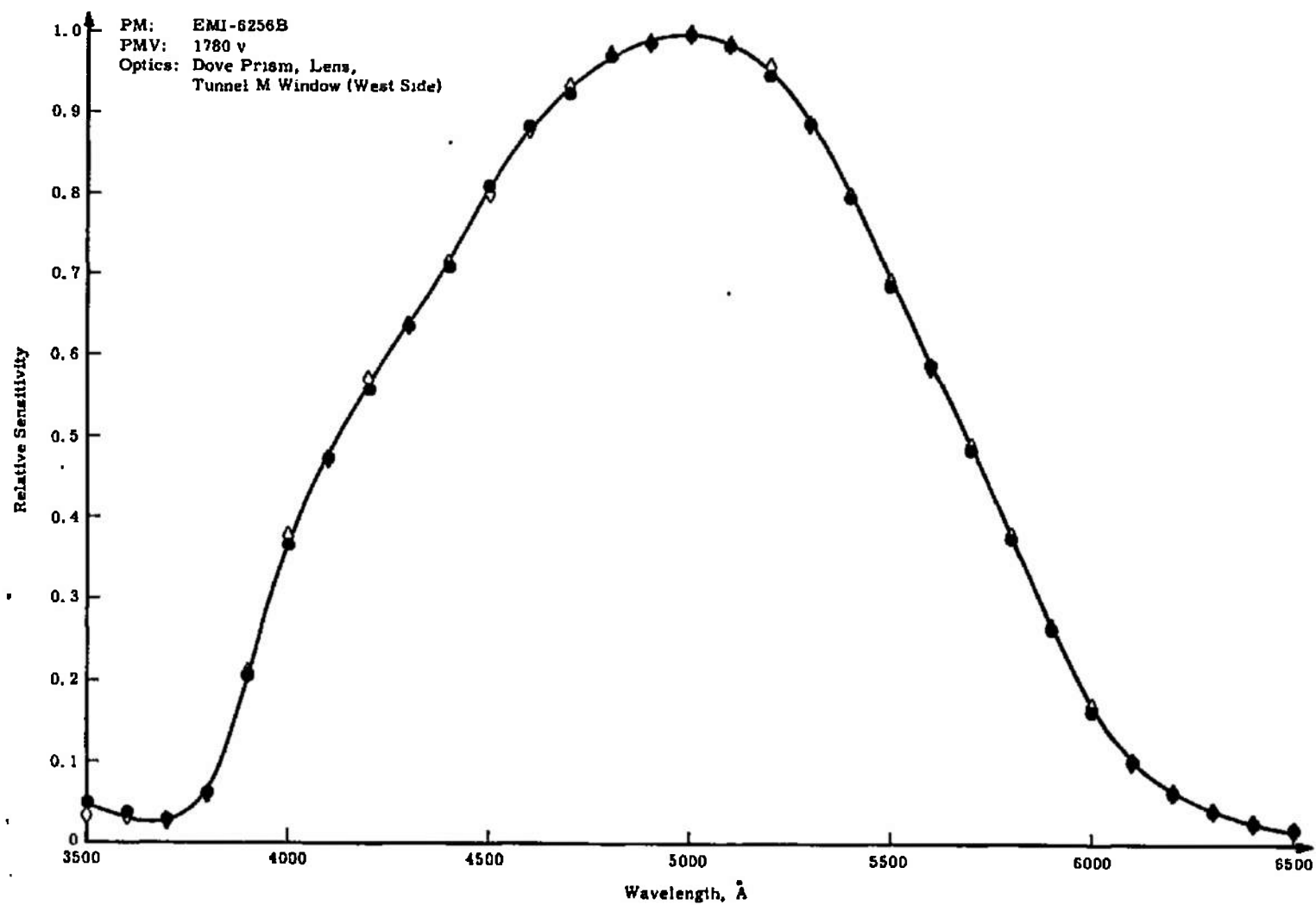Tunnel M Window (West Side)

Fig. II-14 Relative Sensitivity of Tunnel M Optical System

the lamp ribbon was focussed onto the slit of the 1-meter spectrometer. In this manner the relative spectral sensitivity of the entire optical system was checked. Two wavelength scans from 3500 to 6500 Å were made, and the relative sensitivity of the Tunnel M optical system is shown in Fig. II-14.

As explained in Section 4.4 a ratio of band intensities was used for a determination of vibrational temperature. As can be seen from Fig. II-14 a small relative sensitivity correction had to be applied to these ratios. For the rotational scans of the R branch of the N_2^+ [1$^-$] (0,0) band only about a 1-percent relative sensitivity variation is evident, and therefore neglected.

REFERENCES

II-1.   Muntz, E. P. "Measurement of Rotational Temperature, Vibrational Temperature and Molecular Concentration in Non-Radiating Flows of Low Density Nitrogen." University of Toronto Institue of Aerophysics Report 71, Toronto, Canada, April 1961.

II-2.   Muntz, E. P. and Marsden, D. J. "Electron Excitation Applied to the Experimental Investigation of Rarefied Gas Flows." Rarefied Gas Dynamics Symposium, Vol. II, (Edited by J. A. Laurmann), pp. 495-526, Academic Press, Inc., New York, New York, 1963.

II-3.   Center, R. E. "Plural and Multiple Scattering of Fast Electrons in Gases." Physics of Fluids, Vol. 13, pp. 79-88 (1970).

II-4.   Maguire, B. L. "The Effective Spatial Resolution of the Electron Beam Flourescence Probe in Helium." Rarefied Gas Dynamics (Edited by C. L. Brundin), Vol. II, pp. 1497-1517, Academic Press, Inc., New York, N. Y., 1967.

II-5.   Phelps, A. V. "Effect of the Imprisonment of Resonance Radiation on Excitation Experiments." Phys. Rev., Vol. 110, 1958, pp. 1362-1368.

II-6.   Williams, W. D. "Laboratory Verification Studies of Rotational and Vibrational Temperature Measurements by the Electron Beam Technique." AEDC-TR-68-265 (AD683001), February 1969.

II-7. Lewis, J. W. L. and Williams, W. D. "Vibrational Tempera-
       ture Measurements Using the Electron Beam." AIAA,
       Vol. 7, 1969, pp. 1202-1204.

II-8. Bennett, R. G. and Dalby, F. N. "Experimental Determination
       of the Oscillator Strength of the First Negative System of
       N_2^+." J. Chem. Physics, Vol. 31, 1959, pp. 434-441.

II-9. Johnston, H. W. Gas Phase Reaction Rate Theory, p. 144, The
       Ronald Press Company, New York, N. Y., 1966.

DOCUMENT CONTROL DATA - R & D

(Security classification of title, body of abstract and indexing annotation must be entered when the overall report is classified)

1 ORIGINATING ACTIVITY (Corporate author)	2a. REPORT SECURITY CLASSIFICATION
Arnold Engineering Development Center ARO, Inc., Operating Contractor Arnold Air Force Station, Tennessee 37389	UNCLASSIFIED
	2b. GROUP N/A

3. REPORT TITLE

EXPERIMENTAL STUDY OF SIMULATED HIGH ALTITUDE
ROCKET EXHAUST PLUMES

4. DESCRIPTIVE NOTES *(Type of report and inclusive dates)*
Final Report, February 18 to May 1, 1970

5. AUTHOR(S) *(First name, middle initial, last name)*

Wendell Norman, Max Kinslow, and J. W. L. Lewis, ARO, Inc.

6. REPORT DATE	7a. TOTAL NO. OF PAGES	7b. NO. OF REFS
July 1971	176	18

8a. CONTRACT OR GRANT NO. F40600-71-C-0002	9a. ORIGINATOR'S REPORT NUMBER(S)
b. PROJECT NO.	AEDC-TR-71-25
c. Program Element 62302F	9b. OTHER REPORT NO(S) *(Any other numbers that may be assigned this report)*
d.	ARO-VKF-TR-70-258

10. DISTRIBUTION STATEMENT

Approved for public release; distribution unlimited.

11. SUPPLEMENTARY NOTES	12. SPONSORING MILITARY ACTIVITY
Available in DDC.	Air Force Rocket Propulsion Laboratory (RPP), Edwards AFB, California 93523

13. ABSTRACT

The gas dynamic structure of high altitude rocket plumes has been studied in a low density tunnel to obtain basic data on plume size and shape and to determine the extent of the mixing region between the free-stream and rocket gases. The rocket was simulated by specially designed ejectors using helium and CO_2 as the gases, with conditions chosen to simulate a 100,000-lb-thrust rocket at an altitude of 80 km. Data taken included impact pressure surveys, density measurements of the free-stream and plume gas, temperature measurements, and color photographs. The last three of these were taken using electron beam techniques. The result of the study is a set of basic data. Analysis and interpretation of the data will be performed under a separate study.

14. KEY WORDS	LINK A		LINK B		LINK C	
	ROLE	WT	ROLE	WT	ROLE	WT
plumes						
altitude simulation						
temperature						
pressure						
density						
electron beams						
hypersonic wind tunnels						